

RL-TR-96-289  
Final Technical Report  
May 1997



# A COHERENT, OPTICALLY CONTROLLED PHASED ARRAY SYSTEM

Princeton University

Stephen R. Forrest, Ligeng Xu, Robert Taylor,  
P.M. Freitag and H.V. Poor

*APPROVED FOR PUBLIC RELEASE; DISTRIBUTION UNLIMITED.*

DTIC QUALITY INSPECTED 4

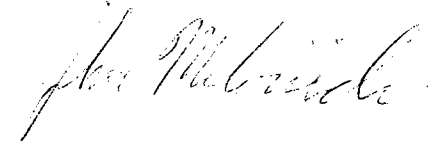
19970728 137

Rome Laboratory  
Air Force Materiel Command  
Rome, New York

This report has been reviewed by the Rome Laboratory Public Affairs Office (PA) and is releasable to the National Technical Information Service (NTIS). At NTIS it will be releasable to the general public, including foreign nations.

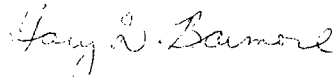
RL-TR-96-289 has been reviewed and is approved for publication.

APPROVED:



JOHN MALOWICKI  
Project Engineer

FOR THE COMMANDER:



GARY D. BARMORE, Maj, USAF  
Deputy Director  
Surveillance & Photonics Directorate

If your address has changed or if you wish to be removed from the Rome Laboratory mailing list, or if the addressee is no longer employed by your organization, please notify RL/OCPC, 25 Electronic Pky, Rome, NY 13441-4515. This will assist us in maintaining a current mailing list.

Do not return copies of this report unless contractual obligations or notices on a specific document require that it be returned.

REPORT DOCUMENTATION PAGE			Form Approved OMB No. 0704-0188	
Public reporting burden for this collection of information is estimated to average 1 hour per response, including the time for reviewing instructions, searching existing data sources, gathering and maintaining the data needed, and completing and reviewing the collection of information. Send comments regarding this burden estimate or any other aspect of this collection of information, including suggestions for reducing this burden, to Washington Headquarters Services, Directorate for Information Operations and Reports, 1215 Jefferson Davis Highway, Suite 1204, Arlington, VA 22202-4302, and to the Office of Management and Budget, Paperwork Reduction Project (0704-0188), Washington, DC 20503.				
1. AGENCY USE ONLY (Leave blank)		2. REPORT DATE May 1997	3. REPORT TYPE AND DATES COVERED FINAL, Jan 93 - Jul 96	
4. TITLE AND SUBTITLE A COHERENT, OPTICALLY CONTROLLED PHASED ARRAY SYSTEM			5. FUNDING NUMBERS C - F30602-93-C-0060 PE - 63726F PR - 2863 TA - 92 WU - 59	
6. AUTHOR(S) Stephen R. Forrest, Ligeng Xu, Robert Taylor, P.M. Freitag, H.V. Poor				
7. PERFORMING ORGANIZATION NAME(S) AND ADDRESS(ES) Princeton University Department of Electrical Engineering Advanced Technology Center for Photonic & Optoelectronic Materials Princeton NJ 08544			8. PERFORMING ORGANIZATION REPORT NUMBER	
9. SPONSORING / MONITORING AGENCY NAME(S) AND ADDRESS(ES) Rome Laboratory/OCPC 25 Electronic Pky Rome NY 13441-4515			10. SPONSORING / MONITORING AGENCY REPORT NUMBER  RL-TR-96-289	
11. SUPPLEMENTARY NOTES  Rome Laboratory Project Engineer: John E. Malowicki, OCPC, (315) 330-4682				
12a. DISTRIBUTION AVAILABILITY STATEMENT  APPROVED FOR PUBLIC RELEASE; DISTRIBUTION UNLIMITED			12b. DISTRIBUTION CODE	
13. ABSTRACT (Maximum 200 words) An optically controlled microwave phased array antenna system is analyzed. Beamforming is accomplished with a large number of antenna elements that can receive any of several different true-time delays from a single fiber using multi-channel optical heterodyne techniques. System performance such as signal-to-noise ratio, signal-to-interchannel interference ratio, and dynamic range (DR) for various modulation-demodulation schemes (i.e. AM, FM, and PM) are quantitatively analyzed. An experimental system insensitive to laser linewidth and IF frequency instabilities is demonstrated. Accurate true-time delay is demonstrated across the L band (0.8 to 1.5 GHz). The DR for one channel is 52 dB/MHz. For a narrow channel spacing of 1 angstrom at 1.55 micrometers, the interchannel interference is < -50dB. Also, monolithic photonic integration using vertical twin-waveguide (TG) structure based on single-step MBE grown InP/InGaAsP material is studied as a means of practical implementation of large scale photonic systems. Finally, high efficiency, high power semiconductor lasers employing a 1.5 micron InGaAsP/InP separate confinement multi-quantum well structure, are investigated for use in high DR, high density RF-optical links.				
14. SUBJECT TERMS True-Time Delay, Phased Array Antenna, Optical Heterodyne, Twin-Waveguide, Semiconductor Lasers			15. NUMBER OF PAGES 286	
			16. PRICE CODE	
17. SECURITY CLASSIFICATION OF REPORT UNCLASSIFIED	18. SECURITY CLASSIFICATION OF THIS PAGE UNCLASSIFIED	19. SECURITY CLASSIFICATION OF ABSTRACT UNCLASSIFIED	20. LIMITATION OF ABSTRACT UNLIMITED	

## Table of contents

Abstract .....	viii
1. Introduction.....	1
1.1 Operation of optically controlled phased array antennas.....	2
1.2 Introduction to laser/waveguide integration in a vertical twin-waveguide structure and low loss lasers with broadened waveguide.....	10
2. Analysis of a true-time delay phased array antenna system using coherent optical detection techniques.....	25
2.1 Introduction.....	28
2.2 System description.....	29
2.3 System evaluation.....	42
2.4 Analog AM antenna links.....	50
2.5 FM and PM phase delay schemes.....	62
2.6 System comparisons.....	71
2.7 Conclusions.....	73
3. First experimental demonstration of a coherent optically controlled phased array system.....	81
3.1 System experiments.....	81
3.2 The effect of the IF amplifier phase response on the system performance.....	92

4	Semiconductor Ridge Waveguide Lasers and Related Devices for Optical Integration.....	97
	4.1 Semiconductor Laser Gain and Output Characteristics.....	97
	4.2 Numerical analysis of a one dimensional TE waveguide structure.....	105
	4.3 Fabrication and performance of ridge lasers and SOAs.....	111
5.	Photonic device integration using vertical twin-waveguide structure.....	125
	5.1 Basic concepts of twin-waveguide structures.....	126
	5.2 Twin-waveguide material design.....	135
	5.3 Monolithic integration of a 1.55 $\mu\text{m}$ wavelength MQW laser/waveguide using TG.....	144
	Appendix 1.....	161
	Appendix 2.....	164
	Appendix 3.....	166
	Appendix 4.....	167
	Appendix 5.....	170
	Appendix 6.....	175
	Appendix 7.....	178
	Appendix A .....	A-1
	Appendix B.....	B-1
	Appendix C.....	C-1
	Appendix D.....	D-1
	Appendix E.....	E-1

## List of Figures

Fig. 1.1	Basic concepts of optically controlled phased array.....	4
Fig. 1.2	Parallel and serial true time-delays.....	6
Fig. 1.3	A coherent optically controlled phased array antenna transmitter.....	9
Fig. 1.4	Monolithic laser/waveguide integration using a single step epitaxy on an etched substrate.....	13
Fig. 1.5	Monolithic integration of laser/waveguide using impurity induced disordering.....	14
Fig. 1.6	Monolithically integrated laser/wavguide in a twin-waveguide structure..	16
Fig. 2.1	The coherent optically controlled phased array antenna transmitter.....	30
Fig. 2.2	Expansion methods for the transmitter structure.....	32
Fig. 2.3	The coherent optically controlled phased array antenna receiver.....	33
	(a) The basic receiver structure, and (b) the receiver structure with less optical receivers and delay lines.	
Fig. 2.4	The schematic diagram of a multistage optical amplification system.....	38
Fig. 2.5	Radar signal spectrum for (a)A single pulse and an incoherent pulse train, and (b)A long coherent pulse train.....	44
Fig. 2.6	Illustration of the channel placement for (a) $ f_{n-1} - f_{LO}  > f_{IF}$ , the NEAR-LO scheme, and (b) $ f_{n-1} - f_{LO}  < f_{IF}$ , the FAR-LO scheme. ....	48

Fig. 2.7	Schematic diagram of an optical coherent AM-WIRNA link.....	51
Fig. 2.8	Signal-to-noise ratio versus signal power of one channel of AM links.....	55
Fig. 2.9	Signal-to-interchannel-interference ratio (SIR) vs. channel spacing of AM links.....	57
Fig. 2.10	Dynamic range (DR) of AM links. ....	59
Fig. 2.11	Relative-intensity-noise effect on the dynamic range of AM links.....	61
Fig. 2.12	Schematic diagram of an optical FM receiver.....	63
Fig. 2.13	Signal-to-noise ratio (SNR) of FM schemes for different laser linewidths... .....	65
Fig. 2.14	Signal-to-interchannel-interference (SIR) vs. channel spacing of (a)the NEAR-LO scheme (b) the FAR-LO FM scheme for a 1 GHz signal.....	67
Fig. 2.15	Schematic diagram for optical PM receivers.....	70
Fig. 3.1	Demonstration of phased array true-time delay antenna feed system with four optical channels and two coherent receivers..... Inset: Schematic diagram of the optical heterodyne AM receiver	82
Fig. 3.2	The intermediate frequency spectrum of the optical heterodyne detection. .....	85
Fig. 3.3	Optical heterodyne signals at 0.8, 1.0 and 1.5 GHz.....	86
Fig. 3.4	The experimental setup for the dynamic range measurement.....	88
Fig. 3.5	True-time delay measurement showing four different time delays. Solid lines are calculations, and dots are experimental data.....	90

Fig. 3.6	Signal-to-interchannel interference ratio versus channel spacing.....	91
Fig. 4.1	Illustration of quasi-Fermi level and photon generation in a direct bandgap semiconductor material.....	101
Fig. 4.2	Cross Section of a ridge laser.....	107
Fig. 4.3	Illustration of 1-D mode calculations in a dielectric stack.....	109
Fig. 4.4	Illustration of calculation for modal reflectivity and far field pattern.....	109
Fig. 4.5	Schematic diagram of ridge laser fabrication procedure.....	113
Fig. 4.6	Calculation of modal reflectivity of a 1.3 $\mu\text{m}$ laser with single-layer anti-reflection coating. ....	115
Fig. 4.7	Threshold current density versus ridge width of semiconductor lasers...	118
Fig. 4.8	Net gain versus threshold current density for QW lasers with different quantum well numbers.....	119
Fig. 4.9	Light output versus current for an SOA. ....	120
Fig. 4.10	Spectrum of amplified optical signal.....	122
Fig. 5.1.	Index profile and wave function of a Twin-guide structure.....	127
Fig. 5.2.	Schematic diagram about the wave propagation in a TG.....	129
Fig. 5.3	TG device structures. (a) Laser/waveguide integration. (b) SOA/ waveguide structure.....	131
Fig. 5.4	Schematic diagram of threshold current versus laser cavity length for a laser/waveguide integration using synchronous TG.....	133

Fig. 5.5	Gain versus current density of a single quantum well material.....	138
Fig. 5.6	One twin-waveguide design example.....	140
Fig. 5.7	The wavefunction of a twin-guide for both the even and odd modes.....	141
Fig. 5.8	The absorption loss for the even and odd mode versus the loss layer thickness. ....	142
Fig. 5.9	The absorption loss for the even and odd modes versus the position of the loss layer.....	143
Fig. 5.10	Index profile and wavefunctions of the 3QW TG structure investigated here.....	145
Fig. 5.11	SEM micrograph of laser/Y-branch waveguide device.....	148
Fig. 5.12	(a) Near field pattern of twin-guide laser with absorption layer. (b) Near field pattern of Y-branch.....	149
Fig. 5.13	L-I curve and spectrum of Twin-guide lasers.....	151
Fig. 5.14	Far field pattern of TG lasers without absorption layer.....	152
Fig. 5.15	Far field pattern of TG lasers with absorption layer.....	153
Fig. 5.16	Polar plot of far field patterns.....	154
Fig. 5.17	Effective index and facet reflectivity versus guide separations for even & odd modes.....	156
Fig. 5.18	Threshold current density versus cavity length for regular laser, TG lasers with and without absorption layers.....	157
Fig. 5.19	Efficiency versus different cavity length for regular laser, TG with and without absorption layer.....	158

## List of Tables

Table 2.1	Losses in an EDFA-based $128 \times 320$ system.....	40
Table 2.2	Comparisons of coherent, IM/DD and WDM/DD phased array antenna systems.....	74
Table 2.3	Comparisons between the AM and FM schemes.....	75
Table 6.1.	Calculated and measured parameters of the lasers studied in this work.....	175

## Abstract

This report describes a successful demonstration of the first optically controlled phased array antenna system using heterodyne receiver techniques. Among our most notable achievements during this period are the following:

1. Invention of an optically controlled phased array antenna using coherent, heterodyne detection for the distribution of multiple true time (TTD) delays to numerous far end antenna elements. This unique system architecture allows for hardware compressive, extremely high performance transmission of delays along a single fiber interconnect between the control and remote antenna nodes.
2. Full analysis of the system employing both AM and FM, RF signal transmission. We find that the system scales easily to accommodate large dimension antennas.
3. Demonstration of the first TTD antenna using heterodyne detection methods. The antenna operated across the L-band with SNR > 50 dB, dynamic range of >50dB and a signal spacing of only 11 GHz. Furthermore, the system was quite simple to implement.
4. Determination of a fundamental noise limitation for analog coherent links: phase-to-intensity noise distortion. A full analysis of this noise process led to optimization of the link performance over the widest range of signal intensities.
5. Demonstration of a laser/modulator integration technology which allows for rapid miniturization of the components used in the phased array antenna.

Many of the accomplishments of this program are included in the thesis of Dr. Ligeng Xu. Attached are the relevant portions of that thesis, along with in-depth descriptions of other results obtained under this program.

We summarize our results by noting that the coherent distribution network is apparently *unique* in its ability to distribute a high density of very high SNR and DR signals to a dense array of antenna elements over a single fiber link. In effect, our system, which was surprisingly simple to implement using off-the-shelf components, may represent today the only viable technology for generating TTD optically controlled phased arrays which meet all of the critical performance requirements of these demanding systems.

We analyze an optically controlled microwave phased array antenna system whereby beam forming is accomplished with a large number of antenna elements that can receive any of several different true-time-delays from a single fiber using multi-channel optical heterodyne techniques. The system performance such as the signal-to-noise ratio, signal-to-interchannel interference ratio, and dynamic range (DR) for various modulation-demodulation schemes (i.e., AM, FM and PM) are quantitatively analyzed. An experimental system insensitive to laser linewidth and IF frequency instabilities is demonstrated for the first time. We demonstrate accurate true-time delay across the L band (from 0.8 to 1.5 GHz). The DR for one channel is 52 dB/MHz. For a narrow channel spacing of 1 Å at 1.55 μm wavelength, the interchannel interference is < -50dB. It is found that this system provides improved controllability over direct detection methods, and can meet the stringent requirements of modern high resolution microwave antenna systems.

Monolithic photonic integration using vertical twin-waveguide (TG) structure based on a single-step MBE grown InP/InGaAsP material is also studied as a means for practically implementing large scale photonic systems such as the above system. Specifically, integration of a MQW laser with a passive waveguide is demonstrated in

this material with a record high 45% light coupling. An InGaAs loss layer is introduced for the first time to ensure a constant laser feedback and output coupling by eliminating even mode propagation, while having little effect on the odd mode.

Finally, we have investigated means to obtain high efficiency, high power semiconductor lasers for use in high DR, and high density RF-optical links, employing a 1.5  $\mu\text{m}$  wavelength InGaAsP/InP separate confinement multi-quantum well structure with broadened waveguides. A record low internal loss of  $1.3 \text{ cm}^{-1}$  (compared to a previous value of  $3.5 \text{ cm}^{-1}$ ) and threshold current density of  $73 \text{ A/cm}^2$  per well have been obtained. Also, record high CW output powers of 4.6 W have been demonstrated for lasers with a 200  $\mu\text{m}$  wide aperture.

## Chapter 1 Introduction

Advances of photonic technologies have brought profound changes to our daily lives. For example, fiber optics makes the high speed, high capacity information super-highway a reality; CD-ROMs provide impeccably clear picture and sound for our enjoyment. Nevertheless, these might represent just the start of exploring the great potential of photonic systems. There are numerous other areas where photonic systems can be used to great advantages, such as fiber-to-the-home, remote sensing and control, and very fast computer chip-to-chip interconnects. Indeed, photonic technologies themselves still have great potential for improvement. Better discrete devices are needed for high power, high modulation speed, narrow linewidth lasers, high bandwidth, high dynamic range receivers, etc. Also, we need integration of photonic devices to reduce size and cost, and to achieve high reliability.

In this dissertation, both system and device-level work are described. The first part presents a novel use of a fiber optic heterodyne system in microwave phased array antennas, where a thorough system analysis has been carried out, and a proof-of-concept experiment has been demonstrated. This system has numerous applications not only for antenna remoting, but also for broad band analog distribution networks such as CATV, optical wireless systems and radar (both military and commercial). Note however, that its practical implementation requires a substantial increase in the scale of integration of the photonic devices (e.g. laser transmitters and optical receivers) used in this and other, similar, broad band systems. Hence, in the second part of this work, we describe a novel approach to achieving high density photonic integrated circuits (PICs) via a versatile, "platform" integration technology. Such a technology, if successful, should be as versatile as Si IC technology in that a wide range of PICs can be realized in a single wafer structure without regard to the specific circuit layout or device combination employed for

a particular application. Specifically, we describe an archetype integrated device--a laser/passive-waveguide Y-coupler, which is a key element in photonic integration, using a vertical twin-waveguide (TG) structure. It is the first time that this type of integration scheme is demonstrated in the InGaAsP/InP material system. Here, for the first time, the TG structure employs a unique "loss" layer structure which affords improved device performance by optical mode control. Next, we demonstrate that an improvement in the design of multiple quantum well (MQW) lasers can lead to record, low internal loss and low threshold current density, extremely high CW power structures.

In this Chapter, Section 1 introduces our work in using optical heterodyne techniques for the control of a microwave phased array antenna system, while Section 2 gives an overview of device work on low loss lasers, and laser/waveguide integration.

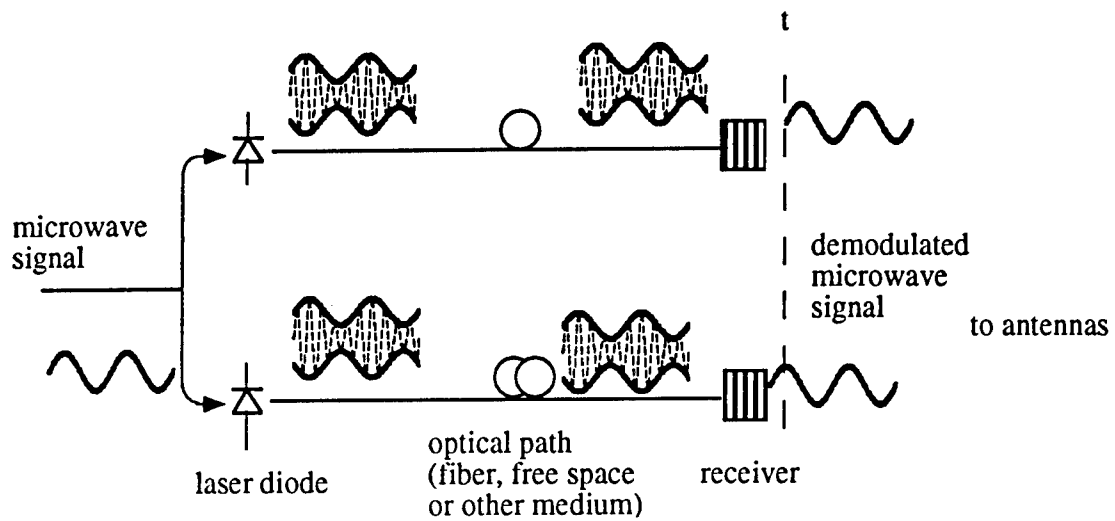
### **1.1 Operation of Optically Controlled Phased Array Antennas**

Electronically steered microwave phased array antenna systems are widely used today in military, area surveillance and communications. Such systems consist of an array (in one or two dimensions) of antenna elements. The radiation direction and pattern are determined by the relative phase and amplitude of radiation from each element. The major advantage of such a system is that it can electronically steer the beam direction with high speed without physically moving the antenna. Other advantages include high resolution and the simultaneous formation of multiple beams[1-3]. There are basically two methods of introducing delays: via phase, or true-time delay. True-time delay systems are free from "beam squint" (i.e. the beam position is independent of microwave emission frequency), and hence has the desired large instantaneous bandwidth. We explain the operation principle of microwave phased array and true-time delay in more detail in the Appendix 1 of this dissertation.

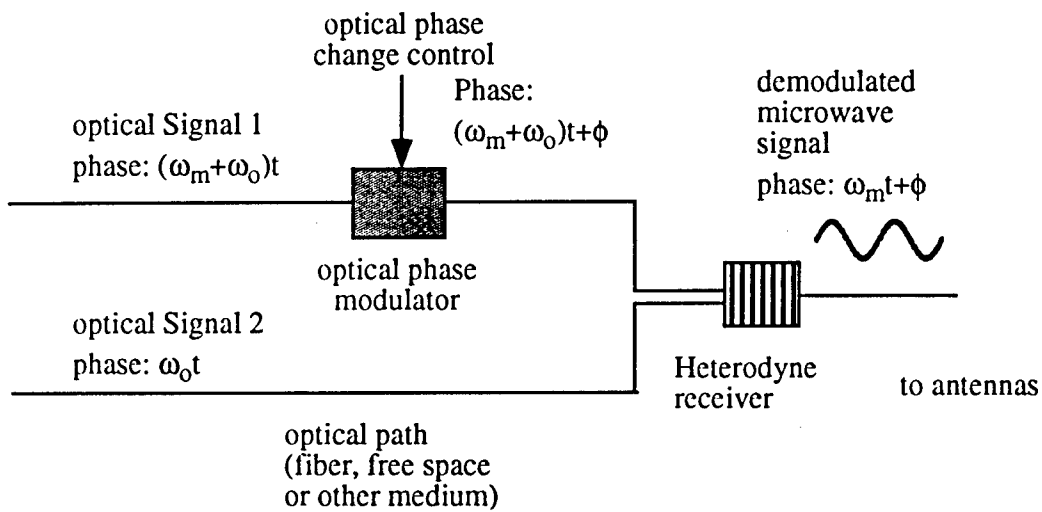
Phased array antenna systems provide great flexibility for radar beam formation, steering and detection. Recently, much effort has been devoted to introducing the phase delay and transmitting microwave signals via optical means [4-13]. This effort has been motivated by the obvious advantages of fiber optic systems. For example, since the microwave signals are modulated on optical carriers which are transmitted through silica fibers, the system is immune to electromagnetic interference. In addition, by using fibers instead of metal waveguides or coaxial cables, and optical devices instead of bulky microwave phase delay devices, such systems can be light-weight and compact and hence have potential usefulness on aircraft and satellite platforms.

The basic ideas of using optics to introduce delays and transmit microwave signals are shown schematically in Figure 1.1 (a) and (b). The first approach is that of true-time-delay, shown in Fig. 1.1(a) [4, 10-13]. Here, the microwave signals are first modulated on optical carriers, which are then transmitted to the antenna elements through different optic path length (in fiber or free space). The optical signals are detected and the original microwave signals are recovered. Since the signals get to the antenna elements at different times, the true-time delays are introduced. The second approach is shown in Fig. 1.1(b) [7, 8]. Here, two optical signals with a frequency difference ( $\omega_m$ ) are generated. Then the phase of one of the optical signals is modulated using an optical phase modulator. Finally a microwave signal is generated through heterodyne mixing of the two optical signals, with the microwave frequency being the difference between the two optical signals. The phase delay is then equal to the optical phase change introduced in one of the optical signals through the optical phase modulator.

There have been many different architectures suggested to transmit and control a series of microwave delays using optical means. Some systems[4-6] use bulk optics



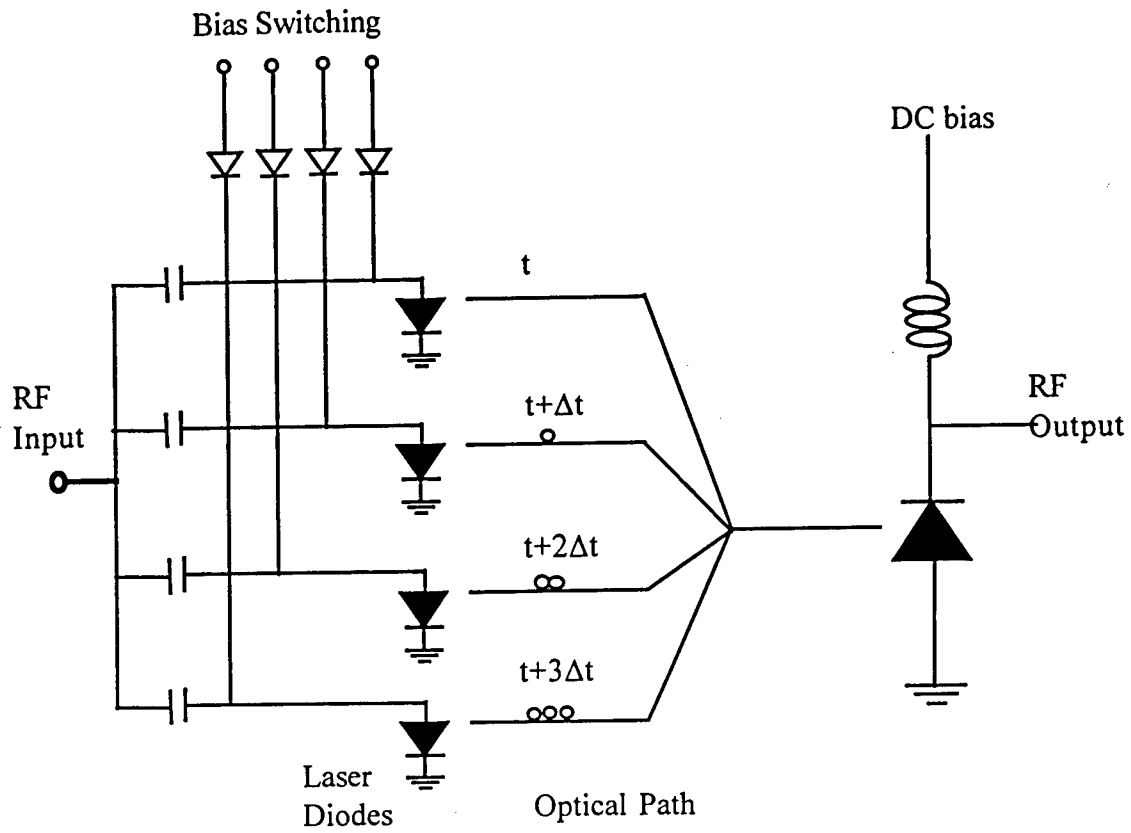
(a)



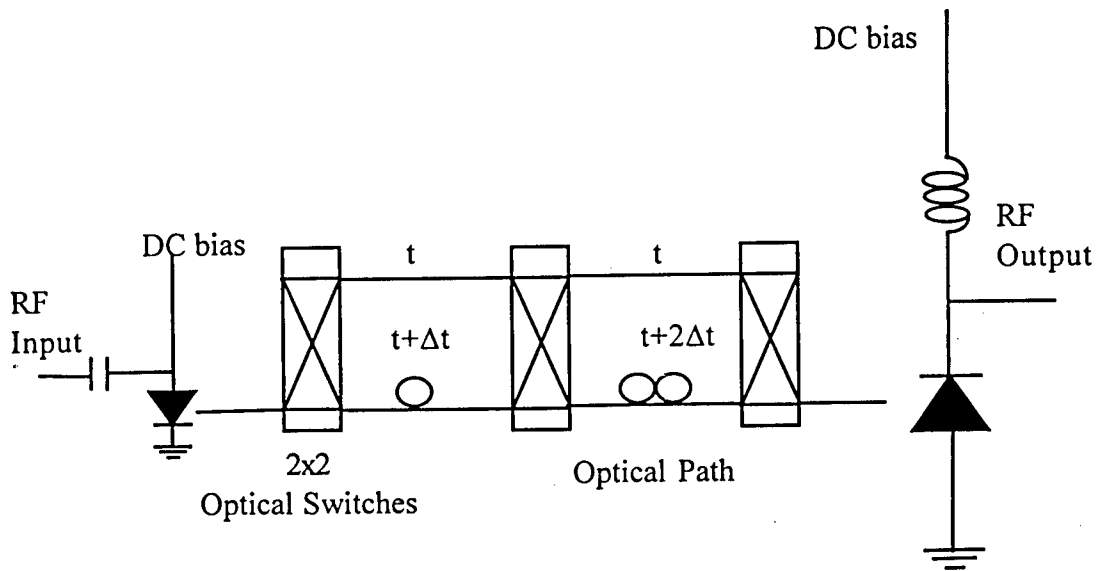
(b)

Figure 1.1 Schematic diagram of basic ideas of optically controlled phased array  
 (a) By using different optical path length, various true-time delays can be introduced.  
 (b) By changing optical phase  $\phi$ , the phase of the final microwave signal is change.

which suffer from thermal and mechanical instabilities. Others[7] use heterodyning of two injection-locked lasers to generate and control the microwave signal and introduce phase delay using optical phase modulators. These typically are not true-time-delay architectures, and hence their instantaneous bandwidths are small. For this reason, true-time-delay systems using intensity-modulation/direct-detection (IM/DD) techniques have been developed[10-11], with two methods to introduce delays, shown in Fig. 1.2(a) and (b). The serial delay method is shown schematically in Fig. 1.2(a) for one antenna element. In this scheme, the light can pass different lengths of fiber from zero to  $15\Delta t$ , with  $\Delta t$  as the smallest increment, depending on the configuration of the configuration of  $2 \times 2$  switches. The high loss of available optical switches makes it difficult to build such a system, although future optical switches with gain (integrated with semiconductor optical amplifiers) might eventually make this architecture practical. Figure 1.2(b) shows a second approach to true-time delay system utilizing an IM/DD scheme consisting of parallel delay lines along with bias-switched lasers selecting between various delays[10, 11] Here, microwave signals directly modulate lasers. When a specific delay line is needed, the laser connected to that delay line is switched on while all the others are kept off. After the delay, the signal reaches the detector via a combiner (a star connector). In these structures, the number of delay lines, lasers and receivers is on the order of  $M \times N$ , where  $M$  is the number of antenna elements and  $N$  is the number of different delays. For a large scale system where both  $M$  and  $N$  exceed 100, this method becomes cumbersome or even impractical. In addition, such fiber optic delay systems require  $N$  fibers of precise and equal lengths extending from the control to the antenna site. This is a particularly stringent requirement for some high bandwidth systems where the distance between the controller and antenna array exceed several tens of meters. Thus, implementation of such optically steered phased array antenna systems are currently hampered by the extreme complexity involved in efficiently transmitting hundreds of high quality (i.e.



(a) Paralell True-Time Delays



(b) Serial True-Time Delays

Figure 1.2 Parallel and Serial True-Time Delays

low loss and low interference) microwave delays from the control site to the antenna array.

To overcome several of these difficulties, and to effectively feed different delays to the antenna elements, Freitag and Forrest[12] proposed a true-time-delay phased array system based on multichannel, broadband coherent detection techniques. The system is unique in that a large number of different delays are transmitted through a single fiber, using on the order of only  $M+N$  optical transmitters and receivers[13,14]. The system can be made optically transparent by employing heterodyne detection plus optical amplifiers. We introduce the basic concept of this architecture in this section. More detailed analytical and experimental results are shown in Chapter 2 and 3.

It is known that the direction and wave pattern incident on or transmitted from an array antenna can be changed by properly varying the phase of the signal emitted from each array element. In the coherent system architecture, microwave signals are modulated on optical carriers with different frequencies (i.e. different optical channels), and are transmitted to antenna elements with the delays imposed by sending each carrier through different fiber lengths. Due to the optical channel selectivity of coherent detection afforded by using heterodyne optic-to-microwave receivers at each antenna element, the delayed signals can be distributed with very high fidelity to the various elements to achieve the desired beam direction.

Figure 1.3 is a schematic diagram of the heterodyne antenna transmitter. Each element in the input laser array has a different fixed optical frequency,  $f_{ok}$ , where  $k$  indicates the  $k$ th laser in the array. The same microwave signal modulates each of the  $N$  lasers in the array, using either direct or external modulation. The optical signals are then coupled to fibers of different lengths to introduce the time delay. Thus,  $N$  is the number

of different delays in the system which determines the bit resolution of the phased array. For example, if  $N=128=2^7$ , then the system has seven bit resolution. Different lengths of fibers correspond to different time delays. For example, a 1mm fiber length difference corresponds to a  $5 \times 10^{-12}$  s delay, which is a  $1.8^\circ$  phase delay for a 1 GHz microwave signal. It is reported that using silica-based planar waveguide technology, the delay can be controlled to a precision of 2 ps[15], corresponding to  $0.7^\circ$  at 1 GHz. The several delayed signals are combined onto a single fiber and sent to the antenna array, where the signals are distributed to the coherent receivers using a  $1 \times M$  splitter. The  $N$  optical signals are subsequently incident on each of the  $M$  coherent receivers, along with a local oscillator (LO) laser signal which is tuned to provide the  $k$ th receiver with an optical frequency  $f_{lok}$ . By tuning  $f_{lok}$ , the signal on any particular optical channel can be coherently detected. The photodetected signals are then demodulated electronically to recover the original microwave signals with different time delays fed to the desired antenna elements. With LO lasers associated with each antenna element tuned to different frequencies, various time-delays are fed to the array elements, thereby steering the beam to different directions.

This optically steered phased array antenna system requires  $M+N$  optical transmitters plus receivers, instead of  $M \times N$  typical of IM/DD systems. Furthermore, all the delays are transmitted on different optical carrier frequencies along a single fiber, thereby obviating the need for cutting and adjusting hundreds of long fibers extending from the control to the antenna site. This also allows for compensation of the optical loss from the combiners, splitters and other optical devices by putting a small number of optical amplifiers (e.g. erbium-doped fiber amplifiers, or EDFAs) along the fiber. Since beam steering is accomplished by tuning the LO to route the different delays to the several antenna elements, the steering speed is determined by how rapidly the LO laser can be tuned. Typically, for laser diodes this is in the range of 1 ns to 1 ms, which is sufficient

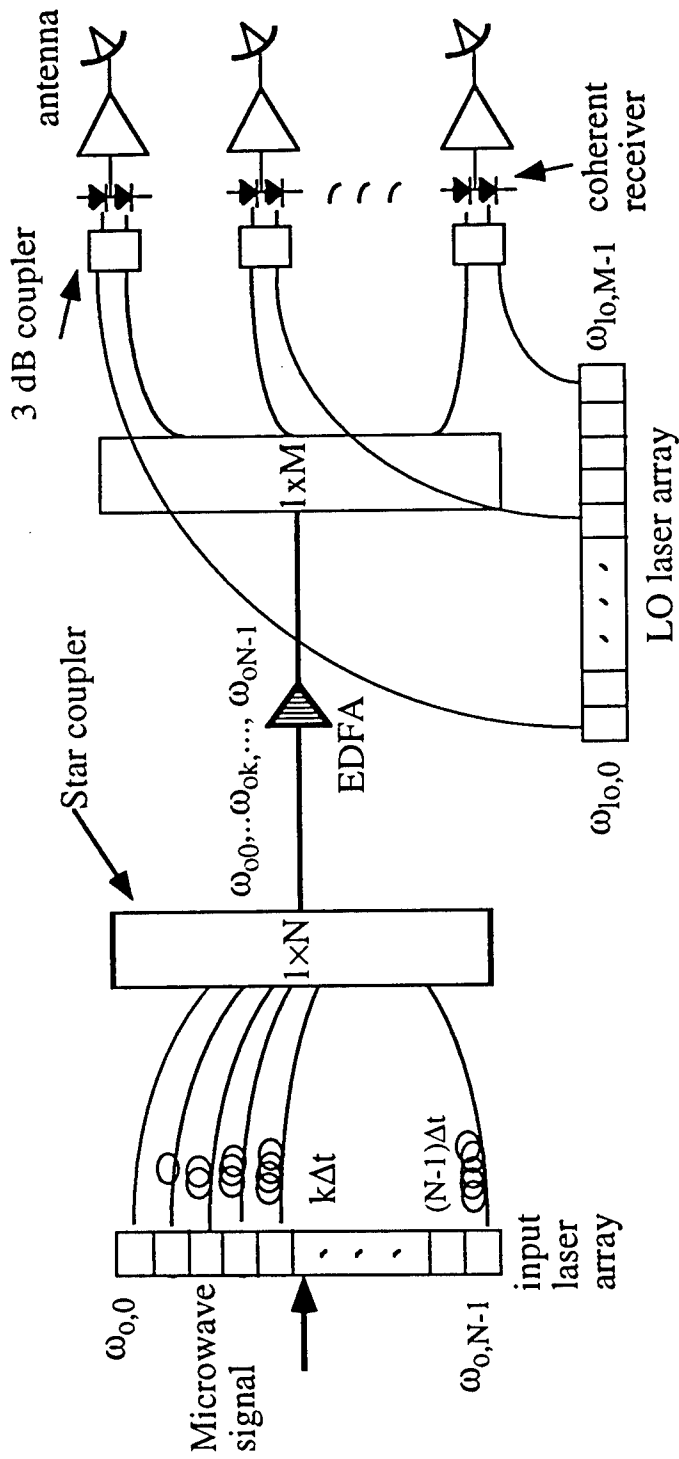


Figure 1.3 A coherent optically controlled phased array antenna transmitter.

for most applications. By individually adjusting the microwave amplifier or receiver gain, the system can easily shape the beam.

In Chapter 2, details of the architecture of the coherent optical controlled phased array antenna are described. Next, the quantitative analysis of important system performance parameters such as signal-to-noise ratio (SNR), dynamic range (DR), and interchannel interference ratio (SIR) are shown. Finally, the SNR, DR and SIR of an example system using AM, FM modulation schemes are calculated.

In Chapter 3, we describe the demonstration of a true-time delay phased array antenna feed system based on multichannel optical heterodyne detection techniques. The system is relatively insensitive to laser linewidth and IF frequency instabilities. We demonstrate the generation of accurate true-time delays for frequencies between 0.8 and 1.5 GHz. The dynamic range for one channel is 52 dB for 1 MHz bandwidth. Even for a very narrow channel spacing of 13 GHz, the interchannel interference is negligible. We also analyze the effect of the IF amplifier phase response on the system performance and find that it is the main source of phase instabilities of the output signal.

## **1.2 Introduction to laser/waveguide integration in a vertical Twin-Guide structure and low loss laser design and fabrication**

### **1.2.1 Laser/waveguide integration**

Photonic integrated circuits (PICs) have become the subject of increasing interest in recent years due to their great potential for high speed, low loss and reliable performance. There are two major approaches for integration. The first is hybrid integration, in which loss, parasitic reflections and capacitance, and mechanical fragility are inherent problems.

A second approach, monolithic integration, is promising for solving many of these difficulties.

One basic PIC building block is an integrated laser/waveguide, where light from a laser can be efficiently coupled into a transparent medium (i.e. the waveguide) for subsequent optical processing, such as modulation, splitting, and efficient coupling into optical fibers. There are several methods for monolithically integrating a laser with a transparent waveguide. One technique employs material regrowth to independently optimize the laser and waveguide devices by separately growing these device structures on locally selected regions of the wafer[16,17]. Unfortunately, this requires several epitaxial growth steps and fabrications which substantially complicates the process, decreases yield (hence increasing the cost), and must be customized for each device combination and geometry employed. In the second approach, a single growth on an etched substrate has been able to provide material for coupling between the laser and waveguide[18]. A schematic diagram of a device employing this technique is shown in Fig. 1.4. The growth on the etched substrate aligns the double heterostructure laser to a passive waveguide. Focused ion beam (FIB) etching generates a deep groove between the butt-coupled laser and waveguide to produce a sharp mirror for laser feedback. The drawback of this is the slow processing speed of the FIB etching, and the sensitivity of the device performance to process and growth variations. A third technique involves disordering of material to locally change the bandgap[19, 20]. Figure 1.5 shows the principle of one of these devices. It uses impurity induced disordering to change the bandgap of a multiple quantum well structure based on GaAs/AlGaAs materials. Figure

1.5 (a) shows the configuration of material for the laser in such a scheme. Here, after the epitaxial layers are grown, the wafer is patterned using a  $\text{Si}_3\text{N}_4$  stripe as a mask for silicon diffusion. The high silicon concentration in the diffused regions enhances the interdiffusion of the discrete layers in the multilayered epitaxial structure, resulting in the formation of a buried heterostructure active region under the stripe. Figure 1.5(b) shows the formation of the transparent waveguide region by diffusing the Si such that the lateral Si diffusions from both sides of the  $\text{Si}_3\text{N}_4$  are allowed to merge and pinch off the active region stripe. This will introduce more Al into the core of the waveguide due to the enhanced interdiffusion from the cladding layers, therefore increasing the bandgap. These two different diffusion regions can be patterned on the same material so that an active laser region can coaxially align with passive waveguide region, forming an integration structure. The drawback of this configuration is that the laser feedback needs to be provided by the passive waveguide facet, which sets constraints on the configuration and length of the passive waveguides.

Another solution, used in this thesis, is to couple light via an evanescent field in a closely spaced vertical twin-waveguide (TG) structure grown in a single epitaxial step[21-26]. In such a device, the two vertically stacked optical waveguides behave like a directional coupler, where the coupling between the two guides can range from weak to strong[23, 24]. It also has been used to select one axial mode and obtain single frequency emission[25]. This approach requires only a single material growth step, providing a structure on which a variety of “active”(e.g. lasers and optical amplifiers) and “passive” (e.g. waveguides, couplers and modulators) devices can be fabricated. In this sense, the

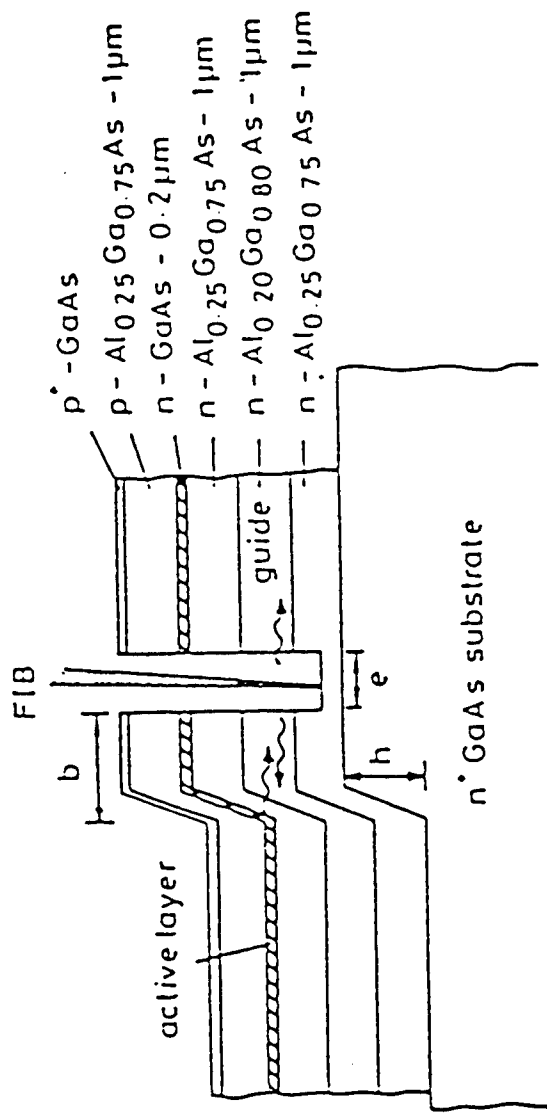


Figure 1.4 Schematic diagram of monolithic laser/waveguide integration using a single step epitaxy on an etched substrate. (Ref. 18).

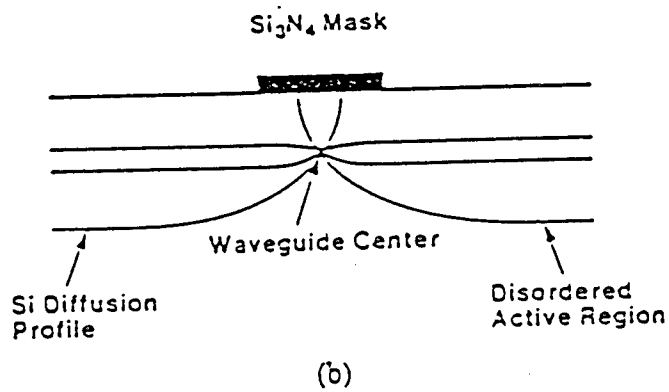
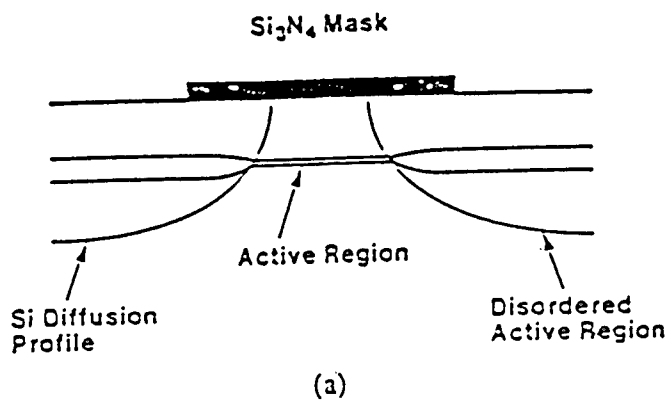


Figure 1.5 Schematic diagram for monolithic integration of laser/waveguide using impurity-induced disordering(Ref. 20).

(a) material structure for laser.

(b) material structure for passive waveguides.

TG structure has the potential of being a “platform” integration technology where multiple PICs can be combined on a single, “universal” wafer structure without regard to the specifics of the devices used or the “optical wiring” patterns forming a particular PIC.

Shown in Fig. 1.6 is a typical integrated laser/waveguide PIC using the TG structure. The top waveguide includes the active region which can provide gain, and the bottom guide has larger bandgap, which serves as the passive waveguide. As shown in the figure, the left edge of the laser is a cleaved or deeply etched facet, while on the right is a shallow facet etched into only the top guide, which affords direct coupling of light from the laser into the waveguide. The analysis of a system consisting of two-coupled planar waveguides can be carried out by using coupled-mode theory or a normal mode analysis[26]. In this dissertation, we analyze the performance of the device methods to calculate the  $TE_0$ =even and  $TE_1$ =odd using normal modes of the complex waveguide structure. The relative light intensities in the upper and bottom guides can be determined in this manner by the beat of the even and odd modes.

Until recently, laser/waveguides in a TG structure have only been obtained with low coupling efficiency and high threshold current[21-25, 27]. Furthermore, one potential problem of the TG structure is the effect of the interaction between even and odd modes, whose coupling length is usually from 100 to 200  $\mu\text{m}$  and varies for different materials and for different fabrication procedures. The length dependence of light coupling makes it difficult to control facet feedback, and the coupling efficiency from

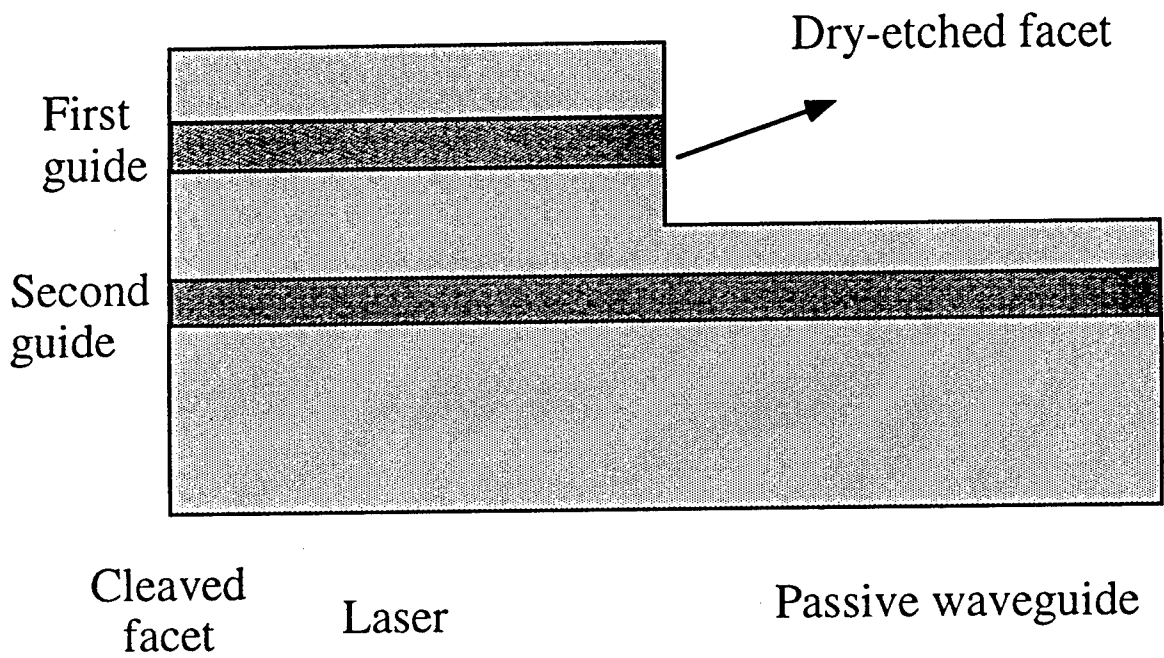


Figure 1. 6 Monolithically integrated laser/waveguide in a twin-waveguide structure.

laser into the passive waveguide[22, 26]. Note, however, for our devices to be compatible with the phased array antenna system investigated here, with long haul communications and optical distribution systems, the integrated devices must be capable of emission at 1.3 and 1.55  $\mu\text{m}$  wavelengths, and have high coupling efficiency. Furthermore, to serve as a truly versatile integration “platform”, methods to reduce device performance sensitivity on inevitable process and materials variations must be developed.

In this dissertation, therefore, we discuss the a demonstration of the monolithic integration of a 1.55  $\mu\text{m}$  wavelength strained layer, MQW laser with a passive waveguide using a vertical TG structure based on InP/InGaAsP system[28]. In order to gain better control of laser facet reflectivity and light coupling from the lasers to the passive waveguides, we use a novel approach: introducing an InGaAs “loss layer” between the two vertical waveguides to eliminate even mode propagation. The presence of only the odd mode in this structure makes the facet reflectivity and light coupling *independent* of variations in the epitaxial structure, cavity length and fabrication details. It is also shown that the loss layer has little effect on the odd mode, such that threshold current density and external efficiency are the same as achieved in structures without the loss layer. This tolerance to details of materials and fabrication procedure indicates that the modified TG structure is an important first step in the realization of a flexible, platform PIC technology.

### 1.2.2 Low loss SCH-MQW laser diodes with broadened-waveguide

The semiconductor laser is one of the most important devices in virtually all advanced photonic systems. Since the invention of the first double heterojunction laser diode nearly three decades ago, enormous achievements toward achieving semiconductor lasers with high efficiency, high power, low noise, wavelength tunability, and narrow linewidth. For a semiconductor laser, the internal optical loss arising from free carrier absorption, material defects, and scattering at the epitaxial interfaces, is one key parameter in determining efficiency, threshold current density and maximum output power. Through our study in this dissertation, we find that a major fraction of the internal optical loss in separate confinement heterostructure multiple-quantum-well (SCH-MQW) InP/InGaAsP lasers comes from the free carrier absorption. Based on this knowledge, we design a laser structure with a broadened, undoped waveguide approximately 1  $\mu\text{m}$  wide to reduce the free carrier absorption, and thus significantly lower the total internal optical loss.

The lowest previously reported values of internal optical losses obtained for 1.5  $\mu\text{m}$  wavelength SCH-QW InGaAsP/InP lasers were  $\geq 3.5 \text{ cm}^{-1}$ [29,30]. In this work, we obtained an internal loss as low as  $1.3 \text{ cm}^{-1}$ , and realize a two-fold increase in differential efficiency in devices longer than 2 mm[30]. A record CW output power of 4.6 W has been demonstrated for such a laser with a 200  $\mu\text{m}$  wide aperture. The introduction of a broadened waveguide reduces the quantum well confinement factor, which by itself might cause an increase of the threshold current density. However, the competing effect

of a lower internal optical loss is so strong that we actually obtain a record low threshold current density of  $73 \text{ A/cm}^2$  per quantum well for a 4 mm long devices. The achievement of such low threshold current densities and high output efficiencies is another crucial milestone in realizing practical, highly integrated PICs such as those demonstrated by our optically controlled microwave antenna system. Such a system requires large scale integrated arrays of lasers and modulators which can deliver a maximum optical power with a minimum power dissipation (i.e. high wall-plug efficiency) such that the device operation is not degraded by thermal interactions with its neighbors. This novel laser structure is thus central to our implementing advanced photonic systems with flexible, integrated high performance PICs and optoelectronic integrated circuits (OEICs).

The second part of this dissertation is organized as follows. Chapter 4 describes the physics and numerical calculations required for designing and analyzing laser and waveguide devices. We summarize the results for material gain and characteristics of lasers, such as L-I curves, efficiency, output and internal loss. The basic concepts of numerical methods for calculating optical modes are described. Finally, we illustrate in detail our processing procedures for ridge lasers and semiconductor optical amplifiers (SOAs) and show performance data of typical devices. Photonic device integration employing twin-waveguide (TG) structure are discussed in Chapter 5. The numerical design, analysis, optimization and experimental results about an integrated laser/waveguide are presented in detail. Chapter 6 described our work on achieving low loss, high power, separate confinement multiple quantum well (SCH-MQW) lasers using broadened waveguide structure. The effects of the waveguide broadening on the internal

loss, efficiency, and the threshold current density are theoretically analyzed. Experimental results of these parameters of the lasers are shown and compared to the numerical results. Finally, in Chapter 7, we give conclusions and some future research directions.

## References

- [1] Merrill L. Skolnik, *Radar Handbook*, New York: McGraw-Hill, 1990.
- [2] Merrill L. Skolnik, *Introduction to Radar Systems*, 2nd Ed., New York: McGraw-Hill, 1980.
- [3] Simon Haykin, *Array Processing Applications to Radar*, Dowden, Hutchinson and Ross, Inc., 1980.
- [4] G.A. Koepf, "Optical processor for phased-array antenna beam formation," *Optical Technology for Microwave Applications*, vol. 477, SPIE, pp. 75-81, 1984.
- [5] P. Sheehan and J. Forrest, "The use of optical techniques for beam forming in phased arrays," *Optical Technology for Microwave Applications*, SPIE, vol. 477, pp.82-89, 1984.
- [6] J. Wallington and J. Griffin, "Optical techniques for signal distribution in phased arrays," *GEC. J. Res.*, vol. 2, no. 2, pp. 66-73, 1984.
- [7] Marc R. Surette, D.R.Hjelme and A.R. Mickelson, "An optically driven phased array antenna utilizing heterodyne techniques", *JLT*, v.11, no.9, pp1500-1509, Sept. 1993.
- [8] J. Guggenmos and R. Johnson, "Fiber based phased array antennas," in *Optical Technology for Microwave Applications III*, SPIE, vol. 789, pp. 70-77, 1987.
- [9] J. S. Pappert, "Ultra-wideband direction finding using a fiber optic beam-forming processor," in *Optoelectronic Signal Processing for Phased-Arrays*, SPIE, vol. 886, pp. 239-246, 1988.
- [10] W. Ng, A.A. Walston, G.L. Tangonan, J.J. Lee, I.L. Newberg and N. Bernstein, "The first demonstration of an optically steered microwave phased array antenna using true-time-delay", *IEEE J. Lightwave Tech.*, vol. 9, no. 9, pp1124-1131, 1991.

- [11] J. J. Lee, S. Livingston, R.Y. Loo, N. P. Bernstein, "System design and performance of a wideband photonic array antenna", *Optoelectronic Signal Processing for Phased-Array Antennas IV*, SPIE vol. 2155, 1994.
- [12] P. M. Freitag and S. R. Forrest "A coherent optically controlled phased array antenna system", *IEEE Mic. and Guided Wave Lett.*, v3, no.9, pp293-295, Sept. 1993.
- [13] L. Xu, R. Taylor, and S. Forrest, "The use of optically coherent detection techniques in true-time delay phased array and systems", *IEEE Journal of Lightwave Technology*, vol. 13, no. 8, pp1663-1678, Aug. 1995.
- [14] L. Xu, R. Taylor, and S. Forrest, "True time-delay phased array antenna feed system based on optical heterodyne techniques," *IEEE Photonics Technology Letters*, vol. 8, no. 1, pp. 160-162, Jan 1996.
- [15] W. W. Ng, D. Yap, A. A. Narayanan, "GaAs and silica-based integrated optical time shift network for phased arrays", *Optoelectronic Signal Processing for Phased-Array Antennas IV*, SPIE vol. 2155, 1994.
- [16] J.E. Zucker, "Monolithically integrated laser/Mach-Zehnder modulators using quantum wells", *Proceedings of Annual Meeting of the IEEE Lasers and Electro-Optics Society*, 1993.
- [17] Y.Tohmori, X. Jiang, S. Arai, F. Koyoma, and Y. Suematsu, "Novel structure GaInAsP/InP 1.5-1.6  $\mu\text{m}$  bundle integrated guide (BIG) distributed Bragg reflector laser," *Japan. J. Appl. Phys.*, vol. 24, pp L399-L401, 1985.
- [18] D. Remiens, L. Menigaux, G.Ben Assayag, J. Gierak, and R. Sudraud, "GaAs/AlGaAs double heterostructure laser monolithically integrated with passive

- waveguide using focused ion beam etching," *Electron. Lett.*, vol 25, no. 20, pp1400-1402, Sept. 1989.
- [19] H. Ribot, K.W. Lee, R.J. Simes, R.H. Yan, and L. A. Codren, "Disordering of GaAs/AlGaAs multiple quantum well structures by thermal annealing for monolithic integration of laser and phase modulator," *Appl. Phys. Lett.*, vol.55, pp.672-674, 1989.
- [20] R.L. Thornton, W.J. Mosby, and T.L. Paoli, "Monolithic waveguide coupled cavity lasers and modulators fabricated by impurity induced disordering," *J. Lightwave Technol.*, vol. 6, pp. 786-792, 1988.
- [21] R.K. Watts, "Evanescent field of thin film laser and passive waveguide," *J. Appl. Phys.*, vol. 44, pp5635-5636, 1973.
- [22] K. Okamoto, A. Yamada, Y. Nakano and K. Tada, "Design and fabrication of monolithically integrated lateral-electrode etched-mirror laser with Y-branch single-mode waveguide in GaAs/AlGaAs," *Jpn. J. Appl. Phys.* Vol 34, no. 9A, Sept. 1995.
- [23] G.A. Wawter, J.L Merz, and L.A. Codren, "Monolithically integrated transverse-junction-stripe laser with an external waveguide in GaAs-AlGaAs," *IEEE J. Quantum Electron.*, vol. 25, pp.154-162, 1989.
- [24] J.C. Campbell and D.W. Bellavance, "Monolithic laser/waveguide coupling by evanescent field," *IEEE J. Quantum Electron.*, vol. QE-13, pp. 253-255, 1977.
- [25] Y. Suematsu, K. Kishino, and T. Kambayashi, "Axial-mode selectives for various types of integrated twin-guide lasers," *IEEE J. Quantum Electron.*, vol. QE-13, pp. 619-622, 1977.

- [26] H. Ribot, P. Sansonetti, and A. Carencio, "Improved design for the monolithic integration of a laser and an optical waveguide coupled by an evanescent field," *IEEE J. of Quantum Electron.*, vol. 26, no. 11, pp 1930-1941, Nov. 1990.
- [27] P. Wright, R. Nelson, and R. Wilson, "Monolithic integration of InGaAsP heterostructure lasers and electrooptical devices", *J. Quantum. Elec.*, vol.18, no. 2, pp 249, Feb. 1982.
- [28] L. Xu, M. Gokhale, P. Studenkov, J. C. Dries, C.-P. Chao, D. Garbuzov, S.R. Forrest, "Monolithic Integration of a 1.55  $\mu\text{m}$  wavelength MQW Laser/waveguide Using a Vertical-Twin-Guide Structure," submitted for publication.
- [29] W.T. Tsang, F.S. Choa, M.C. Wu, Y.K. Chen, A. Sergent, and P.F. Sciortino, Jr.: "Very low threshold single quantum well graded-index separate confinement heterostructure InGaAs/InGaAsP lasers grown by chemical beam epitaxy", *Appl. Phys. Lett.* 1991, **58**, pp2610-2612.
- [30] J.S. Osinski, Y.Zou, P.Grodzinski, A. Mathur, and P.D. Dapkus: "Low-threshold-current-density 1.5  $\mu\text{m}$  lasers using compressively strained InGaAsP quantum wells", *IEEE Photon. Tech. Lett.*, 1992, **4**, pp10-13.
- [31] D. Garbuzov, L. Xu, S. R. Forrest, R. Menna, R. Martinelli, J. C. Connolly, "1.5  $\mu\text{m}$  wavelength, SCH-MQW InGaAsP/InP broadened-waveguide laser diodes with low internal loss and high output power," *Electronics Letters*, vol. 32, no. 18, Sept., 1996.

## Chapter 2 Analysis of A True-Time Delay Phased Array Antenna System Using Coherent Optical Detection Techniques

In this chapter, we analyze a true-time-delay, optically controlled phased array antenna system whereby beam forming is accomplished using a large number of antenna elements that can receive any of several different microwave true-time-delays via the use of coherent optical carriers transmitted through a single fiber. The transmitter and receiver architectures are described in detail. We present calculations for the signal-to-noise ratio (SNR), the signal-to-interchannel interference ratio (SIR) and dynamic range(DR) of one channel for various modulation-demodulation schemes (i.e., AM-heterodyne, FM, PM). We show for an example system that can accommodate 128 antenna elements and provide 128 different delays (7 bits), assuming AM modulation with a bandwidth of 1 MHz, a transmitter power of -5 dBm and a laser linewidth of 10 MHz, we can obtain  $DR \simeq 50dB$  for one channel using a channel separation twelve times of that of the microwave frequency ( $f_m$ ). For the FM scheme,  $DR \simeq 60dB$  can be obtained for one channel with a laser linewidth of 1 MHz, a FM modulation index of one, and a channel spacing of about  $13f_m$ . With a local oscillator laser tuning range of 100 Å, the system can provide seven-bit resolution for a 128 element antenna array. It is found that coherent optically controlled phased array antennas provide improved controllability over direct detection method, and can have the SNR, SIR and DR that meet the stringent requirements of modern high resolution microwave antenna systems.

### Symbols Used in the Chapter

$\beta$	FM modulation index
$\Gamma_i$	Parameters for signal and noise powers of the AM scheme
$\Delta f$	Maximum optical frequency deviation for the FM scheme(= $\beta f_m$ )
$\Delta\nu$	3-dB laser linewidth
$\nu$	Optical carrier frequency
$\phi_s(t)$	Phase of the intermediate frequency signal
$\phi_{phase}(t)$	Phase noise
$\tau$	Pulse width of radar signals
$\omega_{IF}$	Angular intermediate frequency (IF)
$A_s$	IF current amplitude , $2R\sqrt{P_s P_{LO}}$
$ASE$	Amplified spontaneous emission
$B$	Bandwidth of the radar signal
$B_{IF}$	IF bandwidth
$C(f)$	Radar signal spectrum
$c$	Optical signal velocity in fibers
$D$	Channel spacing
$DE_i$	Time delay for the $i$ th antenna element
$DR$	Dynamic range
$F$	Noise figure of the optical amplifier system
$f_m$	Microwave signal frequency
$f_r$	Pulse repetition frequency of radar signals
$f_{IF}$	Intermediate frequency
$G_i$	Optical gain

$G_{tot}$	Total optical gain of one channel
$H_{IF}(f)$	Transfer function of the bandpass filter for IF signals
$H_2(f)$	Transfer function of the final filter
$h$	Planck constant
$i_{IF}(t)$	Intermediate frequency current
$k_B$	Boltzmann constant( $= 1.38 \times 10^{-23} J/K$ )
$L_i$	Optical loss
$M$	Number of antenna elements
$m$	AM modulation index
$N$	Number of different delays corresponding to bit resolution
$n(t)$	Noise current
$n_{int}(t)$	Interference current
$PSD$	Power spectral density
$P_{int-final}$	Interference power at the final output
$P_{in-max}$	RF power input that results in third order power equal to noise power
$P_{in-min}$	RF power input that results in SNR=1
$P_{LO}$	Local oscillator laser power
$P_s$	Optical power of one channel incident on one receiver
$P_{s-final}$	Signal power of the primary channel at the final output
$P_{s-total}$	Total optical signal power incident on one receiver
$R$	Photoresponsivity of detectors
$RIN$	Relative intensity noise of lasers(in units of dB/Hz)
$r$	Resistance of the receiver, usually $50\Omega$
$SIR$	Signal-to-interchannel-interference ratio

$SNR$	Signal-to-noise ratio
$S_n(f)$	PSD of the total noise current at the IF region
$S_{n,thermal}$	PSD of thermal noise
$S_{n,shot}$	PSD of shot noise
$S_{n,LO-ASE}$	PSD of the LO-ASE beat noise
$S_{n,RIN}$	PSD of relative intensity noise
$S_{\dot{\phi}_{phase}}$	PSD of the time derivative of laser phase noise
$T$	temperature
$X$	Number of delays needed on the optical receiver site.
$x(t)$	Modulation signal

## 2.1 Introduction

In Chapter 1, we describe the basic concept of a true-time delay phased array antenna feed system based on multichannel optical heterodyne techniques. In this chapter, we quantitatively analyze the performance of the transmitter and receiver system of Ref.[1][2]. We find that such a multichannel system has very low interchannel interference, high signal-to-noise ratio(SNR), and dynamic range(DR). Semiconductor lasers used in this system reduce both size and cost, and increase robustness and tuning range. Even with the comparatively large semiconductor laser linewidths, Doppler radar can still be implemented using this architecture.

This chapter is organized as follows. In Sec. 2.2, the transmitter and receiver structures, and some system issues are described in detail. Section 2.3 describes the spectra of radar signals, and introduces analytical methods to treat such issues as noise, signal-to-noise ratio (SNR) for one channel, signal-to-interchannel-interference

ratio (SIR), and dynamic range (DR). We also provide parameters for an example system which can accommodate 128 antenna elements and provide 128 different delays, whose performance is evaluated in the following sections. In Secs. 2.4 and 2.5, we provide the results of calculations for SNR, SIR, DR, channel spacing, and the number of channels that can be accommodated for optical AM, FM and PM modulation schemes. In Sec. 2.6, some detailed comparisons are made concerning the advantages and disadvantages of optical coherent and two other true-time delay architectures currently under investigation. We present conclusions in Sec. 2.7.

## 2.2 System Description

### 2.2.1 More about the Transmitter Antenna

In Chapter 1, we describe the operating principles of the true-time delay phased array antenna transmitter using optic heterodyne techniques, shown again here in Fig. 2.1. In an antenna array system, a greater number of delays leads to a higher angular resolution and steering accuracy. In Fig. 2.1, the number of different delays which corresponds to the number of optical channels is limited by the tuning range of the LO laser. Currently, wide tuning ranges of  $\sim 83nm$  of single mode operation have been demonstrated for DBR lasers [3]. Using external cavities and gratings, the tuning range can also approach several tens of nanometers with a very narrow linewidth[4]. For very large scale systems where the tuning range of an LO laser is insufficient, one can employ several LO's for each optical receiver. In this case, each LO covers a different region of the tuning spectrum within the total frequency band occupied

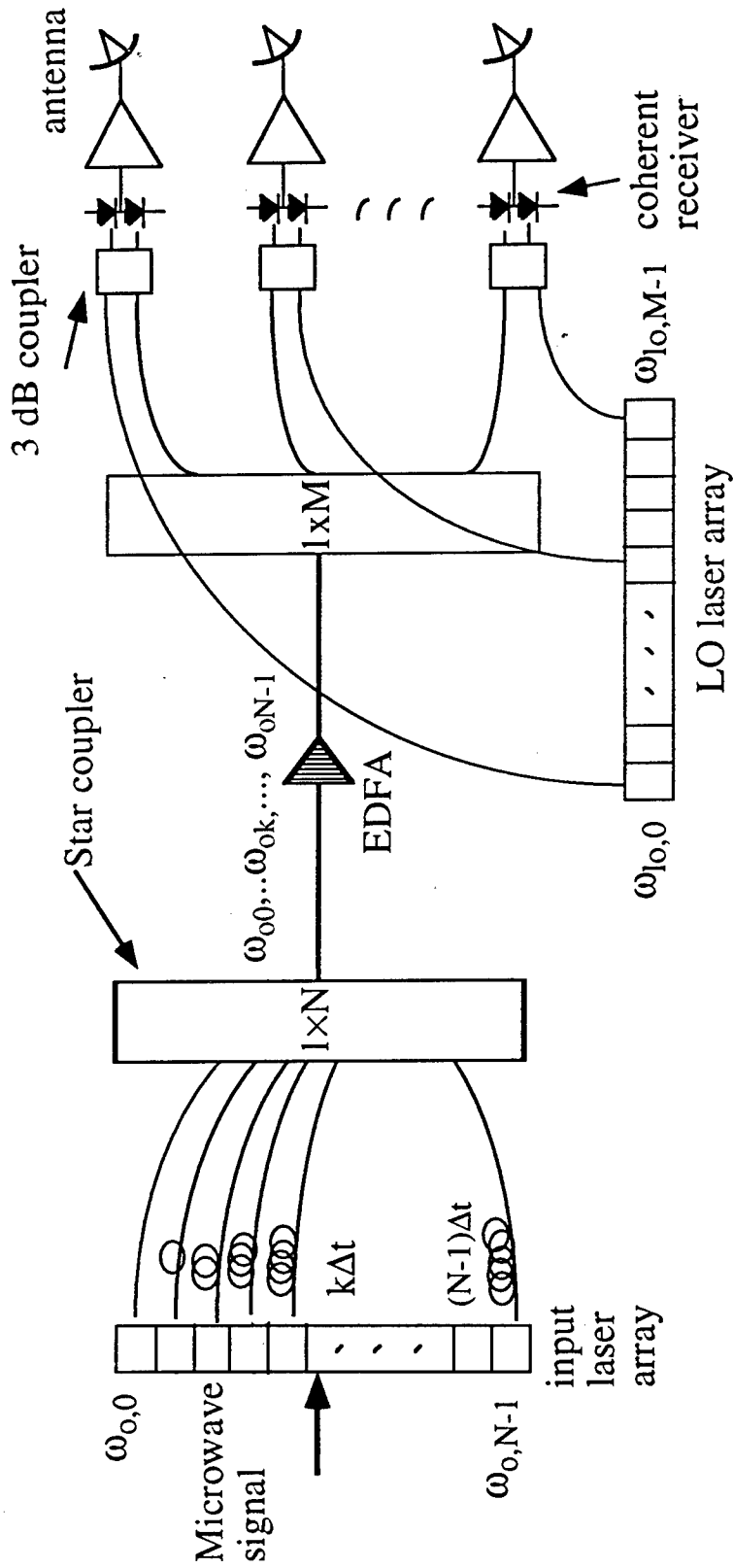
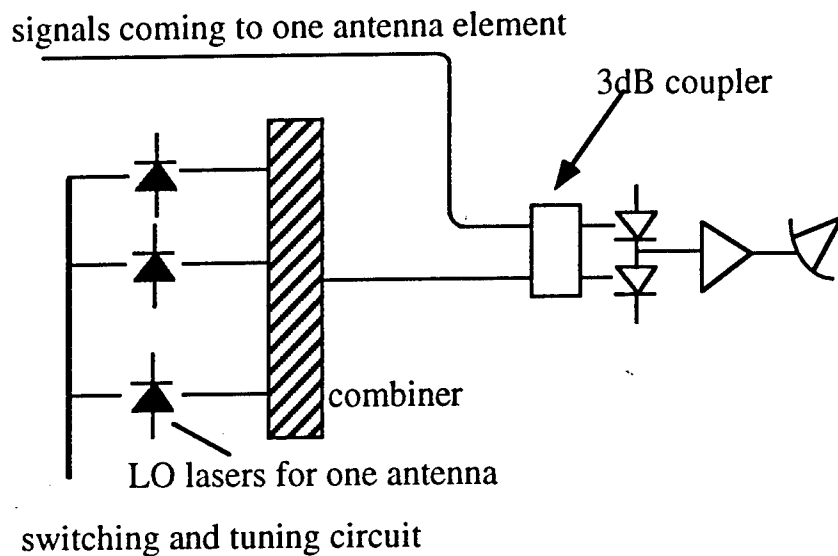


Figure 2.1 The coherent optically controlled phased array antenna transmitter

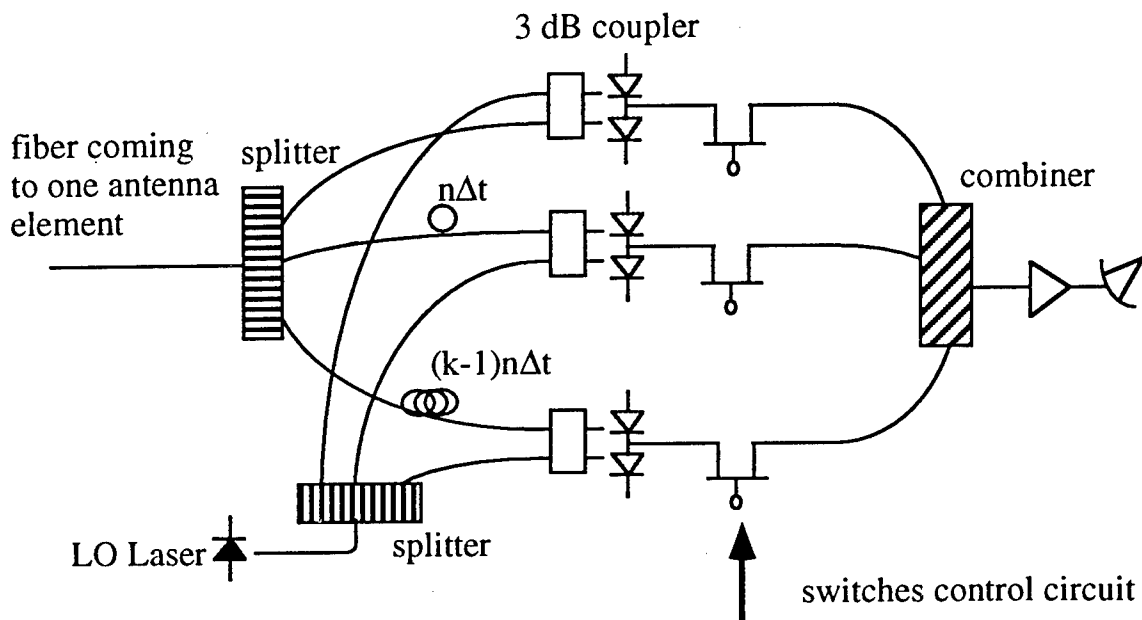
by all channels. This scheme is shown in Fig. 2.2a. An alternative means is to use several receivers corresponding to several different delays transmitted to one antenna element, which is shown in Fig. 2.2b. For example, assume that the  $n$  delay lines at the combiner input introduce the delays:  $0, \Delta t, 2\Delta t, \dots, (n - 1)\Delta t$  in ascending order. Each signal is again split into  $k$  branches which introduce additional delays  $0, n\Delta t, 2n\Delta t, \dots, (k - 1)n\Delta t$  after which they reach the different antenna element receivers. The antenna element only receives one of the several signals from these different receivers using electronic switches. By this means, the total number of different delays for the system is  $kn$ .

### 2.2.2 The Receiver Antenna

Using a structure similar to that of the transmitter in Fig. 2.1, the system is also capable of detecting signals arriving from different directions. This is accomplished by delaying signals received from the several antenna elements so that they are added in phase to obtain a detectable output. Figure 2.3a shows the basic receiver architecture. The signals from the various antenna elements are modulated on different optical carriers corresponding to different optical channels. The optical signals are then combined and transmitted from the antenna site to the optical receiver site, where they are incident on each optically coherent receiver through various lengths of fibers which introduce the true time delays. Here, each receiver corresponds to a particular delay. When the frequency of an LO laser is tuned to some optical channel, the associated optical receiver outputs the delayed microwave signal modulated on this channel. In the receive mode, the signal arriving at each antenna is delayed by



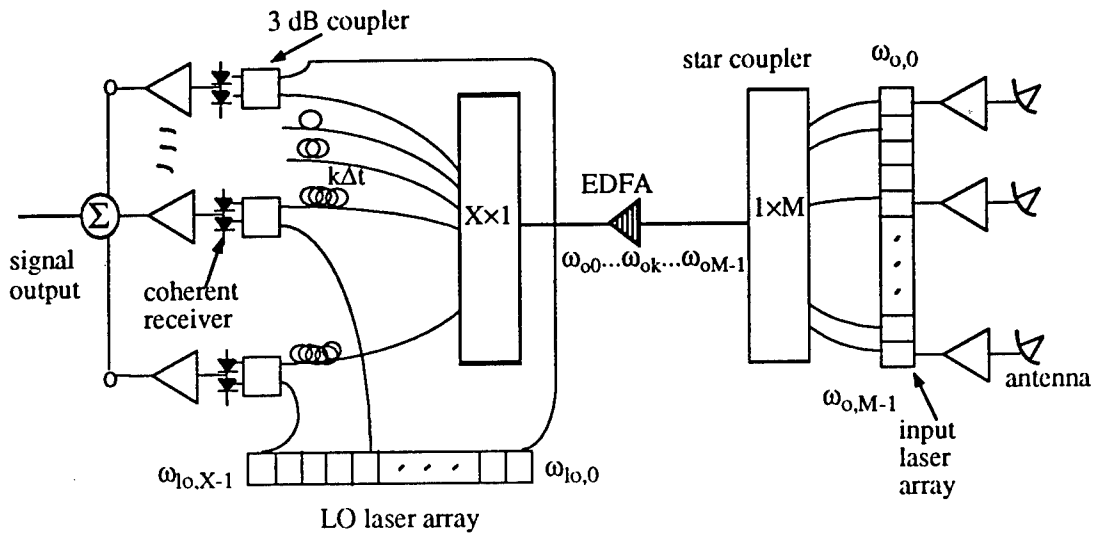
(a)



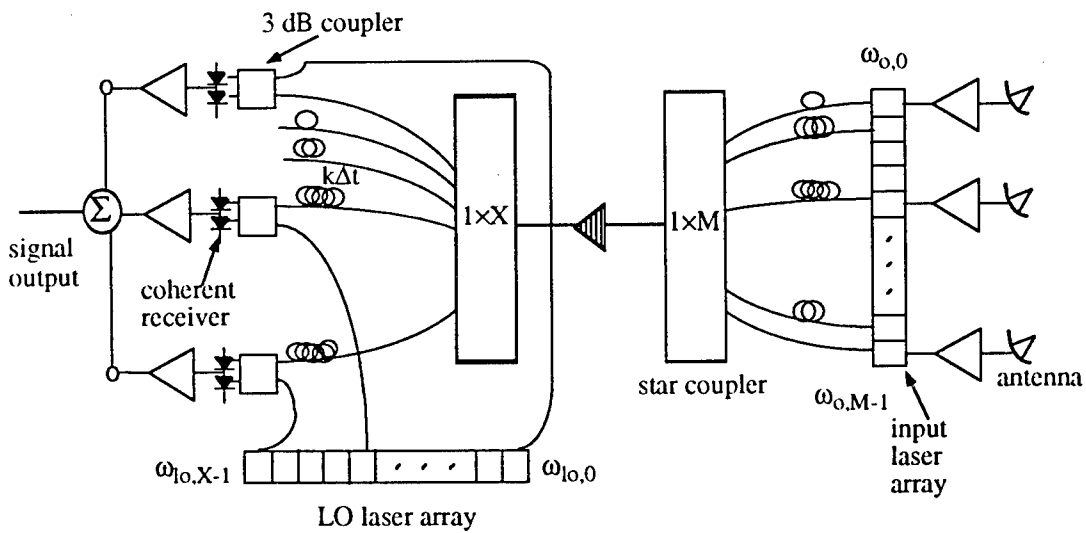
(b)

Figure 2.2 Expansion methods for the transmitter structure using (a) the multiple local laser scheme, and (b) the multiple receiver scheme

Using these methods, the system can accommodate more delays with a limited laser tuning range than the structure in Figure 2.1 .



(a)



(b)

Figure 2.3 The coherent optically controlled phased array antenna receiver  
 (a) The basic receiver structure and  
 (b) the receiver structure using less optical receivers and delay lines.

an amount consistent with the beam direction, and the signals are then brought in phase and summed to obtain the total signal. Employing a sufficiently large number of optical receivers with various lengths of fibers ensures that the system can provide proper delays for each direction. From Fig. 2.3(a), we see that the receiver has advantages similar to that of the transmitter, such as using a single fiber as the main transmission line, amplification along this fiber etc.

The receiver is slightly more complex than the transmitter in terms of the number of delay lines used. Nevertheless, the number of optical delay lines (corresponding to the number of optical receivers) is linearly proportional to  $N$ , where  $N$  is the number of different delays required to achieve a given bit resolution. We will see below that the difference between the number of delays and delay lines arises since the transmitting and receiving signals of one antenna element do not necessarily share the same path in the optically coherent detection scheme. To understand how many delay lines are required, consider a one dimensional, linear phased array antenna. Assume that there are  $M$  antenna elements, and that there are  $N$  different, equally spaced delays at time intervals of  $0, \Delta t, 2\Delta t, \dots, (N - 1)\Delta t$ , where  $\Delta t$  is the smallest time increment. For receiving signals arriving from various angles, the delays introduced for the antenna elements 1 to  $M$  can either increase or decrease monotonically. For broadside detection (the signal oriented perpendicular to the plane of the antenna array), the signals received from all antenna elements should be fed with  $M$  identical delays. For directions near to but not at the broadside direction, the signals received from many neighboring antenna elements have to be fed with identical delays due to lack of digital resolution. In the antenna transmitter, one delayed signal can be fed to any number of antenna elements simultaneously. For the antenna receiver,

however, one would like to use one optical receiver to receive all the signals requiring the same delay. But as we show in Appendix 3, this imposes extremely stringent requirements on the transmitter lasers, and also requires precise delays. Therefore, practical receivers must provide more than  $N$  delay lines to detect signals near the broadside direction. Employing coherent detection techniques, one receiver and its corresponding delay line can be used for different antenna elements at each different detection angle. Hence, the total number of delay lines is still much smaller than that required for the IM/DD detection scheme. In Appendix 4, we show that for the special case of  $M = N$ , the total number of delay lines ( $X$ ) is approximately  $M \ln M$ . For the case where  $N > M$ ,  $X = (N - M) + M \ln M$ . These are both much smaller than  $M \times N$  required for an IM/DD system if  $M, N > 10$ .

We see from the above that for  $N \gg M$ ,  $X \approx N$ , where  $N$  is the smallest number of delays the system must provide for the required detection resolution. For the case where  $N$  is not much larger than  $M$ , we can further reduce the number of optical receivers (and delay lines) by the architecture shown in Fig. 2.3(b). Here, we introduce delays at both the optical receivers and the antenna elements. In this case, the total delay for the signal from one antenna element is the sum of the delays corresponding to the antenna element and the receiver. By appropriately arranging the delays for the antenna elements, the antenna can be pointed to every desired direction while the number of delay lines and optical receivers is reduced. In Appendix 4, an arrangement of the delays at the antenna site is analyzed and it is found that when  $N = jM$ , the total number of delays needed at the receiver site ( $X$ ) is  $(1.5 + 1/j)N$  when  $j$  is an integer, and  $X = (1.5[j] + 1)M$  when  $j$  is not an integer, but where  $[j]$  is the least integer that is not smaller than  $j$ . Here,  $X$  is approximately linearly

proportional to  $N$ . For example, if there are 128 antenna elements and the system requires 128 different delays (7 bit resolution), then using the arrangement given in Appendix 4, only 320(=  $(1.5 + 1) \times 128$ ) delay lines are needed at the optical receiver site. Such a system requires 128 optical transmitters and 320 coherent receivers with corresponding delays. We call this a “128  $\times$  320” system.

The analysis can easily be extended for two dimensional beam forming and steering (i.e. a planar phased array), where the smallest time increments  $\Delta t_1$ ,  $\Delta t_2$  for the two spatial dimensions (elevation and azimuth) are different, and with  $N_1$  and  $N_2$  being the number of different delays for the two dimensions, respectively. The number of delay lines and optical receivers are still linearly proportional to the number of different delays,  $N_1 \cdot N_2$ , while for the IM/DD scheme, it is on the order of  $(N_1 \cdot N_2)^2$ . If  $\Delta t_1 = \Delta t_2$ , the number for both coherent and IM/DD systems are smaller than the corresponding systems where  $\Delta t_1 \neq \Delta t_2$ .

For the receiver antenna, the number of antenna elements determines the number of optical channels needed. If the tuning range of one LO laser is not sufficiently wide, multiple LO's can be used to cover the different frequency ranges, similar to the transmitter structure in Fig. 2.2(b). Alternatively, the antenna array can be divided into several sub-groups, each of which has fewer antenna elements and needs a delay feed system with a smaller number of optical channels. The received signal is then just the sum of the output microwave signals from each sub-group.

### 2.2.3 Optical Amplifier Performance

Both semiconductor optical amplifiers (SOA) and erbium-doped fiber amplifiers (EDFA) can be used to compensate for power losses at the combiners, splitters, etc., and to prevent degradation of the signal-to-noise ratio (SNR). The SOA is compact and can be integrated with other devices such as lasers, modulators, combiners/splitters, and has a wide bandwidth. On the other hand, the EDFA can accommodate more power, and the noise figure is low in comparison to the SOA. To achieve a high SNR, the system is most advantageously implemented in several cascaded gain stages as shown in Fig. 2.4. The total effective noise figure of the optical amplifier system with respect to the signal of one channel is[5]:

$$F = L_1(K_1(F_1 - 1) + 1) + \frac{F_2 - 1}{G_1/L_1L_2} + \frac{F_3 - 1}{G_1G_2/L_1L_2L_3} \quad (2.1)$$

where  $G_n$  and  $F_n$  are the gain and noise figure, respectively, for the  $n$ th stage in the amplifier cascade,  $L_n$  is the optical loss before each stage, and  $K_1$  is the number of amplifiers in the first stage. Now,  $K_1$  is in Eq. 2.1 because after the signals combine, the noise in one channel is due to the amplified-spontaneous-emission (ASE) noise from all optical amplifiers in the first stage. Assume  $G_1/L_1 \gg 1$  (since the gain is usually much larger than the loss of the first stage) and  $G_i/L_i > 1$  for  $i = 2, 3$ . In this case, the contribution to the noise from the first stage amplifiers dominates over subsequent stages in the cascade. Provided that the gain of the following stages can compensate the loss of each stage, the noise figure is  $\sim L_1(K_1(F_1 - 1) + 1)$  even if there are additional splittings after the combinations in the architecture shown in Fig. 2.1, as required, for example, by the expanded transmitter in Fig. 2.2(b).

For an EDFA, the noise is mainly due to ASE noise even for multichannel amplifi-

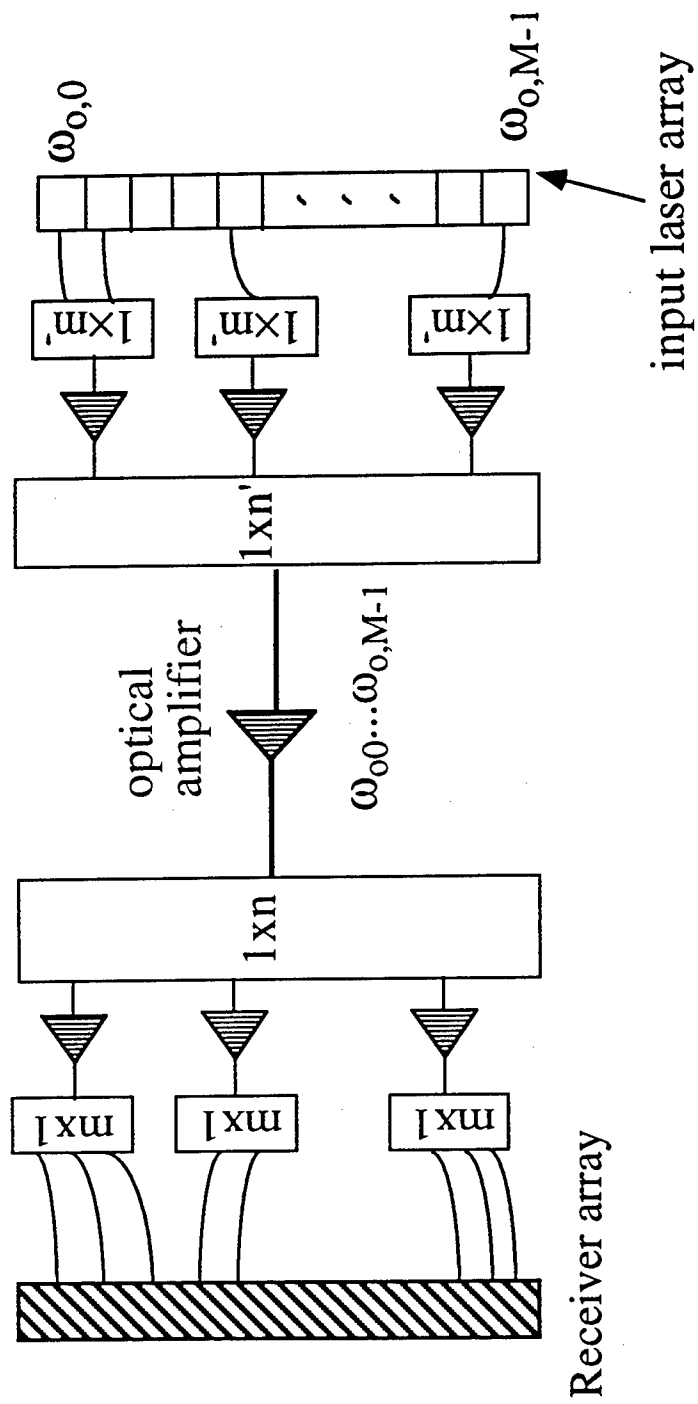


Figure 2.4 The schematic diagram of a multistage optical amplification system.

cation. On the other hand, an SOA has both ASE noise and crosstalk, which depends on the number of channels, the optical input power, and the modulation scheme of the optical signal. These gain depletion effects are difficult to treat, and are usually estimated numerically[6]. For simplicity, therefore we consider here only EDFA-based systems. The performance of an example EDFA-based antenna feed system consisting of 128 transmitter lasers and 320 optical receivers is illustrated in Table 2.1. For this system, the optical gain of one channel is  $-3.2$  dB, indicating that such coherent systems can be made nearly transparent. There have been reports of EDFA's with gains of 54 dB and 3.1 dB noise figure[7]. Thus, using currently available EDFAs, one can achieve the performance predicted in Table 2.1, where the noise figure is approximately  $N \cdot F_1$  for each channel in an  $N$  channel system. The noise figure of the EDFAs of the example  $128 \times 320$  system is 25 dB. As will be shown below, this noise figure determines the overall system performance, especially the SNR and DR. Utilizing optical filters whose passbands are limited to the signal bandwidth after each EDFA, the noise figure can be further reduced to  $\sim L_1 F_1$ , or  $\sim 16$  dB.

#### 2.2.4 Miscellaneous System Issues

Fiber chromatic dispersion will cause signals propagating in different channels to travel at different speeds. This problem is especially acute for systems consisting of a large number of channels where the wavelength difference between some channels is quite large. When the system is used in aerospace applications, the length of the fiber is typically less than several tens of meters. In this case, even if the system covers a large frequency range, dispersion will not cause serious problems. However,

**Table 2.1 Parameters for the Example System**

Component	Optical Loss (dB)	Excess Loss (dB)*	Optical Gain (dB)	Noise Figure (dB)	Optical Signal Power/ Input Signal (dB)
16×1 Combiner (L1)	12	0.2			-12.2
EDFA (G1, F1)			21.2	4	9
8×1 combiner (L2)	9	0.2			-0.2
Fiber	1				-1.2
EDFA(G2, F2)			10.2	4	9
1×16 Splitter (L3)	9	0.2			-3.2
EDFA (G3, F3)			15.2	4	12
1×20 (L4)	13	0.2			-1.2

\*Losses are taken to be 0.1 dB for each splice connection.

for terrestrial systems where the fiber length can exceed a kilometer, dispersion can potentially introduce additional time delays for different channels, which cannot be neglected for precise beam steering. This is especially true for systems with many channels. To solve this problem, the central frequencies of the input laser arrays are fixed, thereby determining the optical group velocity of each channel. Assume that the group velocity of channel  $k$  is  $c_k$ , then after traveling through a fiber of length  $L$ , any other channel  $k$  will have an additional time delay of  $(L/c_k - L/c_o)$  compared to channel 0. To compensate for this additional delay, we make the fiber associated with channel  $k$ ,  $(L/c_k - L/c_o)c_k$  shorter before it combines with other channels. For example, a typical value of dispersion for dispersion-shifted single mode fiber at  $1.55 \mu\text{m}$  is around  $1 \text{ ps/km}\cdot\text{nm}$ . For two optical channels separated in wavelength by  $\Delta\lambda = 1 \text{ nm}$ , and using a  $1 \text{ km}$  long fiber, the time delay difference is  $1 \text{ ps}$ . If the channel separation is  $10 \text{ nm}$  and the fiber length is  $10 \text{ km}$ , the additional delay would be  $100 \text{ ps}$ , which is a significant delay for a  $1 \text{ GHz}$  signal.

For very high frequency antenna systems (i.e. several tens of GHz), it is difficult to directly use coherent detection, because the intermediate frequency (frequency difference between the incoming optical signal and the LO signal) is too high for use with conventional microwave devices. In this case, the coherent system can be used to introduce true-time delay at a low frequency (e.g.  $\sim 1 \text{ GHz}$ ). For producing microwave transmitting signals, microwave mixers and local oscillators are then used to up-shift the delayed signals into the high frequency band desired. Conversely, for receiving, mixers are used to down-shift the frequency before introducing the time delays [8]. These microwave frequency shifts can be achieved up to frequencies as high as several tens of GHz using conventional diode mixers[9].

In this chapter, we discuss digitalized time delays, which will introduce some errors in the desired beam characteristics [10]. For systems with a large number of delays, however, this error tends to be very small.

In the following sections, we calculate the SNR, SIR and DR of one channel in a  $128 \times 320$  example system, illustrating the system performance. However, in a phased array receiver, the final signal is the sum of the signals from each antenna element. Due to their coherence, the signal amplitudes are added, although the noise contributions are added in power. Hence, the system SNR, DR and SIR will be  $M$  times larger than those of one channel, where  $M$  is the number of antenna elements.

## 2.3 System Evaluation

In this section, we discuss general approaches for the quantitative evaluation of the performance of the coherent optically controlled phased array antenna system. We first discuss the typical spectra of radar signals, and then derive expressions to calculate the signal-to-noise ratio (SNR), dynamic range (DR), signal-to-interchannel-interference ratio (SIR), optimum optical channel spacing and the number of optical channels that can be accommodated. In the following sections, we apply these expressions to evaluate the performance of an example antenna receiver which has 128 elements and 7 bit resolution (the  $128 \times 320$  system as discussed in Sec. 2.2.2).

### 2.3.1 The Radar Spectrum

A radar signal typically consists of a sequence of pulsed, high frequency oscillations (see Fig.2.5). The spectrum of this microwave signal can be expressed as[10]:

$$C(f) = 0.5(C_b(f + f_m) + C_b(f - f_m)) \quad (2.2)$$

where

$$C_b(f) = \sum_{n=-\infty}^{\infty} \sin(\pi n \tau f_r) / (\pi n f_r) \delta(f - n f_r)$$

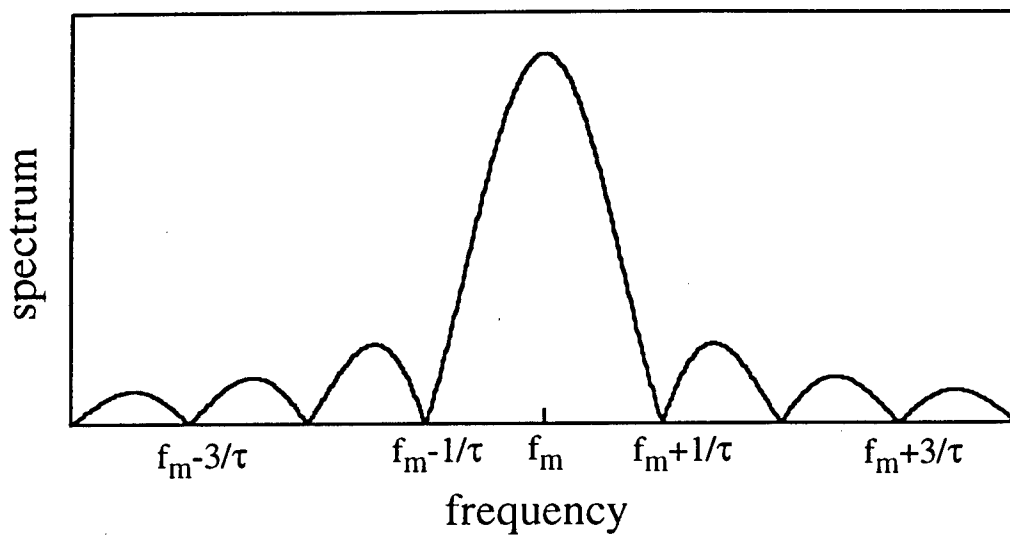
for a long train of coherent pulses, and

$$C_b(f) = \sin(\pi \tau f) / (\pi f)$$

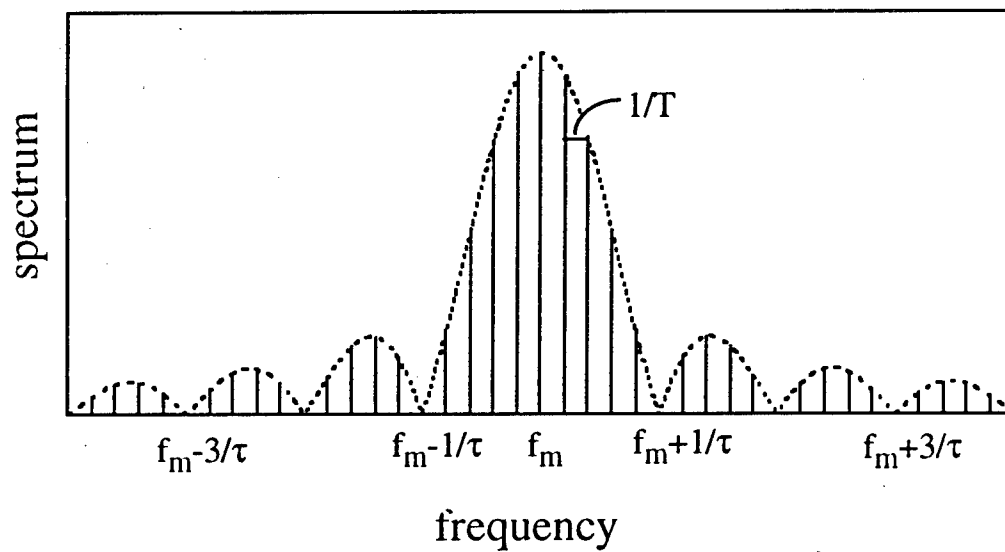
for an incoherent pulse train.

Here,  $f_r$  is the pulse repetition frequency (PRF),  $\tau$  is the pulse width, and  $f_m$  is the microwave oscillation frequency. From Eq. 2.2, we see that the characteristic spectrum of a radar signal is a sinc function centered at  $f_m$ , typically between 1 and 20 GHz, with most of the power concentrated in a comparatively narrow bandwidth which spans a frequency range on the order of  $1/\tau$  with a typical value of 1 MHz. The narrow bandwidth of the signal enables the system to greatly reduce the wideband noise.

For Doppler radar systems, a coherent pulse train is transmitted to obtain a nearly discrete spectrum, so that the frequency shifts within one PRF range can be determined [11]. From the following analysis, we find that the demodulated microwave signals from the optical carrier can still maintain the original spectrum of the modulating microwave signals, thereby ensuring that this system can employ Doppler phenomena.



(a)



(b)

Figure 2.5 The Radar Signal Spectrum  
 (a) A single pulse and an incoherent pulse train,  
 (b) A long coherent pulse train.

### 2.3.2 System Noise

We now consider the noise from optical modulation, transmission and detection. After photodetection, for the simplest case, the IF (intermediate frequency) signal current can be expressed as:

$$i_{IF}(t) = A(t) \cos[\omega_{IF}t + \phi_s(t) + \phi_{phase}(t)] + n(t) + n_{int}(t). \quad (2.3)$$

Here,  $A(t)$  and  $\phi_s(t)$  represent the amplitude and phase modulation, respectively, for the amplitude modulation (AM), frequency modulation (FM) or phase modulation (PM) schemes,  $\omega_{IF} = 2\pi f_{IF}$  is the angular IF frequency,  $\phi_{phase}$  is the laser phase noise,  $n(t)$  is the additive noise of the system, and  $n_{int}(t)$  is the interference signal current from other channels. In this chapter, the noise power spectral density is taken single-side-band. The power spectral density (PSD) of the time derivative of the phase noise is[12]:

$$S_{\dot{\phi}_{phase}} = 4\pi\Delta\nu \quad (2.4)$$

where  $\Delta\nu$  is the sum of the transmitter and LO laser linewidths. The additive noise,  $n(t)$ , consists of thermal noise, shot noise, relative intensity noise, and the beat of the LO laser with the EDFA amplified spontaneous emission (ASE) noise. The PSD of each noise source is given below[12], [13]. The thermal noise  $S_{n,thermal}$  is:

$$S_{n,thermal} = \frac{4k_B T}{r} \quad (2.5)$$

where  $k_B$  is Boltzmann's constant,  $T$  is temperature and  $r$  is the input resistance of the receiver. The shot noise  $S_{n,shot}$  is:

$$S_{n,shot} = 2eR(P_{LO} + P_{s-total}) \quad (2.6)$$

where  $R$  is the responsivity of the detector,  $P_{LO}$  is the optical power of the local oscillator, and  $P_{s-total}$  is the optical power of all signals incident on a receiver. That is,  $P_{s-total}$  is approximately equal to the optical power of one channel that is incident on a receiver ( $P_s$ ) multiplied by the number of channels. The LO-ASE beat noise  $S_{n,LO-ASE}$  is then given by:

$$S_{n,LO-ASE} = 2R^2 h\nu(F - 1)G_{tot}P_{LO} \quad (2.7)$$

where  $h$  is Planck's constant,  $\nu$  is the optical frequency,  $F$  is the optical amplifier noise figure, which can be obtained from Eq.2.1, and  $G_{tot}$  is the total optical gain for one channel. Next, the PSD of the laser relative intensity noise is [12]:

$$S_{n,RIN} = R^2(P_{LO}^2 10^{RIN_{LO}/10} + P_s^2 10^{RIN_s/10}) \quad (2.8)$$

where  $RIN_s$  and  $RIN_{LO}$  are the relative intensity noise contributions (in dB/Hz) of the transmitter and LO lasers, respectively. If balanced optical receivers are considered, then most of the contribution of the relative intensity noise, together with the direct detection and beat terms between signal channels will be canceled [14]. We will see below that the RIN nevertheless contributes to the total noise of coherent receivers. Summing Eqs. (2.5)-(2.7), the PSD of the additive noise current is given by:

$$S_n(f) = 2R^2 h\nu(F - 1)G_{tot}P_{LO} + 2eR(P_{LO} + P_{s-total}) + \frac{4k_B T}{r}. \quad (2.9)$$

When  $P_{LO}$  is sufficiently large (typically  $> 0$  dBm), the shot noise is larger than the thermal noise. Also, the LO-ASE beat noise is larger than the shot noise provided that the optical amplification is sufficiently large. Thus the LO-ASE noise usually dominates the frequency independent noise expression in Eq. 2.9. The discussion in

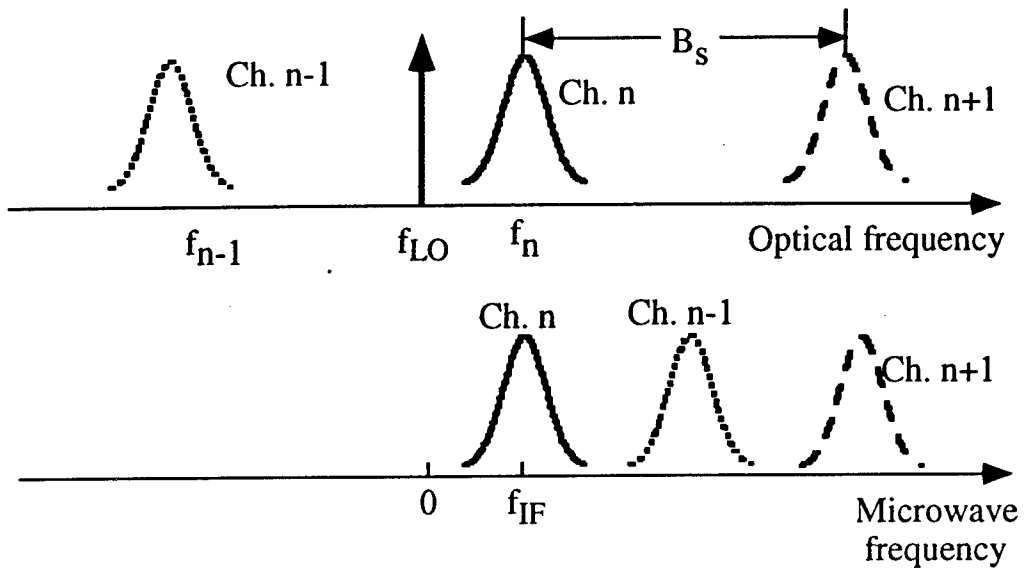
Sec. 2.2 shows that the ASE noise usually comes from the first amplifier stage. Thus, small variations in the subsequent splitting and amplification will have little effect on the actual SNR if the LO-ASE noise dominates.

### 2.3.3 Signal-to-Interchannel-Interference Ratio (SIR) and Dynamic Range(DR)

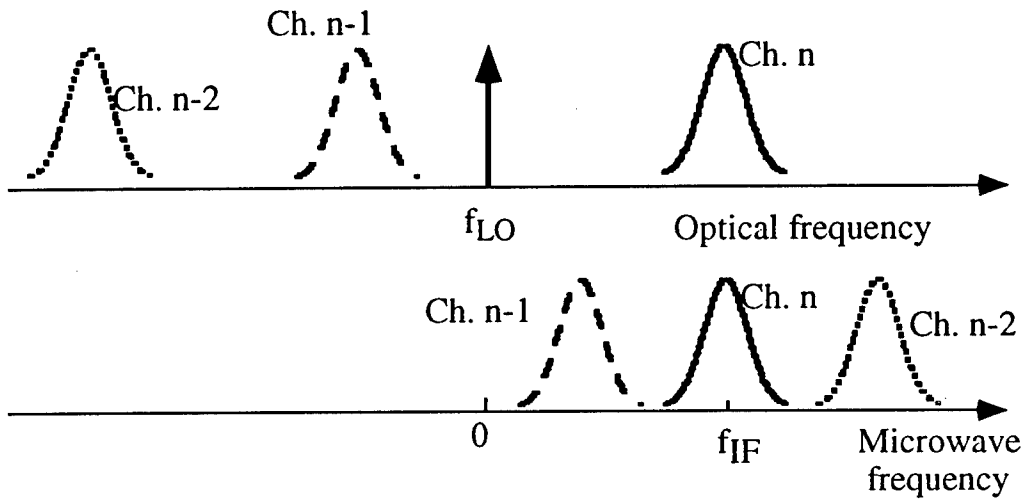
For a large multichannel system, one must consider the bandwidth and minimum channel spacing required to accommodate the desired number of delays while keeping the interchannel interference at an acceptably low level. If balanced coherent receivers are used, interference from all other channels degrades the signal of the primary channel only through the effect of excess shot noise and the LO-undesired channel interference[14]. We have considered the excess shot noise in Eq. 2.6. Here the SIR is defined as the ratio of the power received in the primary signal channel ( $P_{s-final}$ ) to the total LO/undesired channel interference power ( $P_{int-final}$ ) at the output. That is:

$$SIR = \frac{P_{s-final}}{P_{int-final}}. \quad (2.10)$$

Following Glance, *et al* [15], there are two schemes which avoid excessive interference in the IF domain. In both schemes, optical channels are equally spaced in optical frequency domain. In one scheme, the LO frequency is positioned nearest to the primary channel as shown in Fig. 2.6(a). We name this the "NEAR-LO" scheme. In this scheme, a channel spacing of  $D > 2f_{IF}$  is required. Most of the interference for the primary channel,  $k$ , comes from the nearest neighbor channel,  $k - 1$ . Increasing  $D$  will decrease the interference. Alternatively, the LO frequency can be positioned



(a) Near-LO Scheme



(b) Far-LO Scheme

Figure 2.6 Illustration of the channel placement for (a)  $|f_{n-1} - f_{LO}| > f_{IF}$ , the NEAR -LO scheme, and (b)  $|f_{n-1} - f_{LO}| > f_{IF}$ , the FAR-LO scheme.

Here,  $f_{n-1}$  and  $f_n$  are the central optical frequencies of channel n-1 and n,  $f_{LO}$  is frequency of LO laser,  $f_{IF} = |f_n - f_{LO}|$  is the intermediate frequency, and  $B_s$  is the optical channel spacing. The second configuration can save some channel spacing for a high  $f_{IF}$  and a comparatively narrow signal bandwidth.

nearest to one of the adjacent channels (Fig. 2.6(b)). When a high IF frequency and comparatively narrow signal bandwidth are required, as is the case for the AM modulation-demodulation, or a small modulation index for FM and PM, Fig. 2.6(b) only requires an optical channel spacing which is comparable to  $f_{IF}$ , while keeping the interchannel interference at an acceptably low level. For Fig. 2.6(b), the interchannel interference mainly comes from channels  $k - 1$  and  $k - 2$ . In this scheme (called the "FAR-LO" scheme), for a fixed  $f_{IF}$ , the interference is minimum at  $D = 4f_{IF}/3$ , where the channels are also equally spaced in the IF domain. In Sec. 2.4 and 2.5, we will estimate the SIR for both the NEAR-LO and FAR-LO schemes and make some comparisons. Given the optical channel spacing required to get a small SIR and the tuning range available to LO lasers, we will calculate the number of optical channels that can be accommodated in each case.

The dynamic range of the microwave-optic link is defined as the ratio of the maximum input RF power ( $P_{max}$ ) to the minimum input RF power ( $P_{min}$ ). Here,  $P_{min}$  is the RF power that results in  $S/N=1$  at the output, and  $P_{max}$  is the power when the nonlinear distortion power equals the noise power. Hence[12]:

$$DR = 10 \log \left[ \frac{P_{in-max}}{P_{in-min}} \right]. \quad (2.11)$$

## 2.4 Analog AM Antenna Links

### 2.4.1 SNR performance of AM links

Wideband filter-rectifier-narrow-band filter (WIRNA) processing has been suggested[12] as an efficient and laser-phase-noise-insensitive means to receive analog AM signals. A block diagram of a typical WIRNA receiver is shown in Fig. 2.7. Here, a wide bandpass filter is used to pass the IF signal. This is followed by a square law detector and a narrow band filter to demodulate the signal. For the antenna systems in Fig. 2.1 and 2.3, the IF current,  $i_{IF}(t)$  is given by:

$$i_{IF}(t) = \frac{A_s}{\sqrt{2}} [\cos(\omega_{IF}t + \phi_{phase}(t) + mx(t)) - \sin(\omega_{IF}t + \phi_{phase}(t))] + n(t) + n_{int}(t) \quad (2.12)$$

with  $A_s(t) = 2R\sqrt{P_s P_{LO}}$ . Also,  $P_s$  is the optical signal power of one channel and  $P_{LO}$  is the LO power. Here,  $m$  is the modulation index and  $x(t)$  is the normalized modulation signal. The Mach-Zehnder modulated signal is an AM modulated signal in the sense that when the IF current is squared, the signal term can be obtained by a low pass filter. This is evident by taking the square of Eq. 2.12 while neglecting all of the noise terms.

Assume that the interference noise,  $n_{int}(t)$  is negligible and  $mx(t) \ll 1$ , then Eq. (2.12) becomes:

$$i_{IF}(t) = \frac{A_s}{\sqrt{2}} [\cos(\omega_{IF}t + \phi_{phase}(t)) - (1 + mx(t)) \sin(\omega_{IF}t + \phi_{phase}(t))] + n(t). \quad (2.13)$$

Most of the signal power is concentrated around  $f_{IF} \pm f_m$ . For a laser linewidth of  $\Delta\nu = 0$ , more than 95% of the signal power falls within  $f_{IF} \pm (f_m + 2/\tau)$ . Hence,

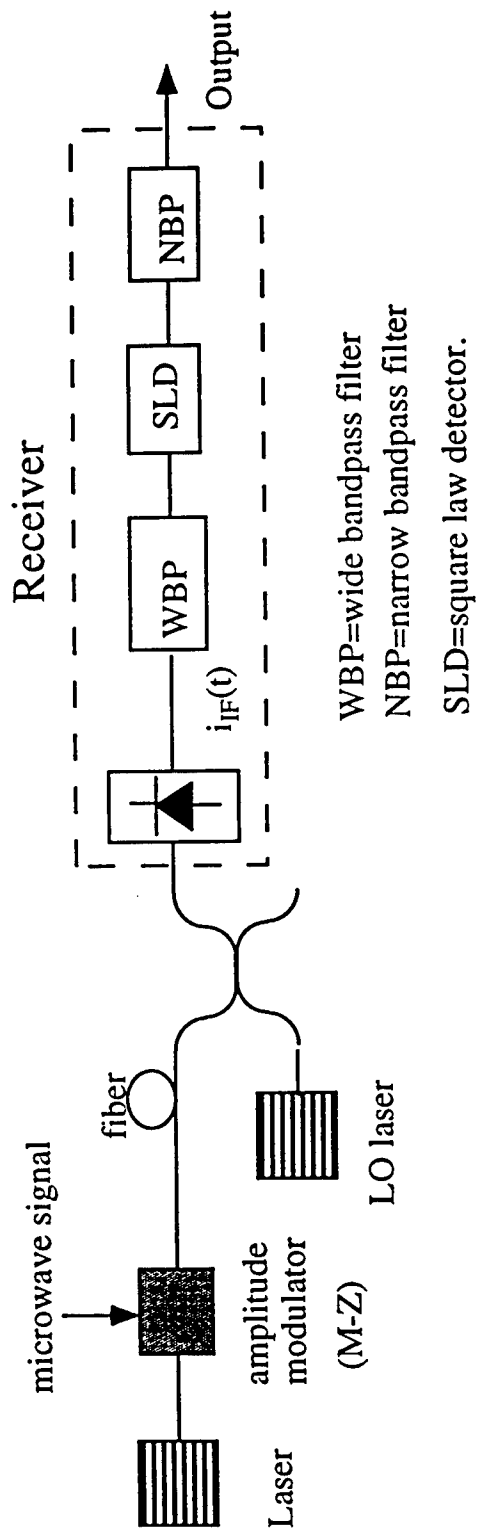


Figure 2.7 Schematic diagram of an AM-WIRNA link.  
 WIRNA stands for wideband filter-rectifier-narrow-band filter receiver.

a rectangular IF filter which covers this frequency range in a WIRNA receiver is desirable. With a non-zero laser linewidth, the signal spectrum is widened and the filter needs to be approximately  $12.7\Delta\nu$  wider to accommodate more than 95% of the signal energy[17]. The IF bandwidth is therefore given by:

$$B_{IF} = 2f_m + 4/\tau + 12.7\Delta\nu. \quad (2.14)$$

The second filter should be centered at  $f_m$  with a bandwidth of several  $1/\tau$  to obtain the final output. For convenience of analysis, an ideal rectangular bandpass filter is assumed. The transfer function of the two filters can thus be expressed as:

$$H_{IF}(f) = \begin{cases} 1 & |f - f_m| < f_m + 2/\tau + 6.4\Delta\nu \\ 0 & \text{otherwise.} \end{cases} \quad (2.15)$$

$$H_2(f) = \begin{cases} 1 & |f - f_m| < 2/\tau \\ 0 & \text{otherwise.} \end{cases} \quad (2.16)$$

The impulse response of the two filters,  $h_{IF}(t)$  and  $h_2(t)$ , can be calculated through the Fourier transform of  $H_{IF}(f)$  and  $H_2(f)$ . This leads to the following expression for the output power after the square law device and narrow band filter[12]:

$$\begin{aligned} P_{out} &= P_{sig} + P_{sd} + P_{sn} + P_{nn} + P_{RIN,ad} \\ &= \Gamma_1 m^2 A_s^4 + (\Gamma_2 m^2 + \Gamma_3) A_s^4 + \\ &\quad (\Gamma_4 m^2 + \Gamma_5) A_s^2 S_n(f) + \Gamma_6 S_n^2(f) + \Gamma_1 A_s^4 (10^{\frac{RIN_{LO}}{10}} + 10^{\frac{RIN_s}{10}}) B. \end{aligned} \quad (2.17)$$

The first term is the signal power, and the remaining terms are noise contributions. The  $\Gamma$  parameters depend on  $B_{IF}$  and  $B$ , with  $\Gamma_3$  also depending on  $f_{IF}$ . The term  $P_{sd}$  is due to phase noise,  $P_{sn}$  is the beat of the signal and the additive noise, and  $P_{nn}$  is the squared additive noise. Also,  $P_{RIN,ad}$  is the noise term induced by the laser RIN

in the LO-desired channel cross term, and cannot be canceled by a balanced receiver. The two terms in  $P_{sd}$  and  $P_{sn}$  are due to the received signal having both a carrier and message term. Laser phase noise causes the signal spectrum to be broadened, and it degrades the SNR in two ways. First, since the IF signal spectrum is broadened, when the signal passes the IF filter, some of the signal spectrum is cut off. Thus, it causes phase-noise-to-intensity-noise conversion. Second, the spectrum of the square of the IF current in Eq. 2.13 has a carrier component at  $2f_{IF}$ , which is also broadened by the laser phase noise. If  $f_{IF}$  is finite, some power of this term falls within the bandwidth, B, and degrades the signal.

For a reasonable optical power,  $P_{sn}$  is always much larger than  $P_{nn}$ . Thus, if the laser linewidth is very narrow, the RIN is very small (-140dB/Hz), and  $mx(t) \ll 1$ . The expression for the SNR then simplifies to:

$$SNR = \frac{4\Gamma_1 m^2 R^2 P_{LO} P_s \bar{G}_{tot}}{\Gamma_5 S_n(f)}. \quad (2.18)$$

Usually the LO-ASE noise is the most significant noise in source  $S_n(f)$ . Thus, Eq. 2.18 further simplifies to:

$$SNR = \frac{2\Gamma_1 m^2 P_s}{\Gamma_5 h\nu F} \quad (2.19)$$

where  $\Gamma_5$  is proportional to B. If  $\Delta\nu$  is not too large, and if the IF frequency is much larger than the microwave signal frequency, then the signal distortion due to the laser phase noise is very low. As both theoretical and experimental results have shown[12],[16], this scheme is basically linewidth insensitive. The demodulated microwave signal can therefore maintain the spectral purity of the original signal. Thus, for systems using lasers with low RIN, narrow linewidth, and high LO power, Eq. 2.19 can be used to calculate the SNR for one optical channel.

Figure 2.8 is a plot of SNR vs.  $P_s$  for one channel in the  $128 \times 320$  example system of Sec. 2.2. For a 1 GHz signal, the laser phase noise ( $\Delta\nu \neq 0$ ) degrades the signal more for a low IF (2 GHz) than for a high IF (9 GHz) due to the reasons discussed above. The SNR is 5 to 10 dB lower for  $f_{IF}=2$  GHz than at 9 GHz. It is shown that for  $\Delta\nu = 10$  MHz, with a high IF and a wide IF bandpass filter, and for  $P_s < P_{LO}$ , the main noise source is the LO-ASE noise, and the SNR increases with  $P_s$ . As  $P_s$  approaches  $P_{LO}$ , the increase of SNR with  $P_s$  saturates. The saturation is due to the dominance of shot noise contributed by the total optical signal power of all the channels, as indicated in Eq. 2.6. Further increase in the optical signal power above  $P_{LO}$  will therefore not improve the SNR performance. As the laser linewidth increases, more of the signal power spectrum is cut off by the IF bandpass filter, causing the phase-noise-to-intensity-noise conversion, which in turn decreases the SNR. Nevertheless, from the calculations we see that if  $P_s$  is not excessively large (i.e.  $< 5$  dBm), this effect is small. From Fig. 2.8, we see that for  $m = 0.1$ ,  $\Delta\nu < 10$  MHz,  $P_s = 0$  dBm,  $f_{IF} = 9$  GHz,  $B_{IF} = 3$  GHz,  $B = 1$  MHz then SNR = 46 dB. Thus, in order to get a high SNR, then a high IF, small  $\Delta\nu$  and high signal power are required.

As the noise is mainly due to the LO-ASE noise, putting an optical filter after each first stage optical amplifier significantly reduces the ASE noise of the adjacent channels. For our example system, the SNR of one channel can be increased by 10 dB using such filter techniques.

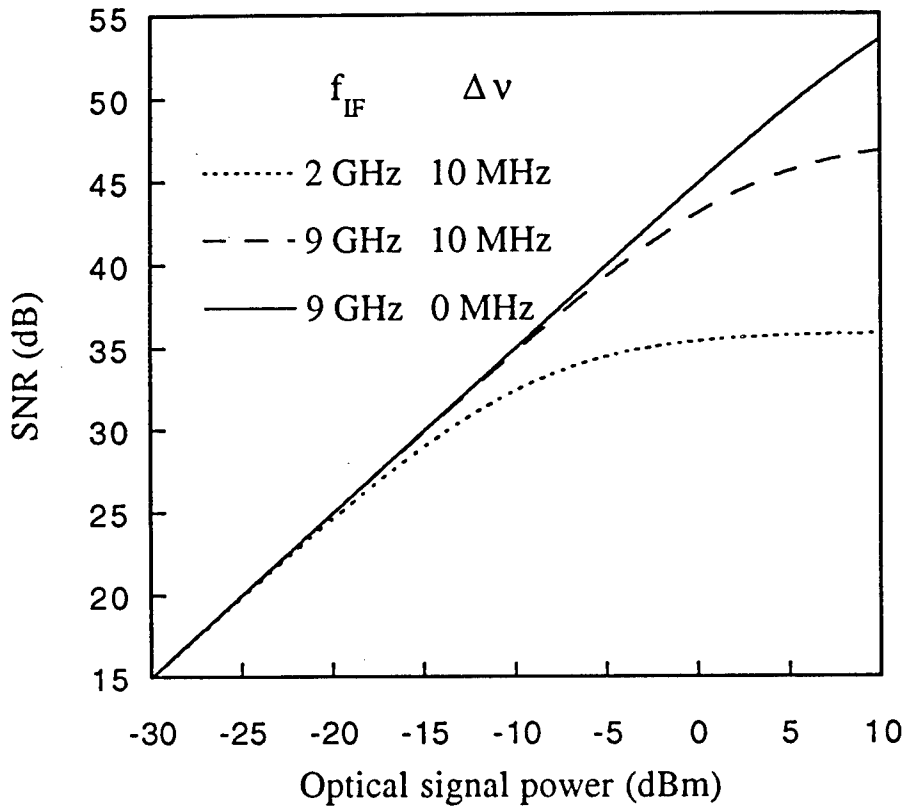


Figure 2.8 Signal-to-noise (SNR) versus signal power of one channel of AM links for  $P_{LO} = 10$  dBm,  $B = 1$  Mz,  $f_m = 1$  GHz,  $R = 0.6$  A/W,  $m = 0.1$ .

## 2.4.2 SIR and the Channel Spacing

To calculate the interchannel interference, we simplify the problem by considering the contribution from neighboring channels whose signal spectrum is noise-free, i.e. we assume  $\text{SNR} \gg 1$ . From Eq. 2.13, the spectrum of one channel of the AM IF signal without noise is given by:

$$C_{AM}(f) = A_s \left[ \delta(f - f_{IF}) + \frac{1}{\sqrt{2}} m C(f - f_{IF}) \right] \quad (2.20)$$

where  $C(f)$  is the spectral coefficient of the radar signal given in Eq. 2.2. Equation 2.12 shows that the IF current has an interference term. After being filtered and squared, there are two terms from interference: one is the beat between the signal and the interference, the other is the square term of the interference. In the limit of small interference, the first term is always much larger than the second. Thus the interference power can be calculated as:

$$P_{int} = \int \{ [s(f)H_{IF}(f)] * [int(f)H_{IF}(f)] \cdot H_2(f) \}^2 df \quad (2.21)$$

where  $s(f)$  and  $int(f)$  are the spectra of the signal and interference currents at the IF stage, respectively, and  $*$  denotes the convolution operation.

Figure 2.9 shows the SIR for the AM scheme where the channel bandwidth accommodates more than 95% of the signal energy. Usually for  $f_m \tau \gg 1$ ,  $B_{IF}$  is slightly larger than  $2f_m$ . For the NEAR-LO scheme shown in Fig. 2.6(a) and 2.9(a), the calculations indicate that when the channel spacing ( $D$ ) is slightly more than  $2f_{IF} + 2f_m$ , then  $SIR > 60$  dB. For the FAR-LO scheme in Fig. 2.6(b) and 2.9(b),  $SIR > 60$  dB when  $D$  is in a small range from  $f_{IF} + f_m$  to  $2f_{IF} - 2f_m$ , and the SIR is at maximum when  $D = 4f_{IF}/3$ . For both schemes, a smaller  $f_{IF}$  leads to a smaller

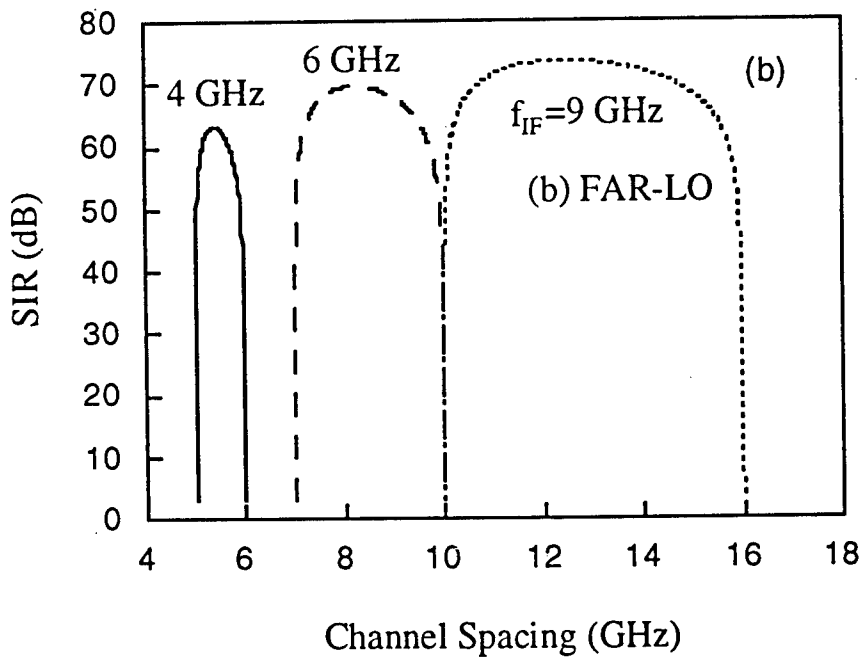
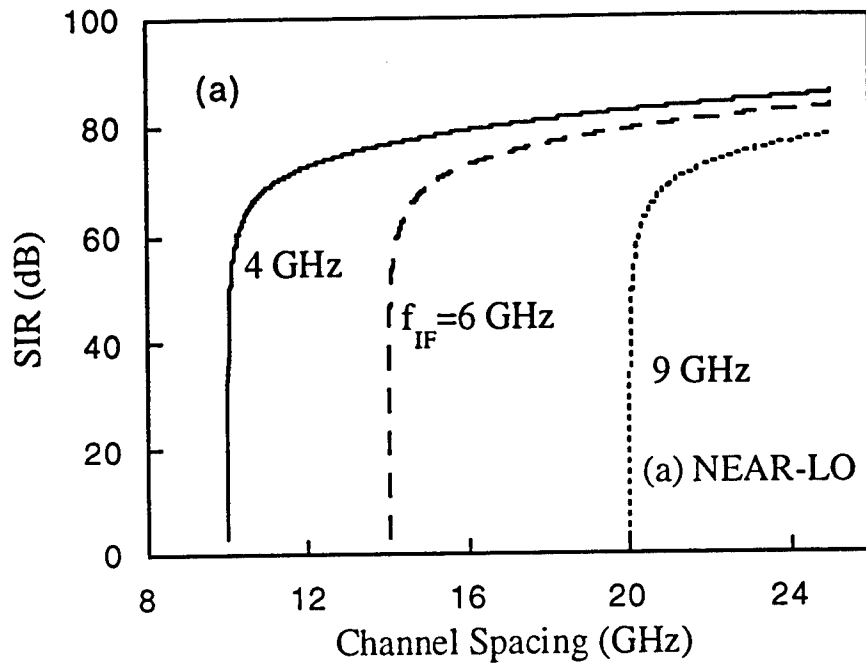


Figure 2.9: Signal-to-interchannel-interference ratio (SIR) vs. channel spacing for (a) the NEAR-LO scheme, and (b) the FAR-LO scheme of Fig. 2.6 for a 1 GHz signal. The SIR is insensitive to the modulation index and optical power, because an ideal balanced receiver is assumed, more channels would have little effect on this result.

D and SIR. For multichannel systems, on one hand, we want D small so that for a given frequency tuning range, more channels can be used; on the other hand, we want to keep both SIR and SNR large to get a high quality signal, and this requires a large  $f_{IF}$  and D. Since the SIR is very high for this system, the SNR and channel spacing are the main concerns in choosing a proper  $f_{IF}$ . To get a high SNR, a large  $f_{IF}$  is required, and the FAR-LO scheme can be used to reduce channel spacing. For  $f_{IF} = 9f_m$  using the FAR-LO scheme and a channel spacing of  $\sim 12f_m$ , the SIR can be as high as 70 dB. These calculations are independent of the modulation depth, optical power, or RF power. When the SNR changes as the optical power or modulation index changes, the SIR does not change. Hence, for proper channel spacing, interchannel interference does little to degrade the system performance.

### 2.4.3 Dynamic range of the AM links

From the results of Sec. 2.4.2, we know that the interchannel interference can always be kept very low while the microwave signal power or the optical signal power changes, and thus it has little effect on the dynamic range. Taking the third order intermodulation distortion as the limit for channel linearity, the dynamic range of AM links is calculated using[12]:

$$DR = 10 \log \left[ 8 \left( \frac{\Gamma_1 A_s^4}{\Gamma_3 A_s^4 + \Gamma_5 A_s^2 S_n(f) + \Gamma_6 S_n(f)^2 + \Gamma_1 A_s^4 (10^{RIN_{Lo}/10} + 10^{RIN_s/10}) B} \right)^{\frac{2}{3}} \right] \quad (2.22)$$

Figure 2.10 shows the calculated DR for different laser linewidths,  $\Delta\nu$ , and different IF frequencies. It is found that within a reasonable signal power range, if  $\Delta\nu$  is not too large (i.e.  $< 10$  MHz), and the  $f_{IF}$  is high (e.g. 9 GHz), the laser phase

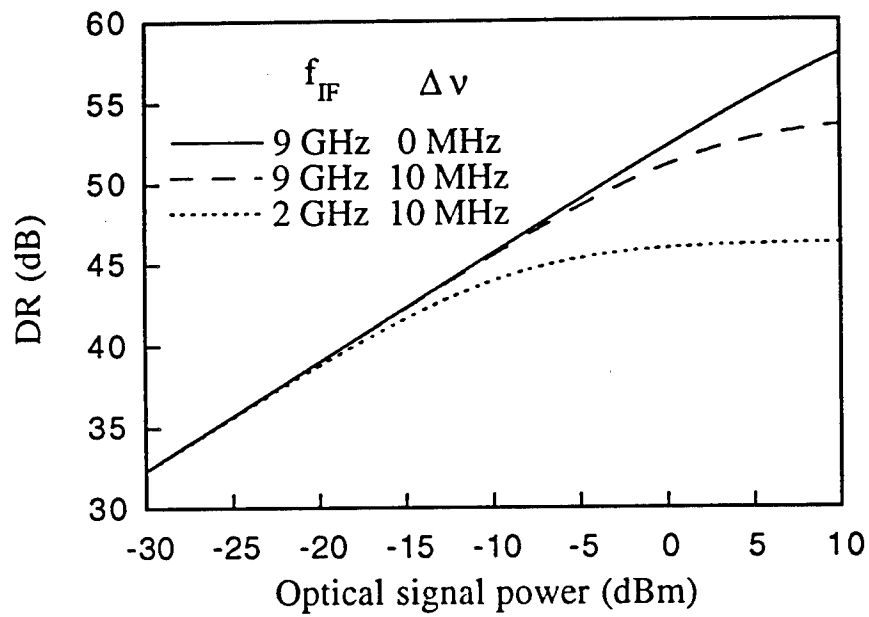


Figure 2.10: Dynamic range (DR) of AM links.

The DR is limited by the noise floor and the third order intermodulation distortion.

noise does not affect the DR performance. When the signal power of one channel at the transmitter is only  $-5$  dBm, the dynamic range is around 50 dB for a 1 MHz bandwidth, which corresponds to 110 dB/Hz. These values suggest reasonably good DR performance.

The above calculations assume that the RIN of lasers is very small ( $< -140$  dB/Hz). Figure 2.11 shows the effect of RIN on the dynamic range of an AM-WIRNA receiver. We see that the system performance is reasonably insensitive to the RIN for most practically achievable laser noise levels[18]. For example, when  $P_{LO} = 10$  dBm, the DR is flat up to  $RIN = -130$  dB/Hz for  $P_s = 0$  dBm, and it is flat up to  $RIN = -120$  dB/Hz for  $P_s = -10$  dBm.

The above calculations also assume a narrow passband of the final filter. In an actual system, the received signal is down-shifted in frequency by mixing with a local oscillator prior to the narrow bandpass filter. Since mixing with a pure local oscillator signal results in a simple frequency transfer of the signal and noise spectra, the noise effect on the optical links remains the same as obtained above, as well as for the FM and PM schemes described in the following section.

The calculations of this section show that for one channel in a "128  $\times$  320" example system, the optical AM scheme achieves a high  $SIR = 70$  dB, and  $DR = 50$  dB for a 1 MHz signal bandwidth. Furthermore, a channel spacing of  $12f_m$  is sufficient (for  $f_{IF} = 9f_m$ ) if the laser linewidth and  $1/\tau$  is much smaller than  $f_m$ , which is usually true. Given that  $1 \text{ \AA} \cong 12 \text{ GHz}$ , a 10 nm laser tuning range can easily accommodate 100 optical channels for a 1 GHz microwave signal.

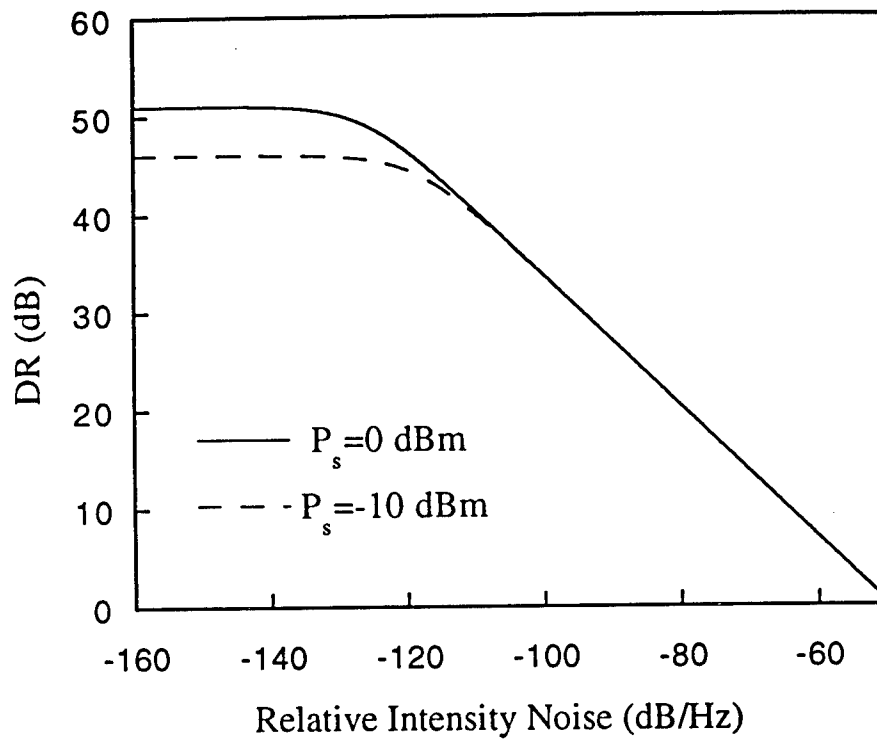


Figure 2.11: Relative -intensity-noise (RIN) effect on the DR of AM links for  $B = 1$  MHz,  $IF = 9$  GHz,  $P = 10$  dBm for LO and laser linewidth of 10 MHz. Both the transmitter and LO lasers are assumed to have the same RIN value.

## 2.5 FM and PM Phase Delay Schemes

### 2.5.1 SNR of the FM Scheme

Figure 2.12 is a schematic diagram for a typical optical FM demodulation receiver[12]. After the heterodyne photodetection, a rectangular bandpass filter ( $B_{IF}$ ) is used to pass most of the power of the selected channel while reducing interference from all other channels. The signal is then demodulated by an electronic differentiator and envelope detector, and then passes a second bandpass filter similar to that used in AM schemes to obtain a noise-reduced output signal. Carson's Law [5] states that to pass nearly 98% of the signal power,  $B_{IF}$  must be:

$$B_{IF} = 2(\beta + 1)B_e, \quad (2.23)$$

where  $B_e$  is equal to the high frequency cutoff of the final pass band of Eq. 2.16, and  $\beta$  is the modulation index. If  $\tau f_m \ll 1$ ,  $B_e$  is approximately equal to  $f_m$ . We now define  $\Delta f$  as the maximum instantaneous optical frequency deviation:

$$\Delta f = \beta B_e \cong \beta f_m. \quad (2.24)$$

Once again we use Ref. [12] as the starting point for analyzing FM link performance. For our architecture, the power spectral density (PSD) around  $f_m$  caused by the additive noise after the discriminator is:

$$S_N = S_n(f)(2\pi f_m \tau_D)^2. \quad (2.25)$$

where  $\tau_D$  is the time constant of the differentiator. The PSD of the noise current

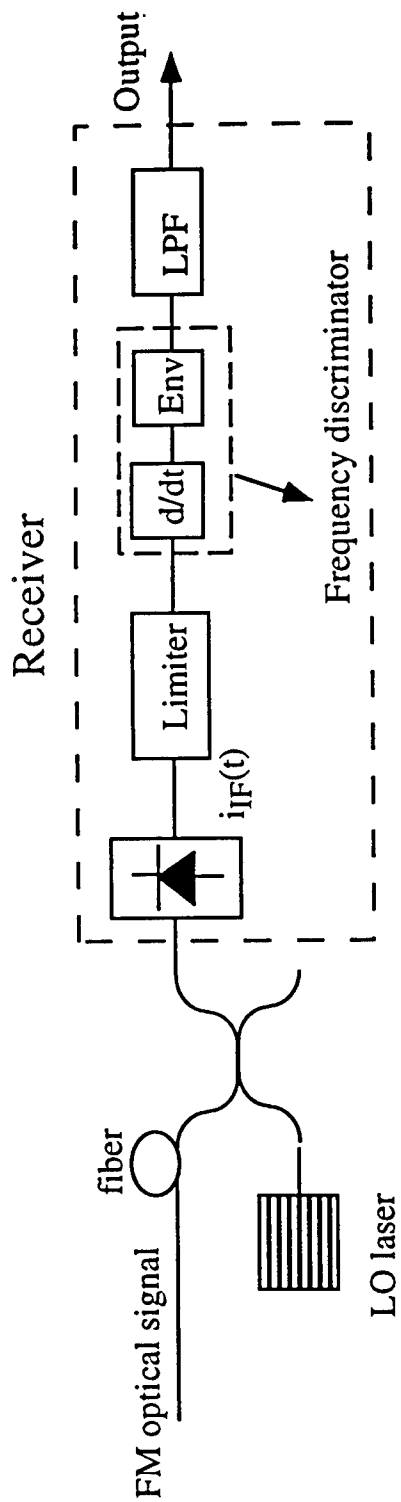


Figure 2.12: The schematic diagram of optical FM links. Here,  $d/dt$  is the microwave differentiator,  $Env$  is the envelope detector and  $LPF$  is the low pass filter.

around  $f_m$  caused by phase noise is then:

$$S_{phase} = 4\pi\tau_D^2 R^2 P_s G_{tot} P_{LO} \Delta\nu. \quad (2.26)$$

Here, the phase noise of lasers becomes white noise in the microwave frequency domain after signal demodulation. Thus the demodulated signal can still have a linewidth equal to that of the original microwave signal.

From Eqs. 2.25 and 2.26, the SNR for FM systems is:

$$SNR = \frac{2\pi^2 \Delta f^2 R^2 P_s G_{tot} P_{LO}}{B [S_n(2\pi f_m)^2 + 4\pi R^2 P_s G_{tot} P_{LO} \Delta\nu]}. \quad (2.27)$$

Usually the LO-ASE beat noise is the most significant contribution to  $S_n(f)$ , in which case the above formula can be simply expressed as:

$$SNR^{-1} = \frac{B}{\Delta f^2} \left[ \frac{4h\nu F f_m^2}{P_s} + \frac{2\Delta\nu}{\pi} \right]. \quad (2.28)$$

It is shown in Eqs. 2.27 and 2.28 that when the product of the signal power and the laser linewidth is large, the phase noise is the most significant noise source. Otherwise the post-detector white noise, especially the LO-ASE noise, is dominant. Figure 2.13 shows the calculations of SNR for one channel in the example system of Table 2.1. Fig. 2.13(a) shows SNR versus the signal power for different laser linewidths. For  $P_s = -10$  dBm, the white noise dominates when the laser linewidth is below 100 kHz. When  $\Delta\nu > 1$  MHz, phase noise tends to dominate. It is also clear from Fig. 2.13(a) that when the optical signal power is large, the laser phase noise limits the highest SNR that one channel can achieve. Further increasing signal power beyond a certain point will not improve the system SNR performance. With the optical link parameters given in Table 2.1 and  $\Delta\nu = 1$  MHz, a final passband of 1 MHz, a signal

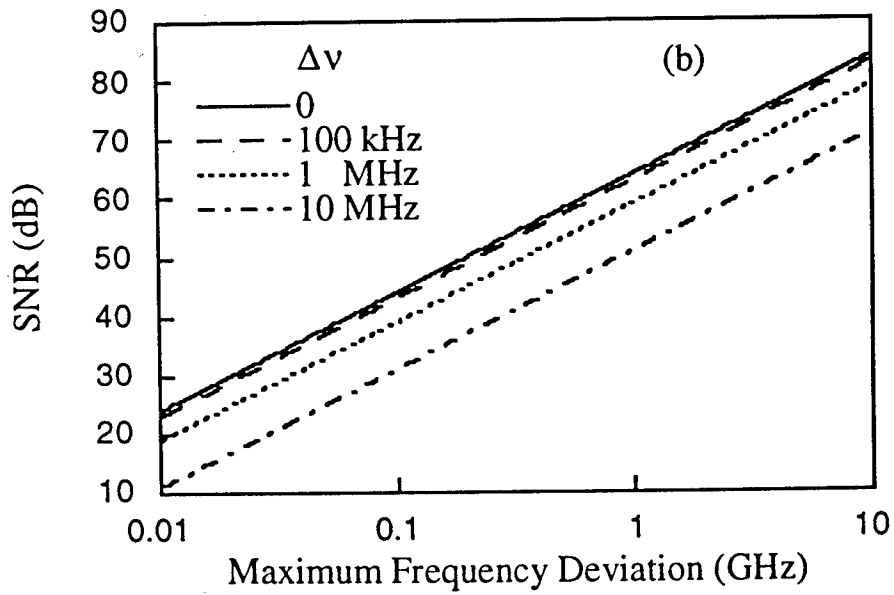
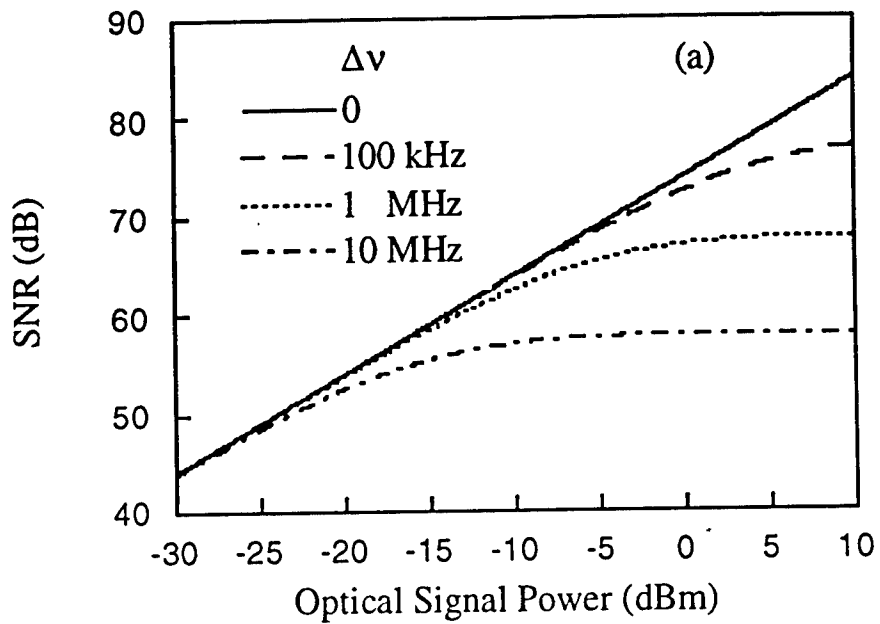


Figure 2.13: Signal-to-noise ratio (SNR) of FM schemes for different laser linewidths for a 1 MHz bandwidth  
 (a) SNR versus the optical signal power and  
 (b) SNR versus the maximum frequency deviation.

power of -10 dBm, a LO power of 10 dBm, and  $\Delta f = 2\text{GHz}$ , we obtain  $\text{SNR} = 64\text{ dB}$ , which is 124 dB/Hz. This is significantly higher than can be obtained using the AM scheme for the same input optical power. Figure 2.13(b) shows the SNR versus the maximum frequency deviation( $\Delta f$ ). We see that increasing the maximum frequency deviation by one order of magnitude increases the SNR by 20 dB since  $\text{SNR} \propto \Delta f^2$  in Eqs. 2.27 and 2.28.

## 2.5.2 SIR and channel spacing for FM links

Most of the signal power in the IF current lies around  $f_{IF} \pm kf_m$  for  $k = 0, 1, 2, \dots$ , and the interference power lies around  $|f_{o,adj} - f_{LO}| \pm kf_m$ . Here,  $f_{o,adj}$  is the central optical frequency of the interference channel and  $f_{LO}$  is the LO frequency. Following Ref. [5], the most significant interference ( $P_{int-IF}$ ) comes from the spectral components that are around  $f_{IF} \pm f_m$ . The SIR can be expressed as:

$$SIR_{FM} = \frac{\Delta f^2 P_{s-IF}}{f_m^2 P_{int-IF}} = \frac{\beta^2 P_{s-IF}}{P_{int-IF}} \quad (2.29)$$

where the  $P_{s-IF}$  is the signal power at the IF stage. Figures 2.14(a) and 2.14(b) show the SIR vs. channel spacing for both kinds of channel arrangements illustrated in Fig. 2.6. For the NEAR-LO scheme in Fig. 2.6(a) where  $|f_{n-1} - f_{LO}| > |f_n - f_{LO}|$ , a high SIR can be achieved for FM schemes. For example, for  $\beta = 2$ ,  $f_{IF} = 9f_m$  and  $B_s = 25f_m$ , then  $\text{SIR} = 64\text{ dB}$ . The channel spacing, however, should be  $> 2(\beta + 1)f_m + 2f_{IF}$ , which is larger than that required for AM transmission. A smaller  $f_{IF}$  leads to a smaller channel spacing, although  $f_{IF}$  should be greater than  $(\beta + 1)f_m$  in order to have a sufficiently wide IF passband to pass most of the signal power. Generally speaking, for FM, if a large modulation index is used, we employ the

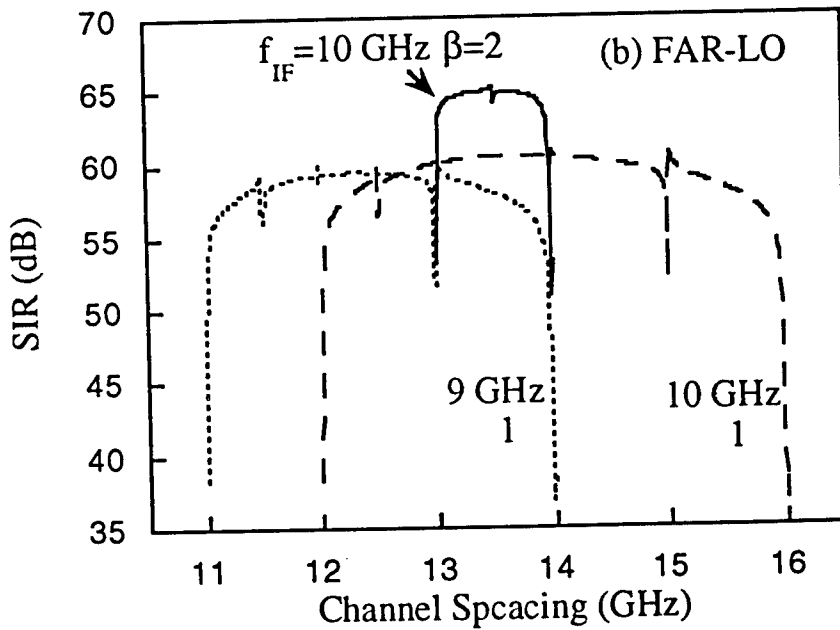
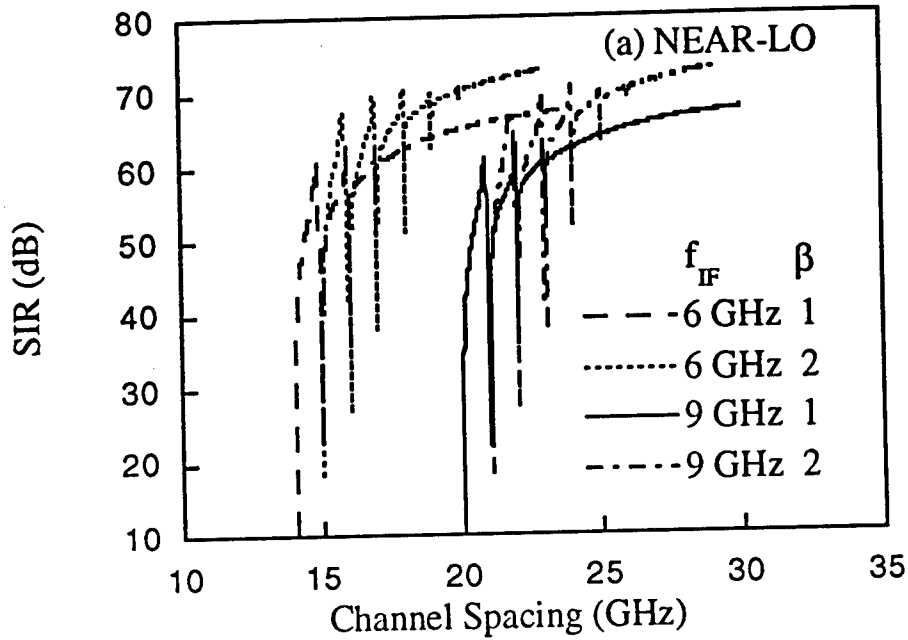


Figure 2.14: Signal-to-interchannel-interference (SIR) vs. channel spacing of (a) the NEAR-LO FM scheme (b) the FAR-LO FM scheme for a 1 GHz signal.

NEAR-LO scheme.

For the FAR-LO scheme in Fig. 2.6(b), then  $|f_{n-1} - f_{LO}| > |f_n - f_{LO}|$ . Assuming  $\beta = 2$  and  $f_{IF} = 10$  GHz, the SIR is around 57 dB when the channel spacing is between  $13f_m$  and  $14f_m$ . As illustrated in Fig. 2.6(b), the FAR-LO scheme is only suitable for narrow channel bandwidths, i.e. for a small modulation index, or a small  $\Delta f$ . The demodulation of the FM signal requires envelop detection at the last step (see Fig. 2.12). Thus a large  $f_{IF}$  is desirable to obtain a high quality signal. Under this situation (high  $f_{IF}$  and low  $\beta$ ), the FAR-LO scheme is preferred because it uses a smaller channel spacing. Due to the large total bandwidths, a 100 Å laser tuning range is needed to accommodate 100 channels.

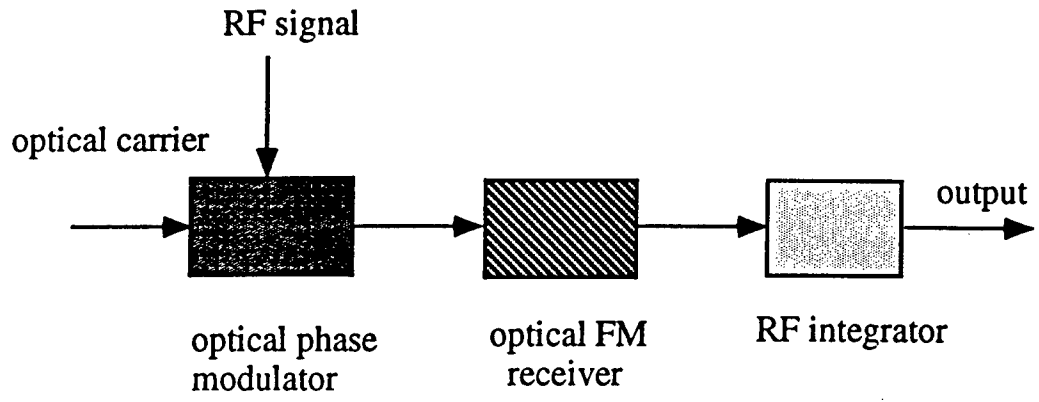
### 2.5.3 Dynamic range of FM systems

To obtain a high SNR and a small distortion of the demodulated signal, a large linear frequency response range of the laser to the modulation current or voltage is desirable. The SNR calculations also show the DR for the corresponding largest linear frequency response. For example, Fig. 2.13 shows that with parameters of the  $128 \times 320$  system given in Table 2.1, a laser linewidth of  $\Delta\nu = 1$  MHz, a signal bandwidth of 1 MHz, an optical signal power of -10 dBm per channel, and a maximum linear optical frequency deviation of 2 GHz, the SNR = 64 dB, and the DR of a single channel is also 64 dB.

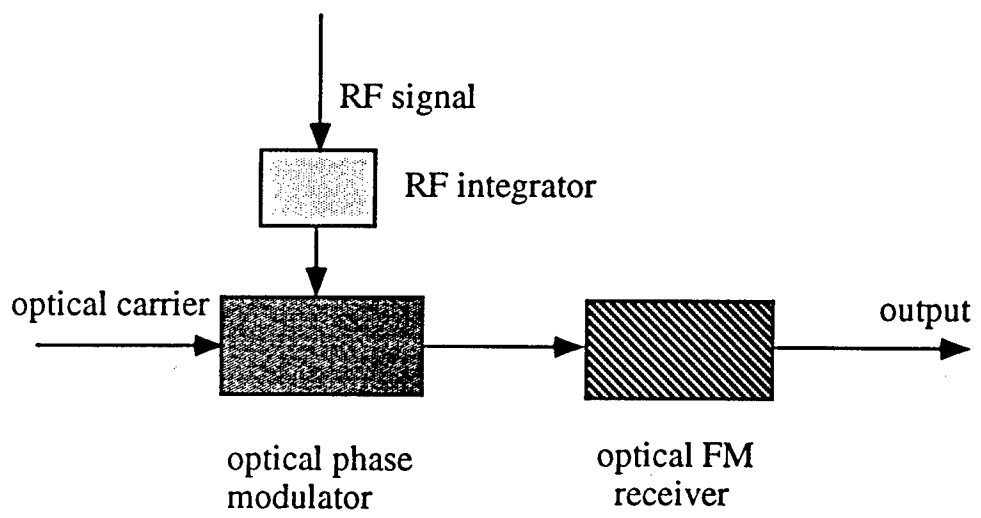
#### 2.5.4 The PM scheme

There are two ways of using optical phase modulation to transmit the radar signal (see Fig. 2.15). Here, the block diagram of the "optical FM receiver" represents the schematic diagram shown in Fig. 2.12. We see that the difference between Figs. 2.15(a) and 2.15(b) is that the RF integrator is placed either before phase modulating the light or after the optical FM receiver. If the RF integrator is placed before phase modulation, the integrated radar signal is still a pulsed oscillation of the original frequency with a phase change, which is similar to the integration of a sinusoidal signal. Thus, for the cases in Fig. 2.15, the phase modulation spectrum is similar to that for FM modulation. For the scheme of Fig. 2.15(a), the performance evaluation is almost the same as the FM scheme discussed above. For the scheme of Fig. 2.15(b), the laser phase noise directly affects the final signal, which might degrade the signal somewhat more severely.

In both FM and PM, there are two main noise sources: LO-ASE noise and laser phase noise. Reducing the laser phase noise or increasing the maximum optical frequency deviation can increase the SNR or DR of the system. For a small modulation index, the FAR-LO scheme in Fig. 2.6(a) can give a much narrower channel spacing while keeping the SIR high. For the case of a large modulation index, the NEAR-LO scheme has to be used and a much larger channel spacing is needed. For a 1 GHz radar signal, 100 channels can be accommodated by lasers with a tuning range of 100 Å. One channel can achieve a 60 dB dynamic range for a 1 MHz signal bandwidth, even with a small modulation index.



(a)



(b)

Figure 2.15: Schematic diagram for optical PM receivers. Here, the optical FM receiver stands for the block diagram "receiver" in Fig. 2.12.

## 2.6 System Comparisons

We now compare the coherent system and a typical archetype IM/DD system. The most important advantage of the coherent optically controlled phased array antenna described here is that it is readily expandable to a large number of elements. The basic system can easily accommodate  $10^2$  channels in a single fiber, and feed any combination of the  $10^2$  true-time delays to  $10^2$  antenna array elements by using only  $10^2$  optical transmitters and coherent receivers. In contrast, a generic IM/DD system[19] typically requires  $10^4$  lasers and  $10^4$  fibers of precisely determined lengths. If the transmitter lasers are far away from the antenna elements, the IM/DD system requires an additional  $10^2$  long transmission fibers to be cut precisely to within 0.1 mm and maintained in the same configuration so that the total optical path of the several transmission fibers are equal. For both the antenna transmitter and receiver, the numbers of lasers, optical receivers and precisely cut fibers of the coherent system are far less than that required for an IM/DD system. In addition, the receiver sensitivity, direction sweep rate, SNR and DR of the coherent scheme is often better than or comparable to IM/DD systems.

In recent years, there have been substantial improvements in coherent detection techniques[20]. For example, there have been several proposals and demonstrations of frequency stabilization schemes[21][22]. External cavity lasers with gratings can have several thousands of GHz tuning range with laser linewidths below 1 MHz [4]. Polarization diversity methods can also be used to maintain polarization control[23]. Thus, although one coherent link is more complex than an IM/DD link because of the difficulties inherent in frequency stabilization of the transmitter lasers, wide tuning

range of the local lasers and polarization control, for a large scale antenna system such as those currently under consideration, the coherent approach is more readily adaptable to large scale arrays.

An alternative architecture is based on wavelength-division-multiplexing, direct-detection (WDM/DD) systems. The transmitter and receiver structures described in Sec. 2.2 of this chapter are also suitable for a WDM/DD system by using tunable optical receivers (e.g., tunable optical filters plus direct detection receivers) instead of coherent receivers. There has been a report of a  $10^2$  channel WDM system using tunable optical receivers [21]. Coherent systems have an inherent advantage over the WDM systems: due to the sharp passband shape of the IF bandpass filter in the microwave frequency range, a coherent system usually has very low interchannel interference. For WDM systems, the passbands of tunable optical filters usually are periodic (the filter is typically interferometric) and the corresponding multichannel system therefore has much larger interchannel interference. This results in reduced SNR and DR than that of a coherent system. For digital signal transmission, the interference of a WDM system might be tolerable, whereas for analog systems such as that employed for radar and CATV signal detection, where a very high SNR and dynamic range is required, this causes severe problems. In comparing other parameters such as receiver sensitivity, minimum channel spacing and switching speed, a coherent system also has superior performance than WDM systems. Furthermore, although a WDM system does not necessarily require polarization control and the modulation/demodulation methods are much simpler, a wide range tunable optical filter switchable for delay transmission is still difficult to fabricate[21].

We summarize the comparisons between typical coherent, IM/DD and WDM/DD systems in Table 2.2. From most of the comparison categories in Table 2.2, the coherent architecture appears to be very promising for large scale phased array antenna systems.

## 2.7 Conclusion

Table 2.3 summarizes some of the calculation results concerning the  $128 \times 320$  example system. Generally, all three schemes can provide good system performance such as high SIR, SNR and DR. The AM technique requires the smallest channel spacing and is relatively insensitive to the laser phase noise. FM and PM can provide a higher DR by using a larger modulation index, although a larger channel spacing is required.

As shown in Secs. 2.4 and 2.5, the AM-WIRNA receiver is relatively laser-phase-noise-insensitive; and for FM receivers, the laser phase noise becomes white noise at the output. Thus, the output microwave signal maintains its original linewidth in the frequency domain. This is a crucial characteristic to ensure that the coherent system can be used for application of the Doppler effect to radar systems, where the receiver should be able to detect very small spectral shifts of the return signals.

In summary, we have analyzed a true-time-delay phased array antenna system using fiber optic techniques with coherent detection. This system has several advantages over conventional electronically steered systems. It has large instantaneous bandwidth and thus is "squint free". Due to the gain control from both the LO lasers and the subsequent electronic amplifiers, it has flexibility for beam shaping

Table 2.2 Comparisons of three kinds of architecture for optically steered phased array antenna system

System architecture	IM/DD	OFDM, direct detection	Coherent heterodyne
Receiver	Direct-detection, single channel	tunable optical filter multichannel	coherent-detection, multichannel
Sensitivity	fair	poor	good
Channel space		< 10 GHz	< 10 GHz
no of channel in 1 link	1	100	100 or more
laser numbers	$M \infty N$	$M+N$	$M+N$
switching speed	1 ns	1 s	1 ns-1 ms
modulation method	IM	IM	AM or FM
SNR and DR	good	poor or fair	good
Cross talk	low	-14 dB	< -50 dB

Table 2.3 Quantitative Evaluation for a 128x320 Example System

modulation scheme	min. optical channel spacing	dynamic range of one channel	S/N for one channel	SIR for one channel
AM	12 GHz (0.1 nm)	50 dB	40 dB ( $m=0.1$ )	> 60 dB
FM ( $\beta=1$ $\Delta\nu=1$ MHz)	12 GHz (0.1 nm)	65 dB	65 dB	> 50 dB

\* Assume that the optical power of one channel is -5 dBm.

For 128 channels, the optical bandwidth at 1.55  $\mu\text{m}$  is:

AM: 12.8 nm

FM: 12.8 nm

and null steering. Both transmitter and receiver structures are discussed. In this chapter, comparisons with direct detection systems are made, and it is shown that the coherent system is adaptable for large scale systems. We also propose a solution for compensating fiber chromatic dispersion which distorts the radiation pattern.

We quantitatively analyzed a  $128 \times 320$  model system which uses a single fiber for a transmission line. The main noise sources for the optical links are the LO-ASE beat noise, as well as the laser phase noise. From the analysis, we see that for a typical radar signal and realistic optical system parameters, such a system can obtain a high SIR (good channel isolation), a high SNR and dynamic range for AM, FM and PM schemes which meet the stringent requirements of modern radar systems.

# Bibliography

- [1] P. M. Freitag and S. R. Forrest "A coherent optically controlled phased array antenna system", *IEEE Microwave and Guided Wave Lett.*, vol. 3, no.9, pp293-295, Sept. 1993.
- [2] L. Xu, R. Taylor, and S. Forrest, "The use of optically coherent detection techniques in true-time delay phased array and systems", *IEEE Journal of Lightwave Technology*, vol. 13, no. 8, pp1663-1678, Aug. 1995.
- [3] Y. Tohmori, Y. Yoshikuni, H. Ishii, F. Kano, T. Tamamura, Y. Kondo, "Over 100 nm wavelength tuning in superstructure grating (SSG) DBR lasers", *Electronics Letters*, vol. 29, no. 4, pp352-354, Feb. 1993.
- [4] Product catalog of Santec USA Corp., New Jersey 07733, 1994.
- [5] A. Carlson, *Communication Systems*, 2nd Ed., New York: McGraw-Hill, 1975.
- [6] T. Durhuus, B. Mikkelsen, and K. Stubkjaer, "Detailed dynamic model for semiconductor optical amplifiers and their crosstalk and intermodulation distortion", *IEEE J. Lightwave Tech.*, vol. 10, no. 8, pp1056-1065, August, 1993.

- [7] R.I. Laming, M. N. Zervas, and D. N. Payne, "Erbium-doped fiber amplifier with 54 dB gain and 3.1 dB noise figure", *IEEE Photon. Tech. Lett.*, vol. 4, no. 12, pp1345-47, Dec. 1992.
- [8] I. L. Newberg, A. A. Walson, H. S. Nussbaum, G. L. Tangonan, Patent Pending "Frequency translation of true time delay signals", GM/Hughes Electronics Corporation.
- [9] Product catalog of MITEQ Corporation, New York 11788.
- [10] Merrill L. Skolnik, *Introduction to Radar Systems*, 2nd Ed., New York: McGraw-Hill, 1980.
- [11] Merrill L. Skolnik, *Radar Handbook*, New York: McGraw-Hill, 1990.
- [12] D.J. Sabido, T.K. Fong, R.F. Kalman and L.G. Kazovsky, "Linewidth- insensitive coherent optical analog links", SPIE vol. 1703, pp504-522, 1992.
- [13] R. Walker, R.C. Steele, and N.G. Walker, "Optical amplifier noise figure in a coherent optical transmission system", *J. of Lightwave. Tech.*, vol. 8, no.9, pp1409-1413, Sept. 1990.
- [14] L. G. Kazovsky, "Multichannel coherent optical communications systems", *J. Lightwave Tech.*, vol. 5, no. 8, pp1095-1102, 1987.
- [15] B. S. Glance, J. Stone, K. J. Pollock, P.J. Fitzgerald, C. A. Burrus, Jr., B. L. Kasper, L.W. Stulz, "Densely spaced FDM coherent star network with optical signals confined to equally spaced frequencies", *J. Lightwave Tech.*, vol. 6, no. 11, pp 1770-81, Nov. 1988.

- [16] T. K. Fong, D. J. Sabido, and L. G. Kazovsky, "Linewidth-insensitive coherent AM analog optical links using semiconductor lasers", *IEEE Photon. Tech. Lett.*, vol. 4, no. 4, pp49-471, April 1993.
- [17] L. G. Kazovsky, "Impact of laser phase noise on optical heterodyne communication systems", *J. Opt. Commun.*, vol. 7, no. 2, pp66-78, 1986.
- [18] M. Yano, Y. Kotaki, H. Ishikawa, S. Yamakoshi, H. Imai, T. Chikama, and T. Touge, "Extremely low-noise facet-reflectivity-controlled InGaAsP distributed-feedback lasers", *IEEE J. of Lightwave Tech.*, vol. 4, pp1454-1458, 1986.
- [19] W. Ng, A.A. Walston, G.L. Tangonan, J.J. Lee, I.L. Newberg and N. Bernstein, "The first demonstration of an optically steered microwave phased array antenna using true-time-delay", *IEEE J. Lightwave Tech.*, vol. 9, no. 9, pp1124-1131, 1991.
- [20] L. G. Kazovsky and P. T. Poggiolini, "STARNET: a multi-gigabit-per-second optical LAN utilizing a passive WDM star", *IEEE J. Lightwave Tech.*, vol. 11, no. 5/6, pp1009-1027, May/June, 1993.
- [21] K. Nosu, H. Toba, K. Inoue, and K. Oda, "100 channel optical FDM technology and its applications to optical FDM channel-based networks", *J. Lightwave Tech.*, vol. 11, no. 5/6, pp764-776, May/June, 1993.
- [22] D. Dunkin, G. Hill, and W. Stallard, "Frequency locking of external cavity semiconductor lasers using an optical comb generator", *Electron. Lett.*, vol. 22, pp388, 1986.

- [23] T. Okoshi, and K. Kikuchi, *Coherent Optical Fiber Communications*, KTK Scientific Publishers/Tokyo, 1987.

## Chapter 3 First Experimental Demonstration of A Coherent Optically Controlled True-Time Delay Phased Array System

In Chapter 2, we analyzed a true-time delay system based on multi-channel, optical heterodyne detection techniques with external modulation, and showed that such a system is readily expandable to large scale systems with high dynamic range and good channel isolation while keeping the optical channel spacing very small[1]. In this paper, we demonstrate a proof-of-concept experiment of this system using four optical channels and two coherent receivers. This is the first time that an optical multi-channel system is used for phased array antennas[2-6]. The system is relatively insensitive to laser linewidth and IF frequency instability. It shows good signal quality, high dynamic range, accurate true-time delay in the microwave bandwidth range from 0.8 to 1.5 GHz. We also demonstrated that the system only need narrow optical channel spacing for very low interchannel interference. Direct as well as external modulation schemes exhibit good signal quality for narrow bandwidth signals. We also analyze the effect of the IF amplifier phase response on the system performance and find that it is the main reason attributed to the small phase instability of the final signal.

### 3.1 The system experiments

Figure 3.1 shows a simple four optical channel, two antenna element demonstration system. The four  $\lambda = 1.55\mu m$  wavelength DFB laser transmitters (see Fig. 3.1) are each thermally tuned to have a different central optical frequency. The light from the four transmitter lasers is amplitude modulated (AM) at microwave bandwidths using LiNbO<sub>3</sub> Mach-Zehnder (M-Z) modulators. The modulated optical signals are then

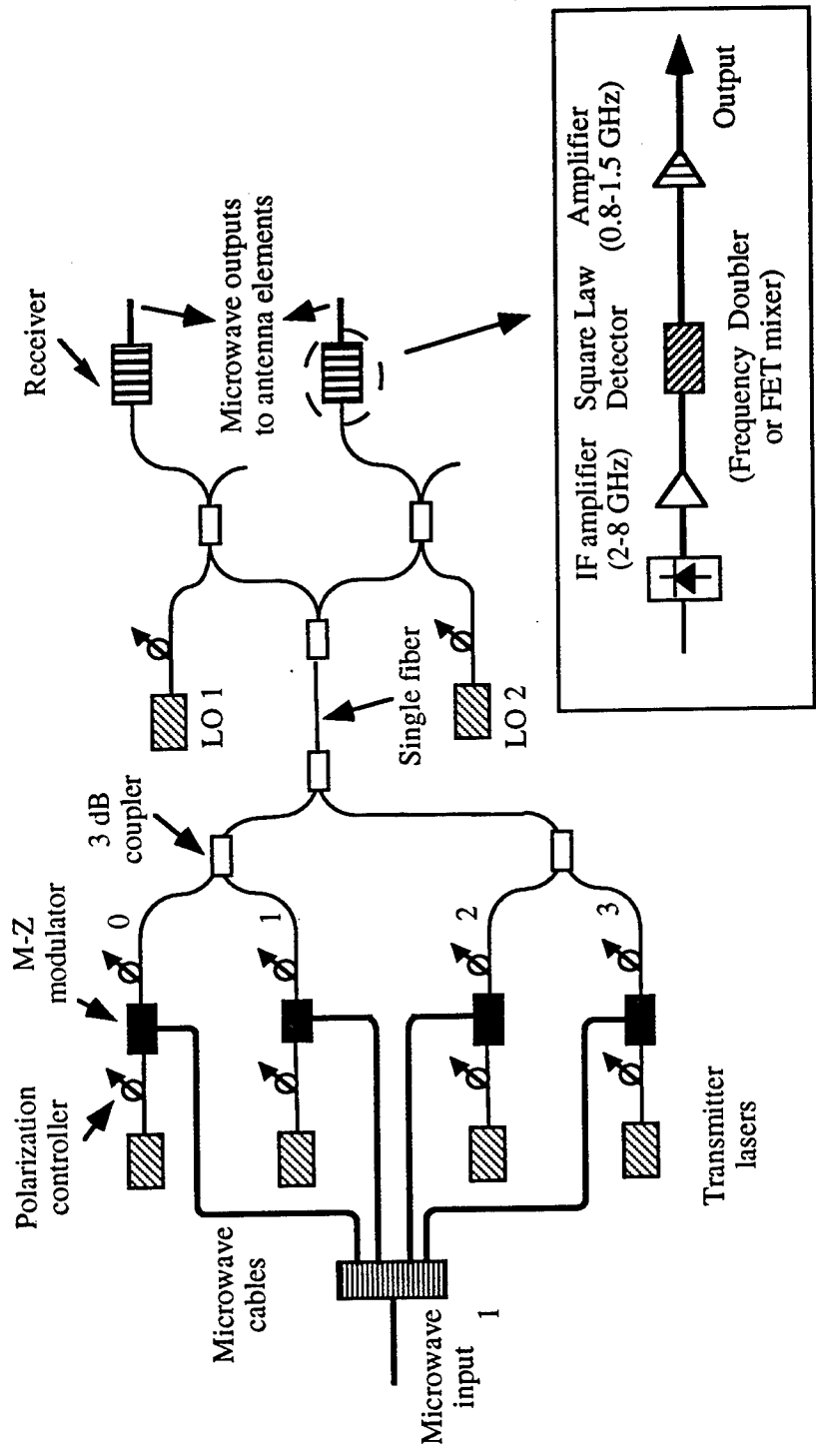


Figure 3.1 Demonstration of a true-time delay phased array antenna feed system with four optical channels and two coherent receivers. Inset: AM WIRNA receiver.

transmitted through different fiber lengths prior to being input to a  $4 \times 1$  combiner composed of a series of  $2 \times 1$  combiners. The signals then pass through a single transmission fiber before being routed to two optical receivers through a series of splitters. Next, these signals are separately mixed with two optical local oscillator (LO) signals at the input of InGaAs p-i-n detectors with 70% quantum efficiency at  $\lambda = 1.55\mu\text{m}$ . By tuning the LO DFB lasers, each receiver is able to detect and demodulate the microwave signal from any of the four transmitter laser channels. The laser frequencies were adjusted by independent current and temperature controllers with a temperature stability of  $\pm 0.02^\circ\text{C}$ . As shown in the following, even with this open-loop control, we still obtain very stable signals and accurate true-time delays. Since the modulated signals arrive at the receivers through different fiber lengths, true-time delays are introduced among the four channels. Additional optical channels can provide more delay combinations, while more splitting before the optical receivers can be used to accommodate additional antenna elements.

The demodulation scheme used is a wideband filter-rectifier-narrow band filter structure (WIRNA, shown in Fig. 3.1 inset)[7], which employs a square-law device (SLD) to demodulate the AM signal. This receiver architecture is relatively insensitive to laser linewidth, and the dynamic range is comparable to that of optical direct detection schemes[1][8]. In our experiment, the intermediate frequency (IF) passband is from 2 to 8 GHz, and the narrow band amplifier operates from 0.8 to 1.5 GHz. The SLD used was either a frequency doubler or a FET mixer, operated at square-law regime. For optically coherent detection, the light polarization needs to be controlled. In our experiment, manual polarization rotators are used to control the polarization. These components did not appear to significantly degrade the system performance

or stability. For example, after a fine adjustment to bring the polarization of the six lasers to be aligned, the system performance keep unchanged for about a day.

Figure 3.2 shows the microwave spectrum right after the photodetection and wide-band amplification. We can see that the highest peak around 4.8 GHz is the IF spectrum. Its 3-dB spectral width is around 10 MHz, which is the summation of the signal and the LO linewidth, plus the instability of the laser central frequencies. The two peaks on the sides of the IF frequency are the AM modulation side bands. Figure 3.3 shows the demodulated signals of one channel with an IF of 4.1 GHz when the externally modulating signal is varied between 0.8, 1 and 1.5 GHz. Here, the optical signal power is -15.8 dBm, and the LO power is -2.7 dBm at the receiver. With the modulation index set at 0.24 for the 8 dBm microwave signal, and the receiver noise corresponding to an optical power of  $50\text{pW}/\text{Hz}^{1/2}$ , the signal-to-noise ratio (SNR) is about 48 dB for a 1 MHz bandwidth. This SNR is independent of frequency from 0.8 to 1.5 GHz, as seen in Fig. 3.3. Calculations based on a previous system analysis[1] give  $\text{SNR} = 50\text{ dB}$  using the measured parameters at the optical receiver, which is in reasonable agreement with the experimental results. The demodulated RF signals have linewidths of  $< 2\text{ MHz}$ , limited by the resolution bandwidth of the spectrum analyzer. On the other hand, the IF signal linewidth is tens of MHz. This clearly indicates that the system is indeed laser-linewidth insensitive, consistent with previous analytical and experimental results[1][7]. For shot noise limited receivers, the SNR should be 71.2 dB/MHz with the above optical powers and modulation index—a 20 dB improvement over our results. The total optical signal loss of the system is about 20 dB, with 12 dB loss from the 3 dB couplers, and 8 dB from the M-Z modulators. Other connector losses are negligible. In this experiment, the optical power loss and

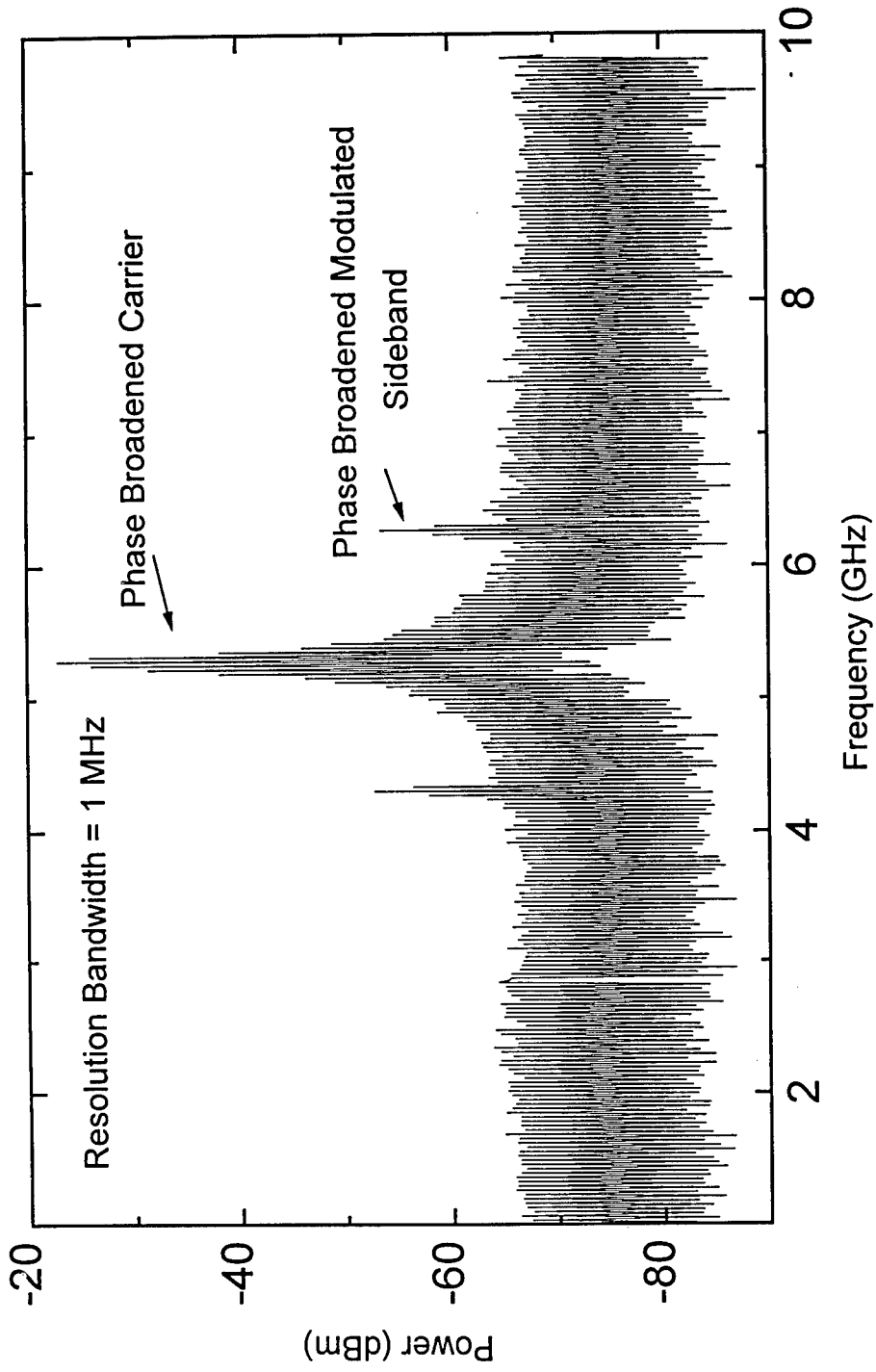


Fig. 3.2 Intermediate frequency spectrum of optical heterodyne detection.

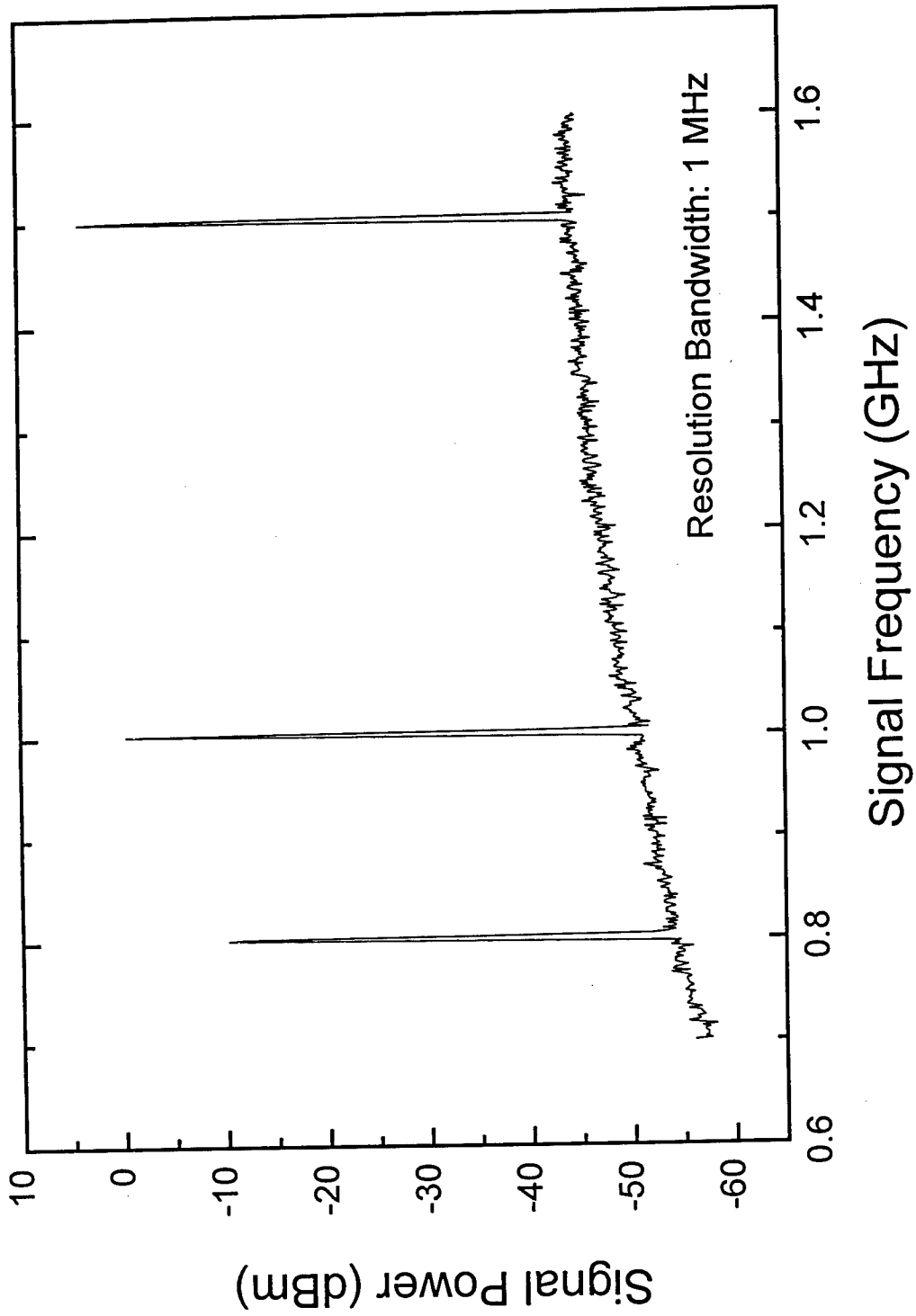


Figure 3.3 Demodulated signals from the coherent links

the high receiver noise are primarily responsible for the SNR degradation.

The dynamic range (DR) of the antenna feed is limited by system noise and third order intermodulation products from the M-Z modulators, provided the optical signal power and LO power are fixed. A two-tone signal method was employed to measure the dynamic range of one channel with the same optical parameters as in Fig. 3.3. The experimental setup for DR measurement is shown in Fig. 3.4. Here, two closely spaced single-frequency signals ( $f_1, f_2$ ) with the same amplitude are combined together to modulate the optical signal. If the third-order intermodulation effect becomes large, there will be frequency components of  $2f_1 - f_2$  and  $2f_2 - f_1$  emerging at the demodulated signal. Here, the DR is 52.3 dB for a signal modulated from 0.8 to 1.5 GHz with a 1 MHz bandwidth. Theoretical calculations[1] show DR = 54 dB with the above system parameters, and 68 dB under shot noise limited situations. The experimental dynamic range can be further improved by increasing the optical signal and LO power along with the use of shot noise limited, balanced optical receivers. Also, highly linear modulators or direct laser modulation can be employed to avoid third order intermodulation products.

To test the true-time delay performance of the system, the microwave output of an HP 8703A network analyzer was connected to the microwave input shown in Fig. 3.1. One of the demodulated microwave outputs from the antenna feed (Fig. 3.1) was then connected to the input of the network analyzer. First, the phase response of microwave signal output from different optical channels and/or different receivers was measured. Next, the phase difference between two channels was compared to the theoretical values. Figure 3.5 shows example measurement results using this

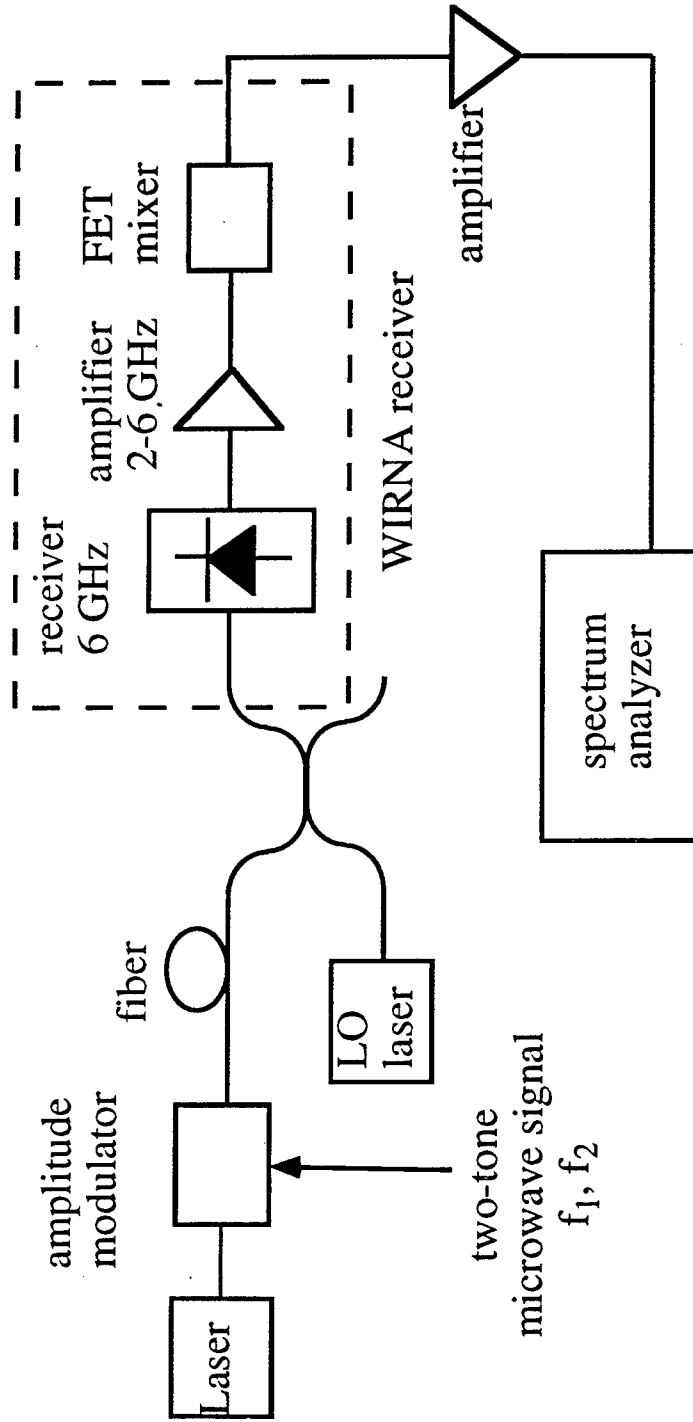


Figure 3.4 The dynamic range measurement setup.

procedure. The solid lines show the theoretical phase delays for the corresponding true-time delays of 85, 217, 360 and 555 ps, and the data points show the test results averaged over 16 sweeps. As shown in Fig. 3.5, the system introduces accurate, frequency independent true-time delays between different channels, indicating that such a multichannel optical heterodyne system can precisely control the microwave phase.

The inset in Fig. 3.5 shows the frequency fluctuation as a function of time for 1 GHz CW operation. The phase fluctuates to within  $\pm 1^\circ$  due to the non-linear phase response of the GaAs IF amplifiers. We will discuss this in detail in the next section.

The signal-to-interchannel interference ratio (SIR) determines the minimum channel spacing. Figure 3.6 shows the measured SIR when the four channels are equally spaced. The signal power is obtained by tuning the LO for channel 2 to IF = 4.1 GHz (inset, Fig. 3.6). The channel interference was then measured by turning off the microwave modulation on optical channel 2. When the channel spacing is < 12 GHz, the beat between the LO and channel 3 is less than 8 GHz which is within the IF amplification bandwidth, causing interference at the SLD. For a channel spacing > 13 GHz, however, the beat signal between the LO and channel 3 is out of the IF passband, resulting in a negligible interchannel interference. Due to the noise floor, we obtain an upper limit of SIR = 50 dB with most of the interference power from channel 3. Calculations indicate that for modulation between 0.8 and 1.5 GHz and a laser linewidth as large as 20 MHz, 2 to 6 GHz is a sufficiently large passband for IF = 4 GHz. In this case the channel spacing can be reduced to  $\sim 11$  GHz, without introducing significant interchannel interference[1]. The experimental results indicate

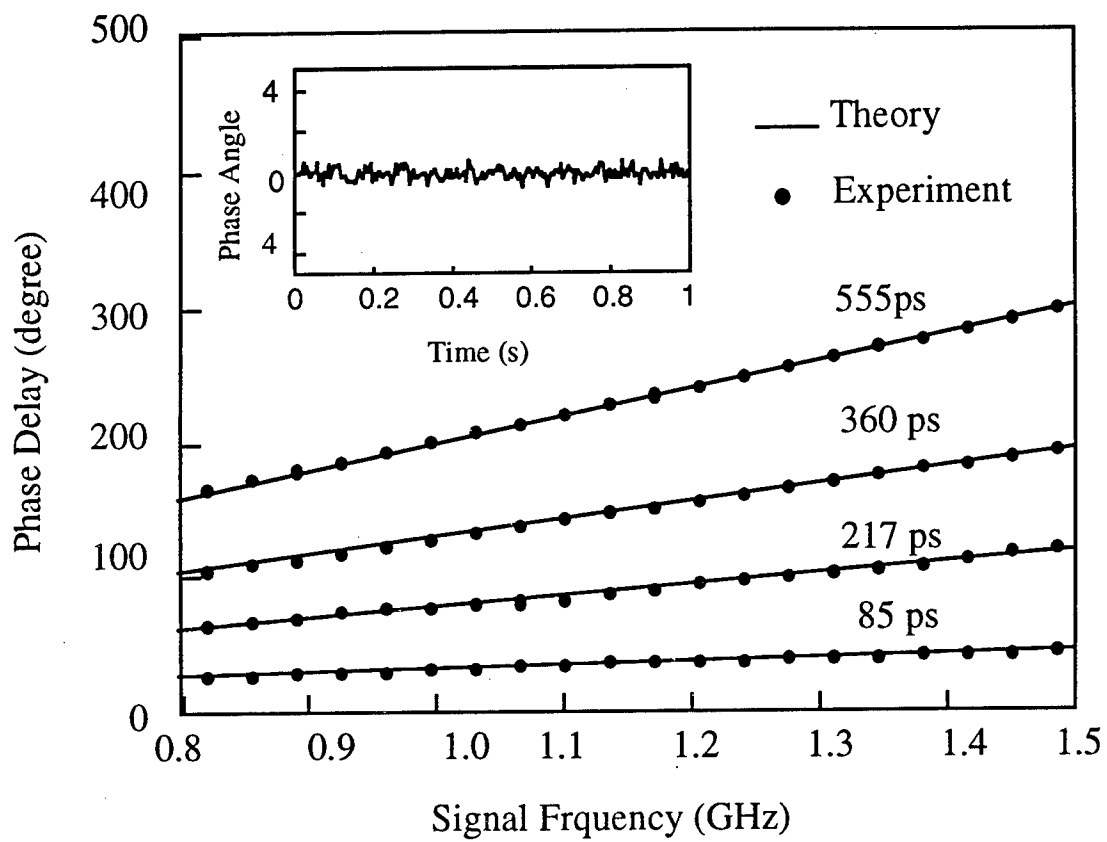


Figure 3.5 True time-delay measurement

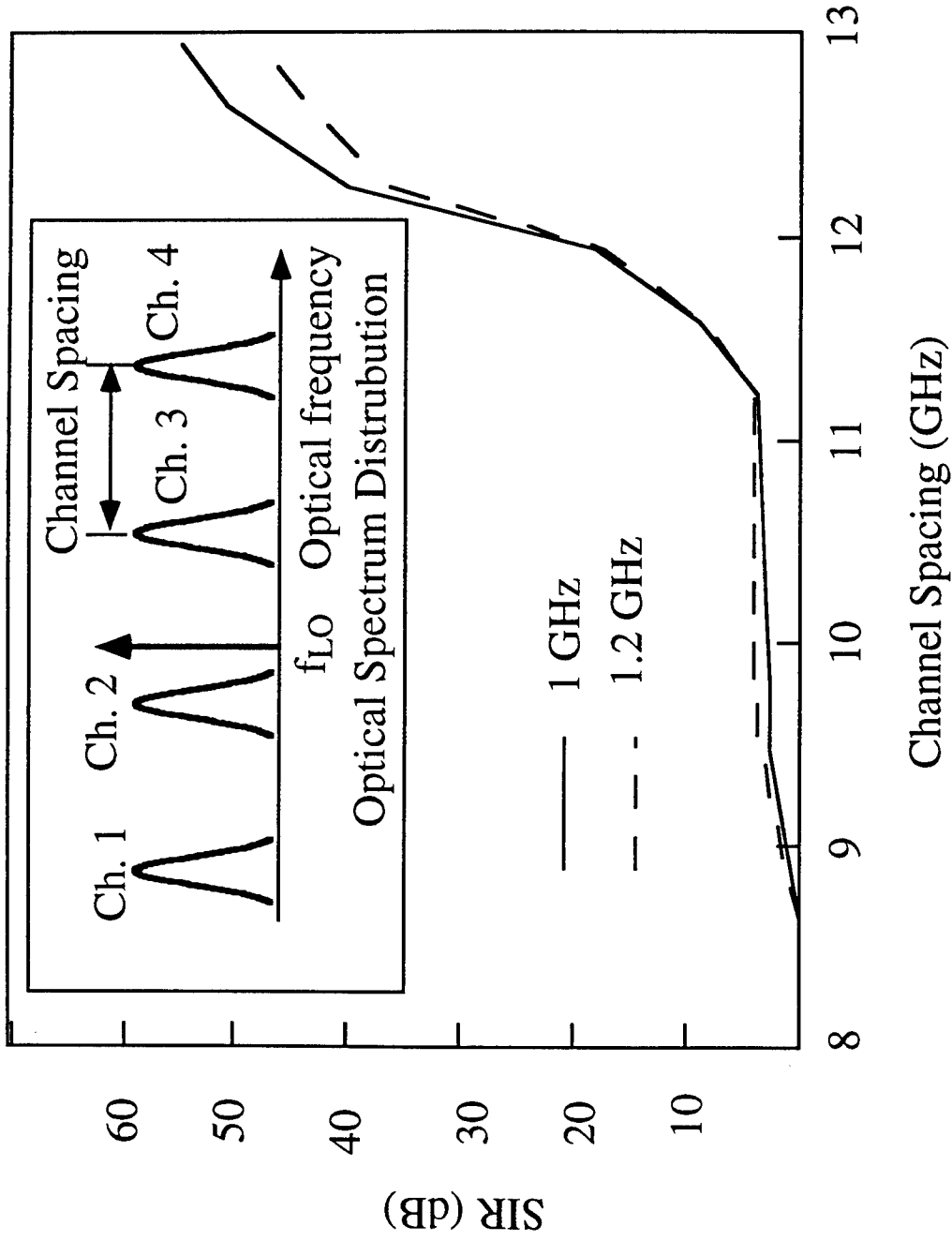


Figure 3.6 Signal-to-interchannel interference ratio versus channel spacing for signals at different frequencies.

that the good passband characteristics of microwave amplifiers and filters leads to a high SIR even for small channel spacing in AM heterodyne systems. Theoretical investigations[1] also show that if balanced receivers are used, the most significant interchannel interference only comes from the adjacent channels even for systems with a large number of channels.

Now let's see one specific issue in our experiment.

### 3.2 The Effect of the IF Amplifier Phase Response on the System Performance

Our coherent optically controlled phased array antenna system is an inherently true-time delay system. As analyzed theoretically in Chapter 2, because of the use of the square-law devices, the phase of the final demodulated signal should not change when the IF changes, and the signal amplitude and phase stability should be as good as that of direct detection systems. But in real experiments, we observe the following two phenomena: 1) the phase of the final signal fluctuates within one or two degrees; 2) as the IF changes, the phase of the signal also changes. Through our study, we find that the two non ideal phenomena are mainly caused by the nonlinear phase response of the IF amplifiers. Therefore, to get accurate true-time delays among different antenna elements and good signal stability, linear phase response is required for the IF amplifiers.

The IF current of a single frequency AM modulated signal right after the photo detection can be simplified and normalized to the following expressions:

$$i_{IF}(t) = (1 + m \sin(\omega_m t)) \sin(\omega_{IF} t)$$

$$i_{IF}(t) = \sin(\omega_{IF}t) + m \cos((\omega_{IF} - \omega_m)t) - m \cos((\omega_{IF} + \omega_m)t) \quad (3.1)$$

where  $\omega_{IF}$  is the angular IF,  $\omega_m$  is the angular modulation frequency, and  $t$  is time. If an IF amplifier is a true-time delay device or has uniform phase response in the IF pass band, then its phase change  $\Delta\phi$  as a function of frequency  $f$  can be expressed as:

$$\Delta\phi(f) = (\Delta t)f + \phi \quad (3.2)$$

where  $\Delta t$  is the signal time delay introduced by the device, and  $\phi$  is the extra phase delay. For true time delay device,  $\phi = 0$ ; and for other devices with uniform phase response,  $\phi = \text{non-zero constant}$ . Assuming the IF amplification is uniform throughout the IF pass band, insert the phase change of Eq. 3.2 to each frequency component of Eq. 3.1, and square it (for simplicity, we assume that the square-law device, SLD is ideal), we get the following expressions for the current after the SLD:

$$i_{SLD}(t) = (1 + m^2/2) + 2m \sin(\omega_m(t + \Delta t)) + 2\omega_m \text{ terms} + \text{terms around } 2\omega_{IF} \quad (3.3)$$

where the second term is the desired signal. It is clear that for this situation, which is the ideal case, the phase and amplitude of the final demodulated signal do not depend on the IF frequency.

For non uniform phase response, the phase change introduced by an IF amplifier is:

$$\Delta\phi(f) = (\Delta t)f + \phi(f) \quad (3.4)$$

where  $\phi(f)$  is a function of frequency. For simplicity, we define the phase change for frequency  $\omega_{IF} - \omega_m$ ,  $\omega_{IF} + \omega_m$  and  $\omega_{IF}$  as  $\phi_1$ ,  $\phi_2$  and  $\phi_3$  in addition to the  $(\Delta t)f$  term. The current after the SLD is therefore:

$$i_{SLD}(t) = (1 + m^2/2) + 2m \sin(\omega_m(t + \Delta t) + \frac{\phi_2 - \phi_1}{2}) \cos(\phi_3 - \frac{\phi_1 + \phi_2}{2}) +$$

$$+2\omega_m \text{ terms} + \text{terms around } 2\omega_{IF} \quad (3.5)$$

Since  $\phi_1$ ,  $\phi_2$  and  $\phi_3$  are functions of frequency and generally are not equal, the phase and amplitude of the final demodulated signal will change as the IF changes. For the same reason, the instability of the IF signal will introduce both phase and amplitude instability in the final signal.

In summary, we demonstrate a proof-of-concept experiment for a novel true-time delay phased array antenna feed system from 0.8 to 1.5 GHz based on optical heterodyne detection techniques. Such a system is comparatively easy to implement using off-the-shelf components. The system has high dynamic range ( $> 52$  dB), good signal-to-noise ratio (48 dB), and a narrow channel spacing (13 GHz) with good channel isolation. The system also demonstrated the transmission of very accurate true-time delays. Practical issues such as phase fluctuations and tolerance to IF frequency variations were analyzed. Means to improve system performance such as dynamic range and phase stability were also proposed. The experimental results were compared to our previous analysis[1], and were in good agreement. This architecture provides a promising approach for a future generation of phased array antenna systems based on fiber optic techniques.

# Bibliography

- [1] L. Xu, R. Taylor, and S. Forrest, "The use of optically coherent detection techniques in true-time delay phased array and systems", *IEEE Journal of Lightwave Technology*, vol. 13, no. 8, pp1663-1678, Aug. 1995.
- [2] G.A. Koepf, "Optical processor for phased-array antenna beam formation," *Optical Technology for Microwave Applications*, vol. 477, SPIE, pp. 75-81, 1984.
- [3] M. R. Surette, D. R. Hjelme and A.R. Mickelson, "An optically driven phased array antenna utilizing heterodyne techniques", *J. Lightwave. Tech.*, vol. 11, no. 9, pp1500-1509, Sept. 1993.
- [4] J. Guggenmos and R. Johnson, "Fiber based phased array antennas," in *Optical Technology for Microwave Applications III*, SPIE, vol. 789, pp. 70-77, 1987.
- [5] J. S. Pappert, "Ultra-wideband direction finding using a fiber optic beam-forming processor," in *Optoelectronic Signal Processing for Phased-Arrays*, SPIE, vol. 886, pp. 239-246, 1988.
- [6] W. Ng, A.A. Walston, G.L. Tangonan, J.J. Lee, I.L. Newberg and N. Bernstein, "The first demonstration of an optically steered microwave phased array antenna

using true-time-delay", *IEEE J. Lightwave Tech.*, vol. 9, no. 9, pp1124-1131, 1991.

- [7] T. K. Fong, D. J. Sabido, and L. G. Kazovsky, "Linewidth-insensitive coherent AM analog optical links using semiconductor lasers", *IEEE Photon. Tech. Lett.*, vol. 4, no. 4, pp469-471, April 1993.
- [8] L. Xu, R. Taylor, and S. Forrest, "True time-delay phased-array antenna feed system based on optical heterodyne techniques," *IEEE Photon. Tech. Lett.*, vol. 4, no. 4, pp160-162, Jan. 1996.

## Chapter 4 Semiconductor Ridge Waveguide Lasers and Related Devices for Optical Integration

In this chapter, we first introduce basic concepts of semiconductor lasers, including gain, efficiency and light output characteristics. Also, numerical methods for calculating optical modes are described. Finally, we explain our processing procedures for ridge lasers and semiconductor optical amplifier (SOAs) and show performance data of typical devices.

### 4.1 Semiconductor Laser Gain and Output Characteristics

#### 4.1.1 Material Gain

In a semiconductor, the electrons are characterized by their energy and momentum as determined by the crystal band structure. The light emission process can be conveniently described as the recombination of a free electron in the conduction band and a hole in the valence band. As in the case of gas lasers, there are three basic photon-electron interactions in a semiconductor material: spontaneous emission, absorption and stimulated emission. By requirements of energy and momentum conservation, a light emitting process has to follow:

$$E_a - E_b = h\nu \quad (\text{Energy conservation})(4.1)$$

$$\hbar k_{\text{valence}} + \hbar k_{\text{photon}} = \hbar k_{\text{conduction}} \quad (\text{Momentum conservation}) \quad (4.2)$$

where  $E_a$  and  $E_b$  are the electron energy levels in conduction band and valence band,  $k$  is the crystal momentum. Since the photon momentum (for infrared light) is small (typically one thousandth of that of an electron), the chance of recombination is large when the semiconductor is a direct bandgap material, whose conduction band minimum has the same momentum as the valence band maximum. Both GaAs, InP/InGaAsP-based materials are direct bandgap materials with a bandgap energy of  $\sim 1$  to  $1.5$  eV appropriate for generating infrared light. Optical gain only occurs when stimulated emission is stronger than absorption, which requires a population inversion---i.e. where the number of electrons in the excited state (conduction band) is greater than the number of electrons in lower state (valence band).

The electron distribution can be expressed by the product of the density of states and the occupation probability. The density of states of carriers in a band of a bulk semiconductor can be expressed as:

$$\rho(E)dE = \frac{1}{2\pi} \left( \frac{2m^*}{h^2} \right)^{3/2} \sqrt{E} dE \quad (4.3)$$

where  $m^*$  is the effective mass of the carrier, and  $m^* = \hbar^2 / (d^2 E / dk^2)$ ,  $E$  is the excess energy of the carrier relative to the band edge. For conduction electrons,  $E$  is measured from the bottom of the conduction band, while for holes  $E$  is measured from the top of the valence band. Since electrons and holes are Fermions, they obey Fermi-Dirac statistics. That is, the probability  $f(E)$  that an energy level  $E$  is occupied at thermal equilibrium is given by

$$f(E) = \frac{1}{\exp\left(\frac{E - E_f}{kT}\right) + 1}, \quad (4.4)$$

where  $E_f$  is the Fermi level. Combining the Eq. (4.3) and (4.4), we can get the density of electrons ( $n$ ) in the conduction band as:

$$n = \int_{E_c}^{\infty} f(E) \rho_c(E) dE. \quad (4.5)$$

where  $\rho_c$  is the density of states of electrons in conduction band. The density of holes ( $p$ ) in valence band is just the density of states unoccupied by the electrons, and it is:

$$p = \int_{-\infty}^{E_v} (1 - f(E)) \rho_v(E) dE. \quad (4.6)$$

where  $\rho_v$  is the density of states of holes in valence band. To generate net gain in a semiconductor, a forward biased  $pn$  junction or  $pin$  structure is usually employed. In this non-equilibrium situation around population inversion, the ordinary Fermi function for distribution probability does not apply. However, due to the intraband relaxation processes (with time scales  $\sim 10^{-11}$  s), the electrons and holes in the conduction band and valence band can reach quasi-equilibrium within the band itself. Therefore, in this region, we introduce the quasi-Fermi levels  $E_n$  and  $E_p$  to describe the distribution of carriers within their respective bands. The functions that describe the electron and hole distribution probabilities are:

$$f_n(E) = \frac{1}{e^{\frac{E - E_n}{kT}} + 1} \quad (4.7)$$

$$f_p(E) = \frac{1}{e^{\frac{E_p - E}{kT}} + 1} \quad (4.8)$$

Note that at the level of  $E_n$ , the electron occupation is 50%; while at the level of  $E_p$ , the hole occupation is also 50%. From Figure 4.1, it is clear that only when  $E_n$  raises into conduction band and  $E_p$  drops into valence band, there is a population inversion between the energy levels  $E_n$  and  $E_p$ . Furthermore, since there are no allowed states in the band gap, stimulated emission gain can only occur for light with frequency of  $\nu$  that satisfies the following equation:

$$F_n - F_p > h\nu > E_g \quad (4.9)$$

The gain coefficient  $g$  is defined by:

$$g = \frac{1}{I(z)} \frac{dI(z)}{dz} \quad \text{or} \quad I(z + \Delta z) = I(z)e^{g\Delta z}, \quad (4.10)$$

where  $z$  is the light propagation direction, and  $I(z)$  is the light intensity. Due to the requirement for momentum conservation, electrons can only recombine with holes of the same momentum. Therefore, we introduce the “reduced density of states” to describe the density of states with which a photon with energy  $h\nu$  can actually interact:

$$\rho(h\nu) = \frac{1}{4\pi^2} \left( \frac{2m_e^* m_h^*}{(m_e^* + m_h^*) \hbar^2} \right)^{3/2} (h\nu - E_g)^{1/2} \quad (4.11)$$

where  $m_e^*$  and  $m_h^*$  are effective masses of electrons and holes, respectively, and  $E_g$  is the band gap. The absorption and stimulated emission of light are proportional to this reduced density of states. The absorption should also be proportional to the electron vacancy probability in the conduction band and the electron occupancy (hole vacancy) in the valence band. Thus the recombination rate  $R_{\text{absorption}}$  can be written as:

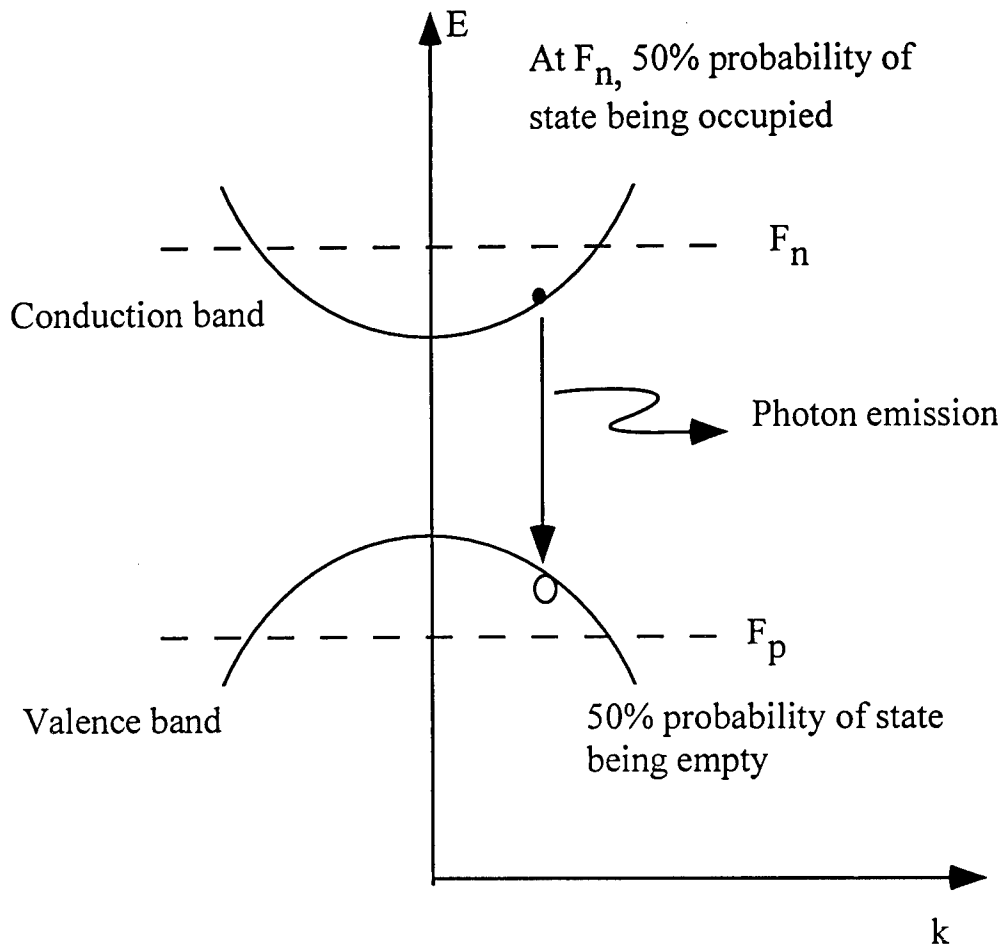


Figure 4.1 Illustration of quasi-Fermi levels and photon generation.

An electron and a hole of same  $k$  can recombine.

$$R_{\text{absorption}} \propto (1 - f_c(E_a))f_v(E_b). \quad (4.12)$$

For the same reason, the generation of light (e.g. recombination of electron and hole pairs) requires the recombination rate to be:

$$R_{\text{recombination}} \propto f_c(E_a)(1 - f_v(E_b)). \quad (4.13)$$

The net recombination rate should be  $R_{\text{recombination}} - R_{\text{absorption}}$ , and it is proportional to  $(f_c(E_a) - f_v(E_b))$ . Using a quantum mechanical approach, we can get the gain coefficient of a laser material as[1]:

$$g(E) = \frac{\lambda^2}{2n^2\hbar^2\tau} \rho(E)(f_c(E_a) - f_v(E_b)) \quad (4.14)$$

where  $\tau$  is the recombination lifetime,  $E$  is the photon energy, and  $\lambda$  is the wavelength. It is clear from Eq. (4.11) and (4.14) that the gain of the bulk semiconductor material increases as the photon energy increases, until the quasi-Fermi (Eqs. 4.7, 4.8) distributions begin to reduce the gain.

For the gain in quantum wells, the band structure changes from the bulk, as does the reduced density of states. For the new band structure, the effective mass depends on energy level.

#### 4.1.2 Light-current output characteristics

Knowing the material gain from the band structure and current density is not enough for analyzing a laser. In this subsection, we provide some well-known results regarding the

characteristics of a laser, including the modal gain, the internal and output loss, the quantum efficiency and characteristics of the lasing spectrum. We will relate measurements of these laser characteristics to material and device parameters.

For a laser, gain only exists in the active region, where for quantum well lasers, is the well region. The effective gain for optical mode is the product of the material gain and the confinement factor of the mode in the gain layer(s). The confinement factor  $\Gamma$ , is the normalized fraction of optical field intensity in the active region. The equation for the effective gain is thus:

$$g_{mode} = \Gamma_{active} g_{active} \quad (4.15)$$

A device can lase only when the modal gain is greater than the internal and output losses. The internal losses ( $\alpha_i$ ) includes optical scattering loss on the interfaces between adjacent layers within the device and the free carrier absorption loss within each layer. The output loss is expressed as:

$$\alpha_o = \frac{1}{2L} \ln \frac{1}{R_1 R_2}, \quad (4.16)$$

where  $L$  is the laser cavity length and  $R_1, R_2$  are the reflectivity of the two laser facets.

Since gain must equal or exceed loss in an optical round trip within the laser cavity, we have two conditions for lasing:

$$g_{th} \Gamma - \alpha_i - \alpha_o = g_{th} \Gamma - \alpha_i - \frac{1}{2L} \ln \frac{1}{R_1 R_2} = 0 \quad (4.17)$$

and

$$\lambda = \frac{2n_{eff} L}{m} \quad (4.18)$$

where  $n_{\text{eff}}$  is the effective index for the mode and  $m$  is an integer. Usually  $L \gg \lambda$  and  $m$  is a large number. So the longitudinal mode spacing can be expressed as:

$$\Delta\lambda = 2n_{\text{eff}}L\left(\frac{1}{m} - \frac{1}{m+1}\right) \approx \frac{2n_{\text{eff}}L}{m^2} = \frac{\lambda^2}{2n_{\text{eff}}L}. \quad (4.19)$$

This equation is useful for estimation of effective index by measuring the spectral spacing of different longitudinal modes.

Above threshold, stimulated emission will rapidly consume injected electron-hole pairs and the carrier density and material gain are fixed at the threshold level. The total output optical power can be expressed as:

$$P_{\text{out}} = \eta_i \frac{\alpha_o}{\alpha_i + \alpha_o} (I - I_{\text{th}}) \frac{h\nu}{q} \quad (4.20)$$

where  $\eta_i$  is the internal quantum efficiency, which is the percentage of current above threshold used for stimulated electron-hole pair recombination. It is clear from Eq. 4.20 that part of the generated light is consumed by the internal loss. Here, we ignore the scattering losses at the facets. Relating the external efficiency ( $\eta_{\text{ext}}$ ) with the internal and output losses gives

$$\eta_{\text{ext}} = \frac{P_{\text{out}} / h\nu}{(I - I_{\text{th}}) / q} = \eta_i \frac{\alpha_o}{\alpha_i + \alpha_o}. \quad (4.21)$$

Since  $\alpha_o = \frac{1}{2L} \ln \frac{1}{R_1 R_2}$ , we can write Eq. 4.21 as:

$$\frac{1}{\eta_{\text{ext}}} = \frac{1}{\eta_i} \left(1 + 2L\alpha_i / \ln \frac{1}{R_1 R_2}\right). \quad (4.22)$$

Assuming that the reflectivities on both facets are known, a measurement of the external efficiency for lasers of different cavity lengths yields the internal quantum efficiency and internal loss via Eq. 5.22.

#### 4.2 Numerical analysis of a one dimensional TE waveguide structure

As stated in the previous section, in order to predict the output characteristics of a laser, one needs to know the optical mode parameters such as confinement factor, modal reflectivity and scattering loss. In this dissertation work, a computer program[3] is extensively used to calculate optical modes of lasers and waveguides. Through the mode calculation, we can obtain the confinement factors of each layer, the transmission, reflectivity and scattering from laser and waveguide facets, far field patterns of lasers, and facet coating effects. Here, we briefly introduce the numerical methods used in this program.

Since we can view the electric field as a wave propagating along the cavity in  $z$  direction, and the propagating wave electric field can be expressed as:

$$E(x, y, z) = E(x, y)e^{-jk_0 n_e z}, \quad (4.23)$$

where  $k_0$  is the propagation constant in vacuum and

$$n_e = n_{eff} - j \frac{\alpha_{eff}}{2k_0} \quad (4.24)$$

is the complex effective index. The calculation of the optical mode for an in-plane laser is a 2-D boundary value problem (Figure 4.2). Thus, combined with Eq. 4.23, Maxwell's Equations give:

$$\nabla^2 E(x, y) = -k_0^2 (n^2(x, y, \lambda_0) - n_c^2) E(x, y), \quad (4.25)$$

where  $n(x, y, \lambda_0) = n_r(x, y, \lambda_0) - j \frac{\alpha(x, y, \lambda_0)}{2k_0}$  is the complex index profile of a laser cross-section, which is also a function of lasing wavelength,  $\lambda_0$ . If we further assume  $E(x, y) = E(x)E(y)$ , and ignore lateral (y) variations for broad-area lasers, we get the following 1-D transverse mode equation[4]:

$$\nabla^2 E(x) = -k_x^2 E(x, y), \quad k_x^2 = k^2(x, \lambda_0) - k_z^2, \quad (4.26)$$

where  $k(x, \lambda_0)$ , of each layer is determined by the material[5].

Now, Eq. (4.26) also holds true for the ridge lasers, since the transverse confinement of the fundamental mode is usually much stronger than lateral confinement, which leads to  $k_x \gg k_y$ . For a numerical analysis with higher precision, the mode distribution can be first found by solving the 1-D transverse mode at different lateral positions, then solving the 3-layer lateral mode using the effective indices calculated for the 1-D transverse case (see Fig. 4.2).

For a dielectric stack (Fig. 4.3), such as in the case of quantum well lasers, the electric field of a TE wave can be expressed as:

$$E_l(x) = A_l e^{-jk_{lx}(x-l_l)} + B_l e^{jk_{lx}(x-l_l)}, \quad k_{lx}^2 = k_l^2 - k_z^2, \quad l = 1 \dots m, \quad (4.27)$$

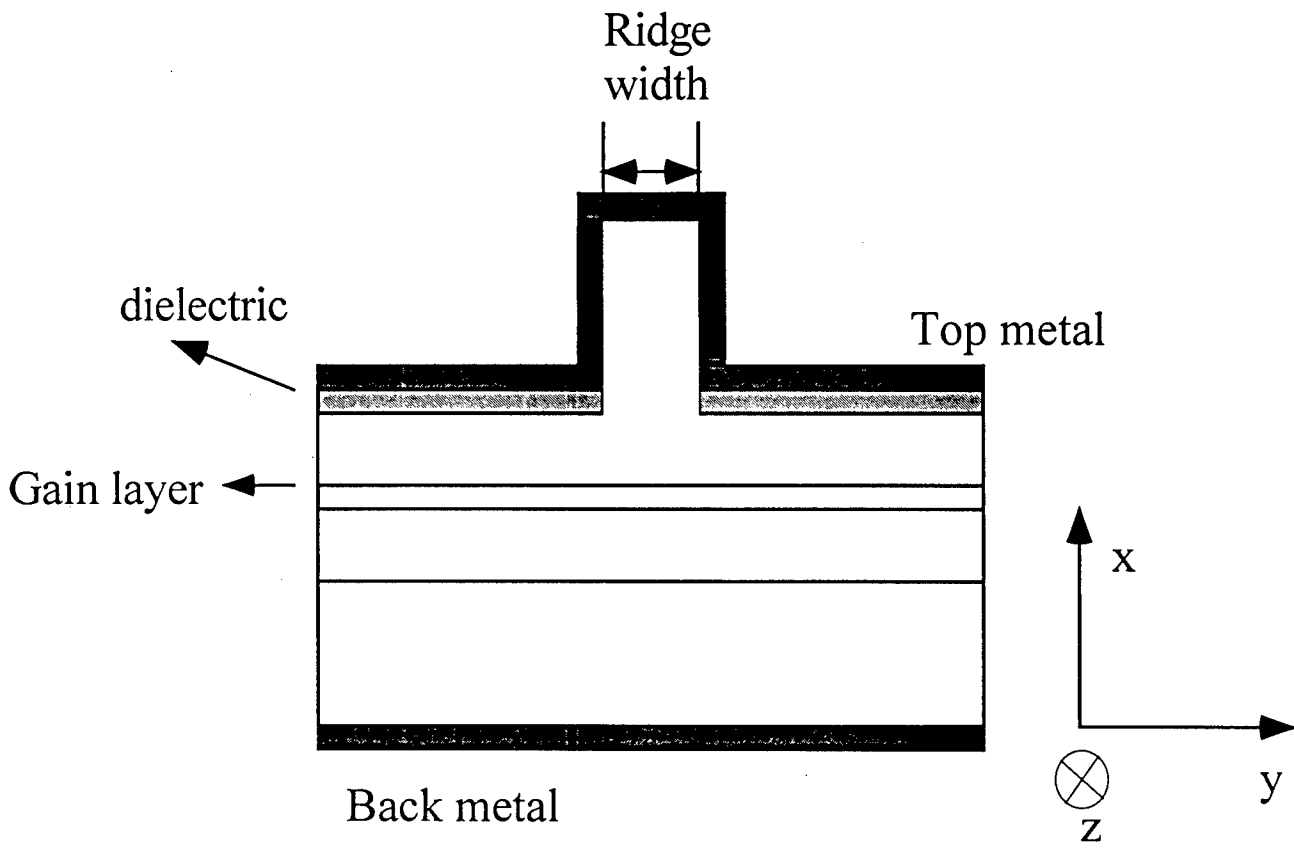


Figure 4.2 Schematic Diagram of Cross Section of a ridge laser.

where  $A_l$  and  $B_l$  are the coefficients of forward (+x) and backward (-x) propagating plane waves and  $x = L_l$  is the position of each interface. For a guided mode, there is no real wave propagating along x or -x, so  $k_{lx}$  and  $k_{mx}$  are imaginary, while  $A_1, B_m$  are zero, and  $B_1, A_m$  are finite, expressing waves decaying exponentially. Solving wave functions to meet the above boundary conditions, along with the electric field continuity requirement at the interfaces, the effective propagation constant and field distribution of the guided modes can be found. Two numerical methods are frequently used: the transmission (or transfer) matrix method [6-7], or the characteristic matrix method[8]. Usually, the transmission matrix method is used to obtain the waveguide mode with effective index and confinement factors, while the characteristic matrices are used in calculating modal reflectivities[3].

Now let us examine the modal reflectivity of a cleaved facet and far-field pattern of waveguide modes. The Fresnel plane wave decomposition method can be used to calculate the far field pattern and estimate the modal reflectivity, scattering, and transmission[9-11]. Using the same argument as above, we need only consider the transverse mode and ignore lateral variations, as shown in Fig. 4.4. The optical mode incident on the  $90^\circ$  facet can be regarded as a wave packet  $E(x)e^{-jk_z z}$ , where  $k_z$  is the effective wavevector. Thus we can use the effective index approximation where the waveguide is considered as a uniform material with  $k = k_z$  at the interface. The mode can then be decomposed to plane waves whose reflection and transmission can be easily

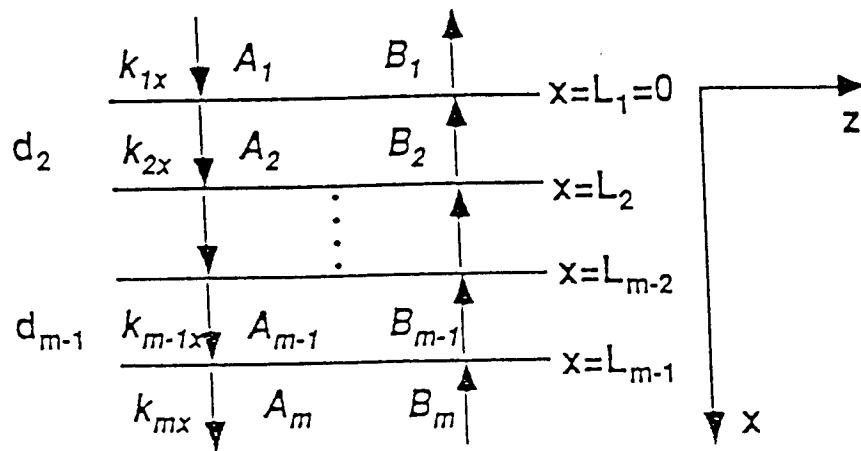


Fig. 4.3 Illustration of 1-D mode calculations in a dielectric stack.

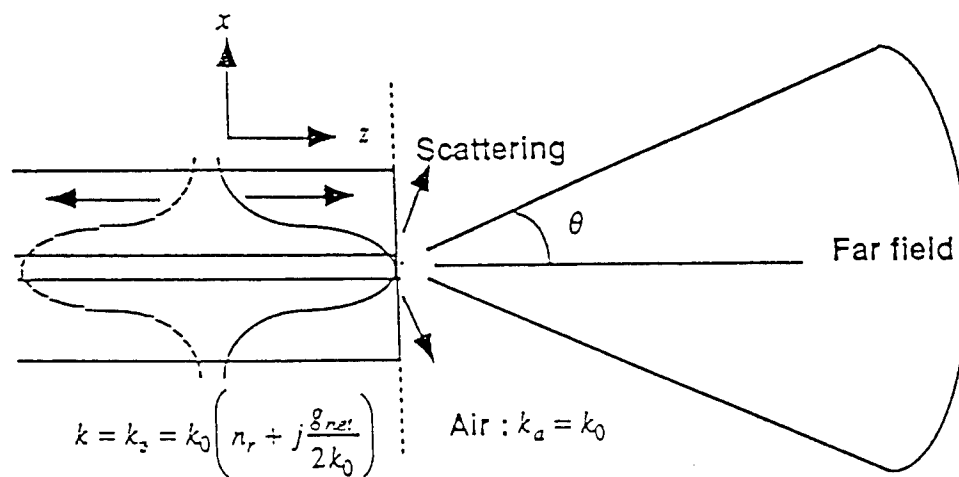


Fig. 4.4 Illustration of calculation for modal reflectivity and far field pattern.

calculated. The plane waves have  $\vec{k} = k_{px}\hat{x} + k_{py}\hat{y}$ , with  $|\vec{k}| = k_z$ . Assuming  $z=0$  at the facet, we have:

$$E(x) = \frac{1}{2\pi} \int_{-\infty}^{+\infty} G(k_{px}) e^{-jk_{px}x} dk_{px}, \quad (4.28)$$

and

$$G(k_{px}) = \frac{1}{2\pi} \int_{-\infty}^{+\infty} E(x) e^{-jk_{px}x} dx, \quad (4.29)$$

where  $G(k_{px})$  is the spatial spectrum of  $E(x)$ . This spectrum  $G(k_{px})$  is the field distribution at different angles, or the far field amplitude. Therefore, the above equation can generate the far field pattern of the mode in any material by replacing  $|\vec{k}|$  with  $k_a$ . Since  $k_{px} = k_a \sin\theta$ . We have the angular distribution of the far field amplitude as:

$$G(\theta) = \int_{-\infty}^{+\infty} E(x) e^{jk_a \sin\theta x} dx. \quad (4.30)$$

The far field intensity pattern is  $G(\theta)G^*(\theta)$ . The reflection at the interface can be calculated based on the plane wave decomposition, and it can be given by the reflection coefficient spectrum  $r(\theta) = |r(\theta)|e^{j\phi(\theta)}$ , which accounts for both the amplitude and the phase shift on reflection. The modal reflectivity is given by the overlap integral of the normalized incident spectrum  $G(\theta)$  and the reflected spectrum  $r(\theta)G^*(\theta)$  such that::

$$R = \left| \int_{-\pi/2}^{\pi/2} G(\theta)r(\theta)G^*(\theta) d\theta \right|^2. \quad (4.31)$$

Since the plane wave reflection coefficient for different angles varies,  $r(\theta)$  is not a constant. Therefore, the reflected light can not be perfectly coupled to the waveguide mode, resulting in scattering. Hence, at the facet there are three process: transmission, reflection and scattering.

### 4.3 Fabrication and performance of ridge lasers and SOAs

#### 4.3.1 Processing techniques

Ridge laser and waveguide are the basic device structures used in the studies of this dissertation. In this section, we discuss the processing techniques and show some of performance data of simple ridge lasers and semiconductor optical amplifiers (SOA).

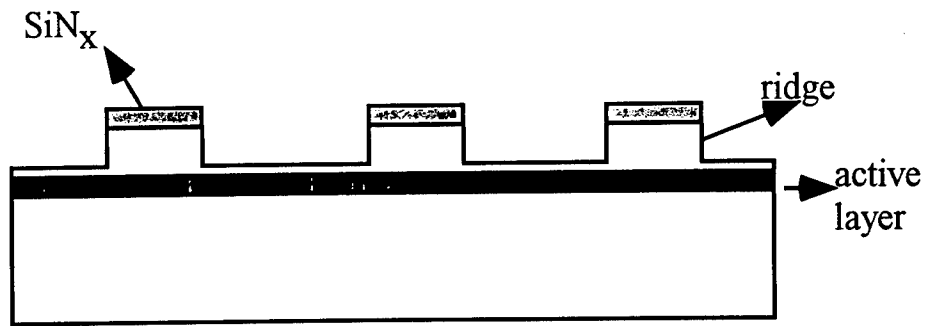
In the previous section, we know that the efficiency of transverse confinement of an optical mode, and the recombination of carriers is determined by the details of the material structure. In order to obtain a low threshold current and a single lateral mode, the device needs both optical and electrical lateral confinement. The easiest way to achieve lateral confinement is to form a ridge. Figure 4.2 shows a cross section of a ridge laser, which is typically 3 to 5  $\mu\text{m}$  wide formed  $\sim 1000 \text{ \AA}$  above the active layer. Top metalization makes direct contact only with the top of the ridge, while other areas of the device are isolated by a dielectric layer (usually  $\text{SiN}_x$ ,  $\text{SiO}_2$  or polyimide). The ridge part has a higher index than its two sides, and provides good optical lateral confinement. When current flows from the top contact to the bottom, the ridge confines the path of the current so that the recombination of electrons and holes only occurs in a region slightly wider than the ridge due to diffusion.

Two processes used for fabricating ridge waveguide lasers are Plasma Enhanced Chemical Vapor Deposition (PECVD) and Reactive Ion Etch (RIE). The PECVD is

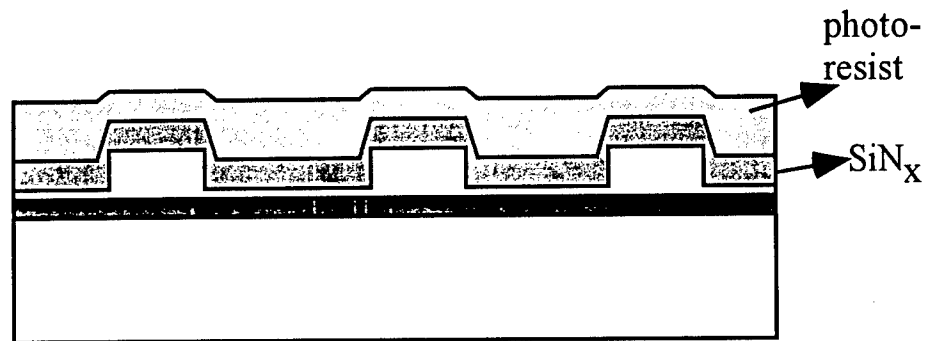
capable of growing very uniform layers of dielectric material, while RIE can uniformly etch the semiconductor and dielectric layers with a very good directionality. RIE can be used both for etching to form a self-alignment mask and a vertical etched facet[3].

The main processing steps to form our lasers are shown in Fig. 4.5. Both dry-etch ( $\text{CH}_4$ ,  $\text{H}_2$  mixture) and wet etch can be used to etch ridges in the InP-based material with a  $\text{SiN}_x$  as the mask. Planarization is accomplished by first using PECVD to deposit a layer of  $\text{SiN}_x$  on top of the wafer; then a layer of photoresist is spun on to planarize the surface so that the photoresist on top of the ridge is thinner than the photoresist elsewhere (which is an effective for narrow ridges  $< 20 \mu\text{m}$ ). The next step is to make a self-alignment mask for etching off the  $\text{SiN}_x$  only on top of the ridges. Here we use oxygen RIE to remove the photoresist. Since the etching process is very uniform and the photoresist on top of the ridges is thinner than other areas, at a certain point, the top of ridges will be exposed while other areas remain covered by photoresist. Thus a self-alignment mask of photoresist on top of the dielectric material is formed. Following this, the exposed dielectric material is etched away using a  $\text{CF}_4$  plasma. Top metal contact is then made by e-beam deposition, and finally, the device is lapped to  $\sim 100 \mu\text{m}$  thick and back contact is made and annealed. Detailed processing procedures and parameters are provided in Appendix 5.

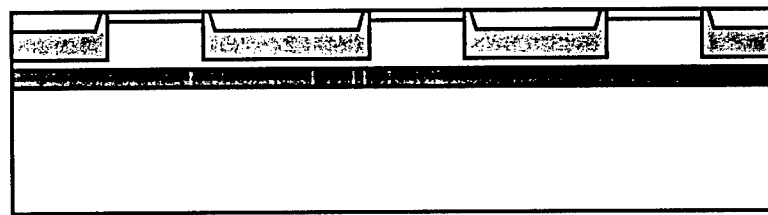
Eliminating the feedback in a semiconductor laser results in a pure gain device, known as a semiconductor optical amplifier (SOA). The feedback can be greatly



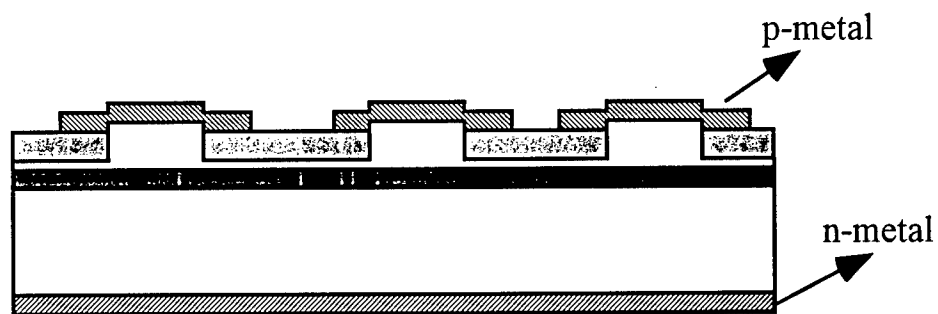
(a) etching semiconductor ridge using  $\text{SiN}_x$  as masks.



(b) planarization using photoresist



(c) using self alignment mask to expose ridges



(d) front and back metal deposition

Fig. 4.5 Schematic diagram of ridge laser fabrication procedure.

reduced in one of two ways: one is to coat the laser facets with anti-reflection film(s); the other is to tilt the waveguide away from perpendicular to the facet so that only very little reflected light can be coupled back to the incident waveguide mode. Some SOAs made in our lab uses a single layer antireflection coating. For a plane wave that is incident perpendicularly on the interface of two materials with indices of  $n_1$  and  $n_2$ , a thin layer of material put between the two materials can be a perfect antireflection coating if it meets the following conditions:

$$n = \sqrt{n_1 n_2} \quad \text{and} \quad (4.32)$$

$$t = \frac{\lambda}{4n}, \quad (4.33)$$

where  $n$  is the index of the film, and  $t$  is the thickness of the film. For the reflection of a waveguide mode, the effective index should be considered and the guided mode should be decomposed into plane waves for reflection analysis, just as what we did in the previous section. Even with ideal processing techniques, the reflection can never be absolutely zero, since the reflection of a film can not be zero simultaneously for light at different incident angles. Usually the reflection will set the upper limit of amplification for an SOA. Above that limit, at which the gain equals to the loss, the SOA becomes a laser. Figure 4.6 shows a numerical calculation at  $l = 1.33$  mm for modal reflection of based on our numerical program[3], assuming an effective index of 3.28. From the calculation, we find that the optimum index and thickness of the thin film should be 1.80 and 1900 Å, respectively. If the index and the thickness are all within 3% of these values, the reflection is  $< 0.1\%$ , allowing for a maximum SOA gain of 30 dB.

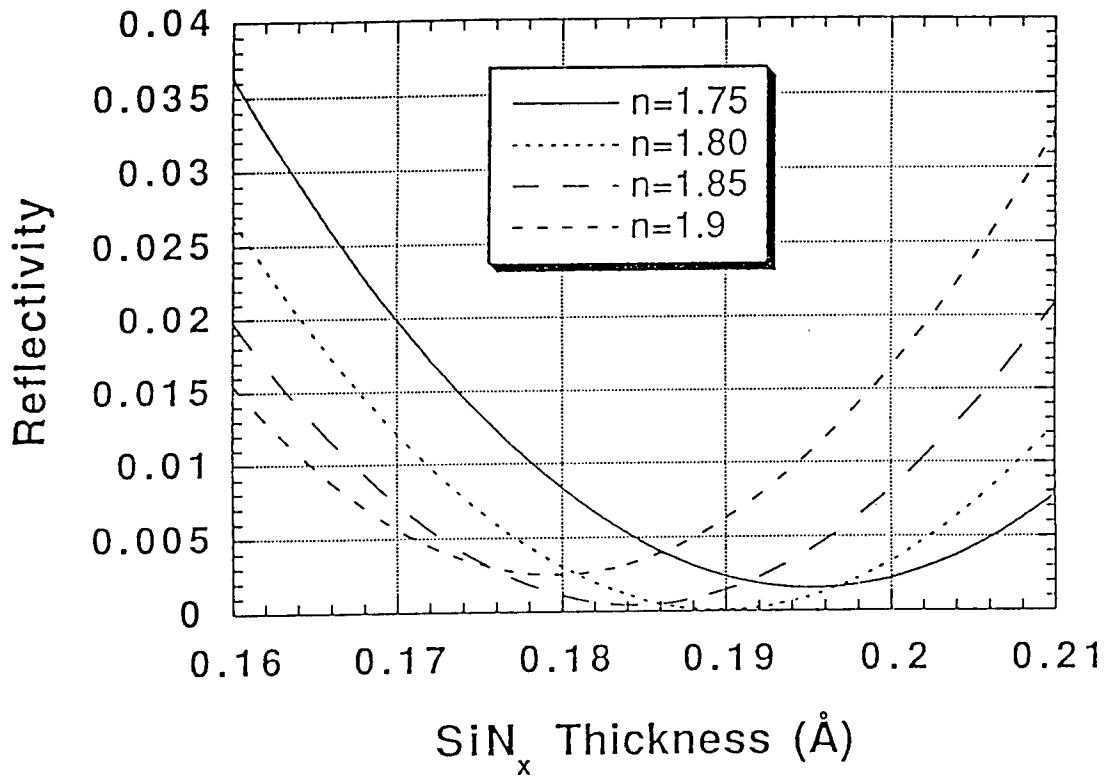


Fig. 4.6 Calculation of modal reflectivity of a 1.3  $\mu\text{m}$  wavelength laser with a single-layer anti-reflection coating.

In our devices, we use a single layer  $\text{SiO}_x$  e-beam evaporated thin film for proof-of-concept experiment. We found that we can roughly control the index of the film by control the pressure of the e-beam chamber before evaporation, which determines the percentage of oxygen in  $\text{SiO}_x$ . We also found that the adhesion of the  $\text{SiO}_x$  film can be improved by increasing the evaporation rate above  $15 \text{ \AA/s}$ . If very high gain is desired, then the index and thickness of the  $\text{SiO}_x$  thin film need to be precisely controlled with a fine oxygen pressure adjustment and an *in-situ* monitoring setup. With the equipment available in our lab, we achieve high reflectivity using an interactive procedure of deposition and measurement. .

#### **4.3.2 Performance of simple MQW ridge lasers and SOAs**

In this subsection, we describe the performance of simple ridge lasers and SOAs to illustrate how we characterize our devices. We will discuss the carrier diffusion length, gain as a function of the number of quantum wells, and facet reflectivity and gain of the SOAs.

For ridge lasers, due to the lateral diffusion of the injected carriers, the actual area the current passing through the active region is larger than the ridge area. In order to determine this diffusion width, we measured the threshold currents for lasers of the same cavity length but with different ridge widths, then plotted the threshold current versus the ridge width. Figure 4.7 shows measured results for lasers made from a 3 QW material

grown at David Sarnoff Research Center (the wafer number: #1709C). In the figure, we plot threshold current versus ridge width for several different cavity lengths. The diffusion width obtained from the data for 2020, 1400, 970 and 390  $\mu\text{m}$  long lasers are 5.07, 5.5, 5.35 and 5.31  $\mu\text{m}$  respectively. Hence, the electric diffusion width for this sample is  $\sim 5.3 \mu\text{m}$ .

Figure 4.8 shows the material net gain (gain minus the internal loss) versus the threshold current density for materials with different numbers of quantum wells (wafers #112895, #112095 and #111695 grown at Pinceton). At threshold, the net gain is equal to the output loss provided that we ignore scattering at the facets. We can see that at low gain, lasers with fewer quantum wells require a lower current density to reach the same net gain; while in the high gain region, more quantum wells help to reduce the threshold current density. Fewer quantum wells need a lower current density to separate the p and n type quasi-Fermi levels necessary for population inversion. As current density increases, gain of the materials with fewer quantum wells saturates and at a certain point it is less than that of the materials with more quantum wells. We will use this effect to choose the right number of quantum wells for the twin-guide lasers to be discussed in Chapter 7.

Figure 4.9 shows the performance of a typical SOA fabricated following the procedure discussed above. It shows the output light power versus the device current with an input light power of 25  $\mu\text{W}$ . The device is a 0.8 mm long by 5  $\mu\text{m}$  wide ridge

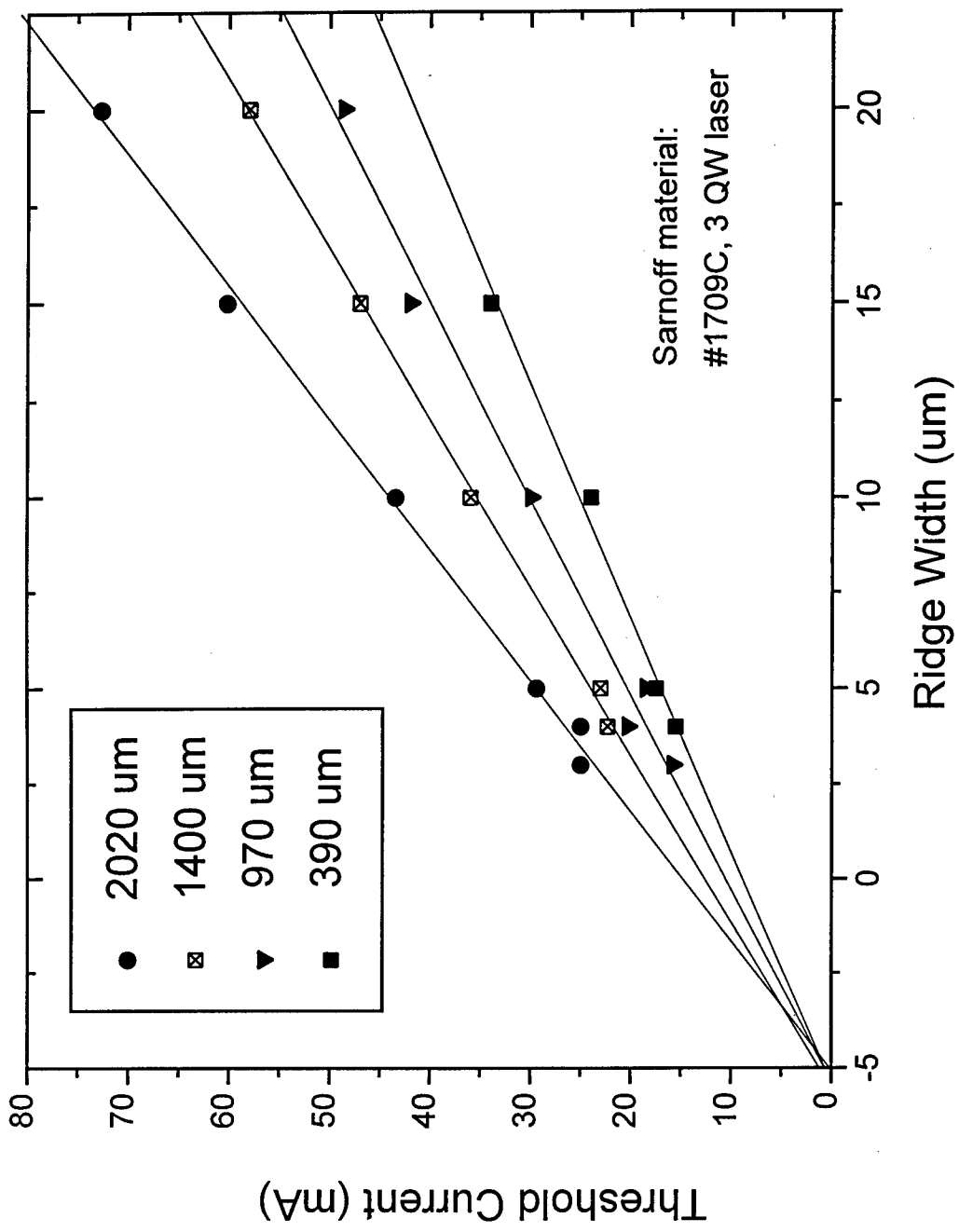


Fig. 4.7 Threshold current versus ridge width for lasers of different lengths. The diffusion length for this device is about 5.3  $\mu\text{m}$ .

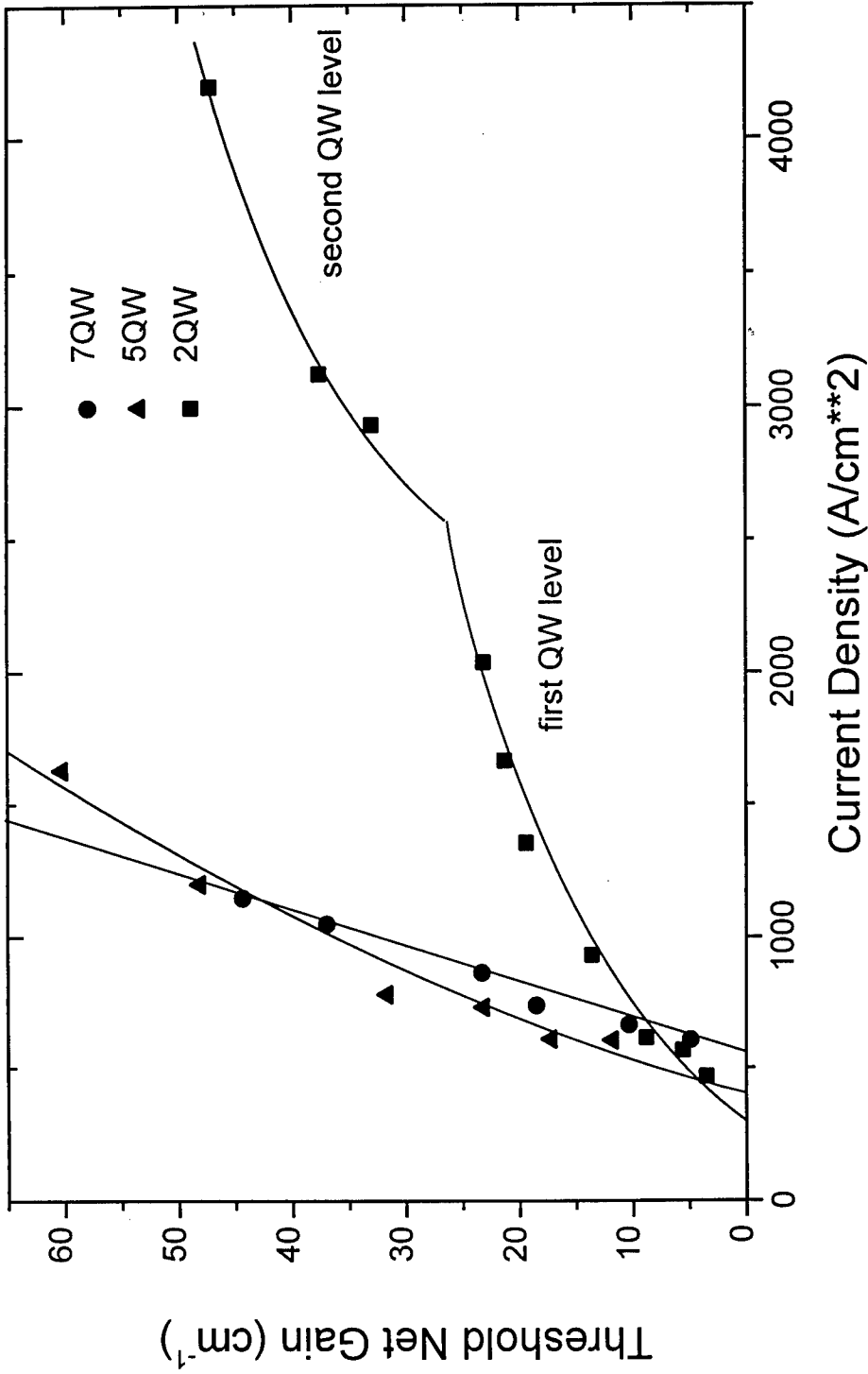


Figure 4.8 Net Gain versus threshold current density for QW lasers with different quantum well numbers.

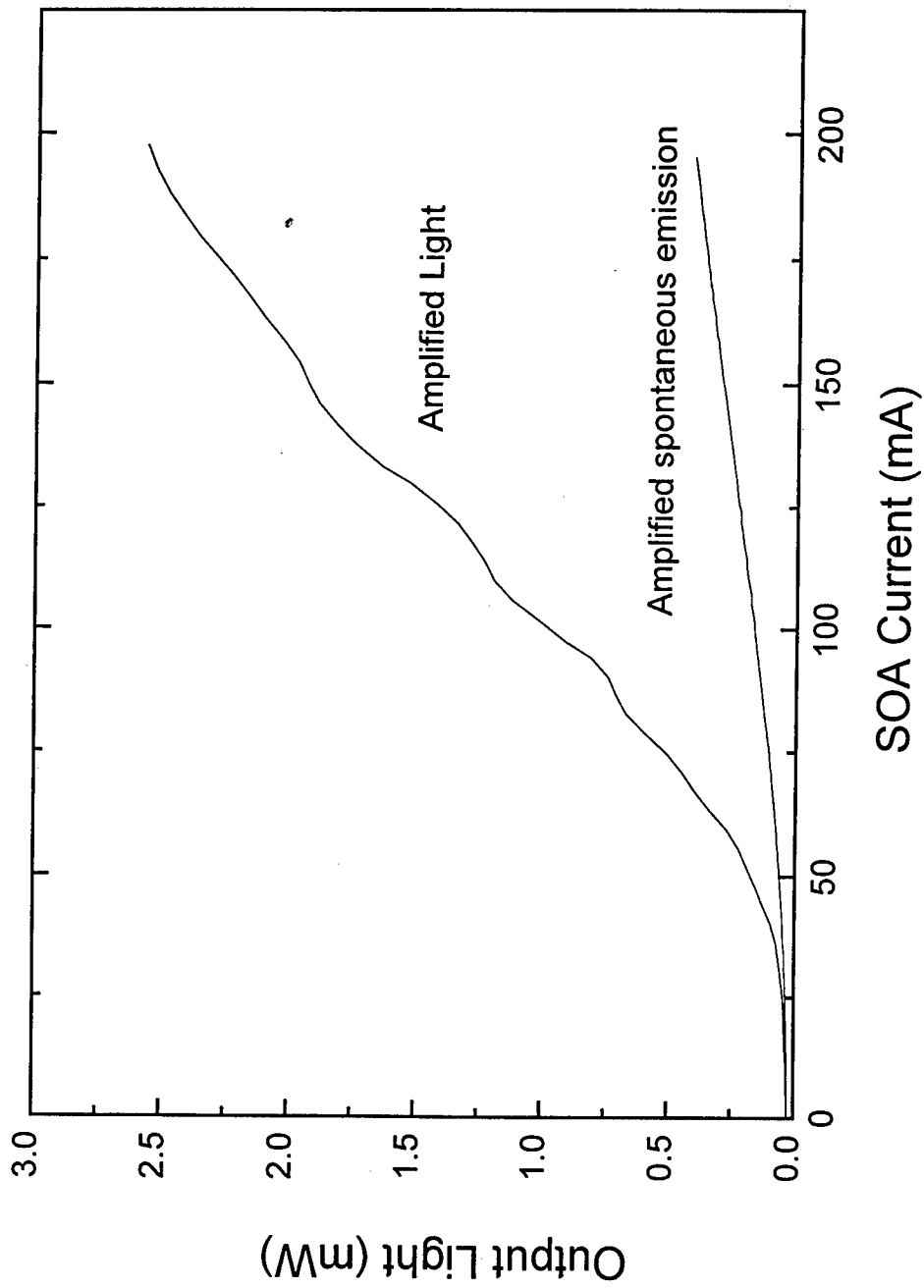


Figure 4.9 SOA light output versus current with an input light of  $25 \mu\text{W}$  at  $1.3 \mu\text{m}$ . The SOA has a 5 QW structure,  $5 \mu\text{m}$  wide ridge and  $0.8 \text{ mm}$  long cavity.

waveguide device with 5 quantum wells. We can see that with a 200 mA driving, the amplification is 20 dB. Figure 4.10 shows the spectrum of amplified light, together with the spontaneous emission from the SOA.

In summary, in this chapter, we discussed the basic principles of semiconductor laser operation, and considered the gain and characteristic parameters such as internal loss, output loss, efficiency and longitudinal mode spacing. We also described numerical methods used for mode calculations, including confinement factor, effective index, reflectivity, far-field pattern. Finally, our processing techniques were described and some of performance data were shown to illustrate the characterization of lasers and SOAs.

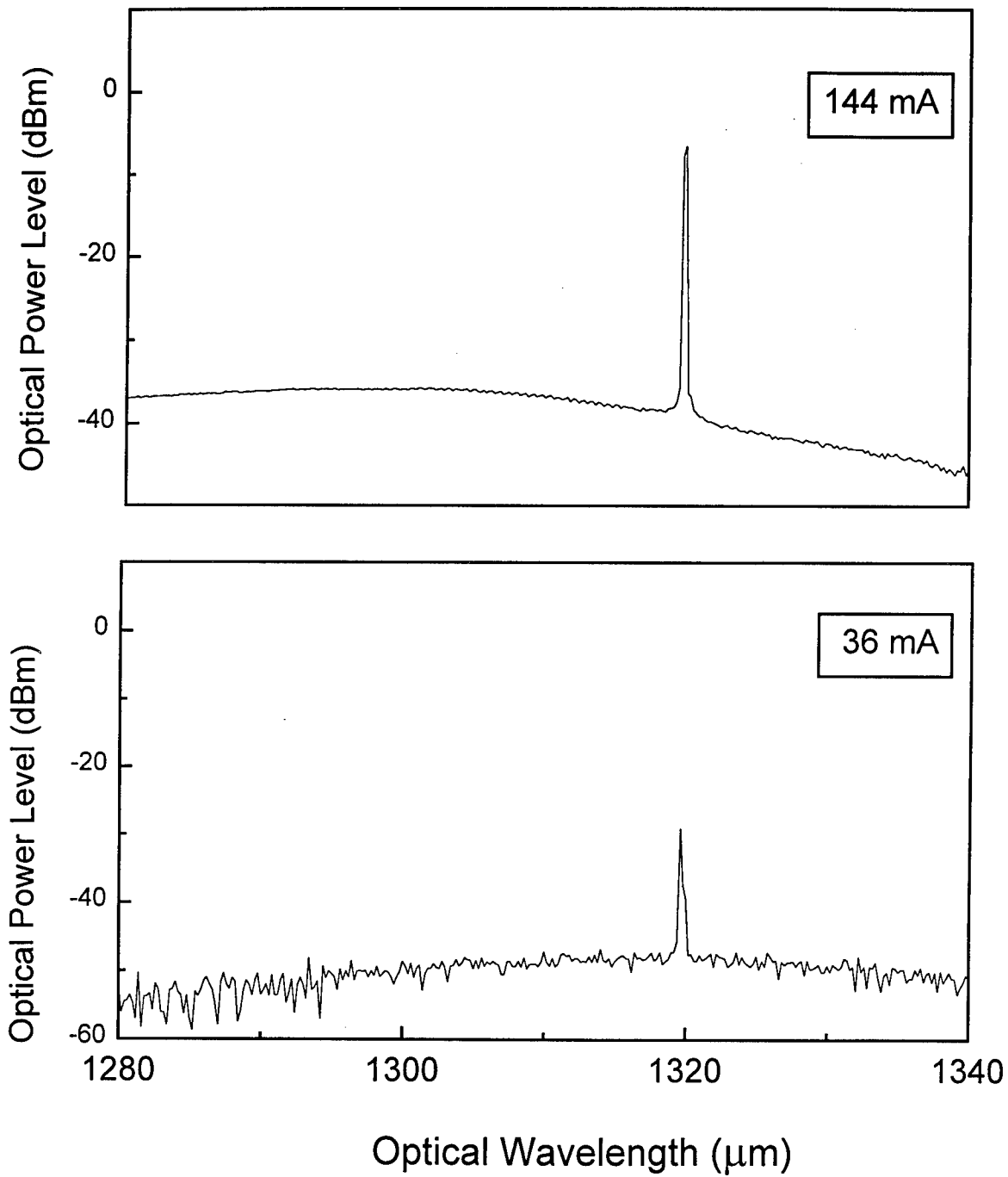


Figure 4.10 Amplified Optical Spectrum.

## References

- [1] Amnon Yariv, *Optical Electronics*, Fourth Ed., Holt, Rinehart and Winston, Inc., 1991.
  
- [2] Clifford R. Pollock, *Fundamental of Optoelectronics*, Richard D. Irwin, Inc., 1995.
  
- [3] Chih-Ping Chao, *Design, Fabrication and Analysis of Folded-Cavity In-Plane Surface-Emitting Lasers for Photonic Integration*, Ph.D. Thesis, University of California at Santa Barbara, 1992.
  
- [4] D. L. Lee, *Eletromagnetic Principles of Integrated Optics*, John Wiley & Sons, 1986.
  
- [5] H.C. Casey, Jr. and M. B. Panish, *Heterostructure Lasers*, Academic Press, Orlando, 1978.
  
- [6] P. Yeh, *Optical Waves in Layered Media*, John Wiley & Sons, 1988.
  
- [7] A. Thelen, *Design of Optical Interference Coatings*, McGraw-Hill, 1988.
  
- [8] P. H. Berning, *Physics of Thin Films*, Academic Press, New York and London, 1950.

[9] J. McKenna, quoted in F. K. reinhart, I. Hayashi, and M.B. Panish, "Mode reflectivity and waveguide properties of double heterostructure injection lasers," J. Appl. Phys. vol. 42, p. 4466, 1971.

[10] D. C. Krupka, "selection of modes perpendicular to the junction plane in GaAs large-cavity double-heterostructure lasers," IEEE J. Quantum Electron. P.390, 1975.

[11] S. T. Lau, T. Shiraishi, P.R. McIssac, A. Behfar-Rad, and J.M. Ballantyne, "Reflection and ransmission of a dielectric waveguide mirror," J. Lightwave Tech., vol. 10, no.5, p.634, 1992.

## Chapter 5 Photonic device integration using vertical twin-waveguide structure

As discussed in Chapter 1, the vertical twin-waveguide (TG) approach for photonic device integration only requires a single material growth step, providing a structure on which a variety of “active”(e.g. lasers and optical amplifiers) and “passive” (e.g. waveguides, couplers and modulators) devices can be fabricated. In this chapter, we quantitatively describe the operation principles of TG devices, and discuss the first demonstration of laser/passive-waveguide integration at the wavelength of  $1.55\ \mu\text{m}$  using a InP/InGaAsP-based TG structure.

Basic concepts of device operation of the TG structure are introduced in Section 1. The theoretical analysis of lightwave propagation—the normal mode coupling theory in a TG structure—is presented. Based on the analysis, we estimate the light coupling efficiency from the active to passive (transparent) waveguides, reflectivity of a half-etched facet, the threshold current density of a laser, and gain of an SOA in integrated devices. The concept of the “loss” layer and the effect of this loss layer on device performance is described in detail. Section 2 covers specific material design issues, including methods for material and device optimization, for obtaining matched waveguides to balance reflectivity and optical coupling, and for choosing the right number of quantum wells to obtain lowest threshold current density. One material design example is given at the end of the section, and tolerance for the material growth variations is quantitatively analyzed. Finally, in Section 3, we present our experiments on integrated lasers/Y-branch passive waveguides. Device performance, such as threshold current density, internal optical loss,

effects of the loss layer, and near and far-field patterns are discussed. A laser to waveguide coupling efficiency of 45% and a threshold current density of  $\sim 800 \text{ A/cm}^2$  for a TG laser are obtained.

## 5.1 Basic Concept of TG Structures

Both coupled-mode[1] and normal-mode[2] theoretical methods can be used to analyze a system of two coupled waveguides. Here, we use the normal mode approach, where a transfer matrix (see Chapter 4) can be employed to find all the normal modes, their effective indices and confinement factors in each layer. In a TG structure, usually only the two lowest TE modes ( $\text{TE}_0$ --the even mode,  $\text{TE}_1$ --the odd mode) propagate in the waveguides. This is especially true when a laser is involved, since TE modes have higher facet reflectivity[3] and reach threshold at lower currents than the TM modes.

Figure 5.1 shows the index profile and wave functions of even and odd modes of a TG structure. The material consists of two closely spaced waveguides. The upper waveguide is the active region providing gain, while the lower waveguide has a larger bandgap, allowing guided waves to propagate with minimal absorption. Both layers have larger indices than the surrounding layers, and are in close proximity ( $< 1 \mu\text{m}$ ) to act as a directional coupler. The phase of the electric field in the two guides is the same in the even mode, while the fields are  $180^\circ$  out of phase in the odd mode. Also note that there is a field node for the odd mode, but not for the even mode between the two guides. With

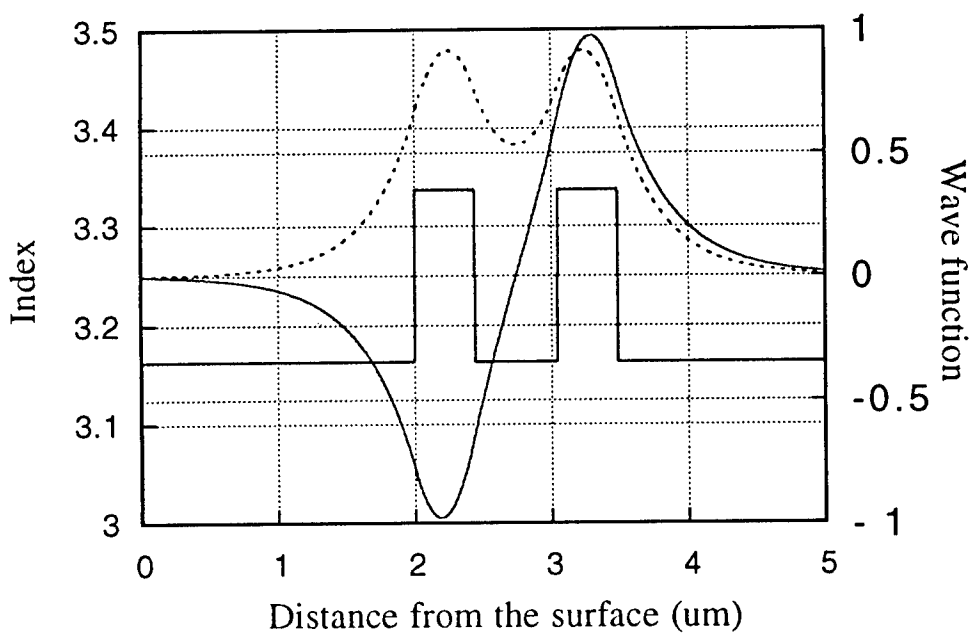


Fig. 5.1 Index profile and wavefunctions of a TG structure.

Here we use two identical guides to illustrate the concept of the even and odd modes.

two modes presence, the electric field along the propagating direction can be expressed as the superposition of the fields of the two normalized TE modes  $\bar{\Psi}_o, \bar{\Psi}_e$  :

$$\bar{E}_z = \bar{\Psi}_o \cdot \exp[-j \cdot k_0 \cdot \text{Re}(n_o) \cdot z] \cdot e^{(g_o/2 \cdot z)} + \bar{\Psi}_e \cdot \exp[-j \cdot k_0 \cdot \text{Re}(n_e) \cdot z] \cdot e^{(g_e/2 \cdot z)} \quad (5.1)$$

where  $k_0=2\pi/\lambda$  is the vacuum propagation constant,  $\text{Re}(n_i)$  and  $\text{Im}(n_i)$  are the real and imaginary parts of the complex effective index  $n_i$  ( $i=o, e$  for odd and even), and the modal gain  $g_i=2k_0\text{Im}(n_i)$ . From Eq. 5.1, it is clear that the optical energy oscillates between the two waveguides in the propagation direction,  $z$ . When the two modes are in phase, the energy is mainly in the upper waveguide, while out of phase modes have the energy confined in lower waveguide. Figure 5.2 schematically shows the light propagation along the TG cavity. The coupling length  $L_c$ , after which the relative phase of the two mode shifts by  $180^\circ$  phase is:

$$L_c = \lambda / [2|\text{Re}(n_e) - \text{Re}(n_o)|], \quad (5.2)$$

where the effective indices can be obtained through numerically solving the normal modes, as shown in Chapter 4. When the effective indices of the two waveguides, when uncoupled, are approximately the same, the active layer confinement factors and the effective indices for the two modes are very close. Thus the modes strongly interact with each other, and the exchange of energy between top and bottom guide is nearly complete[1,4]. We call this the “synchronous waveguide” condition. If the waveguides are not synchronous, one of the modes is strongly confined in the active layer, and has a high gain while the other one strongly confined to the waveguide and has a small gain. The mode beating does not significantly affect the power in the active guide since the

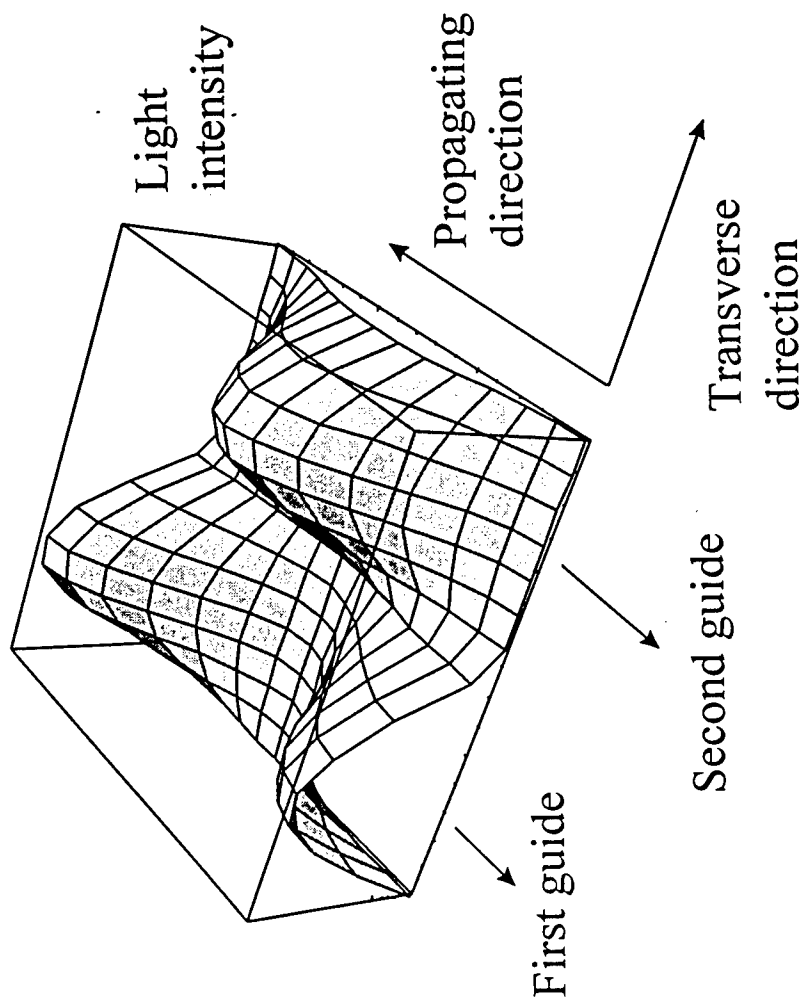
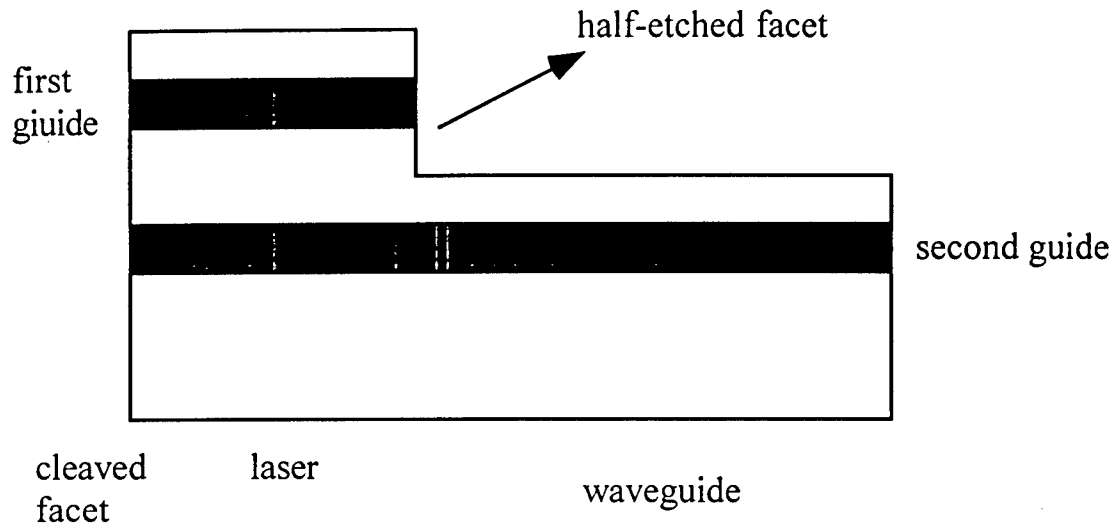


Figure 5.2 Schematic diagram about the wave propagation in a TG with even and odd modes.

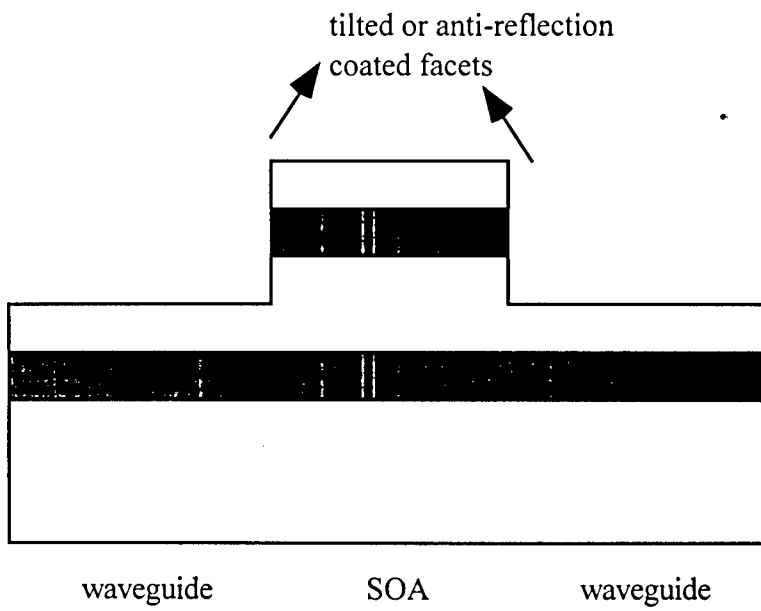
power of a single mode dominates in this guide. However, the beating still affects the optical power in the passive waveguide since the intensity of both modes are comparable.

For a twin guide laser, with both facets cleaved, the reflectivity is approximately the same as that of an ordinary semiconductor laser. At threshold, the gain of a mode has to be equal to its total loss (including mirror loss, internal loss, scattering loss) and the phase of the mode has to satisfy the resonance condition of the cavity. A simple but important integrated TG device is the laser/passive waveguide, shown schematically in Fig. 5.3(a). The left edge of the device is a deep etched or cleaved refractive facet, while on the right is a shallow facet etched only into the top guide, which serves two purposes: providing feedback to lasers and coupling light from the laser directly into the waveguide. Many other devices such as integrated laser/modulators, SOA/waveguides, SOA/modulators, and SOA/couplers, can also be fabricated using similar device configurations. In a TG structure, the laser feedback can also be provided by integrated gratings (e.g. distributed feedback)[5]. Here, we only consider the facet and half-facet reflections.

For the laser/waveguide shown in Fig. 3(a) with both even mode and odd mode presents, the lasing conditions can still be obtained by meeting the requirements that for either mode, the gain equals to the loss, and the phase matches itself after a round trip in the cavity. However, in the TG structure, the reflected light from either mode is coupled into both modes at the half etched facet. A detailed analysis of this condition has been considered previously[6].



(a) Laser/waveguide integration



(b) SOA/waveguide structure

Fig. 5.3 TG device structures.

Here, we quantitatively analyze some of the characteristics of the TG device performance. Due to the interaction of the two modes, light concentrates in either top or bottom guide, depending on the distance from the facets. Consider two extreme situations: most of the optical energy is concentrated in the upper guide, or in the lower guide at the half etched facet. In the first case, the reflectivity at the half-etched facet is strong, leading to low output loss and threshold current. However, only a small amount of light can be coupled from the laser into the passive waveguide. In the latter case, the situation is reversed and the coupling is strong. However, since the reflection is low due to the lower optical density in the upper guide than that in the lower guide, the threshold current density can be very high. Figure 5.4 shows a plot of the threshold current density of the laser as a function of cavity length for such a device with synchronous waveguides. It shows that at some points where the reflection is really small, the threshold current is high.

For the mismatch (non-synchronous waveguides) situation, the reflectivity of the half etched facet does not change much with the cavity length since the relative amount of power is nearly a constant with distance from the facets. However, in this case, the light coupling efficiency is reduced, and still changes with the cavity length since the relative amount of optical energy in the bottom guide is lower and varies with position.

In the case of an SOA integrated with a passive waveguide as shown in Fig. 3(b), both the synchronous and non-synchronous waveguide situations induces a gain

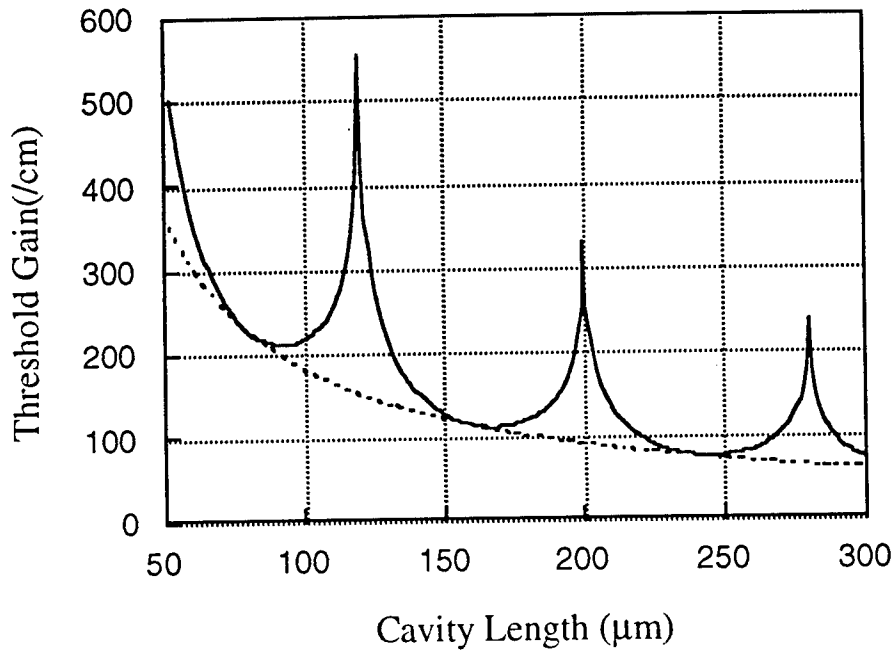


Fig. 5.4 Threshold gain versus cavity length for an integrated laser/waveguide device in TG with two synchronous waveguides.

Here an example device is used. The mode coupling length is  $80 \mu\text{m}$ , and the reflectivities of the modes on cleaved and half-etched facet are 0.33 and 0.078, respectively.

The oscillation of the threshold gain is caused by the changing of amount of the reflected light from the half etched facet due to the even and odd modes coupling.

oscillation with cavity length due to the mode coupling. Since this device performance variation is undesirable, we proposed eliminating the even mode by introducing a thin  $\text{In}_{0.53}\text{Ga}_{0.47}\text{As}$  “loss” (absorption) layer between the two guides, centered around the zero-intensity node of the odd mode. This introduces significant loss to the even mode while not affecting the odd mode significantly. We will examine this point further in the following quantitative analysis and experimental results.

We now consider reflections at the half-etched facet and the coupling efficiency of the laser/waveguide or SOA/waveguide structure. When only the odd mode is present for the device of Fig. 3(a), the light in the lower waveguide is coupled into into the passive waveguide with an efficiency of  $\sim 0.5$ . The coupling efficiency can be calculated by considering the overlap of the odd mode of the TG and the normal mode of only the passive waveguide. Hence a fraction of the energy in the upper waveguide passes to the free space and part of it is reflected. The reflected light is in fact a superposition of even and odd modes. Decomposing the reflected light wave function  $\bar{\Psi}_r$  into  $\bar{\Psi}_o, \bar{\Psi}_e$  [6], we obtain

$$\bar{\Psi}_r = r \cdot \left[ \left( \int_{x_0}^{\infty} \bar{\Psi}_o \cdot \bar{\Psi}_e^* dx \right) \cdot \bar{\Psi}_e + \left( \int_{x_0}^{\infty} \bar{\Psi}_o \cdot \bar{\Psi}_o^* dx \right) \cdot \bar{\Psi}_o \right]. \quad (5.3)$$

Here,  $r$  is the reflectivity of the etched facet, which to first order is taken as the reflectivity for the normal incident light from a cleaved facet. For an InP-based material, therefore  $r \cong 0.56$  for E field. For a simple case of synchronous waveguides where the energy in both guides is approximately equal for both modes, and half-etched facet stops at the mid-point ( $x_0$ ) of the two modes, the overlap integrals for the reflected light with

the odd and even modes are both roughly equal to 0.5. Based on these assumptions, and using Eq. 5.3, the reflected E field to the odd mode is  $(0.56 \cdot 0.5 =) 0.28$ . This corresponds to an intensity reflectivity of 0.078, which is approximately 25% of that of a normal laser of 0.3.

The light coupling ratio calculation is also crucial to the estimation of the gain of an SOA shown in Fig. 2(b). There is an estimated 3 dB coupling loss for both light input to and output from the TG SOA.

In order to reduce the threshold current, one can put high reflection coating on both the cleaved and the half dry-etched facets. In the ideal case, for the odd mode, the reflectivity of the coated cleaved facet is nearly 100%, while it is roughly 25% for the half etched facet. Nevertheless, only 50% of the optical energy can be coupled from the laser cavity to the waveguide in the last case of the TG structure

## 5.2 Twin-guide Material Design

For the reasons discussed in the previous section, we want to design the twin-guide material structure such that only odd modes are amplified by introducing an absorption layer at their nodes. The conditions for only odd mode presence can be expressed by:

$$\Gamma_{go}g - \ln(R_{1o}R_{2o}) / 2L - \Gamma_{ao}\alpha_a - \alpha_o \geq 0 \quad (5.4)$$

and  $\Gamma_{ge}g - \ln(R_{1e}R_{2e}) / 2L - \Gamma_{ae}\alpha_a - \alpha_e < 0 \quad (5.5)$

for the odd and even modes, respectively. Here,  $\Gamma_{ge}$  and  $\Gamma_{go}$  are the confinement factors of even and odd modes in the gain layer and  $g$  is the active layer material gain,  $\ln(R_{1i}R_{2i})/2L$  ( $i = e, o$ ) is the mirror loss;  $\alpha_a$  is the material absorption in the loss layer, and  $\Gamma_{ao}$  and  $\Gamma_{ae}$  are the confinement factors of the two modes within the absorption layer. Finally,  $\alpha_e$ ,  $\alpha_o$  represent the other internal losses including free carrier absorption and scattering for the even and odd modes, respectively. In order to effectively suppress the even mode while not significantly affecting the odd mode, the difference between  $\Gamma_{ao}$  and  $\Gamma_{ae}$  should be large. If the difference between even and odd modes is  $> 10$  dB, the even mode is effectively eliminated. In this situation, the coupling efficiency between the TG regions and the passive waveguides and the reflectivity on the etched facet are constant. Hence, in the devices using this structure, the threshold currents of lasers and gain of SOAs are not sensitive to the device length as those without the absorption layer.

To obtain a balance between reflection and light coupling at the half-etched facet, the light in the upper and lower guides must be equal at this surface. This is usually achieved as follows. First, the active waveguide is chosen (quantum well or double heterostructure plus the confinement and cladding layers). Then the numerical program is used to obtain the effective index of the waveguide. Next, a passive waveguide structure (wider bandgap layers or wider bandgap QW structure) is chosen, leaving only the thickness of the confinement layer as a variable. Numerical analysis is then used to find the optimal thickness of the confinement layer such that the effective index of the

waveguide is equal to that of the active guide. This also ensures the confinement factor in the active layer for both modes is equal.

Another issue of material design is the choice of the number quantum wells required, as determined from the gain vs. current density for a single well in a conventional Fabry-Perot laser structure. For separate confinement heterostructure multiple quantum well lasers (SCH-MQW), if the total active region is less than 1000 Å, then calculations show that the optical confinement factor in quantum well region is proportional to the number of quantum wells, in which case, gain versus threshold current density can be scaled with the QW number[7]. Our calculations show that the TG with the top guide as the SCH-MQW structure also follows the same rule. For the case of the TG with synchronous waveguides, the confinement factor is about half of that of a conventional laser. Thus, given the gain curve of a SCH single quantum well (SCH-SQW) structure, we can estimate the gain curve of the TG as a function of the number of quantum wells. Figure 6.5 shows a gain versus threshold current density curve of a SCH-SQW based on our experiments. The optimum working point is  $J_0$ ,  $G_0$ , where the ratio of  $G_0/J_0$  is at a maximum. To achieve the lowest threshold current density, the optimum number ( $N_{opt}$ ) of quantum wells for a TG structure is:

$$N_{opt} = \frac{\alpha_{in} + \alpha_{out}}{G_0 / 2} \quad (5.6)$$

where the  $G_0/2$  is employed since the gain is only half of that of a conventional laser at the same current density due to the half confinement factor. Here, the output loss can be estimated from the length of the device using the reflectivity calculations in Sec. 5.1. The

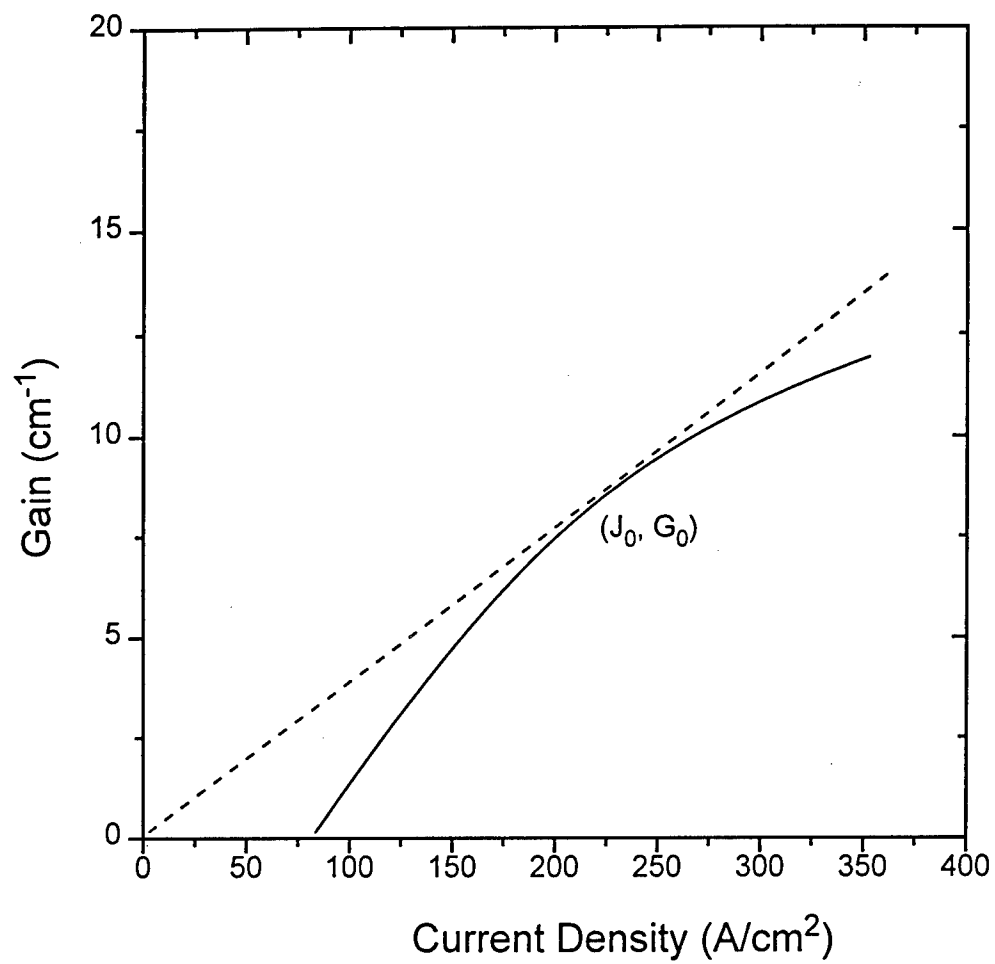


Fig. 5.5 Modal gain versus threshold current density of a single QW laser.

internal optical loss can be estimated by using the method in Sec. 4.3 with a similar structure, or by calculation of the free carrier absorption loss, which is shown to be the major source of the internal loss in Chapter 6.

Figure 5.6 shows a detailed material structure of an example TG. The upper guide consists of 7 QW InGaAsP structure with a bandgap cutoff wavelength of 1.6  $\mu\text{m}$ , while the lower guide has 10 QW with a larger bandgap (with a cutoff wavelength of 1.4  $\mu\text{m}$ ). The thickness of the confinement layers is adjusted so that the two guides are synchronous. Seven active quantum wells are chosen based on our estimation for a low threshold current density in the integrated laser/waveguide with a  $\sim 1$  mm long laser cavity. The spacing between the two guide is 1  $\mu\text{m}$ , and the loss layer is centered at the mid-point between the two guides where the intensity of the odd mode is vanishes. Figure 5.7 shows the wave function of both modes. From here, we obtain confinement factors for the active QWs of 8.9% and 7.4% for the even and odd mode, respectively. The effective index for the two modes are 3.255 and 3.259 and the coupling length is 340  $\mu\text{m}$ .

The thickness and the position of the  $\text{In}_{0.53}\text{Ga}_{0.47}\text{As}$  loss layer are crucial to the performance of the device. Based on our calculation of confinement factor, we plot the optical loss for both modes versus  $\text{In}_{0.53}\text{Ga}_{0.47}\text{As}$  layer thickness and position for an  $\text{In}_{0.53}\text{Ga}_{0.47}\text{As}$  absorption coefficient at 1.55  $\mu\text{m}$  wavelength of  $\alpha = 10^4 \text{ cm}^{-1}$  in Figs. 5.8 and 5.9. From Fig. 5.8, it is clear that a 20 nm thick loss layer causes  $\sim 18 \text{ cm}^{-1}$  loss for

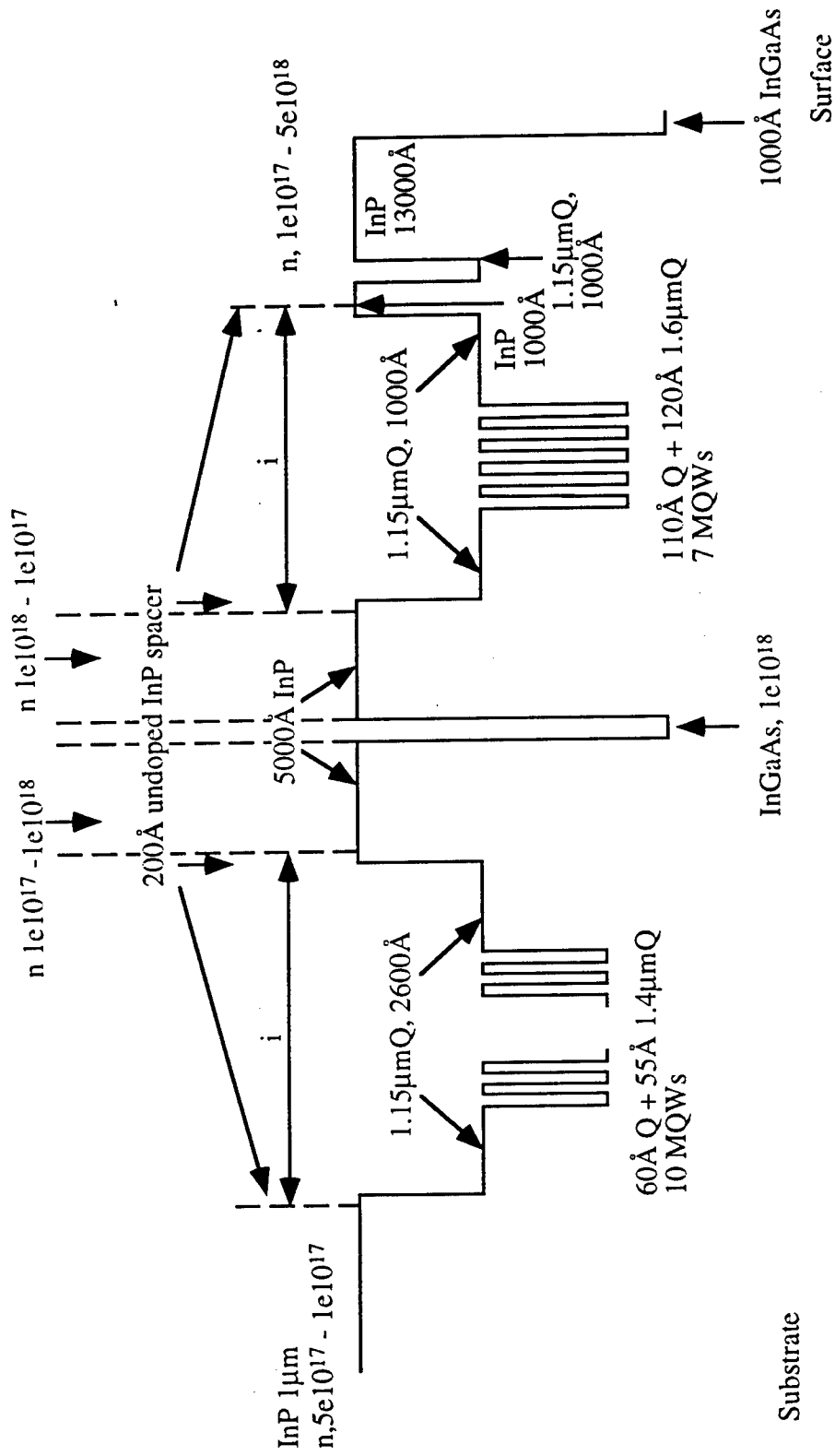


Fig. 5.6 One twin-guide design example.

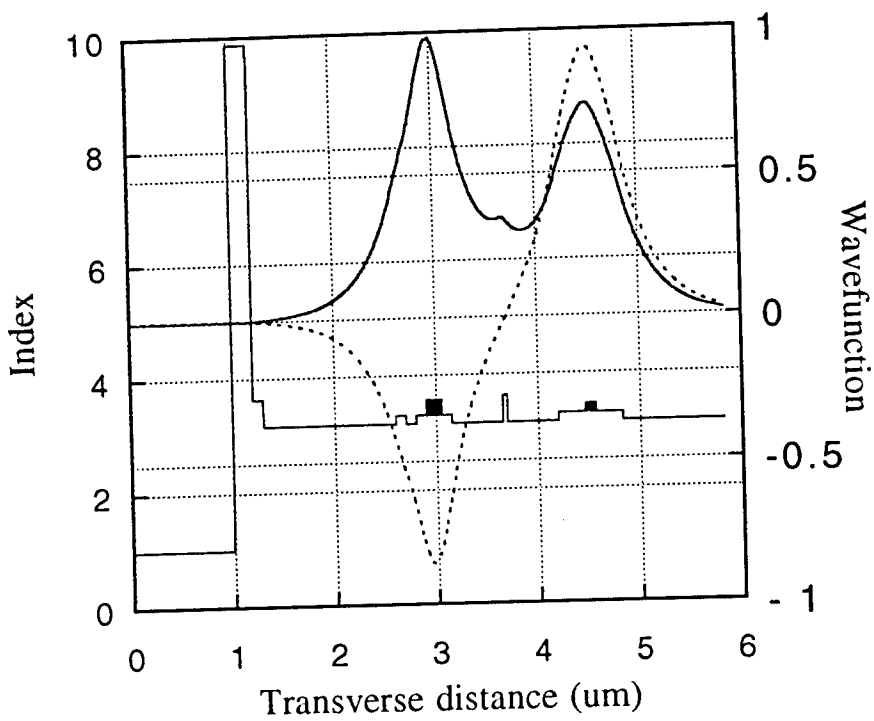


Fig. 5.7 The wave functions of the even and odd modes for an example TG structure.

(top guide 1.55  $\mu\text{m}$ , bottom guide 1.3  $\mu\text{m}$ )

Active Layer Confinement: even mode 8%, odd mode 7%;  
 Loss layer confinement even mode 0.6%, odd mode 0.002%.

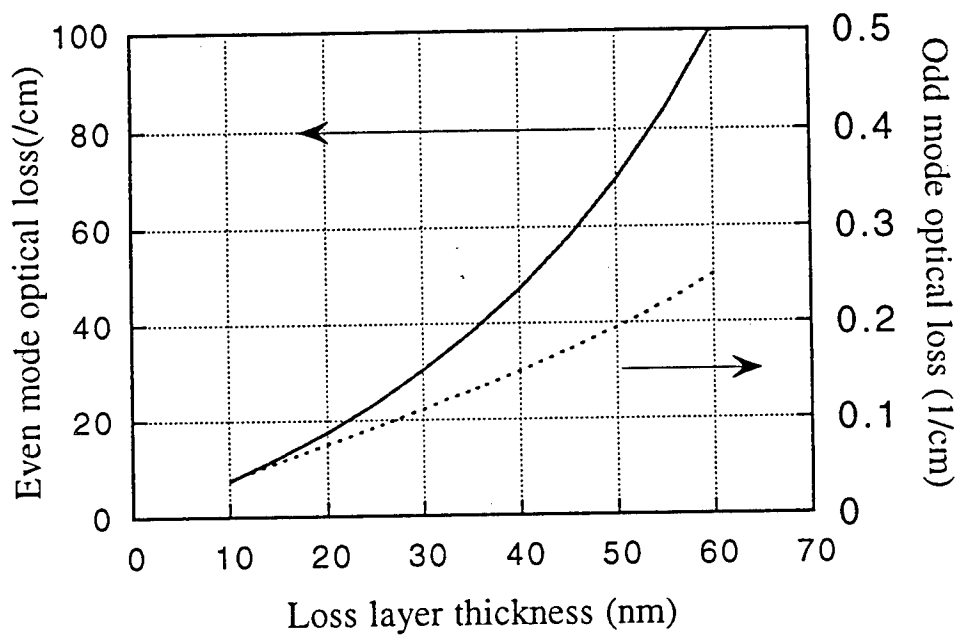


Fig. 5.8 Optical loss for the even and mode modes due to the loss layer.

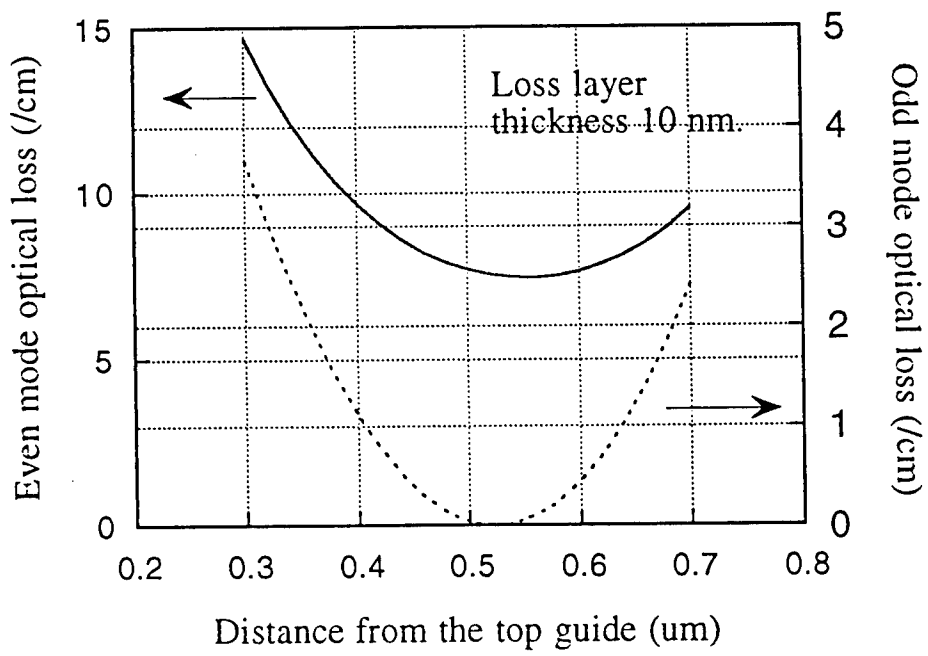


Fig. 5.9 Optical loss versus the position of the loss layer.

the even mode, while only  $0.1 \text{ cm}^{-1}$  for the odd mode. Hence, although the odd mode has a lower QW confinement factor than that of the even mode, it still reaches the lasing condition first. Figure 5.9 shows the effect of the position of the loss layer on the optical loss introduced. For this calculation, the distance between the two guides is  $1 \mu\text{m}$ , while only the position of the  $10 \text{ nm}$  thick loss layer with regard to the bottom of the top guide is varied. The loss for the odd mode is more sensitive to position. With a  $120 \text{ nm}$  position change, the loss for odd mode changes from approximately zero to  $1 \text{ cm}^{-1}$ . Therefore, we can position the loss layer such that it introduces significant loss for the even mode while only slightly affecting the odd mode.

### **5.3 Monolithic integration of a $1.55 \mu\text{m}$ wavelength MQW laser/waveguide using TG.**

In this section, monolithic integration of a  $1.55 \mu\text{m}$  wavelength multiple quantum well (MQW) laser with a passive waveguide using a vertical twin-waveguide (TG) structure is described. This InP/InGaAsP structure is grown in a single step in the by gas-source molecular beam epitaxy. An  $\text{In}_{0.53}\text{Ga}_{0.47}\text{As}$  loss layer is incorporated in the structure to improve the control of laser feedback and output coupling through elimination of even mode propagation. It is shown that the introduction of the loss layer has little effect on the odd mode, with the same threshold current density and external efficiency for both structures.

Fig. 5.10 shows the TG material index profile and wavefunctions of the two modes. The material is grown on a (100) n-type InP substrate. First, a  $1 \mu\text{m}$  thick layer of

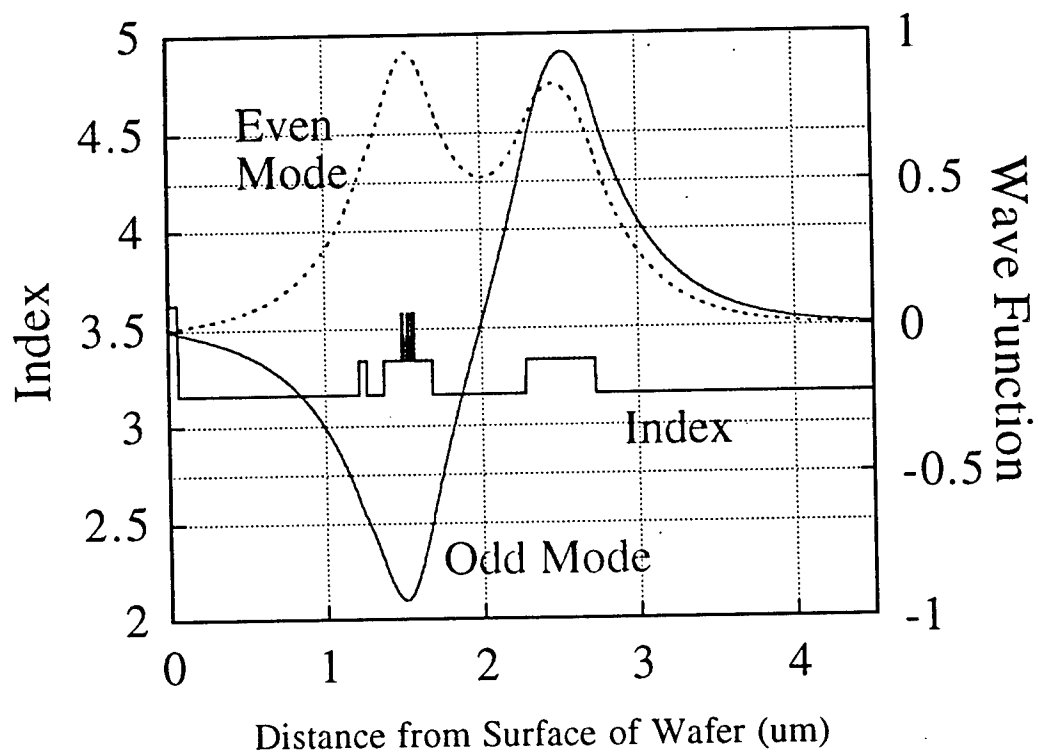


Fig. 5.10 Index profile and wave functions of the 3 QW TG structure.

n-InP is grown followed by a 430 nm thick InGaAsP layer with a bandgap of 1.0 eV, which forms the large bandgap passive waveguide. Next, a 600 nm thick InP cladding layer is grown on top of the InGaAsP waveguide. For materials with a loss layer, this InP cladding is followed by a 100 Å thick  $\text{In}_{0.47}\text{Ga}_{0.53}\text{As}$  absorption layer sandwiched between two 300 nm thick InP layers. The second, upper waveguide consists of a MQW active region surrounded by confinement layers. The active region consists of three, 13 nm thick InGaAsP QWs (bandgap  $E_g \approx 0.77$  eV, with 1% compressive strain) separated by 20 nm InGaAsP barriers with a bandgap of 1.0 eV. The same barrier material was used for the two 113 nm confinement layers. On top of the active guide, a 110 nm thick layer of p-type Be:InP is grown followed by a 51 nm thick InGaAsP ( $E_g = 1.0$  eV) which is used as an etch stop layer. Finally a  $\sim 1$   $\mu\text{m}$  thick layer of heavily doped p-type InP is grown, followed by a 70 nm thick InGaAs layer which serves as the p-contact layer.

The material structure was designed to have synchronous waveguides, thereby ensuring that both modes propagate at approximately the same velocity, and the exchange of power can be comparatively complete in both guides in the absence of the loss layer, as discussed in Sec. 2. At the center of the InP layer between the two guides, the light intensity of the odd mode is zero while that of the even mode is non-zero. By placing a 100 Å thick InGaAs layer centered at this point, the confinement factors of the even and odd modes are calculated to be 0.3% and  $4 \times 10^{-4}$  % respectively. With an absorption of  $10^4$   $\text{cm}^{-1}$ , the loss due to this layer for even and odd mode propagation is 30  $\text{cm}^{-1}$  and 0.04  $\text{cm}^{-1}$  respectively. Since both modes have approximately the same confinement factor

(4.06%, 4.08%) in the QW region, the odd mode will reach the lasing condition at lower current and hence be favored in this structure.

One laser facet in the integrated device is cleaved, while the second facet is formed by dry etching. The device configuration is shown in the micrograph from a scanning electron microscope (see Fig. 5.11). The device fabrication procedure is as follows. First, the laser region is protected by a  $\sim 300$  nm thick  $\text{SiN}_x$  mask, therefore allowing formation of the second facet by reactive ion etching using  $\text{CH}_4:\text{H}_2$  (1:7) gas mixture. The facet etch is halted midway between the upper and lower guides. The scanning electron micrograph shows a perpendicular, very smooth dry-etched facet. Next, a second  $\text{SiN}_x$  mask is deposited to allow for simultaneous wet etching (5/Citric:1/ $\text{H}_2\text{O}_2$  for InGaAs and 3/HCl:1/ $\text{H}_2\text{SO}_4$  for InP) of the laser and passive waveguide ridges. The passive waveguide are angled at  $7^\circ$  with respect to the cleaved facet to reduce reflections back to the laser cavity. After this, a 600 nm of  $\text{SiN}_x$  is deposited for laser contact isolation, followed by a e-beam p-contact metalization (200Å/Ti, 500Å/Pt, 3000Å/Au) on a pre-planarized surface using a polymer photoresist (AK 4210). Finally, the wafer is thinned to  $\sim 100$   $\mu\text{m}$ , and a 270Å/Ge, 450Å/Au, 215Å/Ni, 1000Å/Au n-contact is deposited on the back side. After n-contact annealing (362 °C for 90 seconds), the back laser facet is cleaved.

Figure 5.12 (a) shows the cleaved-facet near-field pattern of the TG laser with the absorption (“loss”) layer. The light intensity from the upper and lower waveguides is approximately equal and the center region is dark, as expected for lasing in the absence of the even mode. Figure 5.12(b) shows the near field of the passive Y-branch. One of our devices shows that 45% of the light are coupled to the passive waveguide from the laser.

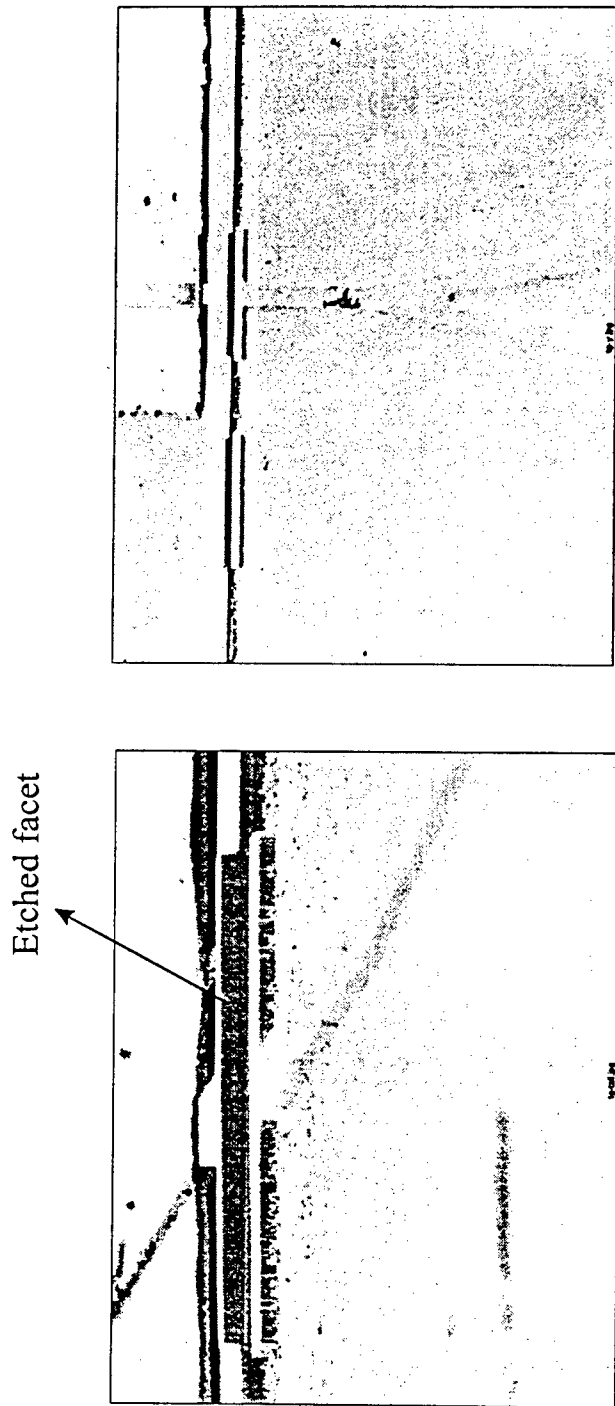
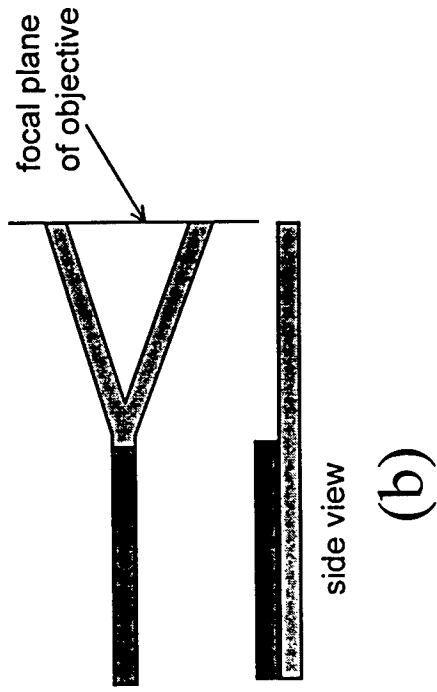
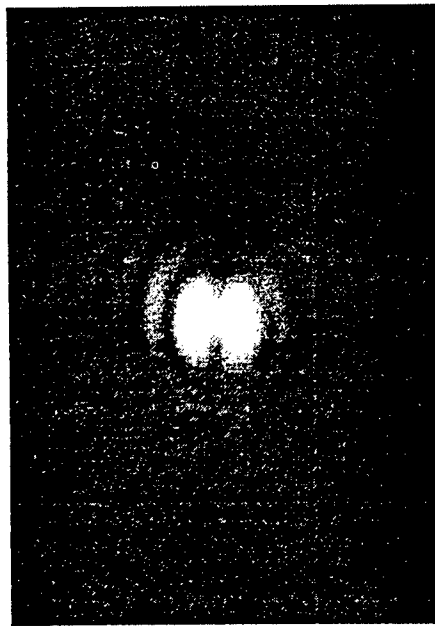
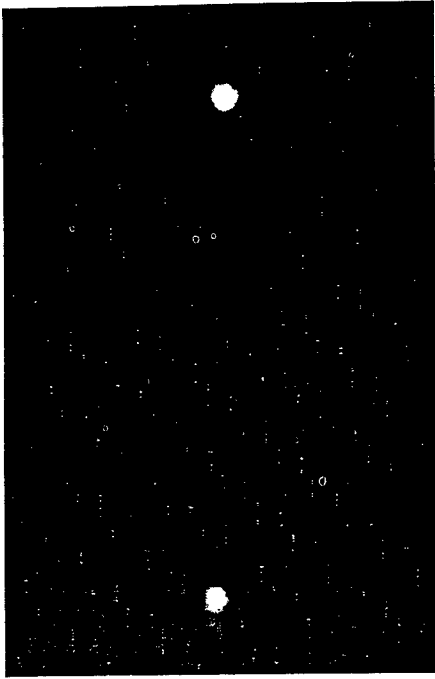
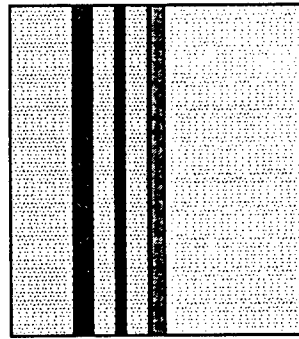


Fig5.11 SEM micrograph of the etched facet and Y-branch passive waveguide.



view  
⇐



active waveguide  
absorption layer  
passive waveguide

(a)

Fig. 5.12 Near Field Patterns of Twin Guide Laser/Waveguide  
(a) cleaved facet, and (b) Passive Y-waveguide

The power output from the cleaved side is 9.4 mW in pulse operation (1% duty cycle) and 4.3 mW output from the passive waveguide. Figure 5.13 shows the light-current characteristic of a TG laser with a 5  $\mu\text{m}$  wide ridge and 1.2 mm long cavity. The threshold current is about 80 mA, compared to a threshold current density of 1,300 A/cm<sup>2</sup>. The inset is the laser spectrum at  $I_{\text{th}}$  and  $2I_{\text{th}}$  and demonstrates an output wavelength of 1.56  $\mu\text{m}$ . It also shows multiple longitudinal modes as current increases. The passive waveguide has about 3 cm<sup>-1</sup> loss due to our deep etching in processing, and it is expected to reduce significantly if a shallow ridge waveguide is made in the passive part. .

To further investigate the effects of the InGaAs loss layer, we measured the transverse far-field pattern of TG lasers (both sides cleaved), with and without the intermediate absorption layer, and compared these measurement to calculations in Figs. 5.14 and 5.15. It is clear that without the absorption layer, lasing occurs on both the even and odd mode; while the device with the absorption layer preserves only the odd mode. Figure 5.16 is the polar plot of the far-field patterns and gives an intuitive picture about the beam shape in the transverse direction. With only one mode present, the percentage of the light in the upper and lower guide is independent of the cavity length. Hence, the threshold current variation for a laser/waveguide in TG structure without the loss layer predicted by Refs. 5 and 8 does not exist in our structure.

Our experiments show that many double-cleaved TG lasers without absorption layers only lase in the odd mode. This can be explained by the difference in reflectivity of the even and odd modes. Figure 5.17 shows the calculated effective index and

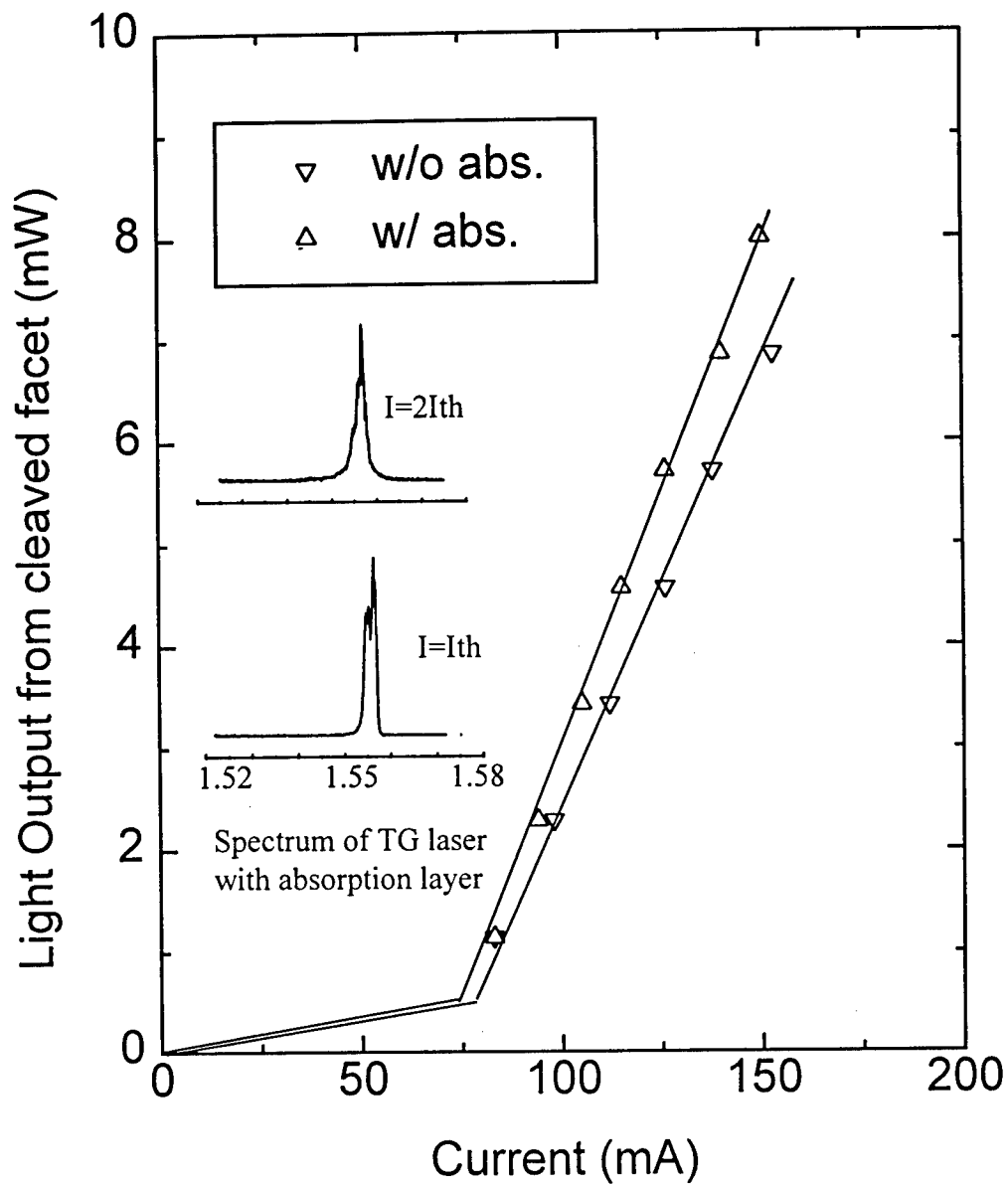
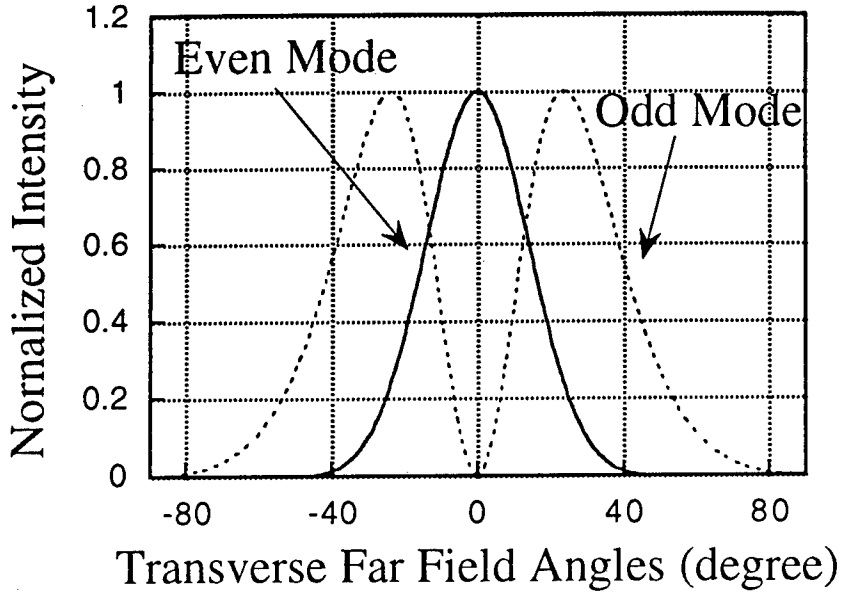
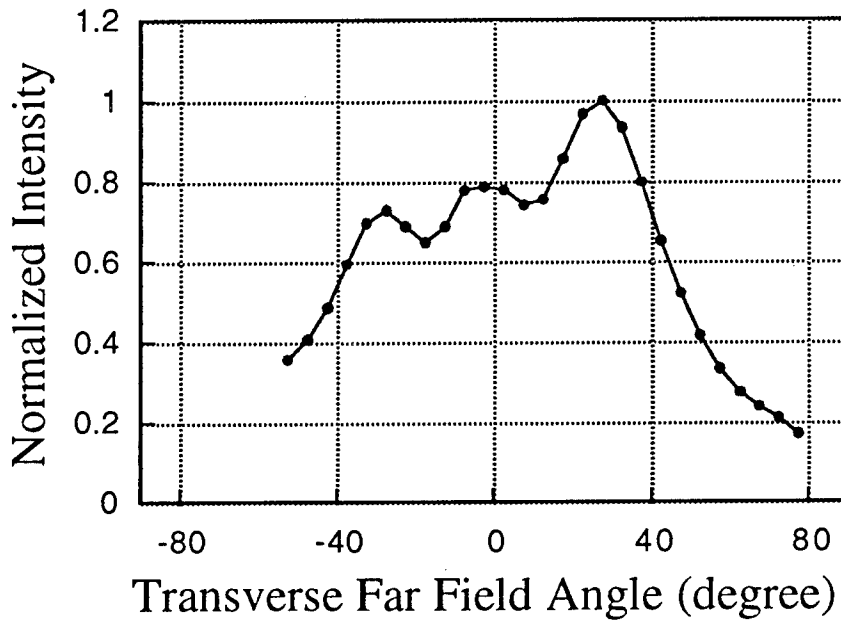


Fig. 5.13 L-I curve of TG lasers with laser cavity length  $\sim 1$  mm and ridge width of 5  $\mu\text{m}$ .



(a) Calculation results



(b) Measurement result

Fig. 5.14 Far field pattern of TG lasers without absorption layers.

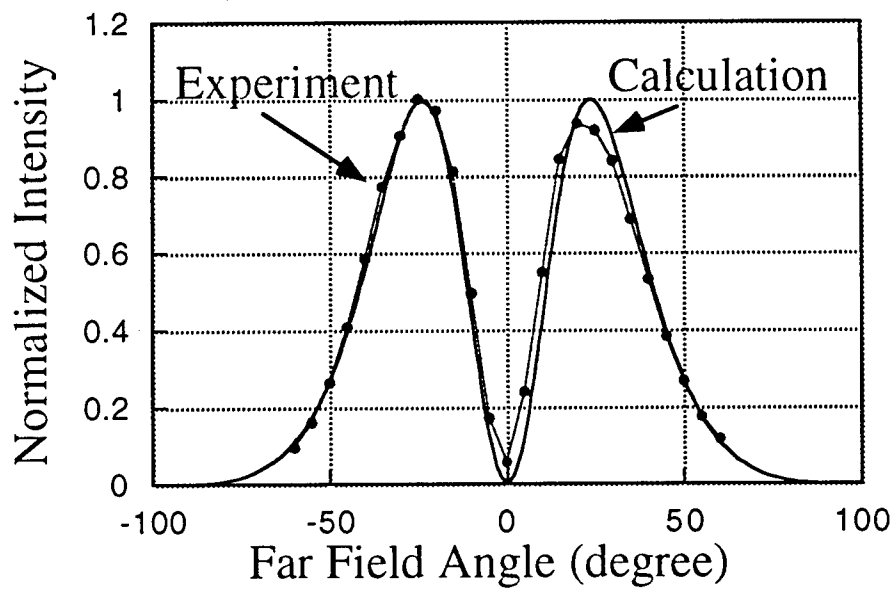
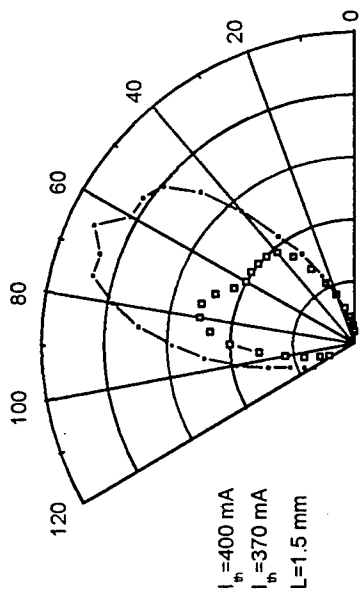
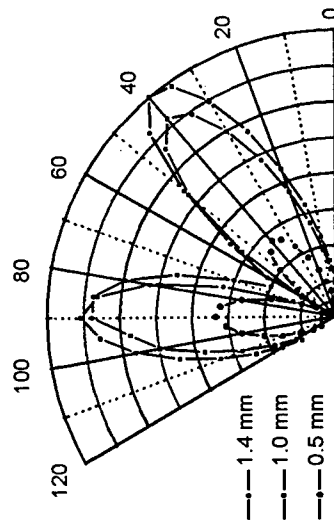


Fig. 5.15 Far field of odd mode from TG lasers with the absorption layer

The even mode is eliminated.



(a) far-field of two modes under different currents.



(b) far-field of the odd mode of different cavity length.

Fig. 5.16 Polar plots of far-field patterns.

reflectivity for even and odd modes versus the separation between the two guides discussed above. For our materials, the separation is  $\sim 600$  nm, where the reflectivity of the odd mode (37%) is higher than that of the even mode (31%). Further investigation is needed to clarify the effects of the reflectivity and the loss layer in elimination of the even mode. For example, testing devices of TG materials with a guide separation of  $1 \mu\text{m}$  to eliminate the reflectivity difference, as shown in Fig. 5.17.

Further experiments show that the loss layer has little effect on the odd mode. Figures 5.18 and 5.19 show the threshold current density and inverse external efficiency versus cavity length for both-side-cleaved 3-QW TG lasers with and without absorption layers. Also shown, for comparison, are results from a simple 3-QW Fabry-Perot laser grown by the same GSMBE process. Both the threshold current densities and inverse external efficiencies of TG lasers with and without absorption layers are found to be equal to within experimental accuracy. This implies that the loss layer does not significantly affect the odd mode. Note however, the threshold current densities of TG lasers are higher than that of simple Fabry-Perot lasers by a factor of 2 to 4. This is attributed to two sources. First, the confinement factors of QWs for TG optical modes are about half of that in the conventional lasers, which requires the QW to provide approximately twice the gain to overcome internal and output losses. Secondly, at high QW gain, the ratio of gain to current density increases. The latter is shown clearly in Fig. 5.18 as the cavity length decreases (or alternatively, as the output loss increases), the threshold current density increases more rapidly. Note that we also observe that conventional lasers lase at the second QW level when the laser cavity length  $L < 400 \mu\text{m}$ ,

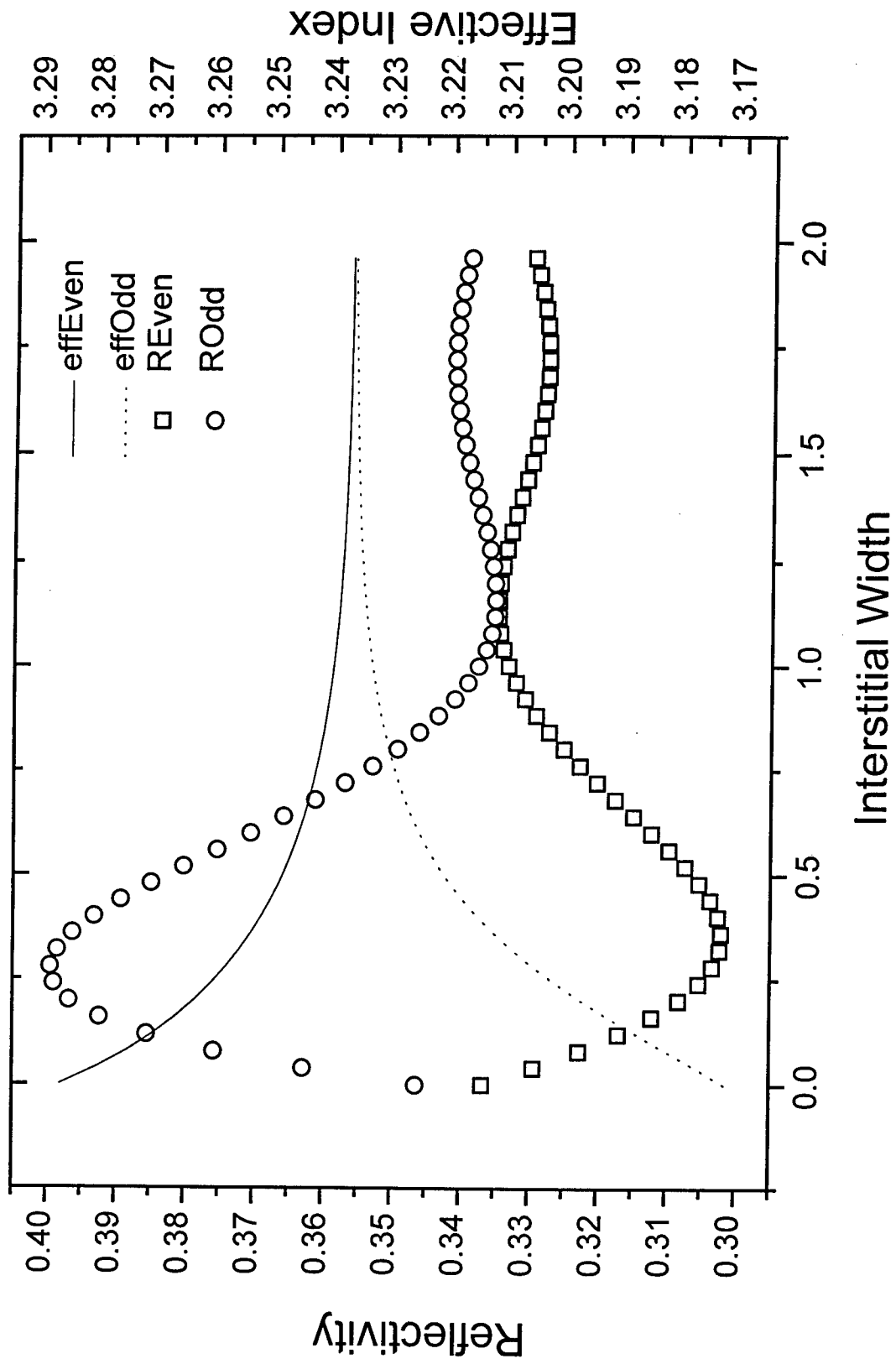


Figure 5.17 Effective index and reflectivity versus guide separation in a TG structure.

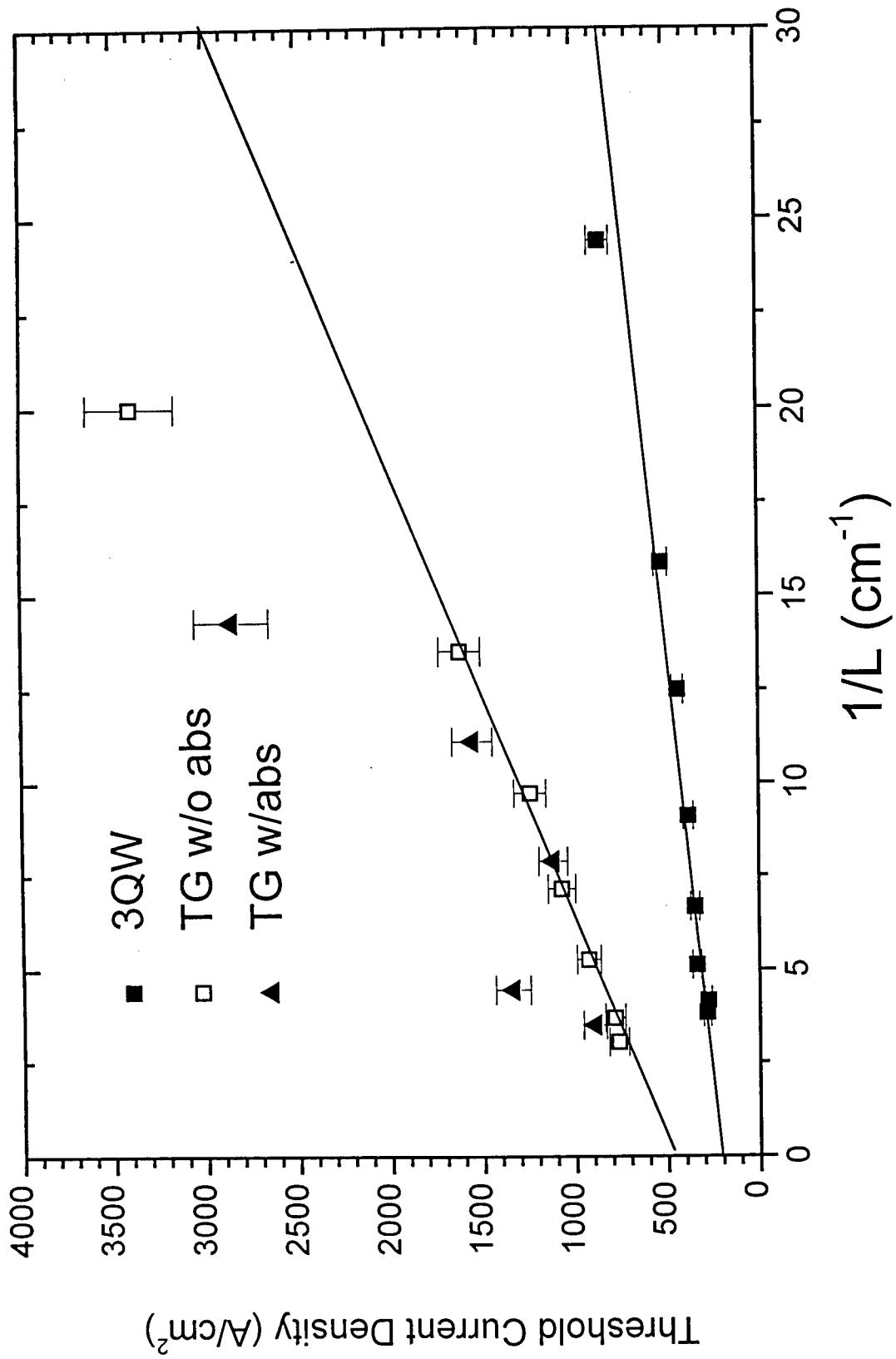


Fig. 5.18 Threshold Current Density of Twin-guide lasers and regular lasers.

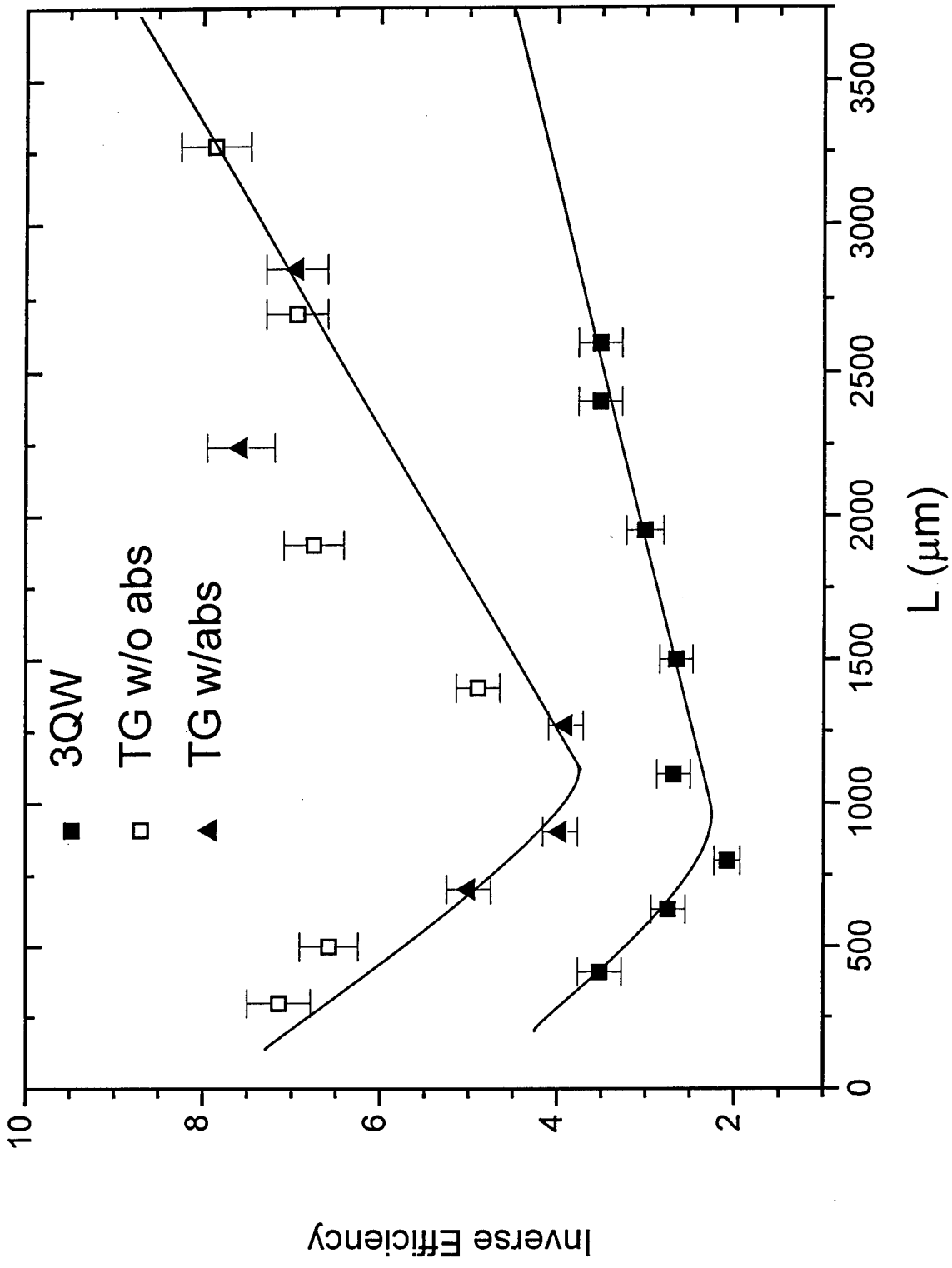


Fig. 5.19 Efficiency versus different cavity length for regular lasers, TG lasers with and without absorption layers.

while the TG laser starts to lase at the second level at  $L < 900 \mu\text{m}$ . The threshold current density in the TG structure can be reduced by introducing more quantum wells, which increases the active region confinement factor, thereby bringing the lasing condition into the low gain/current-density ratio region. From the slope of the inverse efficiency versus cavity length data, it is apparent that the internal losses for TG lasers with and without absorption layers are higher than that of the regular lasers. This is partly due to the increased free carrier absorption loss from the doped second guide. Further investigation is underway to resolve this issue.

In summary, we describe the demonstration of an integrated, InGaAsP/InP laser and waveguide Y-coupler using a vertical twin-waveguide structure operating at a wavelength of  $1.55 \mu\text{m}$ . The coupling efficiency from the laser to the passive waveguide is  $\sim 45\%$ , which is much higher than previously reported value[5]. A novel loss layer is proposed to gain a better mode control by eliminating the even mode. This provides constant light feedback and coupling without increasing the threshold current density or degrading the laser efficiency. This length independence of the coupling efficiency also has advantages for integrated semiconductor optical amplifiers/waveguide structures, where the gain is simply a monotonically increasing function of the length of the amplifier active region. This is a first step toward a "platform" technology with which a variety of active and passive devices can be monolithically integrated together on a single wafer structure.

## References

- [1] A. Yariv, "Coupled-mode theory for guided-wave optics," *IEEE J. Quantum Electron.*, vol. QE-9, pp. 919-933, 1973.
- [2] E. Marom, O.G. Ramer, and S. Ruschin, "Relation between normal-mode and coupled-mode analyses of parallel waveguides," *IEEE J. Quantum Electron.*, vol. QE - 20, pp. 1311-1319, 1984.
- [3] T. Ikegami, "Reflectivity of mode at facet and oscillation mode in double heterostructure injection lasers," *IEEE J. Quantum Electron.*, vol. QE-8, pp.470-476, 1972.
- [4] D. Marcuse, *Light Transmission Optics*. New York: Van Nostrand Reinhold, 1972., pp. 407-421.
- [5] C-P Chao, *Design and fabrication of folded-cavity in-plane surface-emitting lasers for photonic integration*, Ph.D. thesis of University of Santa Barbara, 1993.
- [6] H. Ribot, P. Sansonetti, and A. Carencio, "Improved Design for the monolithic integration of laser and an optical waveguide coupled by an evanescent field", *IEEE J. of Quantum Electronics*, vol. 26, no. 11, pp. 1930-1941, Nov. 1990.
- [7] P. McCilroy, A. Kurobe, and Y. Uematsu, "Analysis and application of theoretical gain curves to the design of multi-quantum-well lasers," *IEEE J. of Quantum Electron.*, vol. QE-21, no. 12, Dec. 1985.
- [8] Sado Adachi, *Physical properties of III-V semiconductor compounds: InP, InAs, GaAs, GaP, InGaAs, and InGaAsP*, New York: Wiley, 1992.
- [9] P.Wright, R. Nelson, and R. Wilson, "Monolithic integration of InGaAsP heterostructure lasers and electrooptical devices", *J. Quantum. Elec.*, vol.18, no. 2, pp 249, Feb. 1982.

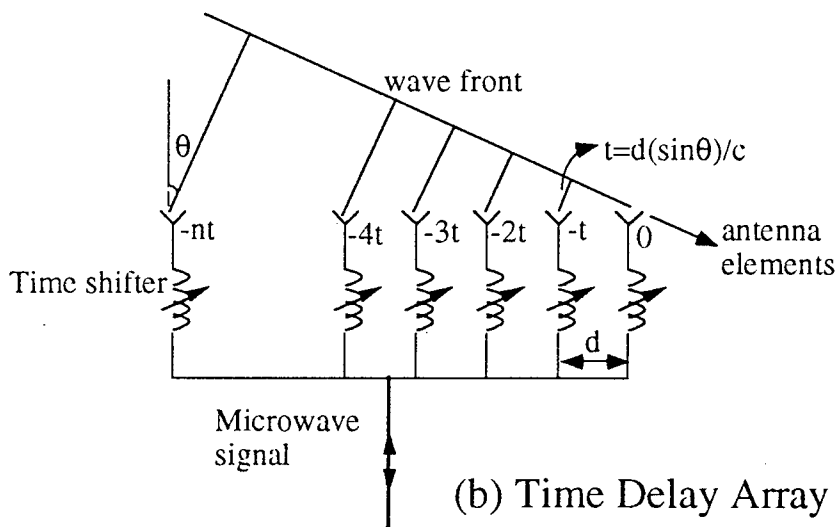
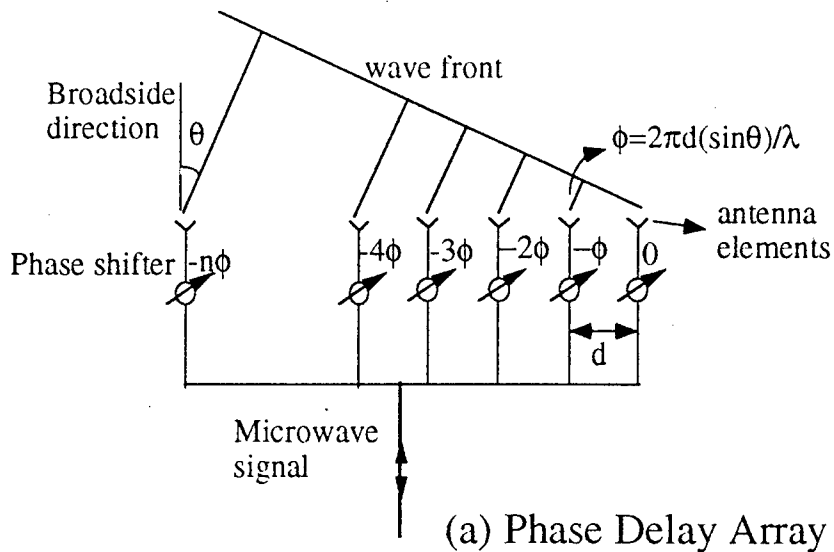
## Appendix 1. Phased array antennas and true-time delay

The basic concept of a phased array antenna is shown in Fig. A1(a). The  $N$  antenna elements are placed with equal spacing  $d$  in a linear array with aperture  $(N-1)d$ . For transmitting an RF beam, the microwave signal is fed with different phase delays to the antenna elements with phase difference  $\phi$  between adjacent elements, as shown in the figure. We define the direction perpendicular to the linear array as "broadside". Along a given direction at angle  $\theta$  to the broadside ( $\theta = 0$ ), the radiation from each antenna element must be phase-shifted by:

$$\phi = 2\pi d \sin \theta / \lambda = 2\pi d f \sin \theta / c \quad (\text{A1})$$

where  $\lambda$  is the wavelength of the radiating microwave beam,  $f$  is the frequency and  $c$  is the speed of the microwave radiation in vacuum. Along this direction, radiation from every antenna element is in phase, and the beam is strongest due to the constructive interference. A phased array receiver performs the reverse operation, where the various phase delays are introduced for the signals received from individual antenna elements to bring them all in phase prior to summation at the receiver amplifier electronics.

Conventionally, there are two major methods to introduce the phase delays: one has signals of different frequencies pass through phase shifters (usually consisting of ferromagnetic materials)[1-2] with approximately the same phase change; the other uses different lengths of cables or waveguides which introduce time delays. The second method is known as true-time-delay (TTD). For signals with very narrow signal bandwidth, the performance from antennas using one or the other of these methods are comparable. When the signal bandwidth is large, however, the TTD method has the advantage of avoiding a phenomenon called beam squint. From Eq.A1, it is clear that the radiation direction is a function of microwave frequency. When frequency changes, the radiation direction for that antenna array also changes, leading to "beam squint". For the



True-time-delay — without "beam squat"

transmit ← → receive

Figure A1 Schematic Diagram of Phased Array and True-Time Delay

same reason, if a signal has a large instantaneous bandwidth, the beam can not focus into a single direction. The change of the radiation angle,  $\Delta\theta$ , versus the change of the signal frequency  $\Delta f$  can be expressed by:

$$\Delta\theta = -\frac{\phi c}{2\pi d \cos\theta f^2} \Delta f, \quad (\text{A2})$$

where the negative sign indicates that as frequency increases, the angle of the radiation decreases. This performance degradation can be avoided by introducing true-time-delay, which is illustrated in Fig. A1(b). The time delay between adjacent antenna elements is  $t$ . Since signals with different frequencies travel with approximately the same speed, they are in phase along  $\theta$ , independent of frequency:

$$t = d \sin\theta / c. \quad (\text{A3})$$

True-time delay systems are free from beam squint and hence have the large instantaneous bandwidth desired for most advanced multibeam, multi-frequency antenna systems currently envisioned.

## Appendix 2: Coherent Receiver Array Operation

A coherent receiver detects the beat between the incident optical signal and the LO signal. For the simple case of amplitude modulation, the normalized beat signal is :

$$i(t) = (1 + mx(t)) \sin(\omega_{IF}t + \phi)$$

where  $m$  is the modulation index,  $x(t)$  is the modulating signal,  $\phi$  is the phase difference between the incoming signal and the LO, and  $\omega_{IF}$  is the frequency difference between the optical carrier and the LO signal, i.e. the intermediate frequency(IF). Assume that one optical receiver is used to detect signals from two antenna elements simultaneously. The transmitter lasers associated with the antenna elements therefore have to be tuned to the same frequency, so that both the detected signals have the same intermediate frequency. Under this condition, and for an ideal situation where the beat between the two incident signals and all other noise are neglected, the IF signal is :

$$i(t) = (1 + mx(t)) \sin(\omega_{IF}t + \phi_1) + (1 + mx(t)) \sin(\omega_{IF}t + \phi_2)$$

If  $\phi_1 = \phi_2 \pm n\pi$ , where  $n$  is an even integer, then the demodulated signal would be  $2mx(t)$ , which is desirable. But if  $\phi_1 = \phi_2 \pm n\pi$ , where  $n$  is an odd integer, the demodulated signal would be zero. Thus, to get the desired signal, both  $\phi_1$  and  $\phi_2$  have to be controlled very precisely. First, it requires an optical phase-locked-loop to control the relative phases of the two lasers. Second, the optical paths from the two transmitter lasers to the same receiver has to be controlled to sub-micrometer precision so that the optical phase difference between the two incoming optical signals is approximately  $2n\pi$ , where  $n$  is an integer. The system is further complicated since for some detecting directions, some lasers must be phase locked, and for other directions, different lasers

need phase-locking. Meeting all of these requirements, where one coherent optical receiver receives signals from several antenna elements simultaneously, is very difficult to achieve using present techniques. Therefore, in the coherent system proposed, for each beam direction, one receiver is used to receive and demodulate the signal from each antenna element.

### Appendix 3: Number of Delay Lines Needed in the Antenna in Fig. 2.3(a)

We now investigate how many delay lines are needed for the antenna receiver shown in Fig. 2.3(a). For any receiving direction, the delays for the antenna elements 1 to  $M$  must increase or decrease monotonically and as uniformly as possible, although there may be digitalization errors. The system has  $N$  different digital delays corresponding  $0, \Delta t, 2\Delta t, \dots, (N-1)\Delta t$ . We define  $DE_i$  as the delay for antenna element  $i$ , where  $i = 1, 2, \dots, M$ . The system can detect  $(2N-1)$  directions which correspond to  $DE_1 - DE_M$  as  $-(N-1)\Delta t, -(N-2)\Delta t, \dots, 0, \Delta t, \dots, (N-1)\Delta t$ .

Detecting signals from broadside requires  $DE_1 - DE_M = 0$ . In this case, the system needs  $M$  identical delays of  $0\Delta t$ . For  $DE_1 - DE_M = \pm\Delta t$ , half of the antenna elements need to be fed delays  $0\Delta t$ , and the other half need  $\Delta t$ . For these three directions, the system therefore requires  $M$  delays  $0\Delta t$  and  $[M/2]$  delays  $\Delta t$ , where  $[M/2]$  is the least integer that is not less than  $M/2$ . For the same reason, for  $DE_1 - DE_M = \pm(k-1)\Delta t$ , the system needs  $[M/k]$  delays  $(k-1)\Delta t$ . For  $M = N$  the total number of delay lines the system needs is  $M + [M/2] + [M/3] + \dots + [M/k] + \dots + 1$ , which equals, approximately,  $M \ln M$  for large  $M$ . For  $N > M$ , when  $|DE_1 - DE_M| < M\Delta t$ , it is the same situation as the  $N = M$ . When  $|DE_1 - DE_M| \geq M\Delta t$ , there are no identical delays needed for the same direction. In this case, the system only needs one delay line for each delay from  $M\Delta t$  to  $(N-1)\Delta t$ . Therefore, the total number of delay lines is  $N - M + M \ln M$ .

#### Appendix 4: Number of Delay Lines Needed in the Antenna in Fig. 2.3(b)

The definitions for  $M$ ,  $N$  and requirements for the delay feed are the same as in Appendix 3. We define the delays associated with antenna elements in Fig. 2.3(b) as “pre-delays”, and the delays associated with each receiver as “post-delays”. If one receiver receives a signal from one antenna element, the effective delay is the sum of the corresponding pre- and post-delays. An array receiver structure requires that for a given pre-delay arrangement for antenna elements 1 to  $M$ , and for any desired signal receiving direction, there always exist  $M$  receivers to receive signals from their respective antenna elements so that the effective delays meet the requirements for that particular direction.

Assume a receiver structure as the following: let  $N = jM$ , where  $j$  is a positive integer. The pre-delays for antenna elements from 1 to  $M$  are:

$$\begin{array}{l}
 \text{elements:} \quad 1 \quad 2 \quad \dots \quad [M/2] \quad [M/2] + 1 \quad \dots \quad M \\
 \text{pre-delays:} \quad 0 \quad j + 1 \quad \dots \quad ([M/2] - 1)(j + 1) \quad [(M - 1)/2](j + 1) + 1 \quad \dots \quad 1. \\
 \text{(unit: } \Delta t)
 \end{array}$$

From antenna element 1 to  $[M/2]$ , and from  $[M/2] + 1$  to  $M$ , the pre-delays increase and decrease, respectively, with spacing  $(j + 1)\Delta t$ . Let  $[Y]$  be the least integer that is not less than  $Y$ . The available post-delays (in units of  $\Delta t$ ) are  $-(j+1)$ ,  $-j$ ,  $\dots$ ,  $-2$ ,  $-1$ ,  $0$ ,  $0$ ,  $1$ ,  $1$ ,  $\dots$ ,  $([M/2]-1)(j+1)$ ,  $([M/2]-1)(j+1)$ ,  $([M/2]-1)(j+1)+1$ ,  $([M/2]-1)(j+1)+2$ ,  $\dots$ ,  $(2j+1)[M/2]-(j+2)$ ,  $(2j+1)[M/2]-(j+1)$ . The total number of delays  $X$  is  $(3j+2)[M/2]-(j+1)$ . For  $M$  even,  $X = (1.5j + 1)M - (j + 1) < (1.5 + 1/j)N$ ; and for  $M$  odd,  $X = (1.5j + 1)M + 0.5j$ . So  $X$  is approximately equal to  $(1.5 + 1/j)N$  for either case. For each receiving direction, the effective delay for the element  $[M/2]$  is kept as the

constant  $(\lfloor M/2 \rfloor - 1)(j + 1)$ . Now we prove that the above structure can perform all the required detections.

(1) We call element 1 to  $\lfloor M/2 \rfloor$  as the first half, and  $\lfloor M/2 \rfloor + 1$  to  $M$  as the second half of the array. The delays for antenna elements 1 to  $M$  either increase or decrease monotonically, and element  $\lfloor M/2 \rfloor$  is the mid-point with the constant delay  $(\lfloor M/2 \rfloor - 1)(j + 1)\Delta t$ . Thus for each antenna direction, effective delays exceeding  $(\lfloor M/2 \rfloor - 1)(j + 1)\Delta t$  can only be used for the first or second half of the array. The largest post-delay needed is then  $\lfloor M/2 \rfloor j \Delta t + (\lfloor M/2 \rfloor - 1)(j + 1)\Delta t$ , which corresponds to the farthest angle away from broadside direction, where the delay difference between adjacent elements is  $j \Delta t$ .

(2) Now we prove that from element 1 to  $\lfloor M/2 \rfloor$ , for every receiving direction, the required post-delays are different, and the shortest required post-delay is zero. We know the required effective delays for element 1 to  $M$  either increase or decrease monotonically and as uniformly as possible. With  $N = jM$ , the largest delay difference required between adjacent antenna elements is  $j \Delta t$ . Here, the pre-delays for elements 1 to  $\lfloor M/2 \rfloor$  increase with equal difference  $(j + 1)\Delta t$ , which is greater than the largest difference required. For any receiving direction, whether the required effective delays increase or decrease monotonically, the post-delays fed to elements 1 to  $\lfloor M/2 \rfloor$  must decrease monotonically, with the delay difference between adjacent elements at least  $\Delta t$ . Thus, for each direction, no two post-delays for elements 1 to  $\lfloor M/2 \rfloor$  are the same. Since the post-delays for element  $\lfloor M/2 \rfloor$  are always kept at zero, the shortest post-delay required here is zero.

For the same reason, the post-delays fed to elements  $\lfloor M/2 \rfloor + 1$  to  $M$  must increase

monotonically, and among them no two can be the same for each direction. The shortest delay needed is for the element  $[M/2]+1$ , when its effective delay is  $j\Delta t$  shorter than that for the element  $[M/2]$ . This delay is  $-(j+1)\Delta t$  for  $M$  is even, and 0 for  $M$  is odd. ( The negative delay here is shorter than the length of the fiber which we define as zero delay, and does not actually correspond to negative length.)

(3) From the conclusion of (1) and (2), we know that all the post-delays (in units of  $\Delta t$ ) needed are:

I. from  $-(j+1)$  to  $-1$ , one for each;

II. from  $([M/2]-1)(j+1)$  to  $[M/2]j\Delta t + ([M/2] - 1)(j+1)\Delta t$ , one for each;

III from 0 to  $([M/2]-1)(j+1)-1$ , at most two for each.

Thus, the total number of post-delays, i.e. the total number of optical receivers needed is  $(3j+2)[M/2] - (j+1)$ , which is approximately equal to  $(1.5 + 1/j)N$ .

For  $j$  not an integer, we could make the arrangement for the pre-delays almost the same as the above while the difference between the adjacent antenna elements is  $([j]+1)\Delta t$ . Then due to the same reasoning, the total number of delay lines needed is approximately  $(3[j]+2)[M/2]$ .

## Appendix 5 Ridge Laser Fabrication

Here, we use  $\text{SiN}_x$  as the isolation dielectric material.

### 1. Sample cleaving and washing

Lap back side of the wafer and take off the indium.

TCE (hot stirring, 100-110 °C, 5min, twice)--ACE (5 min twice) --ISO (hot stirring, 100-110 °C, 5 min, twice)--blow dry—turgitol swab—D.I. water rinse--blow dry

### 2. Ridge etching (3, 5, or 10 mm pattern)

1) Deposition of 2000 Å silicon nitride using PECVD (Plasma Enhanced Chemical Vapor Deposition)

right chamber (PECVD chamber), first wipe chamber with ISO (beginning of the day), set standby temperature at 250 °C, run program DEPPREP.PRC & load sample and do sin250.prc (set deposition time at 8:30') or :

--- back etch (beginning of a day): purge  $\text{CF}_4$ , 900 mTorr, 200 W, 5 min

---flow  $\text{N}_2$  500 mTorr, 200 sccm, 1 min

---SINAP: 250 °C,  $\text{NH}_3$  @ 50 sccm 100 mTorr, 28 W, 30 sec

---flow  $\text{N}_2$  500 mTorr, 200 sccm, 1 min

---250 °C, 900 mTorr,  $\text{N}_2$  @ 120 sccm,  $\text{SiH}_4$ @120,  $\text{NH}_3$ @35, 20 W for 8'30"

---flow  $\text{N}_2$  500 mTorr, 200 sccm, 4 min

2) photolithography for ridge etching (using the nitride as mask)

prebaking 110 °C /10 min. to 1 hour or 5 min. hard bake on 250 °C hot plate( this is critical for P.R.'s adherence on nitride) or directly put the sample on the spinner right after the 250 °C deposition (in the later case, the sample has to be cooled down by blowing of a gas gun)

---spin on HMDS 4k rpm / 40s (adhesion promoter) --- AZ4210 4k rpm / 40s

---hard-baking 105 °C /3 min.

---align the mask for the ridge, the ridge should be perpendicular to the long axis of the oval defects, or do test piece to find out the proper ridge orientation;

exposure 3.7-3.8 s (making the ridge as the dark area , 5 mm, etc.)

---develop in 3.5:1 (water:AZ400) for 1-1.5 min.---check under a microscope

3) etch the nitride to make ridge mask (program ETCH2000.PRC)

O2 @50sccm, 100 mTorr, 100W for 1 min to clean up photo resist

---CF4O2 @ 50 sccm, 100 Torr, 55 W for 1'30" to etch off all nitride

---check under microscope to see if all nitride is gone (color)

---clean PR---dek-tak

4) dry-etch (InGaAs and InP) and selective etch InP to shape the ridge ( first use program ECHPREP.PRC to clean the chamber without the sample inside, then RIE 200W.PRC, left chamber, i.e. the RIE chamber). With this way, it is fast and the beginning of the ridge has a good shape. The RIE200W.PRC has the following procedures 1-8:

1. low vacuum, keep 1'30"

2. 50 mTorr, CH4 @ 4 sccm, H2 @ 28 sccm for 30"

3. keep step 2, power=200 W for certain time ( 3000 angstrom InP can be etched off within 5 minutes)

4. low vacuum for 20"

5. N2 purge, 500 mTorr for 30"

6. low vacuum for 20"

7. O2 @ 20 sccm, 35 mTorr for 30s

8. keep step 7, power=150 W for 3' (etch off some organic deposition during the InP etching) If the color changes from blue to yellow, then the process is done.

9. Using selective etch HCl : H<sub>3</sub>PO<sub>4</sub> (3:1) to get rid of the InP layer.<sup>1</sup>

5) Buffered oxide etch (10:1) to etch off the rest nitride (1 min for 300 Å) Dek-tak to make sure or use dry etch:

CF<sub>4</sub>O<sub>2</sub> @ 50 sccm, 100 Torr, 55 W for 1'30" o etch off all nitride.

### 3. Metal contact

**Using SiN<sub>x</sub> as isolation layer, and Photoresist as the way for planarization.**

- 1) deposition of 6000 Å of SiN<sub>x</sub> on top of the sample where the sample ridge is usually 1 to 1.2 mm.<sup>2</sup> (DEPPREP.PRC, then load sample and do 25' deposition using step 2.1).
- 2) put on HDMS, spin 4k/min, 40s.
- 3) put on AZ4210, spin from 0 to 4k/min, 40s. (this will give a more flat surface, for a 12,000 Å ridge, this step will bring the height different to 2,000-3,000 Å)
- 4) hard bake for 3 min.
- 5) O<sub>2</sub> plasma to etch away the photoresist on the top of the ridge.  
O<sub>2</sub> at 100 mTorr, 100W, 50 sccm for 6' then each time 30-40s (the time needed depends on the size of the wafer, width of the ridge, etc.). If it's done, the ridge will be clean and white seen from the microscope. Otherwise, there will be dot stripe on it. Try to etch additional time if it is still not clean. For one layer of photoresist, it is about 2 μm thick and need approximately 7-8 minutes to etch off. (etching rate: 3,000 Å/min)
- 6) etch off the SiN<sub>x</sub> on top of the ridge using CF<sub>4</sub> plasma. in RIE.
- 7) wash off the Photoresist with ACE-ISO.
- 8) photolithography for contact pad(100 μm pad width)

---

<sup>1</sup> Usually there is etch stop layer about 2000 Å above the I region. Otherwise, dry-etch is used to control the etching depth.

<sup>2</sup> If the ridge is higher, use thicker photoresist (like AZ 4330, or AZ 4610) to get better planarization.

prebaking---spin on---postbaking---toluene(5 min) ---exposure for contact pad,  
alignment to the ridge (keep the ridge toward one edge of the pad) ---develop---  
check the undercut under the microscope

7)making contact pad with angle deposition

dip in H<sub>2</sub>SO<sub>4</sub> (1:6) for 10 sec. to remove any possible oxidation layer (for P  
type contact preparation)

----put in the E-beam machine with an angle holder by Mung, the wider area of  
the pad divided by the ridge should face down (facing the evaporation), rotate  
the holder while evaporating, get 200 Å Ti, 500 Å Pt, 3000 Å gold

---lift off in ACE--ISO---O<sub>2</sub> plasma 300 mTorr, 100 W, 4 min.---- checking

**4. Device isolation (10 mm wide, and etch to the n region)<sup>3</sup>**

If we need to pack one device each time, or do not care too much about the  
leakage current, this step can be skipped.

1) photolithography for isolation (this time use the light field of 10 mm stripes)

2) etch off the SiN<sub>x</sub> using CF<sub>4</sub> in PECVD (see 2.3 for the detail---check the  
profile under the microscope

3) add 2 drops of H<sub>2</sub>O<sub>2</sub> in old HBr solution for total 10-20 min---check under the  
microscope to see the width of undercut to make sure the right depth is  
reached. (If the HBr solution is old, then the etching time should be  
shortened.)

4) wash off the P.R.: ACE, ISO--O<sub>2</sub> plasma

**5. Back contact**

1) Load the sample for back lapping

---make a small piece of Mala with a hole which can accommodate the sample

---

<sup>3</sup> Sometimes, this step is not absolutely necessary.

- at 200C, put black wax on a glass cover, put the Mala on top of it,  
---put the sample upside down in the hole of the Mala, get down the glass cover from oven, and press the Mala and sample to drive off gas and make them flat  
---put a round thick glass at 140°C and put white wax on it  
---put the glass cover on the thick glass, get it down and make the thin glass flat
- 2) lap the sample to 4-6 mil (1 mil=1 thousandth inch=25.4 mm)
- 3) clean the sample
- get the sample down from the thick cover---get off the Mala--TCE to get off the wax on the glass cover--TCE, ACE, ISO, DI, turgitol, DI to clean the sample together with the glass cover---dip the sample in HCl (6:1) for 6 sec, rinse it and blow dry
- 4) put back contact in E-beam.
- Ge: Au: Ni: Au ( 270, 450, 215, 1200 Å)
- 5) get the sample out of the black wax on a hot plate, clean the sample with TCE-ACE-ISO-turgitol-water.
- 6) n-contact annealing
- Check the annealing controller state (make sure the 60 Hz) - load the sample - turn on the foaming gas and the cooling gas - execute the "NCON.RSP" program - wait until the temperature drop down to 70 C.

## 6. Sample cleaving and testing

Notes: in this processing recipe, photoresist is used for planarization. But we can also directly use polyimide as isolation layer and at the same time as the planarization layer.

## Appendix 6 The Processing for Laser-Electroabsorptive Modulator

### The masks

For making of Laser-Electroabsorptive modulators, we need 10 masks, they are saved in Tsingdao\ocm\xu\toad\ea-mod\las-mod.dwg.

The layers are:

Layer name	Field type
active-area	clear
act-protect	clear
waveguide	clear
mod-protect	clear
iso-coat	clear
isolation	dark
side-hole	dark
laser-cont	dark
mod-cont	dark
HR-coat	dark
whole-active	dark & clear (two sets)

### The Processing Steps

1. Pattern the active area (mask "ACTIVE-AREA"):

1) Deposit 2,000 Å SiN<sub>x</sub>.

2) Photolithography to pattern the SiN<sub>x</sub>.

The patten is: (maybe tilted for SOA, see the diagram for processing the active region.)

3) Etch the silicon nitrite not covered by the photoresist.

4) wash-off the photoresist.

5) dry etching (CH<sub>4</sub>/H<sub>2</sub>) down to 1000 Å above of the n<sup>+</sup> InGaAs.

**(If a good facet is needed, use high power to get a better directivity of the plasma. A wet etched test piece is required.)**

6) strip off SiN<sub>x</sub>. (Maybe dry-etching to keep the good facet.)

2 Use "ACT-PROTECT" as the mask for photolithography to protect the whole area A (the active area), then wet etch the InP on top of the InGaAs using wet etch. Take off the P.R. and SiNx.

3 Take off the photoresist and SiNx. Grow a 4000 Å layer of SiNx, transfer the mask "WAVEGUIDE" to SiNx shape the ridge. Use wet etch of Citric Acid: H<sub>2</sub>O<sub>2</sub> first to take off the InGaAs beside the waveguide, then HCl: H<sub>3</sub>PO<sub>4</sub> to take off InP.

### 3. Making the waveguide structure

- 1) Ridge pattern, 4000 Å SiNx, pattern the SiNx as the waveguide ("WAVEGUIDE" mask) and protect the etched facet of lasers.
- 2) Citric acid wet etch InGaAs on region 2 layer 1, layer 5 on region 3.
- 3) HCl: H<sub>2</sub>SO<sub>4</sub> (3:1) wet etch layer 2 (p-InP) on region 2, and layer 6 (n-InP) on region 3, layer 4 on region 1.

After this, area 1 is on top of InGaAs, the 5<sup>th</sup> layer; area 2 is on top of the 3<sup>rd</sup>, I layer; the surface of area 3 is the 7<sup>th</sup> layer, I layer. So the ridges are formed well.

### 4. Put down the isolation layer for metal contact.

- 1) without taking off the old SiNx, grow about 6,000 Å SiNx.
- 2) with "Act-protect" mask, using photo-resist to protect the active area and etch off about 2000 Å SiNx in the modulator area.

### 5. Make the ridge contact for laser ridge:

- 1) Spin on 4210 photoresist 0-4K spin twice (or 4330 once).
- 2) Deposit SiO about 1000 Å using E-beam.
- 3) photolithography "MOD-PROTECT" for covering the modulator region.
- 4) CF<sub>4</sub> dry etching the SiO. (100 mTorr, 50 sccm, 100 W)
- 5) O<sub>2</sub> plasma to etch photoresist to expose the top ridge.
- 6) SiNx etch
- 7) ACE to lift off the SiO on lower ridge and wash off photoresist.
- 8) P metal contact for the top region.

### 6. Make the ridge contact for lower ridge (modulator) and the grounding contact for laser:

- 1) Spin on 4210 photoresist 0-4K spin twice.
- 2) Deposit SiO about 2000 Å using E-beam.
- 3) photolithography for covering the active region. (mask "ACT-PROTECT")
- 4) CF<sub>4</sub> dry etching the SiO.
- 5) O<sub>2</sub> plasma to etch photoresist to expose the bottom ridge.
- 6) SiNx etch
- 7) wet InP etch and stop at InGaAs.
- 8) ACE to lift off the SiO on top ridge and wash off photoresist.

- 9) Dig a hole on nitrite beside the active ridge for N contact of the active region. (mask "SIDE-HOLE")
- 10) N metal contact "MOD-CONT".

7. Make isolations between laser area and modulator area.

- 1) Dry etch to take off SiN<sub>x</sub> not covered by metal, then deposit another 2000 Å SiN<sub>x</sub>  
(this step can totally ignored if the device requirement is not so critical)
- 2) Use "ISOLATION" mask to open a hole on SiN<sub>x</sub> between modulators and lasers.
- 3) Diffusion to make isolation (p-type dopant to isolate the heavily doped N layers)
- 4) Dry-etch to take off SiN<sub>x</sub>

8. High reflection coating for half-etched facet.

- 1) 1000 Å SiN<sub>x</sub>.
- 2) Pattern SiN<sub>x</sub> with P.R. and mask "ISO-COAT" around the etched facet.
- 3) Spin on P.R. and pattern it with "HR-COAT".
- 4) Deposit 500 Å gold.
- 5) lift-off

9. Lapping back side and make back P contact (Ti:Pt:Au).

## Appendix 7 The processing steps of twin-guide TOAD

**The structure of the material: (Fig. A2)**

**The processing procedure:**

1. Pattern the active area:

- 1) Deposit 2,000 Å SiN<sub>x</sub>.
- 2) Photolithography to pattern the SiN<sub>x</sub>.  
The patten is: (maybe tilted for SOA, see the diagram for processing the active region.)
- 3) Etch the silicon nitrite not covered by the photoresist.
- 4) wash-off the photoresist.
- 5) dry etching (CH<sub>4</sub>/H<sub>2</sub>) down to top of the n<sup>+</sup> InGaAs.  
**(If a good facet is needed, use high power to get a better directivity of the plasma. A wet etched test piece is required.)**
- 6) strip off SiN<sub>x</sub>. (Maybe dry-etching to keep the good facet.)

2. Making the waveguide structure

- 1) Ridge pattern, 3000 Å SiN<sub>x</sub>, pattern the SiN<sub>x</sub> as the waveguide.
- 2) Citric acid wet etch InGaAs on region A, layer 1.
- 3) Hcl: H<sub>2</sub>SO<sub>4</sub> (3:1) wet etch layer 2 (p-InP) on region A, and layer 4 (n-InP) on region B.
- 4) Dry-etch layer 3 on region A and layer 5 and part of 6 on region B.
- 5) Hcl: H<sub>2</sub>SO<sub>4</sub> (3:1) wet etch layer 4 on region A, and layer 6 on region B.  
(here we wish the layer 6 including the active layer and several hundred nm  
cladding layer which is also i)
- 6) Strip SiN<sub>x</sub>. **(We may keep this SiN<sub>x</sub> to make the following planarization step easier.)**

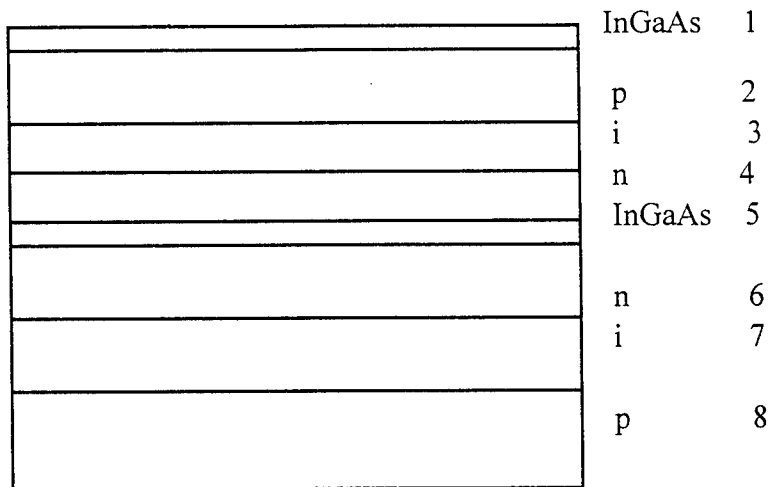
Final results see the ridge making processing steps.

3 Isolations using ion implantation or diffusion.

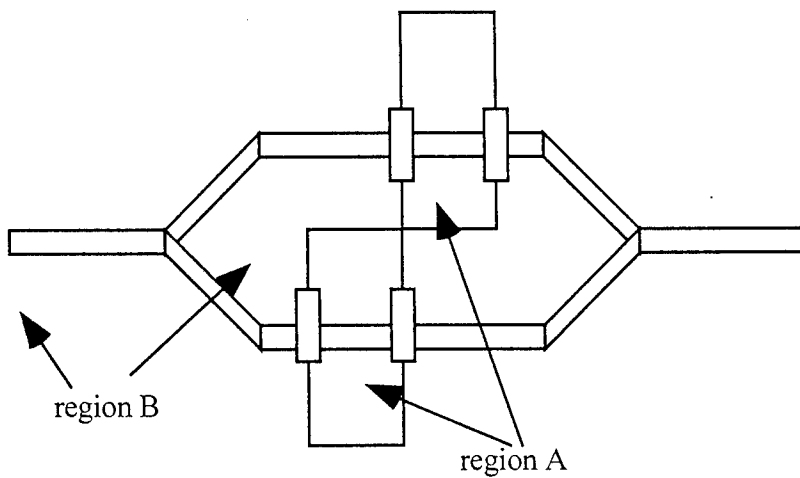
4. Deposit thick SiN<sub>x</sub> (4000 Å) for contact isolation. (Thick enough to cover both the I region.)

5. Make the ridge contact for higher ridge:

- 1) Spin on 4210 photoresist 0-4K spin twice.
- 2) Deposit SiO about 2000 Å using E-beam.



(a) Schematic diagram of the material structure for TG TOAD.



(b) Schematic processing layout for TG TOAD.

Fig. A2 The TG TOAD processing diagram.

- 3) photolithography for covering the lower ridge region.
- 4) CF<sub>4</sub> dry etching the SiO. (100 mTorr, 50 sccm, 100 W)
- 5) O<sub>2</sub> plasma to etch photoresist to expose the top ridge.
- 6) SiN<sub>x</sub> etch
- 7) ACE to lift off the SiO on lower ridge and wash off photoresist.
- 8) P metal contact for the top region.

6. Make the ridge contact for lower ridge and the grounding contact for SOA:

- 1) Spin on 4210 photoresist 0-4K spin twice.
- 2) Deposit SiO about 2000 Å using E-beam.
- 3) photolithography for covering the active region.
- 4) CF<sub>4</sub> dry etching the SiO.
- 5) O<sub>2</sub> plasma to etch photoresist to expose the bottom ridge.
- 6) SiN<sub>x</sub> etch
- 7) wet InP etch and stop at InGaAs.
- 8) ACE to lift off the SiO on top ridge and wash off photoresist.
- 9) Dig a hole on nitride beside the active ridge for N contact of the active region.
- 10) N metal contact

7. take off nitride on the area not covered by metal.

8. Maybe facet etching (dry-etching, 35ARIE.PRC, higher RF power, better directivity.)

9. Lapping back side and make back P contact (Ti:Pt:Au).

## TABLE OF CONTENTS

### APPENDICES

P.M. Freitag and S. R. Forrest, "A Coherent Optically Controlled Phased Array Antenna System", *Microwave and Guided Wave Letters*, Vol. 3, No. 9, pp. 293-295, September 1993.

Ligeng Xu and Stephen R. Forrest, "Optoelectronic Signal Processing for Phased-Array Antennas IV", *Proceedings SPIE - The International Society of Optical Engineering* Vol. 2155, pp. 241-255, January 26-27, 1994 Los Angeles, CA.

Ligeng Xu, Robert Taylor, and Stephen R. Forrest, "The Use of Optically Coherent Detection Techniques for True-Time Delay Phased Array and Systems", *Journal of Lightwave Technology*, Vol. 13, No. 8, pp. 1663-1678, August 1995.

Ligeng Xu, Robert Taylor, and Stephen R. Forrest, "True Time-Delay Phased-Array Antenna Feed System Based on Optical Heterodyne Techniques", *Photonics Technology Letters*, Vol. 8, No. 1, pp. 160-162, January 1996.

Robert Taylor, Vincent Poor, and Stephen R. Forrest, "Phase Noise in Coherent Analog AM-WIRNA Optical Links.

# A Coherent Optically Controlled Phased Array Antenna System

P. M. Freitag and S. R. Forrest

**Abstract**—A true-time delay, optically controlled phased array antenna system whereby a large number (100–2500) of antenna elements can receive a series of microwave delays via use of a coherent optical carrier signal is described. Both transmit and receive antenna arrays are described, and the signal-to-noise ratio for a 128 channel system is calculated to be ~40 dB with an optical link loss of only ~3 dB for a 1 GHz instantaneous bandwidth at a wavelength of  $\lambda = 1.55 \mu\text{m}$ . It is shown that the use of coherent optically controlled phased array antennas provide improved controllability and immunity from noise and system losses over other architectures currently being investigated.

## I. INTRODUCTION

OPTICALLY controlled phased antenna arrays are currently hampered by the extreme complexity required in efficiently transmitting several hundred microwave delays from the controller to the antenna array. These difficulties are compounded by the demands of modern phased array systems including extremely high bandwidth broadcast frequencies (ranging from 20–60 GHz requiring up to 1-GHz instantaneous bandwidth per channel), stringent requirements on signal-to-noise and dynamic range, clutter cancellation, and the need for null steering and generating multiple, squint-free beams at different frequencies [1]. Most architectures distribute a series of time or phase delays to the antenna network [1], [2] via an optical switching matrix followed by amplifiers which compensate for loss (sometimes approaching 100 dB in large scale arrays). One difficulty encountered by this architecture is that all fibers which transport the microwave/optical signals from the input to antenna terminals must be of the same length so as not to introduce extraneous delays, or noise. Hence, these architectures have been proven to be limited by losses, they are difficult to implement, bulky, and costly. We describe a novel architecture based on the coherent optical transmission of signals from input to antenna array, and vice versa. The system is based on coherent, multichannel broadband transmission networks which have been investigated for applications to telecommunications. A 128-element system can have a signal-to-noise ratio (S/N) ratio as high as ~40 dB with an optical link loss of only ~3 dB at a wavelength of  $\lambda = 1.55 \mu\text{m}$  and an instantaneous bandwidth of 1 GHz.

Fig. 1 is a schematic diagram of the transmitter. In an intensity modulated scheme, the microwave signal at frequency

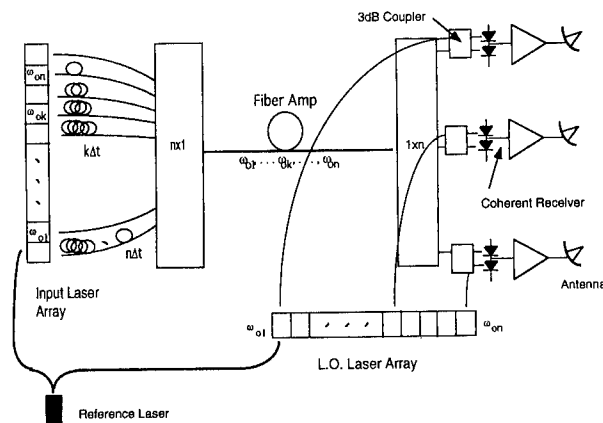


Fig. 1. Schematic diagram of a coherent phased array transmitter antenna.

$\omega_\mu/2\pi$  modulates the output of the wavelength-tunable laser array to generate a signal,  $A_\mu \sin \omega_\mu t$ . The signal which is delayed by  $k$  time increments,  $\Delta t$ , is transmitted by a laser tuned to emit at optical frequency,  $\omega_{ok}$ . Hence, the signal delayed by  $k\Delta t$  is given by (ignoring quadrature terms):  $A_\mu \sin[\omega_\mu(t + k\Delta t)] \sin \omega_{ok}t$ . This signal, along with the  $n - 1$  other tunable delays, are then combined onto the single transmission fiber. Essentially, a “look-up” table is created that associates  $n$  optical frequencies with  $n$  delays of length  $k\Delta t$ . The signals are combined using couplers with optical amplifiers which compensate for combiner losses and prevent degradation of S/N. Either erbium doped fiber amplifiers (EDFA’s) or semiconductor optical amplifiers (SOA’s) can be used in this application. Advantages of the EDFA are a higher S/N than for SOA’s, whereas SOA’s offer a higher degree of device integration. Here, we examine the EDFA approach.

After transmission on the fiber, the signals are distributed to the coherent receivers using an  $n \times 1$  splitter. Again, optical amplifiers compensate for splitter loss and prevent undue S/N degradation. At the antenna end, each of the  $n$  optical signals are incident on  $n$  receivers, along with  $n$  LO signals that are tuned to provide receiver 1 with frequency  $\omega_{o1}$ , receiver 2 with  $\omega_{o2}$ , etc. Given that the  $k$ th LO is at  $B_k \sin(\omega_{ok}t + \phi_k)$ , then the signal at the output of the  $k$ th receiver is proportional to:  $A_\mu B_k G_k \cos \phi_k \sin[\omega_\mu(t + k\Delta t)]/2$ , where  $G_k$  is the product of all the gains and losses in the link. This signal is then delivered to the  $k$ th antenna at the RF frequency (typically 20-60 GHz) by frequency “upshifting” the signal. To sweep the beam, the input laser array (or, alternatively, the LO array) frequencies are changed to create

Manuscript received April 1, 1993.

The authors are with the Advanced Technology Center for Photonics and Optoelectronic Materials (ATC/POEM), Department of Electrical Engineering, Princeton University, Princeton, NJ 08544.

IEEE Log Number 9211323.

TABLE I  
DATA FOR EDFA NETWORK

Component	Optical Loss (dB)	Excess Loss (dB)*	Optical Gain (dB)	Noise Figure (dB)	Optical Signal Power Relative to Input Signal (dB)
16 × 1 Combiner Loss ( $L_{c1}$ )	12	0.2			-12.2
EDFA ( $G_{a1}, F_{a1}$ )			21.2	4	9
8 × 1 Combiner Loss ( $L_{c2}$ )	9	0.2			-0.2
Fiber Loss ( $L_c2$ )	1				-1.2
1 × 8 Combiner Loss ( $L_{c3}$ )	9	0.2			-0.2
EDFA ( $G_{a3}, F_{a3}$ )			10.2	4	9
1 × 16 Loss ( $L_{c4}$ )	12	0.2			-3.2

\*Losses are taken to be 0.1 dB for each splice connection.

a new correspondence between a delay and an output antenna. Phase or frequency modulation can alternatively be employed to encode the microwave signal onto the optical carrier.

The signal is proportional to the LO strength,  $B_k$ . Typically, this can be as high as 10 mW at  $\lambda = 1.55\mu\text{m}$ , thus providing considerable gain at the antenna end. Both microwave amplifier and LO gain can be tuned at each antenna element to arbitrarily "shape" the beam. Frequency reference is provided to each tunable laser in the array by one of several techniques. For heterodyne detection, the receiver can tune from the IF in a frequency-locked loop [3]. Another means for providing simultaneous external reference to all  $n$  channels is to use a mode-locked laser which generates a "comb" [4] of equally spaced Fourier-component frequencies. This comb injection-locks the individual lasers which are roughly "current-tuned" to a particular frequency. Injection locking a continuously current-tunable laser using a comb of frequencies thereby changes the linear relationship between tuning current and wavelength into a "stepwise" laser output spectrum, with steps at the channel frequencies. Phase-locking using a phase-diversity receiver or a phase modulator, is needed to maintain a constant amplitude via the  $\cos \phi_k$  term.

This system requires continuously frequency tunable laser arrays [5]. Using present technology, up to nearly 100 Å tuning has been demonstrated at  $\lambda = 1.55\mu\text{m}$  using three-section DFB lasers [6]. Given that  $1 \text{ Å} = 12 \text{ GHz}$  at  $\lambda = 1.55\mu\text{m}$ , and that each channel can occupy  $a \leq 1 \text{ GHz}$  instantaneous bandwidth (BW), this implies  $\sim 100$  channels occupying 1.2-THz bandwidth can be accommodated. Here, the interchannel spacing must exceed the BW in analog systems by  $\sim 3 - 5$  times to minimize interchannel and image channel interference [7]. It will be shown elsewhere that the interchannel separation is limited by the phase noise and linewidth of the semiconductor laser, given that the channel bandwidth occupied by a  $\sim 1 \mu\text{s}$  radar pulse is very small.

To achieve a high S/N, combiners/splitters with EDFA's are implemented as follows: The  $n$  signals are combined by  $m$ ,  $(n/m + 1) \times 1$  passive couplers followed by  $m$  EDFA's, with  $n$  being the number of delays. The use of multiple, low gain coupler stages minimizes spontaneous emission noise common in systems which combine high loss and high gain in only a few amplifier stages. Each combiner merges  $n/m$  signals along with a pump signal for an EDFA [8]. After

amplification, the signals are combined by an  $m \times 1$  passive coupler and transmitted along the fiber transmission line. An EDFA is also used on the transmission line to further improve signal level. Similar to the combiner, the signals are split by a  $1 \times (m + 1)$  passive splitter, amplified by  $m$  EDFA's, and then further split by  $m$   $1 \times (n/m)$  passive splitters.

The system signal-to-noise ratio,  $(S/N)_s$ , and loss budget are calculated assuming that the signals are transmitted at a channel frequency of  $1.55 \mu\text{m}$  with  $\text{BW} = 1 \text{ GHz}$ , and with 5km between terminals.  $(S/N)_s$  is given by  $(1/F)(S/N)_{\text{trans}}$ , where the laser transmitter RIN at 1 GHz is  $(S/N)_{\text{trans}} = \sim 70 \text{ dB}$  [9] and  $F$ , the noise figure, is found using [10]:

$$F = L_{c1}F_{a1} + \{L_{c1}/G_{a1}\}\{L_{c2}F_{a2} - 1\} + \dots \\ + \{L_{c1}L_{c2} \dots L_{cM-1}/G_{a1}G_{a2} \dots G_{aM-1}\} \\ \times \{L_{cM}F_{aM} - 1\}.$$

Here,  $L_{ci}$  is the loss of the  $i$ th stage,  $F_{ai}$  is the noise figure of the  $i$ -th amplifier, and  $G_{ai}$  is the gain of the  $i$ th channel. Table I gives performance data for the main components of the system for a 128-channel link with  $n = 128$  and  $m = 8$ . The optical gain and output power for an EDFA can be as large as  $\sim 22 \text{ dB}$  and  $18.5 \text{ dBm}$ , respectively, and the noise figure is  $4 \text{ dB}$  [11]. The overall noise figure of the EDFA implementation is  $\sim 30 \text{ dB}$  and the  $(S/N)_s = 70 \text{ dB} - 30 \text{ dB} = \sim 40 \text{ dB}$ . From laser transmitter to the optical receiver, the system has  $\sim 3 \text{ dB}$  of optical loss. Additionally, the gain of the EDFA is relatively flat between  $1.530\mu\text{m}$  and  $1.560\mu\text{m}$  [11]. Therefore, the  $(S/N)_s$  performance for all channels of a WDM system is expected to be  $\sim 40 \text{ dB}$ .

The spectral bandwidth of an EDFA is  $> 0.1 \mu\text{m}$ . Thus, to further extend the number of channels in a multiple beam or large array system, a wavelength multiplexed approach such as that depicted in Fig. 2 is employed. Each  $100\text{-Å}$  subarray is combined onto the single carrier fiber using gratings or filters. Given  $\text{BW} = 1 \text{ GHz}$ , and a *very conservative* channel separation of  $5 \times \text{BW}$  to eliminate undue interchannel interference in a heterodyne system where  $\omega_{1.F.}/2\pi = \text{BW}$ , this 12-THz system has a very large channel capacity of 2500 channels [2]. Finally, in Fig. 3, we show a schematic of the receiver antenna. Comparing this with Fig. 1, similar components and techniques are used for both transmit and receive.

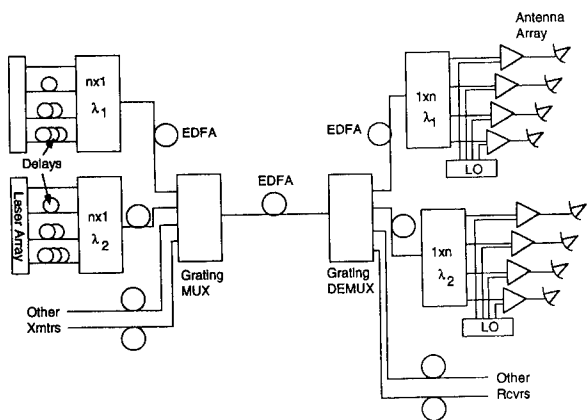


Fig. 2. Wavelength multiplexed, very broad-band phased array antenna.

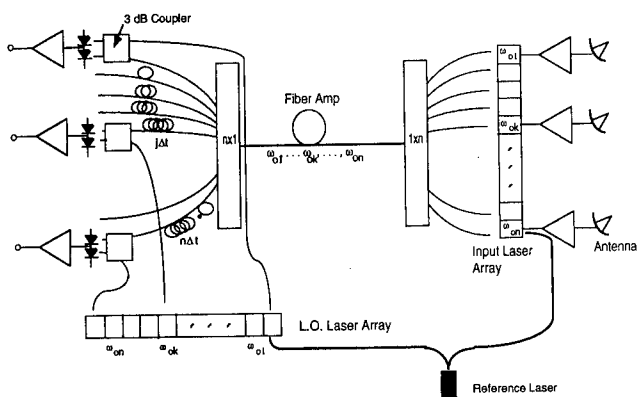


Fig. 3. Schematic diagram of a coherent phased array receiver antenna.

In summary, the coherent optically controlled phased array: 1) accommodates  $\sim 100$  channels in a single fiber. With the addition of a multi-wavelength system, over 2500 channels can be accommodated in this single fiber architecture. 2) Can be used for null steering, multiple beam formation, and squint-free multiple frequency operation. This flexibility results from the high gain due to a combination optical and electronic amplification, and LO gain, and the rapid tunability of the gain elements. The slowest tunable element is the LO, where restabilization of frequency must occur on a time scale somewhat shorter than the beam scan time ( $\sim$  milliseconds). 3) Employs components and techniques already

developed for multichannel coherent communications, taking advantage of progress in tunable lasers, optical amplifiers, and coherent phase and polarization diversity receivers. However, practical realizations would need to incorporate a high degree of integration of both lasers and receivers. Potentially, a 128 element array can deliver very high power signals to the antenna with  $\sim 3$  dB of optical loss and an S/N of  $\sim 40$  dB for  $BW = 1$  GHz at  $\lambda = 1.55 \mu\text{m}$ .

ACKNOWLEDGMENT

The authors thank B. Hendrickson (RADC), I. Newberg, and H. Yen from Hughes Research Laboratories, and H. Fetterman (UCLA) for many helpful discussions. They also thank RADC, DARPA, and the National Center for Integrated Photonic Technology for their support.

REFERENCES

- [1] W. Ng, A. A. Walston, G. L. Tangonan, J. J. Lee, I. L. Newberg, and N. Bernstein, "The first demonstration of an optically steered microwave phased array antenna using true-time-delay," *IEEE J. Lightwave Technol.*, vol. 9, p. 1124, 1991.
- [2] C. Hemmi and C. Takle, "Optically controlled phased array beamforming using time delay," in *Proc. of DOD Fiber Optics Conf. '92*, McLean, VA, 1992, p. 60.
- [3] A. W. Davis, M. J. Pettitt, J. P. King, and S. Wright, "Phase diversity techniques for coherent optical receivers," *IEEE J. Lightwave Technol.*, vol. 5, p. 561, 1987.
- [4] D. Dunkin, G. Hill, and W. Stallard, "Frequency locking of external cavity semiconductor lasers using an optical comb generator," *Electron. Lett.*, vol. 22, 388, 1986.
- [5] L. A. Wang, Y. H. Lo, A. S. Gozdz, P. S. D. Lin, M. Z. Iqbal, and R. Bhat, "Integrated four-wavelength DFB laser array with 10 Gb/s speed and 5 nm continuous tuning range," *IEEE Photonics Technol. Lett.*, vol. 4, p. 318, 1992.
- [6] M. Oberg, S. Nilsson, J. Wallin, D. Karlsson-Varga, L. Backbom, and G. Landgren, "Wide continuous wavelength tuning of a narrow linewidth DBR laser," *IEEE Photonics Technol. Lett.*, vol. 4, p. 230, 1992.
- [7] L. G. Kazovsky, "Multichannel coherent optical communications systems," *J. Lightwave Technol.*, vol. 5, p. 1095, 1987.
- [8] A. Willner, A. Saleh, H. Presby, D. DiGiovanni, and C. Edwards, "Star couplers with gain using multiple erbium-doped fibers pumped with a single laser," *IEEE Photonics Technol. Lett.*, vol. 3, p. 250, 1991.
- [9] M. Yano, Y. Kotaki, H. Ishikawa, S. Yamakoshi, H. Imai, T. Chikama, and T. Touge, "Extremely low-noise facet-reflectivity-controlled InGaAsP distributed-feedback lasers," *IEEE J. Lightwave Technol.*, vol. 4, p. 1454, 1986.
- [10] A. Carlson, *Communication Systems*, second ed. New York: McGraw-Hill, 1975.
- [11] S. Grubb, W. Humer, R. Cannon, T. Windhorn, S. Vendetta, K. Sweeney, P. Leilabady, W. Barnes, K. Jedrzejewski, and J. Townsend, "+21 dBm erbium power amplifier pumped by a diode-pumped Nd:YAG Laser," *IEEE Photonics Technol. Lett.*, vol. 4, p. 553, 1992.

# PROCEEDINGS REPRINT

 SPIE—The International Society for Optical Engineering

*Reprinted from*

## ***Optoelectronic Signal Processing for Phased-Array Antennas IV***

26–27 January 1994  
Los Angeles, California



**Volume 2155**

©1994 by the Society of Photo-Optical Instrumentation Engineers  
Box 10, Bellingham, Washington 98227 USA. Telephone 206/676-3290.

# ANALYSIS OF A COHERENT OPTICALLY CONTROLLED PHASED ARRAY ANTENNA SYSTEM

Ligeng Xu and Stephen R. Forrest  
Advanced Technology Center for Photonics and Optoelectronic Materials(ATC/POEM)  
Department of Electrical Engineering  
Princeton University  
Princeton, NJ 08544

## ABSTRACT

We analyze a true-time delay, optically controlled phased array antenna system whereby beam forming is accomplished using a large number of antenna elements that can receive any of several different microwave true-time-delays via use of coherent optical carriers through a single transmission fiber. We calculate the signal-to-noise ratio (SNR) and the signal-to-interchannel interference ratio (SIR) of one channel for various modulation-demodulation schemes (i.e., AM-heterodyne, FM). We show that for AM modulation, with a bandwidth of 1 MHz, a transmitter power of -10 dBm and a laser linewidth of 1 MHz, we can obtain dynamic a range (DR) of  $\cong 46$  dB, with a channel separation six times of that of the microwave oscillation frequency ( $f_m$ ). For the FM scheme, DR  $\cong 60$  dB for a laser linewidth of 1 MHz, a FM modulation index of 2 and a channel spacing of  $12f_m$ . It is found that coherent optically controlled phased array antennas provide improved controllability, and can have the SNR and DR that meet the stringent requirements of high resolution microwave antenna systems.

## 1. INTRODUCTION

There has been an upsurge of interest in the use of optical fiber for transmission of microwave signals for phased array antenna systems<sup>1-3</sup>. This is due to several advantages of using microwave fiber optic links instead of electronically controlled steering: (a) Fiber optic links have wide instantaneous bandwidth, thus the beam can be steered without "squint" even if the system is rapidly switched between several different frequencies; (b) signals are transmitted through fibers and thus are immune to electromagnetic interference; and (c) fibers are lightweight and thus the systems are suitable for use in both aircraft and satellites.

In order to steer the beam to different directions, the system should have the ability to feed different phase delays ( $N$ ) to many remote antenna elements ( $M$ ). For conventional intensity-modulation/direct-detection (IM/DD) systems<sup>1</sup>, the number of laser diodes needed is therefore proportional to  $M \times N$ , which can be prohibitively large for some requirements. Here we analyze the multichannel broadband coherent optical system proposed by Freitag and Forrest<sup>3</sup> which can feed any of  $N$  true time delays to  $M$  remote antenna elements, which uses only  $(M+N)$  laser diodes interconnected to a single transmission line. It is obvious that such a system architecture is relatively more expandable to large scale antenna implementations.

Fig. 1 is a schematic diagram of a coherent optically controlled phased array transmitter. Each laser in the transmitter laser array has a different fixed central frequency,  $f_{ok}$ , where  $k$  indicates the  $k$ th laser in the array. The same microwave signal modulates each laser in the array, which in turn is coupled to a different delay fiber. The several delayed signals are combined in a single fiber using optical couplers. Before combination, the delays associated with  $k$ th laser is  $ck\Delta t$ , where  $c$  is the velocity of the optical signal, and  $\Delta t$  is a delay increment. Thus the signals with different time delays are transmitted through a single fiber to the antenna array, where the signals are distributed to the coherent receivers using a  $1 \times M$  splitter (two levels of splitters are shown in Fig. 1). Each of the  $N$  optical signals are incident on  $M$  coherent receivers, along with  $M$  local oscillator (LO) laser signals which are tuned to provide  $k$ th receiver with frequency  $f_{lok}$ . By tuning  $f_{lok}$  to different frequencies, signals modulated on a particular optical carrier are coherently detected. The photodetected signals (i.e., the intermediate frequency, or the IF) are demodulated

electronically to obtain the original, time-delayed microwave signals which are subsequently fed to the antennas. With LO lasers associated with each antenna element tuned to different frequencies, various time-delay combinations are fed to the array elements, thereby steering the beam to different angles.

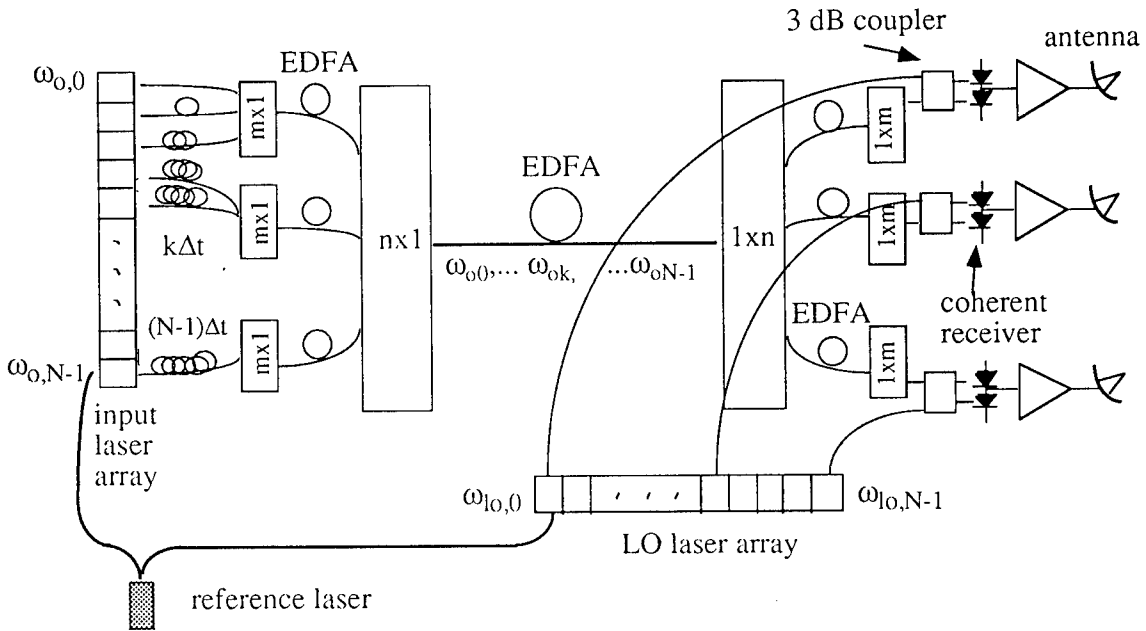


Fig. 1 Transmitter of coherent optically controlled phased array antenna

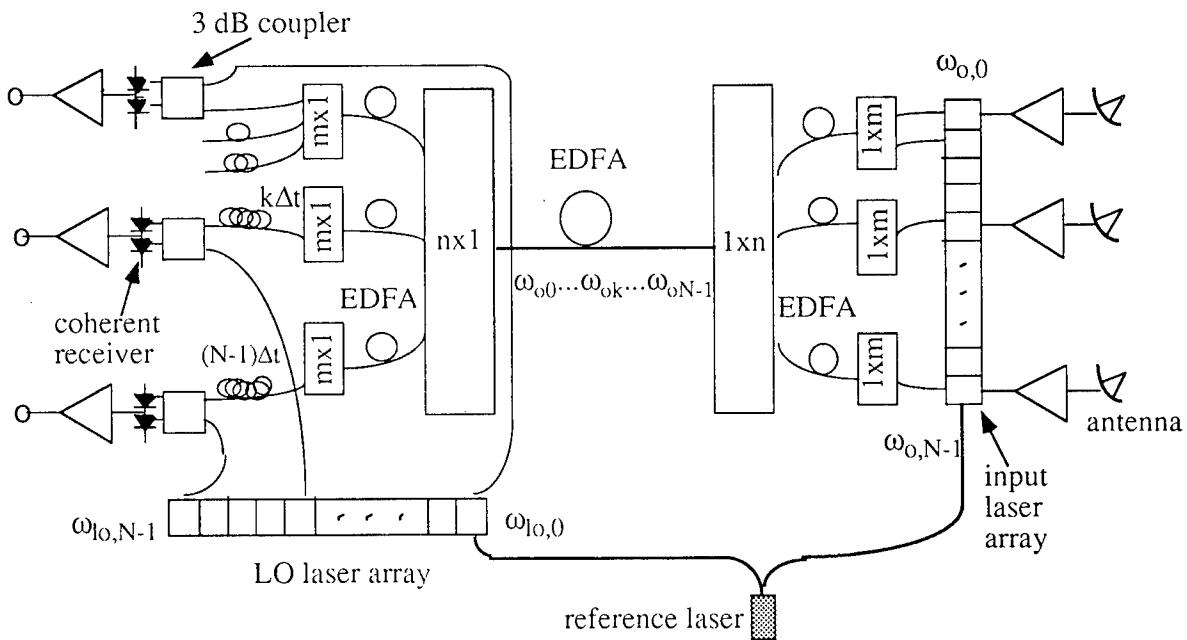


Fig. 2 Receiver diagram of coherent optically controlled phased array antenna

The receiver has a similar structure to the transmitter, as shown in Fig. 2. Corresponding to the antenna array, there are a sequence of lasers, each with a different, fixed central frequency. The signal received from each antenna modulates the associated laser, which is then coupled to a fiber. The signals are combined and transmitted through a single fiber to the receiver end, where the signals split, pass through different lengths of fibers, and illuminate an array of photodetectors together with the LO laser signals. The tunability of the LO lasers allows one to choose different time-delays appropriate for the signal received by each antenna from a particular direction.

Erbium-doped fiber amplifiers (EDFA) are used to compensate for power losses at the combiners and splitters, and to prevent the degradation of signal-to-noise ratio (S/N) performance. To achieve a higher S/N, combiners/splitters with EDFAs are implemented in several cascaded gain stages as shown in Figs. 1 and 2. Some performance parameters of an example system consisting of 128 transmitter lasers and 128 receivers are listed in Table 1. For this system, the gain of the optical power of one channel that illuminates each receiver is -3.2 dB, indicating that such coherent systems can be made nearly transparent. The spectral bandwidth of an EDFA  $>0.1\mu\text{m}$ . Thus, to further extend the number of channels in a large array, the systems in Figs. 1 and 2 can be used as a basic unit of a wavelength multiplexed architecture as described previously<sup>1</sup>. In this case, the multiplexing can lead to a system with  $\sim 1000$  channels.

Component	Optical loss (dB)	Optical gain (dB)	Noise Figure (dB)
16x1 combine (L1)	12.2		
EDFA (G1,F1)		21.2	4
8x1 combiner (L2)	9.2		
Fiber (L2)	1		
EDFA(G2, F2)		10.2	4
1x8 combiner (L3)	9.2		
EDFA (G3,F3)		9.2	4
1x16 combiner (L4)	12.2		

\* The excess loss of splice connection is included and is taken to be 0.1 dB for each.

**Table 1 Data for the coherent links**

In remainder of this paper, we assess the performance of the coherent, optically controlled phased array antenna system. The paper is organized as follows: In Sec. 2, the spectra of radar signals are described and the analytical treatment to be used is introduced. Issues such as the system noise sources, the signal-to-noise ratio (SNR) for one channel, the signal-to-interchannel-interference ratio (SIR), the dynamic range (DR) and fiber dispersion are all considered. In Secs. 3 and 4, the calculation results are discussed for SNR, SIR, DR, channel spacing, and the number of channels that can be accommodated for optical AM and FM modulation schemes. In Sec. 5, we compare the advantages and disadvantages of coherent FM, AM and other architectures currently under investigation. In Sec. 6, we present conclusions.

## 2. GENERAL DESCRIPTION

### 2.1 The radar signal spectra

A radar signal typically consists of a sequence of pulsed high frequency oscillations. The spectrum of this microwave signal can be expressed as<sup>4</sup>:

$$C(f) = 0.5(C_b(f + f_m) + C_b(f - f_m)) \quad 0 < f < \infty \quad (1)$$

where

$$C_b(f) = \sum_{n=-\infty}^{\infty} \tau \sin(\pi n f_r) / (\pi n f_r) \quad \text{for a long train of coherent pulses, and}$$

$$C_b(f) = \sum_{n=-\infty}^{\infty} \tau \sin(\pi f) / (\pi f) \quad \text{for non-coherent pulses or a single pulse.}$$

Here,  $f_r$  is the pulse repetition frequency (PRF),  $\tau$  is the pulse width and  $f_m$  is the microwave oscillation frequency. From Eq. (1), we see that the characteristic spectrum of a radar signal is a sinc function centered at  $f_m$ , typically between 1 and 20 GHz, and where most of the power falls in a comparatively narrow bandwidth which spans a frequency range on the order of  $1/\tau$  with a typical value of 1 MHz.

## 2.2 System noise and signal-to-noise ratio (SNR)

After photodetection, the IF signal can be expressed as:

$$i_{IF}(t) = A(t) \cos[\omega_{IF}t + \phi_{phase} + \phi(t)] + n(t) + n_{int}(t) \quad (2)$$

Here,  $A(t)$  and  $\phi(t)$  represent the amplitude and phase modulation, respectively, for the AM or FM scheme,  $\omega_{IF} = 2\pi f_{IF}$  is the angular intermediate frequency (IF),  $\phi_{phase}$  is the laser phase noise,  $n(t)$  is the additive current noise of the system, and  $n_{int}(t)$  is the interference signal from other channels. The power spectral density (PSD) of the time derivative of the phase noise in the range of  $0 < f < \infty$  is:

$$S_{\dot{\phi}_{phase}} = 4\pi\Delta\nu \quad (3)$$

where  $\Delta\nu$  is the sum of the transmitter and LO laser linewidths. The additive noise,  $n(t)$ , consists of thermal noise, shot noise, relative intensity noise, and the beat of the LO laser with the EDFA amplified spontaneous emission (ASE) noise. Thus the PSD of each term is given as<sup>5,6</sup>:

$$S_{n,thermal} = \frac{4kT}{r} \quad (4)$$

for the thermal noise, where  $k$  is Boltzmann's constant,  $T$  is temperature and  $r$  is the input resistance of the receiver. The shot noise is:

$$S_{n,shot} = 2eR(P_{LO} + P_{S-total}) \quad (5)$$

where  $R$  is the responsivity of the detector,  $P_{LO}$  is the optical power of the local oscillator, and  $P_{S-total}$  is the optical power of all signals incident on a receiver. That is,  $P_{S-total}$  equals the optical power of one channel that is incident on a receiver ( $P_S$ ) times the number of channels. The LO-ASE beat noise is then given by:

$$S_{n,LO-ASE} = 2R^2 h\nu F \cdot GP_{LO} \quad (6)$$

where  $h$  is Planck's constant,  $\nu$  is the optical frequency and  $FG$  is the product of the effective noise figure and gain for the EDFA ASE noise. Given the parameters in Table 1,  $FG$  of a three stage EDFA cascade for a single delay channel is<sup>6</sup>:

$$F \cdot G = ((F_1 G_1 / L_2 + F_2) G_2 / L_3 + F_3) G_3 / L_3 \cong 13\text{dB} \quad (7)$$

Next, the laser relative intensity noise is expressed as<sup>5</sup>:

$$S_{n,RIN} = R^2 \left( P_{LO}^2 10^{\frac{RIN_{LO}}{10}} + P_s^2 10^{\frac{RIN_s}{10}} \right) \quad (8)$$

where  $RIN_s$  and  $RIN_{LO}$  are the relative intensity noise contributions of the transmitter and LO lasers, respectively, in dB/Hz. Putting the expressions from Eq's. (4)-(8) together, the total noise in the range of  $0 < f < \infty$  is given by:

$$S_n(f) = \eta = 2R^2 h\nu F \cdot GP_{LO} + 2eR(P_{LO} + P_{s-total}) + \frac{4kT}{r} + R^2 \left( P_{LO}^2 10^{\frac{RIN_{LO}}{10}} + P_s^2 10^{\frac{RIN_s}{10}} \right) \quad (9)$$

When the  $P_{LO}$  is sufficiently large (typically  $> 1$  mW), the shot noise is larger than the thermal noise. Also, the LO-ASE beat noise is always about 10 dB more than the shot noise in this system. Thus when the RIN is small (i.e.  $< -160$  dB/Hz), the ASE-LO noise dominates the frequency independent noise expression in Eq. (9).

In Secs. 3 and 4, we calculate the SNR for one channel. In an array antenna system, the signal is the sum of the signal from each channel. Due to the coherence of the signals, the final SNR will be  $N$  times larger than the SNR of one channel, where  $N$  is the number of antenna elements.

### 2.3 Signal-to-interchannel-interference ratio (SIR)

For a large multichannel system, one must consider the channel bandwidth and minimum channel spacing required to accommodate the desired number of channels while keeping the interchannel interference an acceptably low level demanded by the system fidelity requirements. The SIR is the ratio of the power received in the desired signal channel ( $P_{s-final}$ ) to the total interference power ( $P_{int-final}$ ) from the other channels at the output. That is:

$$SIR = \frac{P_{s-final}}{P_{int-final}} \quad (10)$$

For optical heterodyne detection, assuming that the optical and RF power for each channel are the same, then the most significant interference for channel  $k$  comes from the adjacent channel  $(k-1)$  with a lower central frequency if the LO frequency is less than the optical signal frequency; or from channel  $(k+1)$  otherwise. Due to the dominance of the neighboring channel in contributing to the SIR, our numerical calculations in Sec. 3 and 4 only consider this interference from adjacent channels for simplicity. Figure 3 is a schematic diagram showing the relation between the IF frequency ( $f_{IF}$ ), the channel spacing ( $B_s$ ) and the channel bandwidth ( $B_{IF}$ ). For proper operation,  $B_{IF}$  should be large enough to pass most of the power of a desired signal in the IF stage, and  $f_{IF} > B_{IF}/2$ . To minimize the interference, no significant power in the adjacent channels should fall into the passband of the desired channel after photodetection. Thus  $B_s$  should be greater than  $2f_{IF} + B_{IF}$ .

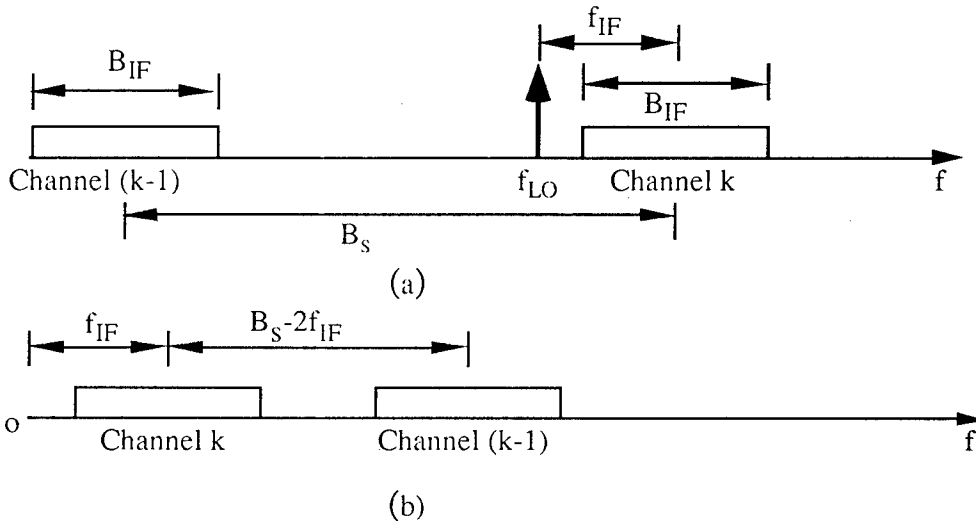


**Fig. 3 Schematic diagram of channel allocations for multichannel coherent system**  
 (a) different channels at optical frequency domain; (b) different channels at IF stage after photodetection.

## 2.4 Dynamic range

The dynamic range of the microwave-optic link is defined as the ratio of the maximum input RF power ( $P_{in-max}$ ) to the minimum input RF power  $P_{in-min}$  that can be carried by the fiber optic link<sup>5</sup>. Hence:

$$DR = 10 \log \left[ \frac{P_{in-max}}{P_{in-min}} \right] \quad (11)$$

$P_{in-min}$  is the RF power that results in  $S/N=1$  at the output, and  $P_{in-max}$  is the power that results in the nonlinear distortion power equal to the noise power.

## 2.5 Correction to the time-delay error caused by dispersion

Chromatic dispersion of the fiber will cause signals in different channels to travel at different speeds. This problem is especially acute for systems consisting of a large number of channels where the wavelength difference between channels 0 and N can be quite large (~100 nm). When the system is used in aircraft or satellite applications, the length of the fiber is several tens of meters. In this case, even if the system covers a large frequency range, the dispersion will not cause serious problems. However, for terrestrial systems where the fiber length can exceed a kilometer, dispersion will introduce additional time delays for different channels, which cannot be neglected for precise beam steering. This is especially true for systems using high microwave frequencies (10-100 GHz). We propose the following method for solving this problem. As stated in Sec. 1, in both the transmitter and receiver for the antenna system, the central frequencies of the transmitter laser array are fixed, thereby determining the optical group velocity of each channel. Assuming the group velocity of channel k is  $c_k$ , then after traveling through a fiber of length L, any other channel k will have additional time delay of  $(L/c_k - L/c_0)$  compared to channel 0. To compensate for this additional delay, we make the fiber associated with channel k,  $(L/c_k - L/c_0)c_k$  longer before it combines with other channels.

## 3. ANALOG AM LINKS FOR ANTENNA SIGNALS

### 3.1. SNR performance of AM links

Wideband filter-rectifier-narrow-band filter (WIRNA) processing is proposed<sup>5</sup> to demodulate the coherent AM signal. Figure 4 is a block diagram of the WIRNA receiver. The IF current,  $i_1(t)$  is given by<sup>5</sup>:

$$i_1(t) = \frac{A_s}{\sqrt{2}} [\cos(\omega_{IF}t + \phi(t) + mx(t)) - \sin(\omega_{IF}t + \phi(t))] + n(t) + n_{int}(t) \quad (12)$$

with  $A_s(t) = 2R\sqrt{P_s P_{LO}}$ . Here, m is the modulation index and x(t) is the normalized modulation signal. Assuming that  $n_{int}(t)$  (which will be discussed further in Sec. 3.2) is equal to 0 and  $mx(t) \ll 1$ , Eq. (12) becomes:

$$i_1(t) = \frac{A_s}{\sqrt{2}} [\cos(\omega_{IF}t + \phi(t)) - (1 + mx(t))\sin(\omega_{IF}t + \phi(t))] + n(t) \quad (13)$$

Most of the signal power is concentrated around  $f_{IF} \pm f_m$ . Thus, for a laser linewidth of  $\Delta\nu=0$ , more than 95% of the signal power falls between  $f_{IF}-f_m-2/\tau$  and  $f_{IF}+f_m+2/\tau$ . Hence, a rectangular IF filter which covers this frequency domain for a WIRNA receiver is desirable. With a non-zero laser linewidth, the signal spectrum is widened and the filter needs to be  $12.7\Delta\nu$  wider to accommodate more than 95% of the signal energy<sup>7</sup>. The IF bandwidth is therefore given by:

$$B_{IF} = 2f_m + 4/\tau + 12.7\Delta\nu \quad (14)$$

The second filter should be centered at  $f_m$  with a bandwidth of several  $1/\tau$  to obtain the final output. For convenience of analysis, a rectangular bandpass filter is assumed. The transfer function of the two filters can be expressed as:

$$H_{IF}(f) = \begin{cases} 1 & |f - f_{IF}| < f_m + 2/\tau + 6.4\Delta\nu \\ 0 & \text{otherwise} \end{cases} \quad (15)$$

$$H_2(f) = \begin{cases} 1 & |f - f_m| < 2/\tau = B/2 \\ 0 & \text{otherwise} \end{cases} \quad (16)$$

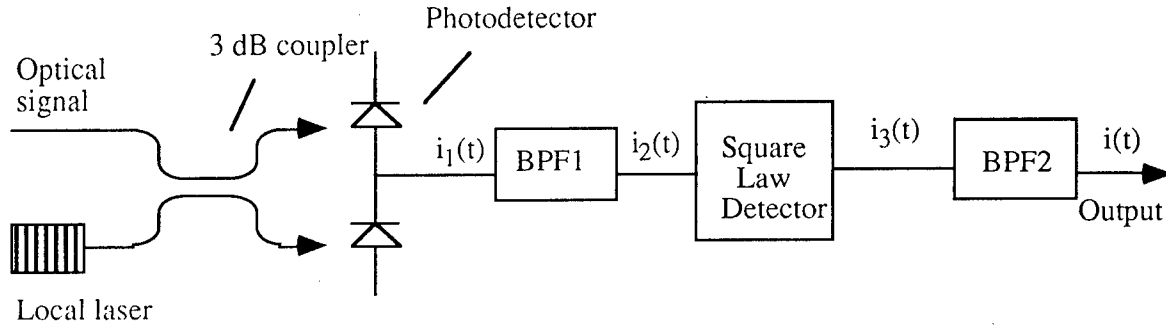


**Fig. 4 Schematic diagram of AM-WIRNA receiver**  
BPF1: IF bandpass filter, BPF2: final bandpass filter

The impulse response of the two filters,  $h_{IF}(t)$  and  $h_2(t)$ , can be calculated through the Fourier transform of  $H_{IF}(f)$  and  $H_2(f)$ . This leads to the following expression for the output power<sup>5</sup>:

$$\begin{aligned} P_{out} &= P_{sig} + P_{sd} + P_{sn} + P_{nn} + P_{RIN,ad} \\ &= \Gamma_1 m^2 A_s^4 + (\Gamma_2 m^2 + \Gamma_3) A_s^4 + (\Gamma_4 m^2 + \Gamma_5) A_s^2 \eta + \Gamma_6 \eta^2 \\ &\quad \Gamma_1 A_s^4 (10^{RIN_s/10} + 10^{RIN_{Lo}/10}) B \end{aligned} \quad (17)$$

where  $\eta = S_n(f)$ . The first term is the signal power, and the rest are noise contributions. All the  $\Gamma$  parameters depend on  $B_{IF}$  and  $B$ , with  $\Gamma_3$  also depending on  $f_{IF}$ . The term  $P_{sd}$  is due to phase noise,  $P_{sn}$  is the beat of the signal and the additive noise,  $P_{nn}$  is the squared additive noise. Also,  $P_{RIN,ad}$  is the additional noise term caused by the laser RIN. The two terms in  $P_{sd}$  and  $P_{sn}$  are due to the received signal having both a carrier and message term.

For a reasonable optical power,  $P_{sn}$  is always much larger than  $P_{nn}$ . Thus if the laser linewidth is very narrow, the RIN is very small (-160dB/Hz), and  $m^2 x^2(t) \ll 1$ , the expression for SNR simplifies to:

$$SNR = \frac{4\Gamma_1 m^2 R^2 P_{Lo} P_s}{\Gamma_5 \eta} \quad (18)$$

Usually the ASE-LO is the most significant noise in source  $S_n(f)$ . Thus, Eq. (18) further simplifies to:

$$SNR = \frac{2\Gamma_1 m^2 P_s}{\Gamma_5 h\nu F \cdot G} \quad (19)$$

where  $\Gamma_5$  is proportional to  $B$ . When the laser linewidth  $\Delta\nu$  is large,  $P_{sd}$ , the phase-to-intensity noise conversion term, needs to be considered. The spectrum of the square of the IF current in Eq. (12) has a

dominant component at  $2f_{IF}$  which is broadened by laser phase noise. For wide IF bandwidth, this can be expressed as  $A_s^2 \cos(2\pi f_{IF} t + 2\phi(t)) / 4$ . The power spectral density of this term has a Lorentz shape<sup>8</sup>. Reference [5] shows that when  $f_{IF}$  is very large for reasonable optical signal power,  $P_{SD}$  is typically much less than  $P_{SN}$ . But for a multichannel system,  $f_{IF}$  should be kept small to maintain a narrow channel spacing to accommodate more channels. When  $f_{IF}$  becomes smaller, however, more power due to this term falls in  $B$ , thereby degrading the system SNR performance. The ratio of signal power to this noise power will depend on  $B_{IF}$ ,  $B$ ,  $f_{IF}$  and modulation index  $m$ .

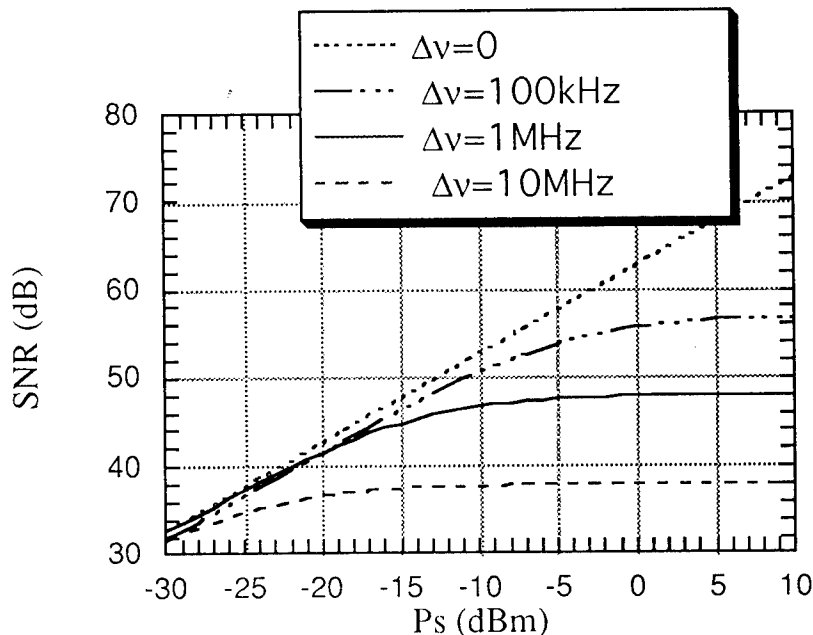


**Fig. 5 SNR of AM scheme for various laser linewidths**  
 $f_m=1$  GHz,  $f_{IF}=1.5$  GHz,  $B=1$  MHz,  $P_{LO}=10$  dBm,  $RIN=0$ ,  $R=0.6$  A/W,  $m=0.1$

Figure 5 shows the calculated SNR versus the signal power per channel for an AM system. It is shown that a wide laser linewidth,  $\Delta\nu$ , ultimately determines the maximum achievable SNR. When  $f_{IF}$  is small, increasing the optical signal power above a certain level will not improve the SNR performance. Contrary to the situation in Ref. 5 in which a very large  $f_{IF}$  is assumed, this occurs when the signal power is still quite low. For example, for  $f_m = 1$  GHz,  $B = 1$  MHz,  $f_{IF} = 1.5$  GHz,  $m = 0.1$ , with  $\Delta\nu = 100$  kHz, the SNR tends to be independent of  $P_s$  for  $P_s > 1$  mW. For  $\Delta\nu = 1$  MHz, power independence of SNR is at  $P_s > 0.1$  mW, and for  $\Delta\nu = 10$  MHz, at  $P_s > 0.01$  mW. It is also shown that  $SNR > 50$  dB for  $f_{IF} = 1.5$  GHz,  $\Delta\nu = 100$  kHz, and assuming the signal power of one channel is  $-10$  dBm. Calculations also show that with  $f_{IF}$  as large as  $10f_m$ , the effect of the laser linewidth will be negligible for  $\Delta\nu < 1$  MHz.

### 3.2 SIR and the channel spacing

As signal power is usually much larger than the noise power for each channel, to calculate the interchannel interference, we simplify the problem by considering the contribution from neighboring channels whose signal spectrum is noise free. From Eq. (13) the spectrum of one channel of the AM IF signal without noise is given by:

$$C_{AM}(f) = A_s \left[ \delta(f - f_{IF}) + \frac{1}{\sqrt{2}} m \cdot C(f - f_{IF}) \right] \quad (20)$$

Here,  $C(f)$  is the spectral coefficient of the radar signal given in Eq. (1). Equation (13) shows that the IF current has an interference term. After being filtered and squared, there are beats between signal and interference, and the square of interference. In the limit of small interference, the first effect is always much larger than the second. Thus the interference power can be calculated as:

$$P_{int} = \int \left\{ [s(f)H_{IF}(f)] * [int(f)H_{IF}(f)] \cdot H_2(f) \right\}^2 df \quad (21)$$

where  $s(f)$  and  $int(f)$  are the spectra of the signal and interference current at the IF stage, respectively,  $H_{IF}(f)$  and  $H_2(f)$  are the transmission characteristics of the two filters (see Eq. (15) and (16)), and  $*$  denotes the convolution operation.

Figure 6 shows the SIR calculations for the AM scheme where the channel bandwidth accommodates more than 95% of the signal energy. Usually for  $f_m \tau \gg 1$ ,  $B_{IF}$  is just slightly larger than  $2f_m$ . The calculations show that when  $B_s$  is slightly more than  $2f_{IF} + 2f_m$ , then  $SIR > 60$ dB, regardless of the modulation depth, optical power or RF power. Usually the channel spacing needs to be somewhat wider to meet the requirement of square-law detection, and to tolerate the laser linewidth and the instability of the laser central frequency.

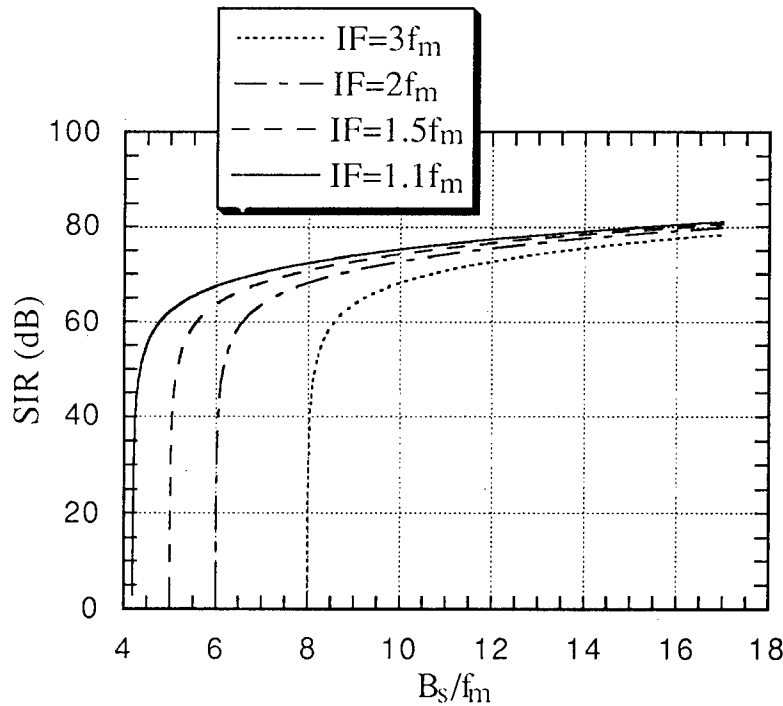


Fig. 6 SIR of AM scheme

$$f_m \tau = 1000, B = 2/\tau$$

For our example system, using AM to achieve a high SIR and SNR, a channel spacing of slightly larger than  $6f_m$  is sufficient (for  $f_{IF} = 1.5f_m$ ) if laser linewidth and  $1/\tau$  is much smaller than  $f_m$ . A 100 Å laser

tuning range can be obtained using multisection distributed feedback lasers<sup>9</sup>. Given that  $1 \text{ \AA} = 12 \text{ GHz}$ , we could easily accommodate 128 optical channels for a 1 GHz microwave signal.

### 3.3 Dynamic range of the AM links

From the calculation results of Sec. 3.2, we know that the interference can be kept very low, and thus it has little effect on the dynamic range calculations. Taking the 3rd order intermodulation as the limitation for linearity, the dynamic range of AM links is calculated using<sup>5</sup>:

$$DR = 10 \log \left[ 8 \cdot \left( \frac{\Gamma_1 A_s^4}{\Gamma_3 A_s^4 + \Gamma_5 A_s^2 \eta + \Gamma_6 \eta^2 + \Gamma_1 (10^{RIN_s/10} + 10^{RIN_{Lo}/10})} \right)^{\frac{2}{3}} \right] \quad (22)$$

Figure 7 shows the calculated DR for different laser linewidths,  $\Delta\nu$ . When the signal power of one channel at the transmitter is only -7 dBm, this implies the optical power at the antenna is around -10 dBm. Assuming a laser linewidth of 1 MHz and a receiver output bandwidth of 1 MHz, the dynamic range of one receiver can be as high as 53 dB, which is about 5 dB lower than that obtained for  $\Delta\nu = 0$ . When  $P_s = -20 \text{ dBm}$  and the laser linewidth is less than 1 MHz, the dynamic range is approximately 50 dB, which corresponds to 110 dB/Hz. These values suggest reasonably good link DR performance.

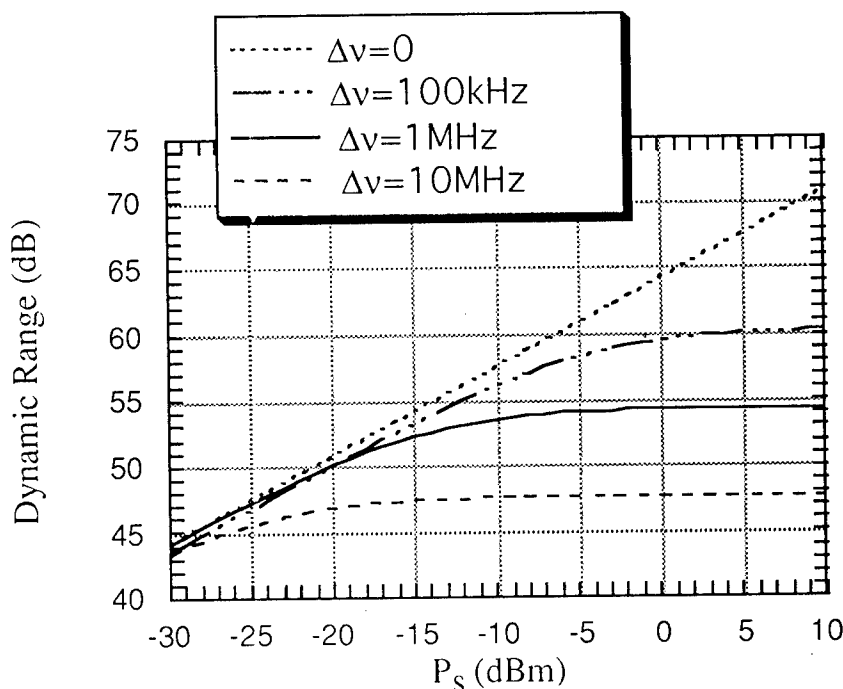


Fig. 7 Dynamic Range of AM for different laser linewidths  
 $P_{LO}=10 \text{ dBm}$ ,  $RIN=0$ ,  $R=0.6 \text{ A/W}$ ,  $f_m=1 \text{ GHz}$ ,  $B=1 \text{ MHz}$ ,  $f_{IF}=1.5 \text{ GHz}$

## 4. FM PHASE DELAY SCHEME

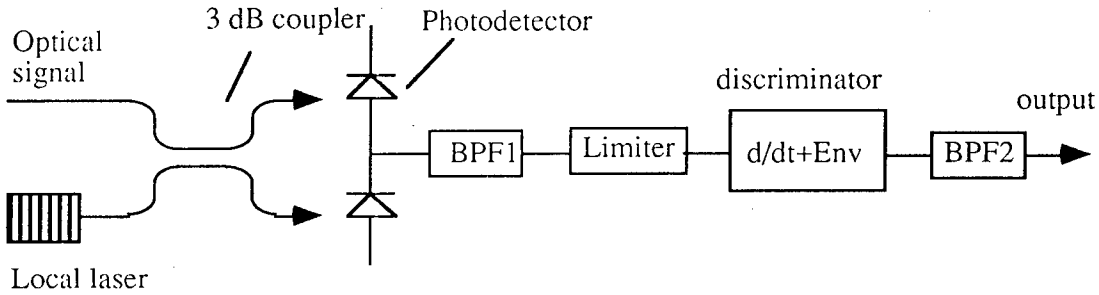
### 4.1 SNR of the FM Scheme

Figure 8 is a schematic diagram for a typical optical FM demodulation receiver. Either direct FM laser modulation or external FM modulation can be used. After transmission and heterodyne photodetection, a rectangular bandpass filter (B<sub>IF</sub>) is used to pass most of the power of the desired channel while reducing the interference from other channels. The signal is then demodulated by an electronic differentiator and envelope detector, and then passes a second bandpass filter similar to that used in AM schemes to obtain a noise-reduced output signal. Carson's law states that to pass nearly 98% of the signal power, B<sub>IF</sub> must be:

$$B_{IF} = 2(\beta + 1)B_e \quad (23)$$

where B<sub>e</sub> is equal to the high frequency cutoff of the final pass band of Eq. (16), and β is the modulation index. If τ<sub>m</sub> << 1, B<sub>c</sub> is approximately equal to f<sub>m</sub>. We now define f<sub>Δ</sub> as the maximum instantaneous optical frequency deviation. In this case:

$$f_{\Delta} = \beta B_e \cong \beta f_m \quad (24)$$



**Fig. 8 Schematic diagram of FM receiver**  
BPF1: the IF bandpass filter, BPF2: the final bandpass filter

Once again, we use Ref. 5 as starting point for analyzing FM link performance. For our specific problem, the power spectral density (PSD) around f<sub>m</sub> caused by the additive noise after the discriminator is:

$$S_{N_n} = \eta(2\pi f_m \tau_D)^2 \quad (25)$$

where τ<sub>D</sub> is the time constant of the differentiator. The PSD caused by phase noise is then:

$$S_{N-phase-FM} = 4\pi\tau_D^2 R^2 P_s P_{LO} \Delta\gamma \quad (26)$$

Hence the SNR for the FM systems is:

$$SNR = \frac{2\pi^2 f_{\Delta}^2 R^2 P_s P_{LO}}{B \left[ \eta(2\pi f_m)^2 + 4\pi R^2 P_s P_{LO} \Delta\gamma \right]} \quad (27)$$

Usually the ASE-LO beat noise is the most significant contribution to S<sub>n</sub>(f), in which case the above formula can be simply expressed as:

$$SNR = B^{-1} \left[ \frac{4h\gamma(F \cdot G)f_m^2}{P_s f_{\Delta}^2} + \frac{2\Delta\gamma}{\pi f_{\Delta}^2} \right]^{-1} \quad (28)$$

From Eq. (28), it is clear that when the product of the signal power and the laser linewidth is large, the phase noise is the most significant noise source. Otherwise the post-detector white noise is dominant. Figure 9 shows that for P<sub>s</sub> = 50 μW, the white noise (especially that from ASE-LO beat noise) dominates

when the laser linewidth is below 100 kHz. When  $\Delta\nu > 1$  MHz, phase noise tends to be dominant. With the optic link parameters given in Table 1 and  $\Delta\nu = 10$  MHz, a final passband of 1 MHz, a signal power of  $50 \mu\text{W}$ , a LO power of 10 mW and  $f_{\Delta} = 2$  GHz, we obtain  $\text{SNR} = 66$  dB, which is 126 dB/Hz. This is significantly higher than what can be obtained by the AM scheme for the same input optical power.

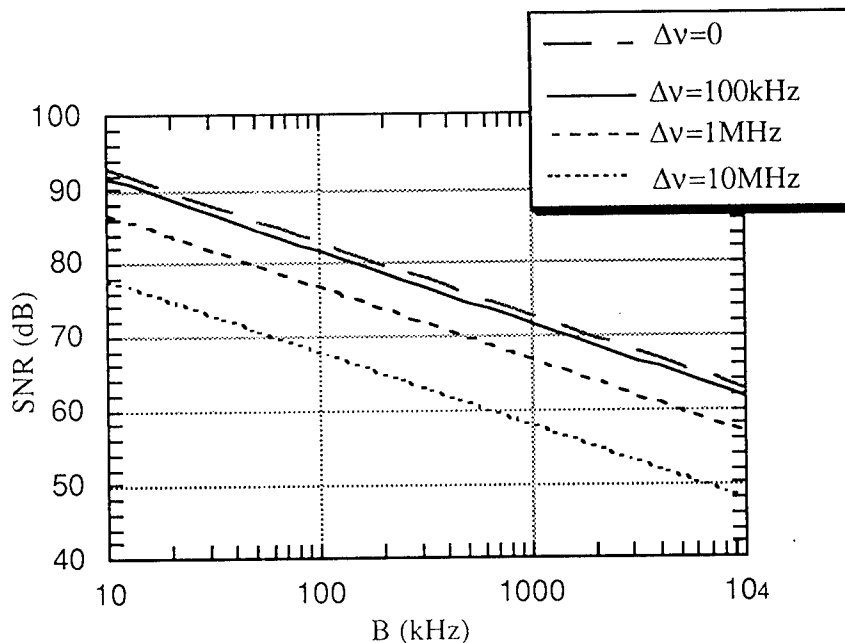


**Fig. 9 SNR of coherent FM link for radar signal input**  
 $\Delta\nu$ : laser linewidth,  $P_s=50 \mu\text{W}$ ,  $P_{LO}=10 \text{ mW}$ ,  $f_m=1 \text{ GHz}$ ,  $f_{\Delta}=2 \text{ GHz}$

#### 4.2 SIR and channel spacing for FM links

Most of the signal power in the IF current lies around  $f_{IF} \pm kf_m$  for  $k = 0, 1, 2, \dots$ , and the interference power lies around  $|f_{o,adj} - f_{LO}| \pm kf_m$ . Here,  $f_{o,adj}$  is the central optical frequency of the interference channel and  $f_{LO}$  is the LO frequency. Following Ref. 10, the most significant contribution to the interference ( $P_{int-IF}$ ) comes from the spectrum that falls within  $B$  after demodulation, i.e.:

$$SIR_{FM} = \frac{f_{\Delta}^2 R^2 P_{LO} P_s}{f_m^2 P_{int-IF}} = \frac{\beta^2 P_{s-IF}}{P_{int-IF}} \quad (29)$$

The  $SIR_{FM}$  following Eq. (29) is plotted in Fig. 10 where we observe that very high SIR can be achieved for FM schemes. For example, for  $\beta = 2$ ,  $f_{IF} = 3f_m$  and  $B_s = 13f_m$ , then  $SIR = 64$  dB. The channel spacing, however, is more than  $4(\beta+1)f_m$ . Through calculations using Eq. (27), it is shown that for a 1 GHz radar signal with  $f_{\Delta} = 2$  GHz and a channel spacing of 12 GHz, SNR is more than 50 dB and SIR more than 60 dB. Thus, like AM, we find that a 100 Å laser tuning range can be used in systems which accommodate 100 channels.

### 4.3 Dynamic range of FM systems

To obtain a higher SNR and a small distortion of the demodulated signal, a large linear frequency response range of the laser output to the modulation current is desirable. The SNR calculations also show the DR for the corresponding largest linear frequency response. For example, Fig. 9 shows that for system parameters given in Table 1, a laser linewidth of  $\Delta\nu = 1$  MHz, a final bandwidth of 1 MHz, an optical signal power of  $50 \mu\text{W}$ , and for a maximum linear optical frequency deviation of 2 GHz, the SNR = 66 dB, and the DR of a single channel is also 66 dB.

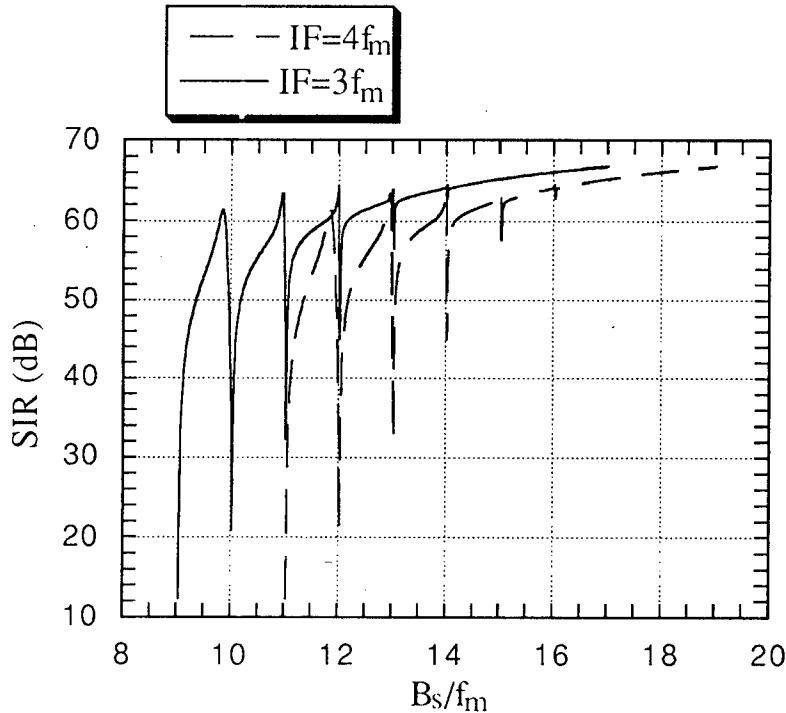


Fig. 10 SIR of FM scheme

$$\beta=2, f_m\tau=1000, B=2/\tau$$

### 5. SYSTEM COMPARISONS

AM coherent detection requires a minimum channel spacing of  $6f_m$ , while FM requires  $4(\beta+1)f_m$ . Thus FM channels usually occupy larger optical bandwidth. However, in comparing Eq. (19) and (28), we see that when the laser linewidth,  $\Delta\nu$ , is very small, the SNR of FM is  $\beta^2/m^2$  times that of AM. Thus, FM generally has better SNR and DR performance than comparable AM schemes.

The advantage of the coherent optically controlled phased array antenna described here is that it is readily expandable to many elements. As for the basic system, it can easily accommodate  $\sim 100$  channels in a single fiber, and feed any combination of  $\sim 100$  true-time delays to  $\sim 100$  antenna array elements. Its central element is a tunable semiconductor laser array. Using wavelength division multiplexing (WDM) or optical crossbar switching, this can be expanded to accommodate larger scale antenna arrays. In contrast, an IM/DD system<sup>1</sup> requires  $\sim 10,000$  lasers and  $\sim 10,000$  fibers of precisely determined length. If the transmitter lasers are far away from the antenna elements, the IM/DD system requires an additional  $\sim 100$

long fibers to be cut precisely and maintained in the same configuration so that the total optical path of the several transmission fibers are equal. The coherent approach takes advantage of good frequency selectivity of coherent links, and thus employs most of the useful bandwidth of optical fibers. The channel spacing occupied by a coherent channel is the narrowest compared to that of all other system approaches. It is shown here that there is little interference between channels for appropriate channel spacing and modulation/demodulation methods.

From our analysis in Secs. 3 and 4, we see that the final output signal maintains its original linewidth in frequency domain. This is a crucial characteristic for application of the Doppler effect to radar systems, where the receiver should be able to detect very small spectral shifts of the return signal. This cannot be fulfilled by the direct generation of radar signals using optical heterodyne techniques, where the linewidth of the signal would be in the order of the laser linewidth<sup>2</sup>.

• Due to losses from combiners and splitters which are necessary for multichannel systems, and due to the phase noise that is intrinsic to heterodyne detection, even with the use EDFA's the AM system does not have as good an SNR performance as that of direct detection. However, using such techniques as high signal and LO power, reduction of laser linewidth through external cavities, etc., it is possible to get dynamic range as high as 50 dB. For the FM scheme, we can improve both SNR and DR performance over that of IM/DD schemes.

## 6. CONCLUSION

We have analyzed a coherent phased array antenna system which utilizes fibers for producing true-time-delays and optical coherent detection for the phase delay feed. This system has most of the advantages of true-time-delay phased array antenna systems. For example, the system has large instantaneous bandwidth and thus is "squint free". Due to the gain control from both the LO lasers and the subsequent electronic amplifiers, it has flexibility for beam shaping and null steering. We discuss a model system which uses a single fiber to transmit ~100 channels. The system can feed any of 100 different time delays to any of 100 antenna elements. With WDM or crossbar switch techniques, such a system can be expanded to large scale antenna arrays in which a realistic phased array antenna system could be built. We also propose a solution for compensating fiber chromatic dispersion which distorts the radiation pattern.

The main noise sources for the optical links are the ASE-LO beat noise, as well as the laser phase noise. From our analysis, we see that for a typical radar signal and realistic optical system parameters, we can obtain a signal-to-noise ratio and dynamic range for both AM and FM schemes which meet the stringent requirements of modern radar systems.

## ACKNOWLEDGMENTS

We thank RADC/Griffiss AFB (B. Hendrickson) for support of this work.

## REFERENCES

- [1] W. Ng, A.A. Walston, G.L. Tangonan, J.J. Lee, I.L. Newberg and N. Bernstein, "The first demonstration of an optically steered microwave phased array antenna using true-time-delay", *IEEE J. Lightwave Tech.*, v. 9, no. 9, pp1124-1131, 1991.
- [2] Marc R. Surette, D. R. Hjelme and A.R. Mickelson, "An optically driven phased array antenna utilizing heterodyne techniques", *J. Lightwave. Tech.*, v. 11, no. 9, pp1500-1509, Sept. 1993.
- [3] P. M. Freitag and S. R. Forrest "A coherent optically controlled phased array antenna system", *IEEE Microwave and Guided Wave Lett.*, v. 3, no.9, pp293-295, Sept. 1993.
- [4] Merrill L. Skolnik, *Introduction to Radar Systems*, second ed., New York: McGraw-Hill, 1980.
- [5] D.J. Sabido, T.K. Fong, R.F. Kalman and L.G. Kazovsky, "Linewidth-insensitive coherent optical analog links", *SPIE* v.1703, pp504-522, 1992.
- [6] R. Walker, R.C. Steele, and N.G. Walker, "Optical amplifier noise figure in a coherent optical transmission system", *J. of Lightwave. Tech.*, v. 8, no.9, pp1409-1413, Sept. 1990.

- [7] L. G. Kazovsky, "Impact of laser phase noise on optical heterodyne communication systems", *J. Opt. Commun.*, 7 (1986) 2, pp66-78.
- [8] K. Kikuchi, T. Okoshi, M. Nagamatsu, and N. Henmi, "Degradation of bit-error rate in coherent optical communications due to spectral spread of the transmitter and the local oscillator", *J. of Lightwave Tech.*, v. 2, no. 6, pp1024-1033, Dec. 1984.
- [9] M. Oberg, S. Nilsson, J. Wallin, D. Karlsson-Varga, L. Backbom and G. Landgren, "Wide continuous wavelength tuning of a narrow linewidth DBR laser", *IEEE Photonics Tech. Lett.*, v.4, pp230-232, 1992.
- [10] A. Carlson, Communication Systems, second ed., New York: McGraw-Hill, 1975.

# The Use of Optically Coherent Detection Techniques for True-Time Delay Phased Array and Systems

Ligeng Xu, Robert Taylor, and Stephen R. Forrest, *Fellow, IEEE*

**Abstract**—We analyze a true-time-delay, optically controlled phased array antenna system whereby beam forming is accomplished using a large number of antenna elements that can receive any of several different microwave true-time-delays via the use of coherent optical carriers transmitted through a single fiber. The transmitter and receiver architectures are described in detail. We present calculations for the signal-to-noise ratio (SNR), the signal-to-interchannel interference ratio (SIR) and dynamic range (DR) of one channel for various modulation-demodulation schemes (i.e., AM-heterodyne, FM, PM). We show for an example system that can accommodate 128 antenna elements and provide 128 different delays (7 bits), assuming AM modulation with a bandwidth of 1 MHz, a transmitter power of  $-5$  dBm and a laser linewidth of 10 MHz, we can obtain  $DR \approx 50$  dB for one channel using a channel separation twelve times of that of the microwave frequency ( $f_m$ ). For the FM scheme,  $DR \approx 60$  dB can be obtained for one channel with a laser linewidth of 1 MHz, a FM modulation index of one, and a channel spacing of about  $13f_m$ . With a local oscillator laser tuning range of  $100 \text{ \AA}$ , the system can provide seven-bit resolution for a 128 element antenna array. It is found that coherent optically controlled phased array antennas provide improved controllability over direct detection method, and can have the SNR, SIR and DR that meet the stringent requirements of modern high resolution microwave antenna systems.

## NOMENCLATURE

$\beta$	FM modulation index	$DE_i$	Time delay for the $i$ th antenna element
$\Gamma_i$	Parameters for signal and noise powers of the AM scheme	DR	Dynamic range
$\Delta f$	Maximum optical frequency deviation for the FM scheme ( $=\beta f_m$ )	$F$	Noise figure of the optical amplifier system
$\Delta\nu$	3-dB laser linewidth	$f_m$	Microwave signal frequency
$\nu$	Optical carrier frequency	$f_r$	Pulse repetition frequency of radar signals
$\phi_s(t)$	Phase of the intermediate frequency signal	$f_{IF}$	Intermediate frequency
$\phi_{\text{phase}}(t)$	Phase noise	$G_i$	Optical gain
$\tau$	Pulse width of radar signals	$G_{\text{tot}}$	Total optical gain of one channel
$\omega_{IF}$	Angular intermediate frequency (IF)	$H_{IF}(f)$	Transfer function of the bandpass filter for IF signals
$A_s$	IF current amplitude, $2R\sqrt{P_s P_{LO}}$	$H_2(f)$	Transfer function of the final filter
ASE	Amplified spontaneous emission	$h$	Planck constant
$B$	Bandwidth of the radar signal	$i_{IF}(t)$	Intermediate frequency current
$B_{IF}$	IF bandwidth	$k_B$	Boltzmann constant ( $= 1.38 \times 10^{-23} \text{ J/K}$ )
$C(f)$	Radar signal spectrum	$L_i$	Optical loss
$c$	Optical signal velocity in fibers	$M$	Number of antenna elements
$D$	Channel spacing	$m$	AM modulation index
		$N$	Number of different delays corresponding to bit resolution
		$n(t)$	Noise current
		$n_{\text{int}}(t)$	Interference current
		PSD	Power spectral density
		$P_{\text{int-final}}$	Interference power at the final output
		$P_{\text{in-max}}$	RF power input that results in third order power equal to noise power
		$P_{\text{in-min}}$	RF power input that results in $SNR = 1$
		$P_{LO}$	Local oscillator laser power
		$P_s$	Optical power of one channel incident on one receiver
		$P_{s\text{-final}}$	Signal power of the primary channel at the final output
		$P_{s\text{-total}}$	Total optical signal power incident on one receiver
		$R$	Photoresponsivity of detectors
		RIN	Relative intensity noise of lasers (in units of dB/Hz)
		$r$	Resistance of the receiver, usually $50 \text{ \Omega}$
		SIR	Signal-to-interchannel-interference ratio
		SNR	Signal-to-noise ratio
		$S_n(f)$	PSD of the total noise current at the IF region
		$S_{n,\text{thermal}}$	PSD of thermal noise
		$S_{n,\text{shot}}$	PSD of shot noise
		$S_{n,\text{LO-ASE}}$	PSD of the LO-ASE beat noise
		$S_{n,\text{RIN}}$	PSD of relative intensity noise
		$S_{\dot{\phi}_{\text{phase}}}$	PSD of the time derivative of laser phase noise
		$T$	temperature
		$X$	Number of delays needed on the optical receiver site
		$x(t)$	Modulation signal

Manuscript received November 28, 1994; revised April 21, 1995. This work was supported by Griffiss/Rome Labs. (B. Hendrickson and E. Walge) and NCIPT.

The authors are with the Advanced Technology Center for Photonics and Optoelectronic Materials, Department of Electrical Engineering, Princeton University, Princeton, NJ 08544 USA.

IEEE Log Number 9413046.

## I. INTRODUCTION

**P**HASED ARRAY antenna systems provide great flexibility for radar beam formation, steering and detection [1]–[3]. Recently, much effort has been devoted to introducing and transmitting the phase delay of microwave signals via optical means [4]–[13]. This effort has been motivated by the obvious advantages of fiber optic systems. For example, since the microwave signals are modulated on optical carriers which are transmitted through silica fibers, the system is immune to electromagnetic interference. In addition, by using fibers instead of metal waveguides or coaxial cables, and optical devices instead of bulky microwave phase delay devices, such systems can be light-weight and hence have potential usefulness on aircraft and satellite platforms. Finally, if the system employs true-time-delay [2] and [10], it can have very large instantaneous bandwidth which is useful for multi-frequency communication and radar systems free from “beam squint” [10].

There have been many different architectures suggested to transmit and control a series of microwave delays using optical means. Some systems [4]–[6] use bulk optics which suffer from thermal and mechanical instabilities. Others [7] use heterodyning of two injection-locked lasers to generate and control the microwave signal. These typically are not true-time-delay architectures, and hence their instantaneous bandwidths are small. For this reason, true-time-delay systems using intensity modulation/direct detection (IM/DD) techniques have also been developed [8]–[12]. The high loss and interchannel interference due to relatively low on/off ratios of optical switches makes it difficult to build such a system based on cascaded (or serial) fiber-optic delay lines. Thus, IM/DD systems typically utilize parallel delay lines along with bias-switched lasers and detectors selecting between various delays. In these structures, the number of delay lines, lasers and receivers is on the order of  $M \cdot N$ , where  $M$  is the number of antenna elements and  $N$  is the number of different delays. For a large scale system where both  $M$  and  $N$  exceed  $10^2$ , this method becomes quite cumbersome or even impractical. In addition, such fiber optic delay systems require  $N$  fibers of precise and equal lengths from the control to the antenna site. This is a particularly stringent requirement for some high bandwidth systems where the distance between the controller and antenna array exceed several tens of meters. Thus, implementation of such optically steered phased array antenna systems are currently hampered by the extreme complexity involved in efficiently transmitting hundreds of high quality (i.e. low loss and low interference) microwave delays from the control site to the antenna array.

To overcome several of these difficulties, and to effectively feed different delays to the antenna elements, Freitag and Forrest proposed a true-time-delay phased array system based on multichannel, broadband coherent detection techniques [13]. The system was unique in that a large number of different delays are transmitted through a single fiber, using on the order of only  $M + N$  optical transmitters and receivers. The system can be made optically transparent by employing heterodyne detection plus optical amplifiers. In this paper,

we quantitatively analyze the performance of the coherent optically controlled phased array transmitter and receiver system of [13]. We find that such a multichannel system has very low interchannel interference, high signal-to-noise ratio (SNR), and dynamic range (DR). Semiconductor lasers used in this system reduce both size and cost, and increase robustness and tuning range. Even with the comparatively large semiconductor laser linewidths, Doppler radar can still be implemented using this architecture.

The paper is organized as follows. In Section II, the transmitter and receiver structures, and some system issues are described in detail. Section III describes the spectra of radar signals, and introduces analytical methods to treat such issues as noise, signal-to-noise ratio (SNR) for one channel, signal-to-interchannel-interference ratio (SIR), and dynamic range (DR). We also provide parameters for an example system which can accommodate 128 antenna elements and provide 128 different delays, whose performance is evaluated in the following sections. In Sections IV and V, we provide the results of calculations for SNR, SIR, DR, channel spacing, and the number of channels that can be accommodated for optical AM, FM and PM modulation schemes. In Section VI, comparisons are made concerning the advantages and disadvantages of coherent and other architectures currently under investigation. We present conclusions in Section VII.

## II. SYSTEM DESCRIPTION

### A. The Transmitter Antenna

It is known that the direction and wave pattern incident on or transmitted from an array antenna can be changed by properly varying the phase of the signal emitted from each array element. In the coherent system architecture, microwave signals are modulated on optical carriers with different frequencies (i.e. different optical channels), and are transmitted to antenna elements with the delays imposed by sending each carrier through different fiber lengths. Due to the optical channel selectivity of coherent detection afforded by using heterodyne optical-to-microwave receivers at each antenna element, the delayed signals can be distributed to the various elements to achieve the desired beam direction.

Fig. 1 is a schematic diagram of the antenna transmitter. Each element in the input laser array has a different fixed optical frequency,  $f_{ok}$ , where  $k$  indicates the  $k$ th laser in the array. The same microwave signal modulates each of the  $N$  lasers in the array, using either direct or external modulation. The optical signals are then coupled to fibers of different lengths to introduce the true time delay. Thus,  $N$  is the number of different delays in the system which determines the bit resolution of the phased array. For example, if  $N = 128 = 2^7$ , then the system has seven bit resolution. Different lengths of fibers correspond to different time delays. For example, a 1-mm fiber length difference corresponds to a  $5 \times 10^{-12}$ s delay, which is a  $1.8^\circ$ -phase delay for a 1-GHz microwave signal. It is reported that using silica based planar waveguide technology, the delay can be controlled to a precision of 2 ps [11], which corresponds to 0.7 degree for a 1-GHz signal.

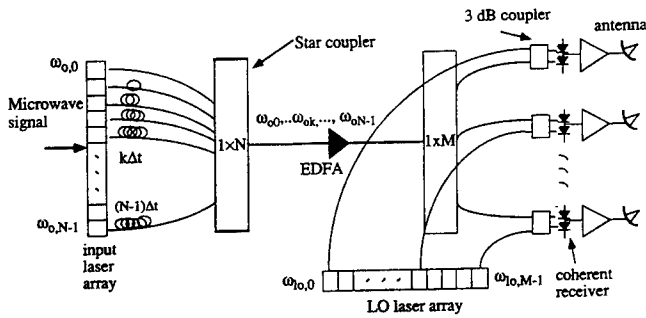


Fig. 1. The coherent optically controlled phased array antenna transmitter.

Next, the several delayed signals are combined onto a single fiber and sent to the antenna array, where the signals are distributed to the coherent receivers using a  $1 \times M$  splitter. The  $N$  optical signals are subsequently incident on each of the  $M$  coherent receivers, along with a local oscillator (LO) laser signal which is tuned to provide  $k$ th receiver with a frequency  $f_{lok}$ . By tuning  $f_{lok}$ , the signal on any particular optical channel can be coherently detected. The photodetected signals are then demodulated electronically to recover the original microwave signals with different time delays fed to the desired antenna elements. With LO lasers associated with each antenna element tuned to different frequencies, various time-delays are fed to the array elements, thereby steering the beam to different directions.

This optically steered phased array antenna system requires  $M + N$  optical transmitters plus receivers, instead of  $M \times N$  typical of IM/DD systems. Furthermore, all the delays are transmitted on different optical carrier frequencies along a single fiber, thereby obviating the need for cutting and adjusting hundreds of long fibers extending from the control to the antenna site. This also allows for compensation of the optical loss from the combiners, splitters and other optical devices by putting a small number of optical amplifiers (e.g. erbium-doped fiber amplifiers, or EDFA's) along the fiber. Since beam steering is accomplished by tuning the LO to route the different delays to the several antenna elements, the steering speed is determined by how rapidly the LO laser can be tuned. Typically, for laser diodes this is in the range of 1 ns~1 ms [14], which is sufficient for most applications. By individually adjusting the microwave amplifiers or the receiver gain, the system can easily shape the beam.

In an antenna array system, a greater number of delays leads to a higher angular resolution and steering accuracy. In Fig. 1, the number of different delays which corresponds to the number of optical channels is limited by the tuning range of the LO laser. Currently, wide tuning ranges of ~83 nm of single mode operation have been demonstrated for DBR lasers [15]. Using external cavities and gratings, the tuning range can also approach several tens of nanometers with a very narrow linewidth [16]. For very large scale systems where the tuning range of an LO laser is insufficient, one can employ several LO's for each optical receiver. In this case, each LO covers a different region of the tuning spectrum within the total frequency band occupied by all channels. This scheme is shown in Fig. 2(a). An alternative means is to use several

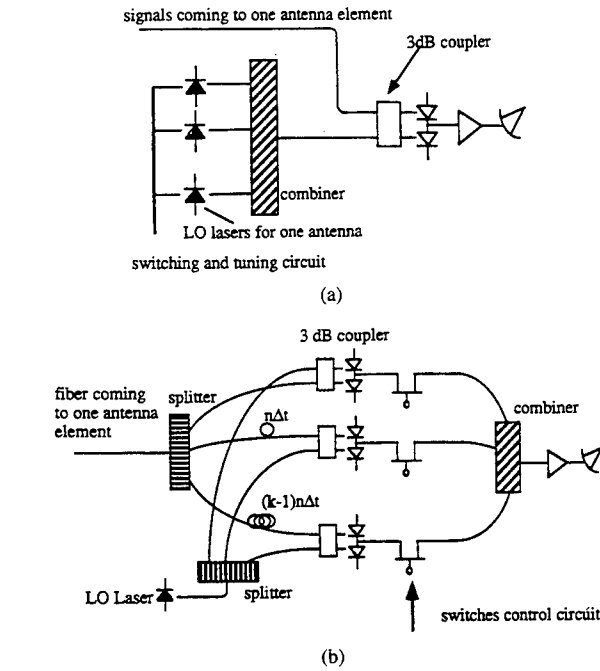


Fig. 2. Expansion methods for the transmitter structure using (a) the multiple local laser scheme, and (b) the multiple receiver scheme. Using these methods, the system can accommodate more delays than in Fig. 1 with a limited laser tuning range.

receivers corresponding to several different delays transmitted to one antenna element, which is shown in Fig. 2(b). For example, assume that the  $n$  delay lines at the combiner input introduce the delays:  $0, \Delta t, 2 \Delta t, \dots, (n-1) \Delta t$  in ascending order. Each signal is again split into  $k$  branches which introduce additional delays  $0, n\Delta t, 2n\Delta t, \dots, (k-1)n \Delta t$  after which they reach the different antenna element receivers. The antenna element only receives one of the several signals from these different receivers using electronic switches. By this means, the total number of different delays for the system is  $kn$ .

### B. The Receiver Antenna

Using a structure similar to that of the transmitter in Fig. 1, the system is also capable of detecting signals arriving from different directions. This is accomplished by delaying signals received from the several antenna elements so that they are added in phase to obtain a detectable output. Fig. 3(a) shows the basic receiver architecture. The signals from the various antenna elements are modulated on different optical carriers corresponding to different optical channels. The optical signals are then combined and transmitted from the antenna site to the optical receiver site, where they are incident on each optically coherent receiver through various lengths of fibers which introduce the true time delays. Here, each receiver corresponds to a particular delay. When the frequency of an LO laser is tuned to some optical channel, the associated optical receiver outputs the delayed microwave signal modulated on this channel. In the receive mode, the signal arriving at each antenna is delayed by an amount consistent with the beam direction, and the signals are then brought in phase and

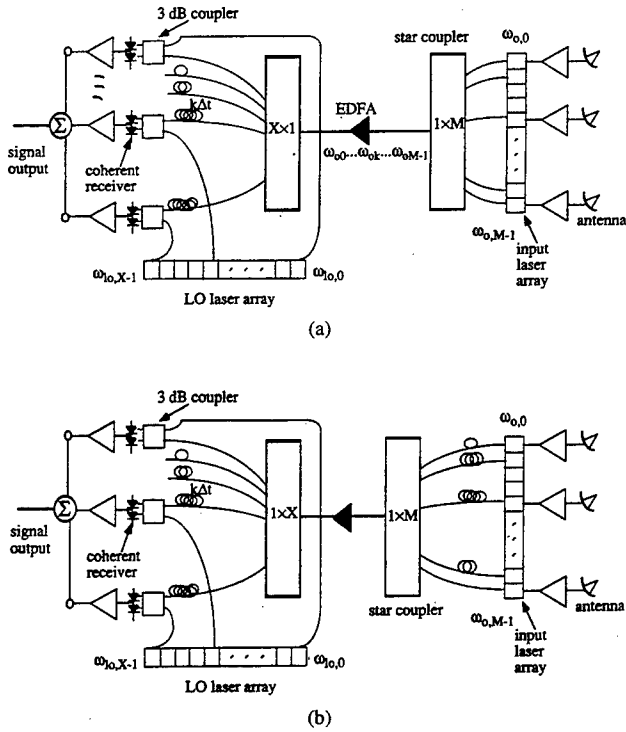


Fig. 3. The coherent optically controlled phased array antenna receiver. (a) The basic receiver structure, and (b) the receiver structure with less optical receivers and delay lines.

summed to obtain the total signal. Employing a sufficiently large number of optical receivers with various lengths of fibers ensures that the system can provide proper delays for each direction. From Fig. 3(a), we see that the receiver has advantages similar to that of the transmitter, such as using a single fiber as the main transmission line, amplification along this fiber etc.

The receiver is slightly more complex than the transmitter in terms of the number of delay lines used. Nevertheless, the number of optical delay lines (corresponding to the number of optical receivers) is linearly proportional to  $N$ , where  $N$  is the number of different delays required to achieve a given bit resolution. We will see below that the difference between the number of delays and delay lines arises since the transmitting and receiving signals of one antenna element do not necessarily share the same path in the optically coherent detection scheme. To understand how many delay lines are required, consider a one dimensional, linear phased array antenna. Assume that there are  $M$  antenna elements, and that there are  $N$  different, equally spaced delays at time intervals of  $0, \Delta t, 2 \Delta t, \dots, (N-1) \Delta t$ , where  $\Delta t$  is the smallest time increment. For receiving signals arriving from various angles, the delays introduced for the antenna elements 1 to  $M$  can either increase or decrease monotonically. For broadside detection (the signal oriented perpendicular to the plane of the antenna array), the signals received from all antenna elements should be fed with  $M$  identical delays. For directions near to but not at the broadside direction, the signals received from many neighboring antenna elements have to be

fed with identical delays due to lack of digital resolution. In the antenna transmitter, one delayed signal can be fed to any number of antenna elements simultaneously. For the antenna receiver, however, one would like to use one optical receiver to receive all the signals requiring the same delay. But as we show in Appendix A, this imposes extremely stringent requirements on the transmitter lasers, and also requires precise delays. Therefore, practical receivers must provide more than  $N$  delay lines to detect signals near the broadside direction. Employing coherent detection techniques, one receiver and its corresponding delay line can be used for different antenna elements at each different detection angle. Hence, the total number of delay lines is still much smaller than that required for the IM/DD detection scheme. In Appendix B, we show that for the special case of  $M = N$ , the total number of delay lines ( $X$ ) is approximately  $M \ln M$ . For the case where  $N > M$ ,  $X = (N - M) + M \ln M$ . These are both much smaller than  $M \times N$  required for an IM/DD system if  $M, N > 10$ .

We see from the above that for  $N \gg M$ ,  $X \approx N$ , where  $N$  is the smallest number of delays the system must provide for the required detection resolution. For the case where  $N$  is not much larger than  $M$ , we can further reduce the number of optical receivers (and delay lines) by the architecture shown in Fig. 3(b). Here, we introduce delays at both the optical receivers and the antenna elements. In this case, the total delay for the signal from one antenna element is the sum of the delays corresponding to the antenna element and the receiver. By appropriately arranging the delays for the antenna elements, the antenna can be pointed to every desired direction while the number of delay lines and optical receivers is reduced. In Appendix C, an arrangement of the delays at the antenna site is analyzed and it is found that when  $N = jM$ , the total number of delays needed at the receiver site ( $X$ ) is  $(1.5 + 1/j)N$  when  $j$  is an integer, and  $X = (1.5[j] + 1)M$  when  $j$  is not an integer, but where  $[j]$  is the least integer that is not smaller than  $j$ . Here,  $X$  is approximately linearly proportional to  $N$ . For example, if there are 128 antenna elements and the system requires 128 different delays (7 bit resolution), then using the arrangement given in Appendix C, only 320  $(= (1.5 + 1) \times 128)$  delay lines are needed at the optical receiver site. Such a system requires 128 optical transmitters and 320 coherent receivers with corresponding delays. We call this a "128  $\times$  320" system.

The analysis can easily be extended for two dimensional beam forming and steering (i.e. a planar phased array), where the smallest time increments  $\Delta t_1, \Delta t_2$  for the two spatial dimensions (elevation and azimuth) are different, and with  $N_1$  and  $N_2$  being the number of different delays for the two dimensions, respectively. The number of delay lines and optical receivers are still linearly proportional to the number of different delays,  $N_1 \cdot N_2$ , while for the IM/DD scheme, it is on the order of  $(N_1 \cdot N_2)^2$ . If  $\Delta t_1 = \Delta t_2$ , the number for both coherent and IM/DD systems are smaller than the corresponding systems where  $\Delta t_1 \neq \Delta t_2$ .

For the receiver antenna, the number of antenna elements determines the number of optical channels needed. If the tuning range of one LO laser is not sufficiently wide, multiple LO's can be used to cover the different frequency ranges,

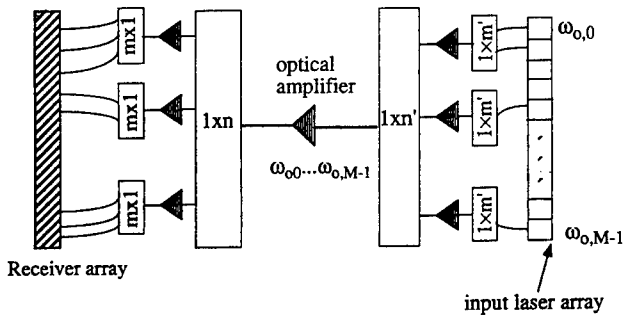


Fig. 4. The schematic diagram of a multistage optical amplification system.

similar to the transmitter structure in Fig. 2(b). Alternatively, the antenna array can be divided into several sub-groups, each of which has fewer antenna elements and needs a delay feed system with a smaller number of optical channels. The received signal is then just the sum of the output microwave signals from each sub-group.

### C. Optical Amplifier Performance

Both semiconductor optical amplifiers (SOA) and erbium-doped fiber amplifiers (EDFA) can be used to compensate for power losses at the combiners, splitters, etc., and to prevent degradation of the signal-to-noise ratio (SNR). The SOA is compact and can be integrated with other devices such as lasers, modulators, combiners/splitters, and has a wide bandwidth. On the other hand, the EDFA can accommodate more power, and the noise figure is low in comparison to the SOA. To achieve a high SNR, the system is most advantageously implemented in several cascaded gain stages as shown in Fig. 4. The total effective noise figure of the optical amplifier system with respect to the signal of one channel is [17]

$$F = L_1(K_1(F_1 - 1) + 1) + \frac{F_2 - 1}{G_1/L_1 L_2} + \frac{F_3 - 1}{G_1 G_2/L_1 L_2 L_3} \quad (1)$$

where  $G_n$  and  $F_n$  are the gain and noise figure, respectively, for the  $n$ th stage in the amplifier cascade,  $L_n$  is the optical loss before each stage, and  $K_1$  is the number of amplifiers in the first stage. Now,  $K_1$  is in (1) because after the signals combine, the noise in one channel is due to the amplified-spontaneous-emission (ASE) noise from all optical amplifiers in the first stage. Assume  $G_1/L_1 \gg 1$  (since the gain is usually much larger than the loss of the first stage) and  $G_i/L_i > 1$  for  $i = 2, 3$ . In this case, the contribution to the noise from the first stage amplifiers dominates over subsequent stages in the cascade. Provided that the gain of the following stages can compensate the loss of each stage, the noise figure is  $\sim L_1(K_1(F_1 - 1) + 1)$  even if there are additional splittings after the combinations in the architecture shown in Fig. 1, as required, for example, by the expanded transmitter in Fig. 2(b).

For an EDFA, the noise is mainly due to ASE noise even for multichannel amplification. On the other hand, an SOA has both ASE noise and crosstalk, which depends on the number of channels, the optical input power, and the modulation scheme of the optical signal. These gain depletion effects are difficult to treat, and are usually estimated numerically

[18]. For simplicity, therefore we consider here only EDFA-based systems. The performance of an example EDFA-based antenna feed system consisting of 128 transmitter lasers and 320 optical receivers is illustrated in Table I. For this system, the optical gain of one channel is  $-3.2$  dB, indicating that such coherent systems can be made nearly transparent. There have been reports of EDFA's with gains of 54 dB and 3.1-dB noise figure [19]. Thus, using currently available EDFA's, one can achieve the performance predicted in Table I, where the noise figure is approximately  $N \cdot F_1$  for each channel in an  $N$  channel system. The noise figure of the EDFA's of the example  $128 \times 320$  system is 25 dB. As will be shown below, this noise figure determines the overall system performance, especially the SNR and DR. Utilizing optical filters whose passbands are limited to the signal bandwidth after each EDFA, the noise figure can be further reduced to  $\sim L_1 F_1$ , or  $\sim 16$  dB.

### D. Miscellaneous System Issues

Fiber chromatic dispersion will cause signals propagating in different channels to travel at different speeds. This problem is especially acute for systems consisting of a large number of channels where the wavelength difference between some channels is quite large. When the system is used in aerospace applications, the length of the fiber is typically less than several tens of meters. In this case, even if the system covers a large frequency range, dispersion will not cause serious problems. However, for terrestrial systems where the fiber length can exceed a kilometer, dispersion can potentially introduce additional time delays for different channels, which cannot be neglected for precise beam steering. This is especially true for systems with many channels. To solve this problem, the central frequencies of the input laser arrays are fixed, thereby determining the optical group velocity of each channel. Assume that the group velocity of channel  $k$  is  $c_k$ , then after traveling through a fiber of length  $L$ , any other channel  $k$  will have an additional time delay of  $(L/c_k - L/c_0)$  compared to channel 0. To compensate for this additional delay, we make the fiber associated with channel  $k$ ,  $(L/c_k - L/c_0)c_k$  shorter before it combines with other channels. For example, a typical value of dispersion for dispersion-shifted single mode fiber at  $1.55 \mu\text{m}$  is around 1 ps/km-nm. For two optical channels separated in wavelength by  $\Delta\lambda = 1$  nm, and using a 1 km long fiber, the time delay difference is 1 ps. If the channel separation is 10 nm and the fiber length is 10 km, the additional delay would be 100 ps, which is a significant delay for a 1-GHz signal.

For very high frequency antenna systems (i.e. several tens of GHz), it is difficult to directly use coherent detection, because the intermediate frequency (frequency difference between the incoming optical signal and the LO signal) is too high for use with conventional microwave devices. In this case, the coherent system can be used to introduce true-time delay at a low frequency (e.g.  $\sim 1$  GHz). For producing microwave transmitting signals, microwave mixers and local oscillators are then used to up-shift the delayed signals into the high frequency band desired. Conversely, for receiving, mixers are used to down-shift the frequency before introducing the

time delays [20]. These microwave frequency shifts can be achieved up to frequencies as high as several tens of GHz using conventional diode mixers [21].

In this paper, we discuss digitalized time delays, which will introduce some errors in the desired beam characteristics [2]. For systems with a large number of delays, however, this error tends to be very small.

In the following sections, we calculate the SNR, SIR and DR of one channel in a  $128 \times 320$  example system, illustrating the system performance. However, in a phased array receiver, the final signal is the sum of the signals from each antenna element. Due to their coherence, the signal amplitudes are added, although the noise contributions are added in power. Hence, the system SNR, DR and SIR will be  $M$  times larger than those of one channel, where  $M$  is the number of antenna elements.

### III. SYSTEM EVALUATION

In this section, we discuss general approaches for the quantitative evaluation of the performance of the coherent optically controlled phased array antenna system. We first discuss the typical spectra of radar signals, and then derive expressions to calculate the signal-to-noise ratio (SNR), dynamic range (DR), signal-to-interchannel-interference ratio (SIR), optimum optical channel spacing and the number of optical channels that can be accommodated. In the following sections, we apply these expressions to evaluate the performance of an example antenna receiver which has 128 elements and 7 bit resolution (the  $128 \times 320$  system as discussed in Section II-B).

#### A. The Radar Spectrum

A radar signal typically consists of a sequence of pulsed, high frequency oscillations. The spectrum of this microwave signal can be expressed as [2]

$$C(f) = 0.5(C_b(f + f_m) + C_b(f - f_m)) \quad (2)$$

where

$$C_b(f) = \sum_{n=-\infty}^{\infty} \sin(\pi n \tau f_r) / (\pi n f_r) \delta(f - n f_r)$$

for a long train of coherent pulses,

and

$$C_b(f) = \sin(\pi \tau f) / (\pi f)$$

for an incoherent pulse train.

Here,  $f_r$  is the pulse repetition frequency (PRF),  $\tau$  is the pulse width, and  $f_m$  is the microwave oscillation frequency. From (2), we see that the characteristic spectrum of a radar signal is a sinc function centered at  $f_m$ , typically between 1 and 20 GHz, with most of the power concentrated in a comparatively narrow bandwidth which spans a frequency range on the order of  $1/\tau$  with a typical value of 1 MHz. The narrow bandwidth of the signal enables the system to greatly reduce the wideband noise.

For Doppler radar systems, a coherent pulse train is transmitted to obtain a nearly discrete spectrum, so that the frequency shifts within one PRF range can be determined [1].

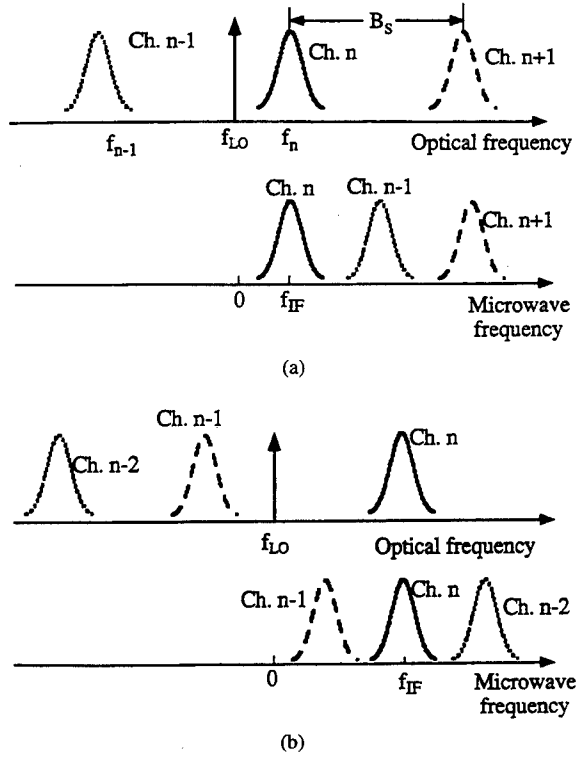


Fig. 5. Radar signal spectrum for (a) a single pulse and an incoherent pulse train, and (b) a long coherent pulse train.

From the following analysis, we find that the demodulated microwave signals from the optical carrier can still maintain the original spectrum of the modulating microwave signals, thereby ensuring that this system can employ Doppler phenomena.

#### B. System Noise

We now consider the noise from optical modulation, transmission and detection. After photodetection, for the simplest case, the IF (intermediate frequency) signal current can be expressed as

$$i_{IF}(t) = A(t) \cos[\omega_{IF}t + \phi_s(t) + \phi_{\text{phase}}(t)] + n(t) + n_{\text{int}}(t) \quad (3)$$

Here,  $A(t)$  and  $\phi_s(t)$  represent the amplitude and phase modulation, respectively, for the amplitude modulation (AM), frequency modulation (FM) or phase modulation (PM) schemes,  $\omega_{IF} = 2\pi f_{IF}$  is the angular IF frequency,  $\phi_{\text{phase}}$  is the laser phase noise,  $n(t)$  is the additive noise of the system, and  $n_{\text{int}}(t)$  is the interference signal current from other channels. In this paper, the noise power spectral density is taken single-side-band. The power spectral density (PSD) of the time derivative of the phase noise is [22]

$$S_{\dot{\phi}_{\text{phase}}} = 4\pi\Delta\nu \quad (4)$$

where  $\Delta\nu$  is the sum of the transmitter and LO laser linewidths. The additive noise,  $n(t)$ , consists of thermal noise, shot noise, relative intensity noise, and the beat of the LO laser with the EDFA amplified spontaneous emission (ASE) noise. The PSD of each noise source is given below [22],

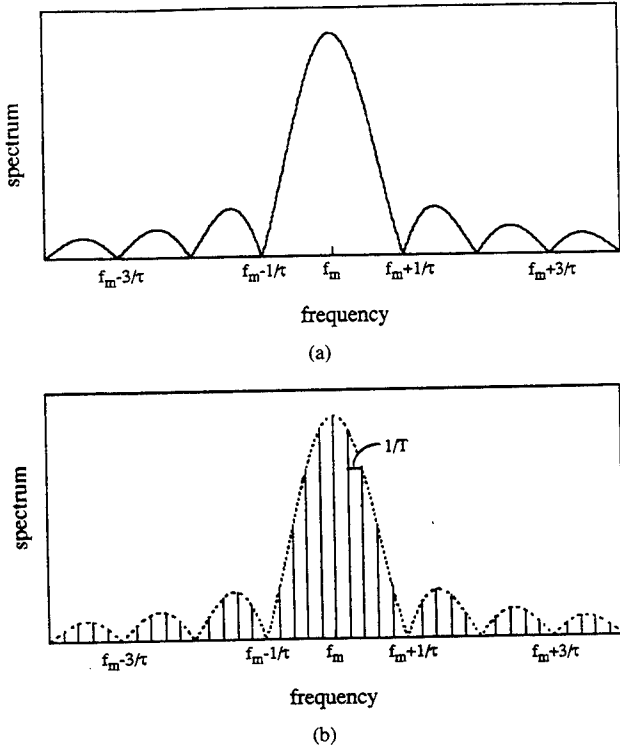


Fig. 6. Illustration of the channel placement for (a)  $|f_{n-1} - f_{LO}| > f_{IF}$ , the NEAR-LO scheme, and (b)  $|f_{n-1} - f_{LO}| < f_{IF}$ , the FAR-LO scheme. Here,  $f_n$  and  $f_{n-1}$  are the central optical frequencies of channel  $n$  and  $n-1$ ,  $f_{LO}$  is frequency of LO laser,  $f_{IF} = |f_n - f_{LO}|$  is the intermediate frequency, and  $B_s$  is the optical channel spacing. The second configuration can save some channel spacing for a high  $f_{IF}$  and a comparatively narrow signal bandwidth.

[23]. The thermal noise  $S_{n,thermal}$  is

$$S_{n,thermal} = \frac{4k_B T}{r} \quad (5)$$

where  $k_B$  is Boltzmann's constant,  $T$  is temperature and  $r$  is the input resistance of the receiver. The shot noise  $S_{n,shot}$  is

$$S_{n,shot} = 2eR(P_{LO} + P_{s-total}) \quad (6)$$

where  $R$  is the responsivity of the detector,  $P_{LO}$  is the optical power of the local oscillator, and  $P_{s-total}$  is the optical power of all signals incident on a receiver. That is,  $P_{s-total}$  is approximately equal to the optical power of one channel that is incident on a receiver ( $P_s$ ) multiplied by the number of channels. The LO-ASE beat noise  $S_{n,LO-ASE}$  is then given by

$$S_{n,LO-ASE} = 2R^2 h\nu (F-1) G_{tot} P_{LO} \quad (7)$$

where  $h$  is Planck's constant,  $\nu$  is the optical frequency,  $F$  is the optical amplifier noise figure, which can be obtained from (1), and  $G_{tot}$  is the total optical gain for one channel. Next, the PSD of the laser relative intensity noise is [22]

$$S_{n,RIN} = R^2 (P_{LO}^2 10^{RIN_{LO}/10} + P_s^2 10^{RIN_s/10}) \quad (8)$$

where  $RIN_s$  and  $RIN_{LO}$  are the relative intensity noise contributions (in dB/Hz) of the transmitter and LO lasers, respectively. If balanced optical receivers are considered, then most of the contribution of the relative intensity noise, together with

the direct detection and beat terms between signal channels will be canceled [24]. We will see below that the RIN nevertheless contributes to the total noise of coherent receivers. Summing (5)–(7), the PSD of the additive noise current is given by

$$S_n(f) = 2R^2 h\nu (F-1) G_{tot} P_{LO} + 2eR(P_{LO} + P_{s-total}) + \frac{4k_B T}{r}. \quad (9)$$

When  $P_{LO}$  is sufficiently large (typically  $>0$  dBm), the shot noise is larger than the thermal noise. Also, the LO-ASE beat noise is larger than the shot noise provided that the optical amplification is sufficiently large. Thus the LO-ASE noise usually dominates the frequency independent noise expression in (9). The discussion in Section II shows that the ASE noise usually comes from the first amplifier stage. Thus, small variations in the subsequent splitting and amplification will have little effect on the actual SNR if the LO-ASE noise dominates.

### C. Signal-to-Interchannel-Interference Ratio (SIR) and Dynamic Range (DR)

For a large multichannel system, one must consider the bandwidth and minimum channel spacing required to accommodate the desired number of delays while keeping the interchannel interference at an acceptably low level. If balanced coherent receivers are used, interference from all other channels degrades the signal of the primary channel only through the effect of excess shot noise and the LO-undesired channel interference [24]. We have considered the excess shot noise in (6). Here the SIR is defined as the ratio of the power received in the primary signal channel ( $P_{s-final}$ ) to the total LO/undesired channel interference power ( $P_{int-final}$ ) at the output. That is

$$SIR = \frac{P_{s-final}}{P_{int-final}}. \quad (10)$$

Following Glance, *et al.* [25], there are two schemes which avoid excessive interference in the IF domain. In both schemes, optical channels are equally spaced in optical frequency domain. In one scheme, the LO frequency is positioned nearest to the primary channel as shown in Fig. 6(a). We name this the "NEAR-LO" scheme. In this scheme, a channel spacing of  $D > 2f_{IF}$  is required. Most of the interference for the primary channel,  $k$ , comes from the nearest neighbor channel,  $k-1$ . Increasing  $D$  will decrease the interference. Alternatively, the LO frequency can be positioned nearest to one of the adjacent channels [Fig. 6(b)]. When a high IF frequency and comparatively narrow signal bandwidth are required, as is the case for the AM modulation-demodulation, or a small modulation index for FM and PM, Fig. 6(b) only requires an optical channel spacing which is comparable to  $f_{IF}$ , while keeping the interchannel interference at an acceptably low level. For Fig. 6(b), the interchannel interference mainly comes from channels  $k-1$  and  $k-2$ . In this scheme (called the "FAR-LO" scheme), for a fixed  $f_{IF}$ , the interference is minimum at  $D = 4f_{IF}/3$ , where the channels are also equally spaced in the IF domain. In Sections

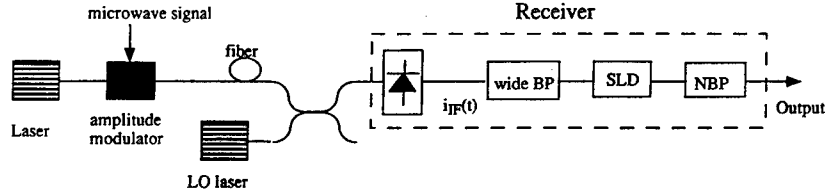


Fig. 7. Schematic diagram of an AM-WIRNA link. WIRNA stands for wideband filter-rectifier-narrow-band filter receiver. WBP = wide bandpass filter, NBP = narrow bandpass filter, and SLD = square law detector.

IV and V, we will estimate the SIR for both the NEAR-LO and FAR-LO schemes and make some comparisons. Given the optical channel spacing required to get a small SIR and the tuning range available to LO lasers, we will calculate the number of optical channels that can be accommodated in each case.

The dynamic range of the microwave-optical link is defined as the ratio of the maximum input RF power ( $P_{\max}$ ) to the minimum input RF power ( $P_{\min}$ ). Here,  $P_{\min}$  is the RF power that results in  $S/N = 1$  at the output, and  $P_{\max}$  is the power when the nonlinear distortion power equals the noise power. Hence [22]

$$\text{DR} = 10 \log \left[ \frac{P_{\text{in-max}}}{P_{\text{in-min}}} \right]. \quad (11)$$

#### IV. ANALOG AM ANTENNA LINKS

##### A. SNR Performance of AM Links

Wideband filter-rectifier-narrow-band filter (WIRNA) processing has been suggested [22] as an efficient and laser-phase-noise-insensitive means to receive analog AM signals. A block diagram of a typical WIRNA receiver is shown in Fig. 7. Here, a wide bandpass filter is used to pass the IF signal. This is followed by a square law detector and a narrow band filter to demodulate the signal. For the antenna systems in Figs. 1 and 3, the IF current,  $i_{\text{IF}}(t)$  is given by

$$i_{\text{IF}}(t) = \frac{A_s}{\sqrt{2}} [\cos(\omega_{\text{IF}}t + \phi_{\text{phase}}(t) + mx(t)) - \sin(\omega_{\text{IF}}t + \phi_{\text{phase}}(t))] + n(t) + n_{\text{int}}(t) \quad (12)$$

with  $A_s(t) = 2R\sqrt{P_s P_{\text{LO}}}$ . Also,  $P_s$  is the optical signal power of one channel and  $P_{\text{LO}}$  is the LO power. Here,  $m$  is the modulation index and  $x(t)$  is the normalized modulation signal. The Mach-Zehnder modulated signal is an AM modulated signal in the sense that when the IF current is squared, the signal term can be obtained by a low pass filter. This is evident by taking the square of (12) while neglecting all of the noise terms.

Assume that the interference noise,  $n_{\text{int}}(t)$  is negligible and  $mx(t) \ll 1$ , then (12) becomes

$$i_{\text{IF}}(t) = \frac{A_s}{\sqrt{2}} [\cos(\omega_{\text{IF}}t + \phi_{\text{phase}}(t)) - (1 + mx(t)) \times \sin(\omega_{\text{IF}}t + \phi_{\text{phase}}(t))] + n(t). \quad (13)$$

Most of the signal power is concentrated around  $f_{\text{IF}} \pm f_m$ . For a laser linewidth of  $\Delta\nu = 0$ , more than 95% of the signal power falls within  $f_{\text{IF}} \pm (f_m + 2/\tau)$ . Hence, a rectangular

IF filter which covers this frequency range in a WIRNA receiver is desirable. With a non-zero laser linewidth, the signal spectrum is widened and the filter needs to be approximately  $12.7 \Delta\nu$  wider to accommodate more than 95% of the signal energy [27]. The IF bandwidth is therefore given by

$$B_{\text{IF}} = 2f_m + 4/\tau + 12.7 \Delta\nu. \quad (14)$$

The second filter should be centered at  $f_m$  with a bandwidth of several  $1/\tau$  to obtain the final output. For convenience of analysis, an ideal rectangular bandpass filter is assumed. The transfer function of the two filters can thus be expressed as

$$H_{\text{IF}}(f) = \begin{cases} 1 & |f - f_{\text{IF}}| < f_m + 2/\tau + 6.4 \Delta\nu \\ 0 & \text{otherwise.} \end{cases} \quad (15)$$

$$H_2(f) = \begin{cases} 1 & |f - f_m| < 2/\tau \\ 0 & \text{otherwise.} \end{cases} \quad (16)$$

The impulse response of the two filters,  $h_{\text{IF}}(t)$  and  $h_2(t)$ , can be calculated through the Fourier transform of  $H_{\text{IF}}(f)$  and  $H_2(f)$ . This leads to the following expression for the output power after the square law device and narrow band filter [22]

$$\begin{aligned} P_{\text{out}} &= P_{\text{sig}} + P_{\text{sd}} + P_{\text{sn}} + P_{\text{nn}} + P_{\text{RIN,ad}} \\ &= \Gamma_1 m^2 A_s^4 + (\Gamma_2 m^2 + \Gamma_3) A_s^4 \\ &\quad + (\Gamma_4 m^2 + \Gamma_5) A_s^2 S_n(f) + \Gamma_6 S_n^2(f) \\ &\quad + \Gamma_1 A_s^4 \left( 10^{\frac{\text{RIN}_{\text{LO}}}{10}} + 10^{\frac{\text{RIN}_s}{10}} \right) B. \end{aligned} \quad (17)$$

The first term is the signal power, and the remaining terms are noise contributions. The  $\Gamma$  parameters depend on  $B_{\text{IF}}$  and  $B$ , with  $\Gamma_3$  also depending on  $f_{\text{IF}}$ . The term  $P_{\text{sd}}$  is due to phase noise,  $P_{\text{sn}}$  is the beat of the signal and the additive noise, and  $P_{\text{nn}}$  is the squared additive noise. Also,  $P_{\text{RIN,ad}}$  is the noise term induced by the laser RIN in the LO-desired channel cross term, and cannot be canceled by a balanced receiver. The two terms in  $P_{\text{sd}}$  and  $P_{\text{sn}}$  are due to the received signal having both a carrier and message term. Laser phase noise causes the signal spectrum to be broadened, and it degrades the SNR in two ways. First, since the IF signal spectrum is broadened, when the signal passes the IF filter, some of the signal spectrum is cut off. Thus, it causes phase-noise-to-intensity-noise conversion. Second, the spectrum of the square of the IF current in (3) has a carrier component at  $2f_{\text{IF}}$ , which is also broadened by the laser phase noise. If  $f_{\text{IF}}$  is finite, some power of this term falls within the bandwidth,  $B$ , and degrades the signal.

For a reasonable optical power,  $P_{\text{sn}}$  is always much larger than  $P_{\text{nn}}$ . Thus, if the laser linewidth is very narrow, the RIN is very small ( $-140$  dB/Hz), and  $mx(t) \ll 1$ . The expression

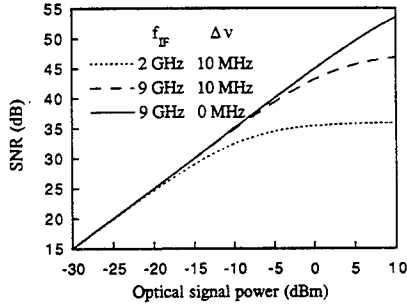


Fig. 8. Signal-to-noise ratio (SNR) versus signal power of one channel of AM links for  $P_{LO} = 10$  dBm,  $B = 1$  MHz,  $f_m = 1$  GHz,  $R = 0.6$  A/W,  $m = 0.1$ .

for the SNR then simplifies to

$$\text{SNR} = \frac{4\Gamma_1 m^2 R^2 P_{LO} P_s G_{tot}}{\Gamma_5 S_n(f)} \quad (18)$$

Usually the LO-ASE noise is the most significant noise in source  $S_n(f)$ . Thus, (18) further simplifies to

$$\text{SNR} = \frac{2\Gamma_1 m^2 P_s}{\Gamma_5 h\nu F} \quad (19)$$

where  $\Gamma_5$  is proportional to  $B$ . If  $\Delta\nu$  is not too large, and if the IF frequency is much larger than the microwave signal frequency, then the signal distortion due to the laser phase noise is very low. As both theoretical and experimental results have shown [22], [26], this scheme is basically linewidth insensitive. The demodulated microwave signal can therefore maintain the spectral purity of the original signal. Thus, for systems using lasers with low RIN, narrow linewidth, and high LO power, (19) can be used to calculate the SNR for one optical channel.

Fig. 8 is a plot of SNR versus  $P_s$  for one channel in the  $128 \times 320$  example system of Section II. For a 1 GHz signal, the laser phase noise ( $\Delta\nu \neq 0$ ) degrades the signal more for a low IF (2 GHz) than for a high IF (9 GHz) due to the reasons discussed above. The SNR is 5 to 10 dB lower for  $f_{IF} = 2$  GHz than at 9 GHz. It is shown that for  $\Delta\nu = 10$  MHz, with a high IF and a wide IF bandpass filter, and for  $P_s < P_{LO}$ , the main noise source is the LO-ASE noise, and the SNR increases with  $P_s$ . As  $P_s$  approaches  $P_{LO}$ , the increase of SNR with  $P_s$  saturates. The saturation is due to the dominance of shot noise contributed by the total optical signal power of all the channels, as indicated in (6). Further increase in the optical signal power above  $P_{LO}$  will therefore not improve the SNR performance. As the laser linewidth increases, more of the signal power spectrum is cut off by the IF bandpass filter, causing the phase-noise-to-intensity-noise conversion, which in turn decreases the SNR. Nevertheless, from the calculations we see that if  $P_s$  is not excessively large (i.e.  $< 5$  dBm), this effect is small. From Fig. 8, we see that for  $m = 0.1$ ,  $\Delta\nu < 10$  MHz,  $P_s = 0$  dBm,  $f_{IF} = 9$  GHz,  $B_{IF} = 3$  GHz,  $B = 1$  MHz then  $\text{SNR} = 46$  dB. Thus, in order to get a high SNR, then a high IF, small  $\Delta\nu$  and high signal power are required.

As the noise is mainly due to the LO-ASE noise, putting an optical filter after each first stage optical amplifier significantly reduces the ASE noise of the adjacent channels. For our

example system, the SNR of one channel can be increased by 10 dB using such filter techniques.

### B. SIR and the Channel Spacing

To calculate the interchannel interference, we simplify the problem by considering the contribution from neighboring channels whose signal spectrum is noise-free, i.e. we assume  $\text{SNR} \gg 1$ . From (13), the spectrum of one channel of the AM IF signal without noise is given by

$$C_{AM}(f) = A_s \left[ \delta(f - f_{IF}) + \frac{1}{\sqrt{2}} m C(f - f_{IF}) \right] \quad (20)$$

where  $C(f)$  is the spectral coefficient of the radar signal given in (2). Equation 12 shows that the IF current has an interference term. After being filtered and squared, there are two terms from interference: one is the beat between the signal and the interference, the other is the square term of the interference. In the limit of small interference, the first term is always much larger than the second. Thus the interference power can be calculated as

$$P_{int} = \int \{ [s(f)H_{IF}(f)] * [\text{int}(f)H_{IF}(f)] \cdot H_2(f) \}^2 df \quad (21)$$

where  $s(f)$  and  $\text{int}(f)$  are the spectra of the signal and interference currents at the IF stage, respectively, and  $*$  denotes the convolution operation.

Fig. 9 shows the SIR for the AM scheme where the channel bandwidth accommodates more than 95% of the signal energy. Usually for  $f_m \tau \gg 1$ ,  $B_{IF}$  is slightly larger than  $2f_m$ . For the NEAR-LO scheme shown in Figs. 6(a) and 9(a), the calculations indicate that when the channel spacing ( $D$ ) is slightly more than  $2f_{IF} + 2f_m$ , then  $\text{SIR} > 60$  dB. For the FAR-LO scheme in Figs. 6(b) and 9(b),  $\text{SIR} > 60$  dB when  $D$  is in a small range from  $f_{IF} + f_m$  to  $2f_{IF} - 2f_m$ , and the SIR is at maximum when  $D = 4f_{IF}/3$ . For both schemes, a smaller  $f_{IF}$  leads to a smaller  $D$  and SIR. For multichannel systems, on one hand, we want  $D$  small so that for a given frequency tuning range, more channels can be used; on the other hand, we want to keep both SIR and SNR large to get a high quality signal, and this requires a large  $f_{IF}$  and  $D$ . Since the SIR is very high for this system, the SNR and channel spacing are the main concerns in choosing a proper  $f_{IF}$ . To get a high SNR, a large  $f_{IF}$  is required, and the FAR-LO scheme can be used to reduce channel spacing. For  $f_{IF} = 9f_m$  using the FAR-LO scheme and a channel spacing of  $\sim 12f_m$ , the SIR can be as high as 70 dB. These calculations are independent of the modulation depth, optical power, or RF power. When the SNR changes as the optical power or modulation index changes, the SIR does not change. Hence, for proper channel spacing, interchannel interference does little to degrade the system performance.

### C. Dynamic Range of the AM Links

From the results of Section IV-B, we know that the interchannel interference can always be kept very low while the microwave signal power or the optical signal power changes, and thus it has little effect on the dynamic range. Taking the

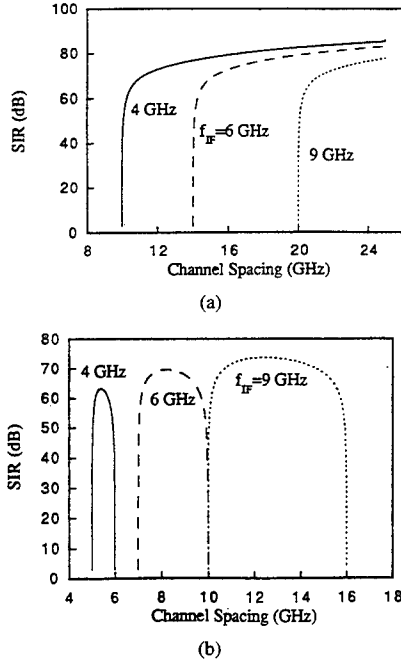


Fig. 9. Signal-to-interchannel-interference ratio (SIR) versus channel spacing of AM links for (a) the NEAR-LO scheme, and (b) the FAR-LO scheme of Fig. 6 for a 1-GHz signal. The SIR is insensitive to the modulation index and optical power. Because an ideal balanced receiver is assumed, more channels would have little effect on this result.

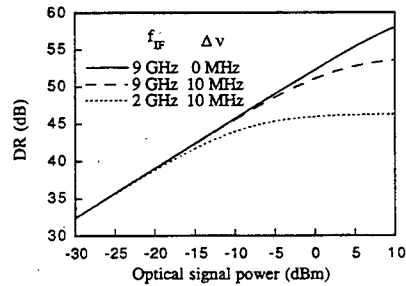


Fig. 10. Dynamic range (DR) of AM links. The DR is limited by the noise floor and the third order intermodulation distortion.

third order intermodulation distortion as the limit for channel linearity, the dynamic range of AM links is calculated using (22), shown at the bottom of the page.

Fig. 10 shows the calculated DR for different laser linewidths,  $\Delta\nu$ , and different IF frequencies. It is found that within a reasonable signal power range, if  $\Delta\nu$  is not too large (i.e.  $< 10$  MHz), and the  $f_{IF}$  is high (e.g. 9 GHz), the laser phase noise does not affect the DR performance. When the signal power of one channel at the transmitter is only  $-5$  dBm, the dynamic range is around 50 dB for a 1-MHz bandwidth, which corresponds to 110 dB/Hz. These values suggest reasonably good DR performance.

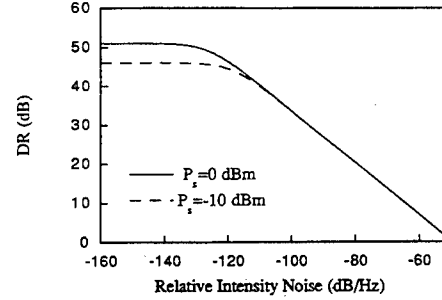


Fig. 11. Relative-intensity-noise (RIN) effect on the DR of AM links for  $B = 1$  MHz,  $f_{IF} = 9$  GHz,  $\Delta\nu = 10$  MHz and  $P_{LO} = 10$  dBm. Both the transmitter and LO lasers are assumed to have the same RIN value.

The above calculations assume that the RIN of lasers is very small ( $< -140$  dB/Hz). Fig. 11 shows the effect of RIN on the dynamic range of an AM-WIRNA receiver. We see that the system performance is reasonably insensitive to the RIN for most practically achievable laser noise levels [28]. For example, when  $P_{LO} = 10$  dBm, the DR is flat up to  $RIN = -130$  dB/Hz for  $P_s = 0$  dBm, and it is flat up to  $RIN = -120$  dB/Hz for  $P_s = -10$  dBm.

The above calculations also assume a narrow passband of the final filter. In an actual system, the received signal is down-shifted in frequency by mixing with a local oscillator prior to the narrow bandpass filter. Since mixing with a pure local oscillator signal results in a simple frequency transfer of the signal and noise spectra, the noise effect on the optical links remains the same as obtained above, as well as for the FM and PM schemes described in the following section.

The calculations of this section show that for one channel in a "128  $\times$  320" example system, the optical AM scheme achieves a high  $SIR = 70$  dB, and  $DR = 50$  dB for a 1-MHz signal bandwidth. Furthermore, a channel spacing of  $12f_m$  is sufficient (for  $f_{IF} = 9f_m$ ) if the laser linewidth and  $1/\tau$  is much smaller than  $f_m$ , which is usually true. Given that  $1 \text{ \AA} \cong 12$  GHz, a 10-nm laser tuning range can easily accommodate 100 optical channels for a 1 GHz microwave signal.

## V. FM AND PM PHASE DELAY SCHEMES

### A. SNR of the FM Scheme

Fig. 12 is a schematic diagram for a typical optical FM demodulation receiver [22]. After the heterodyne photodetection, a rectangular bandpass filter ( $B_{IF}$ ) is used to pass most of the power of the selected channel while reducing interference from all other channels. The signal is then demodulated by an electronic differentiator and envelope detector, and then passes a second bandpass filter similar to that used in AM schemes to obtain a noise-reduced output signal. Carson's Law [17] states

$$DR = 10 \log \left[ 8 \left( \frac{\Gamma_1 A_s^4}{\Gamma_3 A_s^4 + \Gamma_5 A_s^2 S_n(f) + \Gamma_6 S_n(f)^2 + \Gamma_1 A_s^4 (10^{RIN_{LO}/10} + 10^{RIN_s/10}) B} \right)^{\frac{2}{3}} \right]. \quad (22)$$

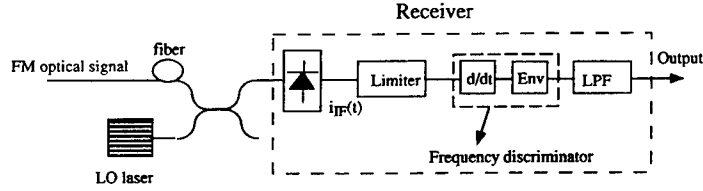


Fig. 12. Schematic diagram of an optical FM receiver. Here,  $d/dt$  is the microwave differentiator, Env is the envelope detector, and LPF is the low pass filter.

that to pass nearly 98% of the signal power,  $B_{IF}$  must be

$$B_{IF} = 2(\beta + 1)B_e \quad (23)$$

where  $B_e$  is equal to the high frequency cutoff of the final pass band of (16), and  $\beta$  is the modulation index. If  $\tau f_m \ll 1$ ,  $B_e$  is approximately equal to  $f_m$ . We now define  $\Delta f$  as the maximum instantaneous optical frequency deviation

$$\Delta f = \beta B_e \cong \beta f_m. \quad (24)$$

Once again we use [22] as the starting point for analyzing FM link performance. For our architecture, the power spectral density (PSD) around  $f_m$  caused by the additive noise after the discriminator is

$$S_N = S_n(f)(2\pi f_m \tau_D)^2 \quad (25)$$

where  $\tau_D$  is the time constant of the differentiator. The PSD of the noise current around  $f_m$  caused by phase noise is then

$$S_{\text{phase}} = 4\pi\tau_D^2 R^2 P_s G_{\text{tot}} P_{LO} \Delta\nu. \quad (26)$$

Here, the phase noise of lasers becomes white noise in the microwave frequency domain after signal demodulation. Thus the demodulated signal can still have a linewidth equal to that of the original microwave signal.

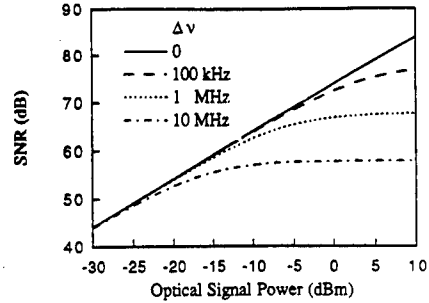
From (25) and (26), the SNR for FM systems is

$$\text{SNR} = \frac{2\pi^2 \Delta f^2 R^2 P_s G_{\text{tot}} P_{LO}}{B[S_n(2\pi f_m)^2 + 4\pi R^2 P_s G_{\text{tot}} P_{LO} \Delta\nu]}. \quad (27)$$

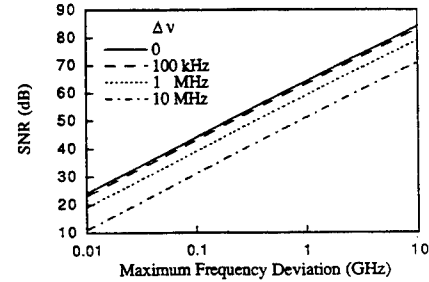
Usually the LO-ASE beat noise is the most significant contribution to  $S_n(f)$ , in which case the above formula can be simply expressed as

$$\text{SNR}^{-1} = \frac{B}{\Delta f^2} \left[ \frac{4h\nu F f_m^2}{P_s} + \frac{2\Delta\nu}{\pi} \right]. \quad (28)$$

It is shown in (27) and (28) that when the product of the signal power and the laser linewidth is large, the phase noise is the most significant noise source. Otherwise the postdetector white noise, especially the LO-ASE noise, is dominant. Fig. 13 shows the calculations of SNR for one channel in the example system of Table I. Fig. 13(a) shows SNR versus the signal power for different laser linewidths. For  $P_s = -10$  dBm, the white noise dominates when the laser linewidth is below 100 kHz. When  $\Delta\nu > 1$  MHz, phase noise tends to dominate. It is also clear from Fig. 13(a) that when the optical signal power is large, the laser phase noise limits the highest SNR that one channel can achieve. Further increasing signal power beyond a certain point will not improve the system SNR performance. With the optical link parameters given in Table I and  $\Delta\nu = 1$  MHz, a final passband of 1 MHz, a signal power of  $-10$  dBm,



(a)



(b)

Fig. 13. Signal-to-noise ratio (SNR) of FM schemes for different laser linewidths. (a) SNR versus the optical signal power, and (b) SNR versus the maximum frequency deviation.

a LO power of 10 dBm, and  $\Delta f = 2$  GHz, we obtain SNR = 64 dB, which is 124 dB/Hz. This is significantly higher than can be obtained using the AM scheme for the same input optical power. Fig. 13(b) shows the SNR versus the maximum frequency deviation ( $\Delta f$ ). We see that increasing the maximum frequency deviation by one order of magnitude increases the SNR by 20 dB since  $\text{SNR} \propto \Delta f^2$  in (27) and (28).

### B. SIR and Channel Spacing for FM Links

Most of the signal power in the IF current lies around  $f_{IF} \pm k f_m$  for  $k = 0, 1, 2, \dots$ , and the interference power lies around  $|f_{o,\text{adj}} - f_{LO}| \pm k f_m$ . Here,  $f_{o,\text{adj}}$  is the central optical frequency of the interference channel and  $f_{LO}$  is the LO frequency. Following [17], the most significant interference ( $P_{\text{int-IF}}$ ) comes from the spectral components that are around  $f_{IF} \pm f_m$ . The SIR can be expressed as

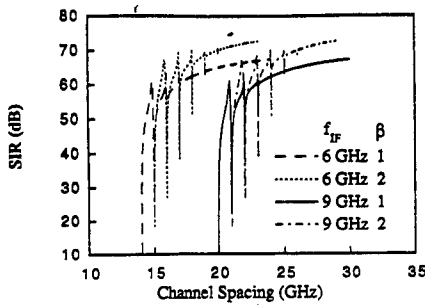
$$\text{SIR}_{\text{FM}} = \frac{\Delta f^2 P_{s\text{-IF}}}{f_m^2 P_{\text{int-IF}}} = \frac{\beta^2 P_{s\text{-IF}}}{P_{\text{int-IF}}} \quad (29)$$

where the  $P_{s\text{-IF}}$  is the signal power at the IF stage. Fig. 14(a) and (b) shows the SIR versus channel spacing for both kinds of channel arrangements illustrated in Fig. 6. For the NEAR-

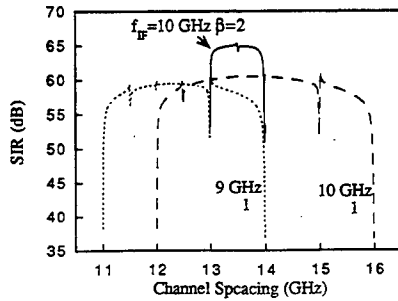
TABLE I  
LOSSES IN AN EDFA-BASED 128 × 320 SYSTEM

Component	Optical Loss (dB)	Excess Loss (dB)*	Optical Gain (dB)	Noise Figure (dB)	Optical Signal Power/ Input Signal (dB)
16×1 Combiner (L1)	12	0.2			-12.2
EDFA (G1, F1)			21.2	4	9
8×1 combiner (L2)	9	0.2			-0.2
Fiber	1				-1.2
EDFA (G2, F2)			10.2	4	9
1×16 Splitter (L3)	9	0.2			-3.2
EDFA (G3, F3)			15.2	4	12
1×20 (L4)	13	0.2			-1.2

\*Losses are taken to be 0.1 dB for each splice connection



(a)



(b)

Fig. 14. Signal-to-interchannel-interference (SIR) versus channel spacing of (a) the NEAR-LO scheme (b) the FAR-LO FM scheme for a 1 GHz signal.

LO scheme in Fig. 6(a) where  $|f_{n-1} - f_{LO}| > |f_n - f_{LO}|$ , a high SIR can be achieved for FM schemes. For example, for  $\beta = 2$ ,  $f_{IF} = 9f_m$  and  $B_s = 25f_m$ , then  $SIR = 64$  dB. The channel spacing, however, should be  $> 2(\beta + 1)f_m + 2f_{IF}$ , which is larger than that required for AM transmission. A smaller  $f_{IF}$  leads to a smaller channel spacing, although  $f_{IF}$  should be greater than  $(\beta + 1)f_m$  in order to have a sufficiently wide IF passband to pass most of the signal power. Generally speaking, for FM, if a large modulation index is used, we employ the NEAR-LO scheme.

For the FAR-LO scheme in Fig. 6(b), then  $|f_{n-1} - f_{LO}| > |f_n - f_{LO}|$ . Assuming  $\beta = 2$  and  $f_{IF} = 10$  GHz, the SIR is around 57 dB when the channel spacing is between  $13f_m$  and  $14f_m$ . As illustrated in Fig. 6(b), the FAR-LO scheme is only suitable for narrow channel bandwidths, i.e. for a small modulation index, or a small  $\Delta f$ . The demodulation of the FM

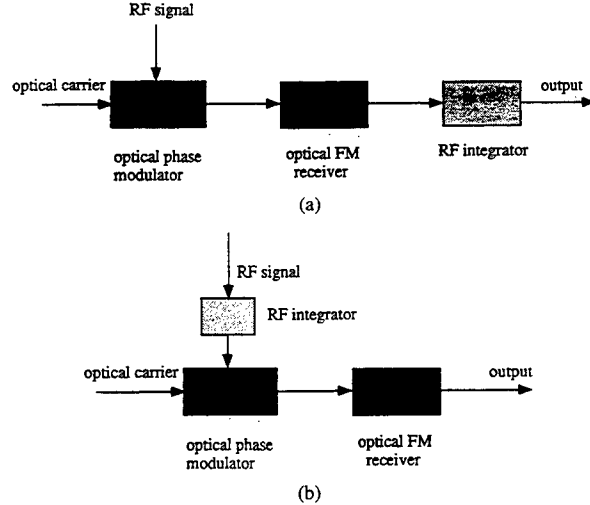


Fig. 15. Schematic diagram for optical PM receivers. Here, the optical FM receiver stands for the block diagram "receiver" in Fig. 12.

signal requires envelop detection at the last step (see Fig. 12). Thus a large  $f_{IF}$  is desirable to obtain a high quality signal. Under this situation (high  $f_{IF}$  and low  $\beta$ ), the FAR-LO scheme is preferred because it uses a smaller channel spacing. Due to the large total bandwidths, a 100 Å laser tuning range is needed to accommodate 100 channels.

### C. Dynamic Range of FM Systems

To obtain a high SNR and a small distortion of the demodulated signal, a large linear frequency response range of the laser to the modulation current or voltage is desirable. The SNR calculations also show the DR for the corresponding largest linear frequency response. For example, Fig. 13 shows that with parameters of the 128 × 320 system given in Table I, a laser linewidth of  $\Delta\nu = 1$  MHz, a signal bandwidth of 1 MHz, an optical signal power of  $-10$  dBm per channel, and a maximum linear optical frequency deviation of 2 GHz, the  $SNR = 64$  dB, and the DR of a single channel is also 64 dB.

### D. The PM Scheme

There are two ways of using optical phase modulation to transmit the radar signal (see Fig. 15). Here, the block diagram of the "optical FM receiver" represents the schematic diagram shown in Fig. 12. We see that the difference between Figs. 15(a) and 15(b) is that the RF integrator is placed either before phase modulating the light or after the optical FM receiver. If the RF integrator is placed before phase modulation, the integrated radar signal is still a pulsed oscillation of the original frequency with a phase change, which is similar to the integration of a sinusoidal signal. Thus, for the cases in Fig. 15, the phase modulation spectrum is similar to that for FM modulation. For the scheme of Fig. 15(a), the performance evaluation is almost the same as the FM scheme discussed above. For the scheme of Fig. 15(b), the laser phase noise directly affects the final signal, which might degrade the signal somewhat more severely.

In both FM and PM, there are two main noise sources: LO-ASE noise and laser phase noise. Reducing the laser phase noise or increasing the maximum optical frequency deviation can increase the SNR or DR of the system. For a small modulation index, the FAR-LO scheme in Fig. 6(a) can give a much narrower channel spacing while keeping the SIR high. For the case of a large modulation index, the NEAR-LO scheme has to be used and a much larger channel spacing is needed. For a 1-GHz radar signal, 100 channels can be accommodated by lasers with a tuning range of 100 Å. One channel can achieve a 60-dB dynamic range for a 1 MHz signal bandwidth, even with a small modulation index.

## VI. SYSTEM COMPARISONS

We now compare the coherent system and a typical archetype IM/DD system. The most important advantage of the coherent optically controlled phased array antenna described here is that it is readily expandable to a large number of elements. The basic system can easily accommodate  $10^2$  channels in a single fiber, and feed any combination of the  $10^2$  true-time delays to  $10^2$  antenna array elements by using only  $10^2$  optical transmitters and coherent receivers. In contrast, a generic IM/DD system [10] typically requires  $10^4$  lasers and  $10^4$  fibers of precisely determined lengths. If the transmitter lasers are far away from the antenna elements, the IM/DD system requires an additional  $10^2$  long transmission fibers to be cut precisely to within 0.1 mm and maintained in the same configuration so that the total optical path of the several transmission fibers are equal. For both the antenna transmitter and receiver, the numbers of lasers, optical receivers and precisely cut fibers of the coherent system are far less than that required for an IM/DD system. In addition, the receiver sensitivity, direction sweep rate, SNR and DR of the coherent scheme is often better than or comparable to IM/DD systems.

In recent years, there have been substantial improvements in coherent detection techniques. For example, there have been several proposals and demonstrations of frequency stabilization schemes [29], [30]. External cavity lasers with gratings can have several thousands of GHz tuning range with laser linewidths below 1 MHz [16]. Polarization diversity methods can also be used to maintain polarization control [31]. Thus, although one coherent link is more complex than an IM/DD link because of the difficulties inherent in frequency stabilization of the transmitter lasers, wide tuning range of the local lasers and polarization control, for a large scale antenna system such as those currently under consideration, the coherent approach is more readily adaptable.

An alternative architecture is based on wavelength-division-multiplexing, direct-detection (WDM/DD) systems. The transmitter and receiver structures described in Section II of this paper are also suitable for a WDM/DD system by using tunable optical receivers (e.g., tunable optical filters plus direct detection receivers) instead of coherent receivers. There has been a report of a  $10^2$  channel WDM system using tunable optical receivers [29]. Coherent systems have an inherent advantage over the WDM systems: due to the sharp passband shape of the IF bandpass filter in the microwave

TABLE II  
COMPARISONS OF COHERENT, IM/DD AND  
WDM/DD PHASED ARRAY ANTENNA SYSTEMS

System architecture	IM/DD	OFDM, direct detection	Coherent heterodyne
Receiver	Direct-detection, single channel	tunable optical filter multichannel	coherent-detection, multichannel
Sensitivity	fair	poor	good
Channel space		<10 GHz	<10 GHz
no of channel in 1 link	1	100	100 or more
laser numbers	M×N	M+N	M+N
switching speed	1 ns	1 s	1 ns-1 ms
modulation method	IM	FM	AM or FM
SNR and DR	good	poor or fair	good
Cross talk	low	-14 dB	< -50 dB

frequency range, a coherent system usually has very low interchannel interference. For WDM systems, the passbands of tunable optical filters usually are periodic (the filter is typically interferometric) and the corresponding multichannel system therefore has much larger interchannel interference. This results in reduced SNR and DR than that of a coherent system. For digital signal transmission, the interference of a WDM system might be tolerable, whereas for analog systems such as that employed for radar and CATV signal detection, where a very high SNR and dynamic range is required, this causes severe problems. In comparing other parameters such as receiver sensitivity, minimum channel spacing and switching speed, a coherent system also has superior performance than WDM systems. Furthermore, although a WDM system does not necessarily require polarization control and the modulation/demodulation methods are much more simple, a wide range tunable optical filter switchable for delay transmission is still difficult to fabricate [29].

We summarize the comparisons between typical coherent, IM/DD and WDM/DD systems in Table II. From most of the comparison categories in Table II, the coherent architecture appears to be very promising for large scale phased array antenna systems.

## VII. CONCLUSION

Table III summarizes some of the calculation results concerning the  $128 \times 320$  example system. Generally, all three schemes can provide good system performance such as high SIR, SNR and DR. The AM technique requires the smallest channel spacing and is relatively insensitive to the laser phase noise. FM and PM can provide a higher DR by using a larger modulation index, although a larger channel spacing is required.

As shown in Sections IV and V, the AM-WIRNA receiver is relatively laser-phase-noise-insensitive; and for FM receivers, the laser phase noise becomes white noise at the output. Thus, the output microwave signal maintains its original linewidth in the frequency domain. This is a crucial characteristic to ensure that the coherent system can be used for application of the Doppler effect to radar systems, where the receiver should be able to detect very small spectral shifts of the return signals.

In summary, we have analyzed a true-time-delay phased array antenna system using fiber optic techniques with coherent detection. This system has several advantages over

TABLE III  
COMPARISONS BETWEEN THE AM AND FM SCHEMES

modulation scheme	min. optical channel spacing	dynamic range of one channel	S/N for one channel	SIR for one channel
AM	12 GHz (0.1 nm)	50 dB	40 dB (m=0.1)	> 60 dB
FM ( $\beta=1$ , $\Delta\nu=1$ MHz)	12 GHz (0.1 nm)	65 dB	65 dB	> 50 dB

\* Assume that the optical power of one channel is -5 dBm.  
For 128 channels, the optical bandwidth at 1.55  $\mu\text{m}$  is:

AM: 12.8 nm  
FM: 12.8 nm

conventional electronically steered systems. It has large instantaneous bandwidth and thus is "squint free". Due to the gain control from both the LO lasers and the subsequent electronic amplifiers, it has flexibility for beam shaping and null steering. Both transmitter and receiver structures are discussed. In this paper, comparisons with direct detection systems are made, and it is shown that the coherent system is adaptable for large scale systems. We also propose a solution for compensating fiber chromatic dispersion which distorts the radiation pattern.

We quantitatively analyzed a  $128 \times 320$  model system which uses a single fiber for a transmission line. The main noise sources for the optical links are the LO-ASE beat noise, as well as the laser phase noise. From the analysis, we see that for a typical radar signal and realistic optical system parameters, such a system can obtain a high SIR (good channel isolation), a high SNR and dynamic range for AM, FM and PM schemes which meet the stringent requirements of modern radar systems.

#### APPENDIX A COHERENT RECEIVER ARRAY OPERATION

A coherent receiver detects the beat between the incident optical signal and the LO signal. For the simple case of amplitude modulation, the normalized beat signal is

$$i(t) = (1 + mx(t))\sin(\omega_{IF}t + \phi)$$

where  $m$  is the modulation index,  $x(t)$  is the modulating signal,  $\phi$  is the phase difference between the incoming signal and the LO, and  $\omega_{IF}$  is the frequency difference between the optical carrier and the LO signal, i.e. the intermediate frequency (IF). Assume that one optical receiver is used to detect signals from two antenna elements simultaneously. The transmitter lasers associated with the antenna elements therefore have to be tuned to the same frequency, so that both the detected signals have the same intermediate frequency. Under this condition, and for an ideal situation where the beat between the two incident signals and all other noise are neglected, the IF signal is

$$i(t) = (1 + mx(t))\sin(\omega_{IF}t + \phi_1) + (1 + mx(t))\sin(\omega_{IF}t + \phi_2)$$

If  $\phi_1 = \phi_2 \pm n\pi$ , where  $n$  is an even integer, then the demodulated signal would be  $2mx(t)$ , which is desirable. But if  $\phi_1 = \phi_2 \pm n\pi$ , where  $n$  is an odd integer, the

demodulated signal would be zero. Thus, to get the desired signal, both  $\phi_1$  and  $\phi_2$  have to be controlled very precisely. First, it requires an optical phase-locked-loop to control the relative phases of the two lasers. Second, the optical paths from the two transmitter lasers to the same receiver has to be controlled to sub-micrometer precision so that the optical phase difference between the two incoming optical signals is approximately  $2n\pi$ , where  $n$  is an integer. The system is further complicated since for some detecting directions, some lasers must be phase locked, and for other directions, different lasers need phase-locking. Meeting all of these requirements, where one coherent optical receiver receives signals from several antenna elements simultaneously, is very difficult to achieve using present techniques. Therefore, in the coherent system proposed, for each beam direction, one receiver is used to receive and demodulate the signal from each antenna element.

#### APPENDIX B NUMBER OF DELAY LINES NEEDED IN THE ANTENNA IN FIG. 3(a)

We now investigate how many delay lines are needed for the antenna receiver shown in Fig. 3(a). For any receiving direction, the delays for the antenna elements 1 to  $M$  must increase or decrease monotonically and as uniformly as possible, although there may be digitalization errors. The system has  $N$  different digital delays corresponding  $0, \Delta t, 2\Delta t, \dots, (N-1)\Delta t$ . We define  $DE_i$  as the delay for antenna element  $i$ , where  $i = 1, 2, \dots, M$ . The system can detect  $(2N-1)$  directions which correspond to  $DE_1 - DE_M$  as  $-(N-1)\Delta t, -(N-2)\Delta t, \dots, 0, \Delta t, \dots, (N-1)\Delta t$ .

Detecting signals from broadside requires  $DE_1 - DE_M = 0$ . In this case, the system needs  $M$  identical delays of  $0\Delta t$ . For  $DE_1 - DE_M = \pm\Delta t$ , half of the antenna elements need to be fed delays  $0\Delta t$ , and the other half need  $\Delta t$ . For these three directions, the system therefore requires  $M$  delays  $0\Delta t$  and  $[M/2]$  delays  $\Delta t$ , where  $[M/2]$  is the least integer that is not less than  $M/2$ . For the same reason, for  $DE_1 - DE_M = \pm(k-1)\Delta t$ , the system needs  $[M/k]$  delays  $(k-1)\Delta t$ . For  $M = N$  the total number of delay lines the system needs is  $M + [M/2] + [M/3] + \dots + [M/k] + \dots + 1$ , which equals, approximately,  $M \ln M$  for large  $M$ . For  $N > M$ , when  $|DE_1 - DE_M| < M\Delta t$ , it is the same situation as the  $N = M$ . When  $|DE_1 - DE_M| \geq M\Delta t$ , there are no identical delays needed for the same direction. In this case, the system only needs one delay line for each delay from  $M\Delta t$  to  $(N-1)\Delta t$ . Therefore, the total number of delay lines is  $N - M + M \ln M$ .

#### APPENDIX C NUMBER OF DELAY LINES NEEDED IN THE ANTENNA IN FIG. 3(b)

The definitions for  $M, N$  and requirements for the delay feed are the same as in Appendix B. We define the delays associated with antenna elements in Fig. 3(b) as "predelays", and the delays associated with each receiver as "postdelays". If one receiver receives a signal from one antenna element,

elements:	1	2	...	$[M/2]$	$[M/2] + 1$	...	$M$
predelays:	0	$j + 1$	...	$([M/2] - 1)(j + 1)$	$[(M - 1)/2](j + 1) + 1$	...	1.
(unit: $\Delta t$ )							

the effective delay is the sum of the corresponding pre- and postdelays. An array receiver structure requires that for a given predelay arrangement for antenna elements 1 to  $M$ , and for any desired signal receiving direction, there always exist  $M$  receivers to receive signals from their respective antenna elements so that the effective delays meet the requirements for that particular direction.

Assume a receiver structure as the following: let  $N = jM$ , where  $j$  is a positive integer. The predelays for antenna elements from 1 to  $M$  are shown in the matrix at the top of the page. From antenna element 1 to  $[M/2]$ , and from  $[M/2] + 1$  to  $M$ , the predelays increase and decrease, respectively, with spacing  $(j + 1) \Delta t$ . Let  $[Y]$  be the least integer that is not less than  $Y$ . The available postdelays (in units of  $\Delta t$ ) are  $-(j + 1), -j, \dots, -2, -1, 0, 0, 1, 1, \dots, ([M/2] - 1)(j + 1), ([M/2] - 1)(j + 1), ([M/2] - 1)(j + 1) + 1, ([M/2] - 1)(j + 1) + 2, (\dots), (2j + 1)[M/2] - (j + 2), (2j + 1)[M/2] - (j + 1)$ . The total number of delays  $X$  is  $(3j + 2)[M/2] - (j + 1)$ . For  $M$  even,  $X = (1.5j + 1)M - (j + 1) < (1.5 + 1/j)N$ ; and for  $M$  odd,  $X = (1.5j + 1)M + 0.5j$ . So  $X$  is approximately equal to  $(1.5 + 1/j)N$  for either case. For each receiving direction, the effective delay for the element  $[M/2]$  is kept as the constant  $([M/2] - 1)(j + 1)$ . Now we prove that the above structure can perform all the required detections.

- 1) We call element 1 to  $[M/2]$  as the first half, and  $[M/2] + 1$  to  $M$  as the second half of the array. The delays for antenna elements 1 to  $M$  either increase or decrease monotonically, and element  $[M/2]$  is the mid-point with the constant delay  $([M/2] - 1)(j + 1) \Delta t$ . Thus for each antenna direction, effective delays exceeding  $([M/2] - 1)(j + 1) \Delta t$  can only be used for the first or second half of the array. The largest postdelay needed is then  $[M/2] j \Delta t + ([M/2] - 1)(j + 1) \Delta t$ , which corresponds to the farthest angle away from broadside direction, where the delay difference between adjacent elements is  $j \Delta t$ .
- 2) Now we prove that from element 1 to  $[M/2]$ , for every receiving direction, the required postdelays are different, and the shortest required postdelay is zero. We know the required effective delays for element 1 to  $M$  either increase or decrease monotonically and as uniformly as possible. With  $N = jM$ , the largest delay difference required between adjacent antenna elements is  $j \Delta t$ . Here, the predelays for elements 1 to  $[M/2]$  increase with equal difference  $(j + 1) \Delta t$ , which is greater than the largest difference required. For any receiving direction, whether the required effective delays increase or decrease monotonically, the postdelays fed to elements 1 to  $[M/2]$  must decrease monotonically, with the delay difference between adjacent elements at least  $\Delta t$ . Thus, for each direction, no two postdelays for elements 1 to  $[M/2]$  are the same. Since the postdelays

for element  $[M/2]$  are always kept at zero, the shortest postdelay required here is zero.

For the same reason, the postdelays fed to elements  $[M/2] + 1$  to  $M$  must increase monotonically, and among them no two can be the same for each direction. The shortest delay needed is for the element  $[M/2] + 1$ , when its effective delay is  $j \Delta t$  shorter than that for the element  $[M/2]$ . This delay is  $-(j + 1) \Delta t$  for  $M$  is even, and 0 for  $M$  is odd. (The negative delay here is shorter than the length of the fiber which we define as zero delay, and does not actually correspond to negative length.)

- 3) From the conclusion of (1) and (2), we know that all the postdelays (in units of  $\Delta t$ ) needed are

- I) from  $-(j + 1)$  to  $-1$ , one for each;
- II) from  $([M/2] - 1)(j + 1)$  to  $[M/2] j \Delta t + ([M/2] - 1)(j + 1) \Delta t$ , one for each;
- III) from 0 to  $([M/2] - 1)(j + 1) - 1$ , at most two for each.

Thus, the total number of postdelays, i.e. the total number of optical receivers needed is  $(3j + 2)[M/2] (j + 1)$ , which is approximately equal to  $(1.5 + 1/j)N$ .

For  $j$  not an integer, we could make the arrangement for the predelays almost the same as the above while the difference between the adjacent antenna elements is  $([j] + 1) \Delta t$ . Then due to the same reasoning, the total number of delay lines needed is approximately  $(3[j] + 2)[M/2]$ .

#### ACKNOWLEDGMENT

The authors would like to thank Professor H. Fettermann, Professor P. Prucnal, and Professor L. G. Kazovsky, Mr. I. Newberg, Dr. C.-P. Chao, Mr. T. Fong, and Mr. C. Lu for their helpful discussions.

#### REFERENCES

- [1] M. L. Skolnik, *Radar Handbook*. New York: McGraw-Hill, 1990.
- [2] ———, *Introduction to Radar Systems*, 2nd Ed. New York: McGraw-Hill, 1980.
- [3] Simon Haykin, *Array Processing Applications to Radar*. Dowden, Hutchinson and Ross, 1980.
- [4] G. A. Koepf, "Optical processor for phased-array antenna beam formation," *Opt. Technol. for Microwave Applicat.*, vol. 477, SPIE, pp. 75-81, 1984.
- [5] P. Sheehan and J. Forrest, "The use of optical techniques for beam forming in phased arrays," *Optical Technology for Microwave Applicat.*, SPIE, vol. 477, pp. 82-89, 1984.
- [6] J. Wallington and J. Griffin, "Optical techniques for signal distribution in phased arrays," *GEC. J. Res.*, vol. 2, no. 2, pp. 66-73, 1984.
- [7] M. R. Surette, D. R. Hjelme, and A. R. Mickelson, "An optically driven phased array antenna utilizing heterodyne techniques," *J. Lightwave Technol.*, vol. 11, no. 9, pp. 1500-1509, Sept. 1993.

- [8] J. Guggenmos and R. Johnson, "Fiber based phased array antennas," in *Opt. Technol. for Microwave Applicat. III, SPIE*, vol. 789, pp. 70-77, 1987.
- [9] J. S. Pappert, "Ultra-wideband direction finding using a fiber optic beam-forming processor," in *Optoelectron. Signal Processing for Phased-Arrays, SPIE*, vol. 886, pp. 239-246, 1988.
- [10] W. Ng, A. A. Walston, G. L. Tangonan, J. J. Lee, I. L. Newberg, and N. Bernstein, "The first demonstration of an optically steered microwave phased array antenna using true-time-delay," *J. Lightwave Technol.*, vol. 9, no. 9, pp. 1124-1131, 1991.
- [11] W. W. Ng, D. Yap and A. A. Narayanan, "GaAs and silica-based integrated optical time shift network for phased arrays," *Optoelectron. Signal Processing for Phased-Array Antennas IV, SPIE*, vol. 2155, 1994.
- [12] J. J. Lee, S. Livingston, R. Y. Loo, and N. P. Bernstein, "System design and performance of a wideband photonic array antenna," *Optoelectron. Signal Processing for Phased-Array Antennas IV, SPIE*, vol. 2155, 1994.
- [13] P. M. Freitag and S. R. Forrest "A coherent optically controlled phased array antenna system," *IEEE Microwave and Guided Wave Lett.*, vol. 3, no. 9, pp. 293-295, Sept. 1993.
- [14] L. G. Kazovsky and P. T. Poggiolini, "STARNET: A multi-gigabit-per-second optical LAN utilizing a passive WDM star," *J. Lightwave Technol.*, vol. 11, no. 5/6, pp. 1009-1027, May/June 1993.
- [15] Y. Tohmori, Y. Yoshikuni, H. Ishii, F. Kano, T. Tamamura and Y. Kondo, "Over 100 nm wavelength tuning in superstructure grating (SSG) DBR lasers," *Electron. Lett.*, vol. 29, no. 4, pp. 352-354, Feb. 1993.
- [16] Product catalog of Santec USA Corp., New Jersey 07733, 1994.
- [17] A. Carlson, *Communication Systems*, 2nd Ed. New York: McGraw-Hill, 1975.
- [18] T. Durhuus, B. Mikkelsen and K. Stubkjaer, "Detailed dynamic model for semiconductor optical amplifiers and their crosstalk and intermodulation distortion," *J. Lightwave Technol.*, vol. 10, no. 8, pp. 1056-1065, Aug. 1993.
- [19] R. I. Laming, M. N. Zervas, and D. N. Payne, "Erbium-doped fiber amplifier with 54 dB gain and 3.1 dB noise figure," *IEEE Photon. Technol. Lett.*, vol. 4, no. 12, pp. 1345-1347, Dec. 1992.
- [20] I. L. Newberg, A. A. Walston, H. S. Nussbaum, and G. L. Tangonan, "Frequency translation of true time delay signals," Patent Pending, GM/Hughes Electronics Corporation.
- [21] Product catalog of MITEQ Corporation, New York.
- [22] D. J. Sabido, T. K. Fong, R. F. Kalman, and L. G. Kazovsky, "Linewidth-insensitive coherent optical analog links," *SPIE*, vol. 1703, pp. 504-522, 1992.
- [23] R. Walker, R. C. Steele, and N. G. Walker, "Optical amplifier noise figure in a coherent optical transmission system," *J. Lightwave Technol.*, vol. 8, no. 9, pp. 1409-1413, Sept. 1990.
- [24] L. G. Kazovsky, "Multichannel coherent optical communications systems," *J. Lightwave Technol.*, vol. 5, no. 8, pp. 1095-1102, 1987.
- [25] B. S. Glance, J. Stone, K. J. Pollock, and P. J. Fitzgerald, C. A. Burrus Jr., B. L. Kasper and L. W. Stulz, "Densely spaced FDM coherent star network with optical signals confined to equally spaced frequencies," *J. Lightwave Technol.*, vol. 6, no. 11, pp. 1770-81, Nov. 1988.
- [26] T. K. Fong, D. J. Sabido, and L. G. Kazovsky, "Linewidth-insensitive coherent AM analog optical links using semiconductor lasers," *IEEE Photon. Technol. Lett.*, vol. 4, no. 4, pp. 49-471, Apr. 1993.
- [27] L. G. Kazovsky, "Impact of laser phase noise on optical heterodyne communication systems," *J. Opt. Commun.*, vol. 7, no. 2, pp. 66-78, 1986.
- [28] M. Yano, Y. Kotaki, H. Ishikawa, S. Yamakoshi, H. Imai, T. Chikama, and T. Touge, "Extremely low-noise facet-reflectivity-controlled InGaAsP distributed-feedback lasers," *J. Lightwave Technol.*, vol. 4, pp. 1454-1458, 1986.
- [29] K. Nosu, H. Toba, K. Inoue, and K. Oda, "100 channel optical FDM technology and its applications to optical FDM channel-based networks," *J. Lightwave Technol.*, vol. 11, no. 5/6, pp. 76-776, May/June, 1993.
- [30] D. Dunkin, G. Hill, and W. Stallard, "Frequency locking of external cavity semiconductor lasers using an optical comb generator," *Electron. Lett.*, vol. 22, p. 388, 1986.
- [31] T. Okoshi and K. Kikuchi, *Coherent Optical Fiber Communications*. Tokyo: KTK, 1987.

**Ligeng Xu**, photograph and biography not available at the time of publication.

**Robert Taylor**, photograph and biography not available at the time of publication.

**Stephen R. Forrest (M'83-SM'88-F'91)**, photograph and biography not available at the time of publication.

# True Time-Delay Phased-Array Antenna Feed System Based on Optical Heterodyne Techniques

Ligeng Xu, Robert Taylor, and Stephen R. Forrest, *Fellow, IEEE*

**Abstract**— We demonstrate a true-time delay phased-array antenna feed system based on multi-channel optical heterodyne detection techniques. The system is relatively insensitive to laser linewidth and IF frequency instabilities. We demonstrate accurate true-time delay from 0.8 to 1.5 GHz. The dynamic range for one channel is 52 dB for 1 MHz bandwidth. For a very narrow channel spacing of 13 GHz ( $\sim 1 \text{ \AA}$  at a transmission wavelength of  $1.55 \mu\text{m}$ ), the interchannel interference is negligible. Such an architecture has potential for large scale system implementations.

**C**URRENTLY, there is much interest in exploring the use of optics for controlling microwave phased array antennas [1]–[6]. This effort is driven by the obvious advantages of optical systems: reduced weight making it suitable for use in airborne and spaceborne systems, immunity from electromagnetic interference, low loss, etc. Among the proposed architectures, fiber optic true-time delay systems [3]–[6] can also provide a very large instantaneous bandwidth.

Recently, we analyzed a true-time delay system based on multi-channel, optical heterodyne detection techniques with external modulation, and showed that such a system is readily expandable to large scale systems with high dynamic range and good channel isolation while keeping the optical channel spacing very small [7]. In this paper, we demonstrate a proof-of-concept experiment of this system using four optical channels and two coherent receivers. The system shows good signal quality, high dynamic range, accurate true-time delay in the microwave bandwidth range from 0.8 to 1.5 GHz, and narrow optical channel spacing with very low interchannel interference. Direct as well as external modulation schemes exhibit good signal quality for narrow bandwidth signals.

Fig. 1 shows a simple four optical channel, two antenna element demonstration system. The four  $\lambda = 1.55 \mu\text{m}$  wavelength DFB laser transmitters (see Fig. 1) are each thermally tuned to have a different central optical frequency. The light from the four transmitter lasers is amplitude modulated (AM) at microwave bandwidths using  $\text{LiNbO}_3$  Mach-Zehnder (M-Z) modulators. The modulated optical signals are then transmitted through different fiber lengths prior to being input to a  $4 \times 1$  combiner composed of a series of  $2 \times 1$  combiners. The signals then pass through a single transmission fiber before being routed to two optical receivers through a series of

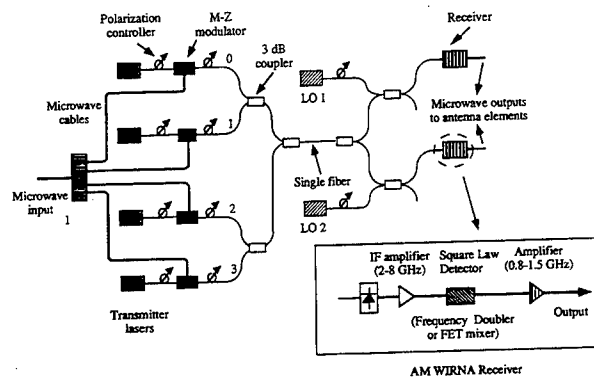


Fig. 1. Demonstration of true-time delay phased array antenna feed system with four optical channels and two coherent receivers. Inset: Schematic diagram of the optical heterodyne AM receiver.

splitters. Next, these signals are separately mixed with two optical local oscillator (LO) signals at the input of InGaAs p-i-n detectors with 70% quantum efficiency at  $\lambda = 1.55 \mu\text{m}$ . By tuning the LO DFB lasers, each receiver is able to detect and demodulate the microwave signal from any of the four transmitter laser channels. The laser frequencies were adjusted by independent current and temperature controllers with a temperature stability of  $\pm 0.02 \text{ }^\circ\text{C}$ . As shown in the following, even with this open-loop control, we still obtain very stable signals and accurate true-time delays. Since the modulated signals arrive at the receivers through different fiber lengths, true-time delays are introduced among the four channels. Additional optical channels can provide more delay combinations, while more splitting before the optical receivers can be used to accommodate additional antenna elements.

The demodulation scheme used [8] is a wideband filter-rectifier-narrow band filter structure (WIRNA, shown in Fig. 1 inset), which employs a square-law device (SLD) to demodulate the AM signal. This receiver architecture is relatively insensitive to laser linewidth, and the dynamic range is comparable to that of optical direct detection schemes [7], [8]. In our experiment, the intermediate frequency (IF) passband is from 2 to 8 GHz, and the narrow band amplifier operates from 0.8 to 1.5 GHz. The SLD used was either a frequency doubler or a FET mixer. For optically coherent detection, the light polarization needs to be controlled. One solution is to use polarization maintaining (PM) fibers and PM fiber couplers throughout the system. In our experiment, however, single mode non-PM fibers and couplers were used along with

Manuscript received July 5, 1995; revised September 5, 1995. This work was supported in part by Rome Labs/Griffiss and NCIPT.

The authors are with the Advanced Technology Center for Photonics and Optoelectronic Materials, Department of Electrical Engineering, Princeton University, Princeton, NJ 08544 USA.

Publisher Item Identifier S 1041-1135(96)00548-4.

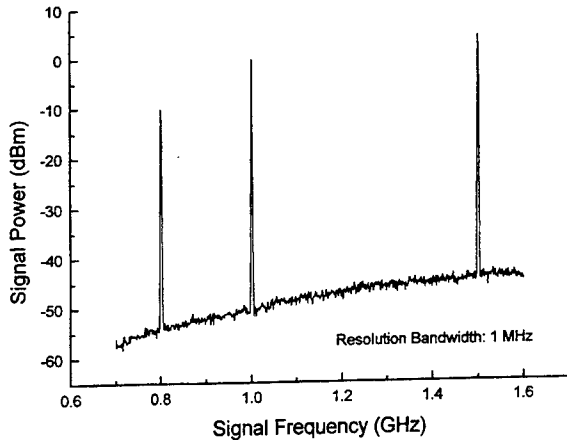


Fig. 2. Optical heterodyne signals at 0.8, 1.0, and 1.5 GHz.

manual polarization rotators. These components did not appear to significantly degrade the system performance or stability.

Fig. 2 shows the demodulated signals of one channel with an IF of 4.1 GHz when the externally modulating signal is varied between 0.8, 1 and 1.5 GHz. Here, the optical signal power is  $-15.8$  dBm, and the LO power is  $-2.7$  dBm at the receiver. With the modulation index set at 0.24 for the 8 dBm microwave signal, and the receiver noise corresponding to an optical power of  $50 \text{ pW/Hz}^{1/2}$ , the signal-to-noise ratio (SNR) is about 48 dB for a 1 MHz bandwidth. This SNR is independent of frequency from 0.8 to 1.5 GHz, as seen in Fig. 2. Calculations based on a previous system analysis [7] give  $\text{SNR} = 50$  dB using the measured parameters at the optical receiver, which is in reasonable agreement with the experimental results. The demodulated RF signals have linewidths of  $< 2$  MHz, limited by the resolution bandwidth of the spectrum analyzer. On the other hand, the IF signal linewidth is tens of MHz. This clearly indicates that the system is indeed laser-linewidth insensitive, consistent with previous analytical and experimental results [7], [8]. For shot noise limited receivers, the SNR should be  $71.2 \text{ dB/MHz}$  with the above optical powers and modulation index—a 20 dB improvement over our results. The total optical signal loss of the system is about 20 dB, with 12 dB loss from the 3 dB couplers, and 8 dB from the M-Z modulators. Other connector losses are negligible. In this experiment, the optical power loss and the high receiver noise are primarily responsible for the SNR degradation.

The dynamic range (DR) of the antenna feed is limited by system noise and third order intermodulation products from the M-Z modulators, provided the optical signal power and LO power are fixed. The two-tone signal method [8] was employed to measure the dynamic range of one channel with the same optical parameters as in Fig. 2. In this case, the DR is 52.3 dB for a signal modulated from 0.8 to 1.5 GHz with a 1 MHz bandwidth. Theoretical calculations [7] show  $\text{DR} = 54$  dB with the above system parameters, and 68 dB under shot noise limited situations. The experimental dynamic range can be further improved by increasing the optical signal and LO power along with the use of shot noise limited,

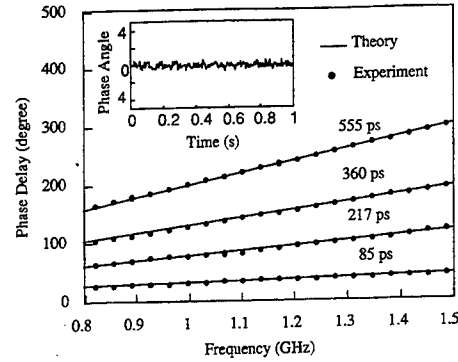


Fig. 3. True-time delay measurement showing four different time delays. Solid lines are calculations, and dots are experimental data. Inset: Phase fluctuation for a 1 GHz modulation as a function of time. Here, a phase fluctuation of  $\pm 1^\circ$  is observed.

balanced optical receivers. Also, highly linear modulators or direct laser modulation can be employed to avoid third order intermodulation products.

To test the true-time delay performance of the system, the microwave output of an HP 8703A network analyzer was connected to the microwave input shown in Fig. 1. One of the demodulated microwave outputs from the antenna feed (Fig. 1) was then connected to the input of the network analyzer. First, the phase response of microwave signal output from different optical channels and/or different receivers was measured. Next, the phase difference between two channels was compared to the theoretical values. Fig. 3 shows example measurement results using this procedure. The solid lines show the theoretical phase delays for the corresponding true-time delays of 85, 217, 360, and 555 ps, and the data points show the test results averaged over 16 sweeps. As shown in Fig. 3, the system introduces accurate, frequency independent true-time delays between different channels, indicating that such a multichannel optical heterodyne system can precisely control the microwave phase.

The inset in Fig. 3 shows the phase fluctuation as a function of time for 1 GHz CW operation. The phase fluctuates to within  $\pm 1^\circ$  due to the nonlinear phase response of the GaAs IF amplifiers. As the laser frequencies fluctuate, the phase response of the amplifiers to the IF frequency and the two AM modulation side lobes changes due to amplifier non idealities, thereby introducing phase fluctuations into the demodulated signal after the SLD. Note that IF amplifiers with improved linear phase response can eliminate the small phase fluctuation of the demodulated signals, even in the presence of instabilities in laser frequency.

The signal-to-interchannel interference ratio (SIR) determines the minimum channel spacing. Fig. 4 shows the measured SIR when the four channels are equally spaced. The signal power is obtained by tuning the LO for channel 2 to  $\text{IF} = 4.1$  GHz (inset, Fig. 4). The channel interference was then measured by turning off the microwave modulation on optical channel 2. When the channel spacing is  $< 12$  GHz, the beat between the LO and channel 3 is less than 8 GHz which is within the IF amplification bandwidth, causing interference at the SLD. For a channel spacing  $> 13$  GHz, however, the beat

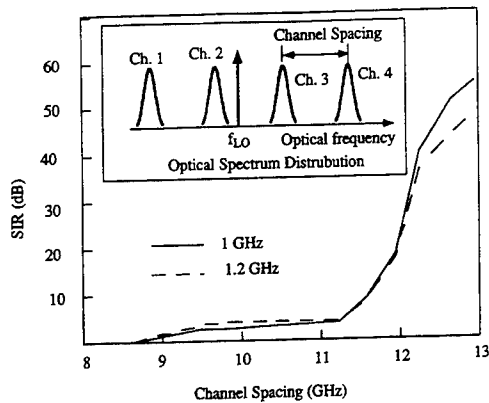


Fig. 4. Signal-to-interchannel interference ratio as a function of channel spacing for two different modulation signals, and IF = 4.1 GHz. Inset: The optical spectral distribution of the different channels used for the measurement in Fig. 4.

signal between the LO and channel 3 is out of the IF passband, resulting in a negligible interchannel interference. Due to the noise floor, we obtain an upper limit of SIR = 50 dB with most of the interference power from channel 3. Calculations indicate that for modulation between 0.8 and 1.5 GHz and a laser linewidth as large as 20 MHz, 2 to 6 GHz is a sufficiently large passband for IF = 4 GHz. In this case the channel spacing can be reduced to  $\sim 11$  GHz, without introducing significant interchannel interference [7]. The experimental results indicate that the good passband characteristics of microwave amplifiers and filters leads to a high SIR even for small channel spacings in AM heterodyne systems. Theoretical investigations [7] also show that if balanced receivers are used, the most significant interchannel interference only comes from the adjacent channels even for systems with a large number of channels.

In summary, we demonstrate a proof-of-concept experiment for a novel true-time delay phased array antenna feed system from 0.8 to 1.5 GHz based on optical heterodyne detection techniques. Such a system is comparatively easy to imple-

ment using off-the-shelf components. The system has high dynamic range ( $>52$  dB), good signal-to-noise ratio (48 dB), and a narrow channel spacing (13 GHz) with good channel isolation. The system also demonstrated the transmission of very accurate true-time delays. Practical issues such as phase fluctuations and tolerance to IF frequency variations were addressed. Means to improve system performance such as dynamic range and phase stability were also proposed. The experimental results were compared to our previous analysis [7], and were in good agreement. This architecture provides a promising approach for a future generation of phased array antenna systems based on fiber optic techniques.

The authors thank Irwin Newberg, Doss Halsey, Brian Hendrickson, Allen Lu, Thomas Fong, and Professor Harold Fetterman for their helpful suggestions.

#### REFERENCES

- [1] G. A. Koepf, "Optical processor for phased-array antenna beam formation," *Opt. Technol. Microwave Applications*, vol. 477, SPIE, pp. 75-81, 1984.
- [2] M. R. Surette, D. R. Hjelm, and A. R. Mickelson, "An optically driven phased array antenna utilizing heterodyne techniques," *J. Lightwave Technol.*, vol. 11, no. 9, pp. 1500-1509, Sept. 1993.
- [3] J. Guggenmos and R. Johnson, "Fiber based phased array antennas," in *Opt. Technol. Microwave Applications III*, SPIE, vol. 789, pp. 70-77, 1987.
- [4] J. S. Pappert, "Ultra-wideband direction finding using a fiber optic beam-forming processor," in *Optoelectronic Signal Processing for Phased-Arrays*, SPIE, vol. 886, pp. 239-246, 1988.
- [5] W. Ng, A. A. Walston, G. L. Tansonan, J. J. Lee, I. L. Newberg, and N. Bernstein, "The first demonstration of an optically steered microwave phased array antenna using true-time-delay," *IEEE J. Lightwave Technol.*, vol. 9, no. 9, pp. 1124-1131, 1991.
- [6] P. M. Freitag and S. R. Forrest, "A coherent optically controlled phased array antenna system," *IEEE Microwave Guided Wave Lett.*, vol. 3, no. 9, pp. 293-295, 1993.
- [7] L. Xu, R. Taylor, and S. Forrest, "The use of optically coherent detection techniques in true-time delay phased array and systems," *IEEE J. Lightwave Technol.*, vol. 13, no. 8, pp. 1663-1678, 1995.
- [8] T. K. Fong, D. J. Sabido, and L. G. Kazovsky, "Linewidth-insensitive coherent AM analog optical links using semiconductor lasers," *IEEE Photon. Technol. Lett.*, vol. 4, no. 4, pp. 49-471, 1993.

# Phase Noise in Coherent Analog AM-WIRNA Optical Links

Robert Taylor, H. Vincent Poor and Stephen Forrest

Advanced Technology Center for Photonics and Optoelectronic Materials

Department of Electrical Engineering

Princeton University, Princeton, NJ 08544

Abstract: Coherent analog Amplitude Modulated - Wideband Rectifier Narrowband (AM-WIRNA) systems have been the focus of many recent studies because of their high performance and relative immunity to phase noise compared to angle modulated systems. Despite their natural advantages over angle modulated systems, AM-WIRNA receivers are still vulnerable to phase noise because of distortion of their phase broadened signals in a finite bandwidth system. We present the first numerical analysis of the effects of this distortion on the performance of AM-WIRNA systems. The analysis accurately models the power spectral density of the phase-to-intensity noise with a root-mean-square deviation from the averaged experimental noise spectrum of 1.2 dB and a maximum deviation of 3.8 dB in the modulation range of  $< 2$  GHz. The accuracy of the analysis is limited primarily by non-idealities in the AM-WIRNA receiver and the accuracy of the analytical IF filter model. Optimal link designs are presented which minimize the impact of phase-to-distortion noise in AM-WIRNA systems. We present experimental data from AM-WIRNA links which use both external cavity and distributed feedback lasers for the signal and local oscillator sources. The numerical analysis predicts the link signal-to-noise ratio (SNR) for different signal laser powers to within 1.4 dB of experiment. We find that systems requiring high SNR such as phased array antennas and AM-CATV are significantly affected by this noise.

<u>Symbol</u>	<u>Definition</u>
$\alpha_{\text{excess}}$	Modulator coupling loss
$\alpha_{\text{fiber}}$	Total fiber loss
$\Delta\nu$	Combined local oscillator (LO) and signal laser linewidth
$\Phi(t)$	Instantaneous phase of the intermediate frequency (IF) signal
$\Phi_{\tau}(t)$	Accumulated phase in a time period $\tau$
$\Phi_{\text{LO}}(t)$	LO laser instantaneous phase
$\Phi_{\text{S}}(t)$	Signal laser instantaneous phase
$\eta_{\text{add}}$	Power spectral density (PSD) of the additive noise
$\eta_{\text{SLD}}$	Square law device (SLD) conversion amplitude $\left[ \frac{1}{\text{Amps}^2} \right]$
$\sigma_{\text{S}_B}^2$	Filtered signal variance
$\sigma_{\text{S}_N}^2$	Filtered noise variance
$\omega_{\text{IF}}$	IF center frequency
$\omega_{\text{LO}}$	LO laser center frequency
$\omega_{\text{m}}$	Modulation frequency
$\omega_{\text{S}}$	Signal laser center frequency
$\xi_{\text{LO}}(t)$	LO laser relative intensity noise (RIN)
$\xi_{\text{S}}(t)$	Signal laser RIN
$A_{\text{balanced}}$	IF signal envelope for a balanced detector receiver
$A_{\text{single}}$	IF signal envelope for a single detector receiver
$B_{\text{IF}}$	Bandwidth of the IF filter
$B_{\text{NBF}}$	Bandwidth of the narrow band filter (NBF)
$C$	Total normalized phase noise power; $C \equiv \int_0^{\infty} K_{\text{phase}}(\omega) d\omega$
CNR	Carrier-to-noise ratio
$e$	Electron Charge ( $= 1.6022 \times 10^{-19}$ C)

$\hat{e}_S$	Signal laser amplitude $\left[ W^{\frac{1}{2}} \right]$
$\hat{e}_{LO}$	LO laser amplitude $\left[ W^{\frac{1}{2}} \right]$
$E[ ]$	Mathematical expectation value
$f_o$	NBF center frequency
$h_{B-IF}(t)$	IF filter impulse response
$h_{B-NBF}(t)$	NBF impulse response
$i_{SLD-envelope}$	Envelope of the current after the SLD
$i_{Photo}$	Photocurrent
$k_B$	Boltzmann constant ( $= 1.38 \times 10^{-23} \text{ J / K}$ )
$K_{phase}$	Normalized (relative to $A^4$ ) phase-to-intensity (PTI) power spectral density
$m$	Modulation index
$n(t)$	Additive noise current
$P_{carrier}$	Electrical carrier power
$P_{in}$	Input power to the modulator
$P_{LO}$	LO laser power
$P_{N^2}$	Output noise-squared power
$P_o$	Modulated optical power
$p_o$	AC modulated optical power
$P_{phase}$	Output PTI noise power
$P_S$	Transmitter laser power
$P_{sig}$	Output signal power
PSD	Power spectral density
$P_{S-N Beat}$	Output signal-noise beat power
$P_{Z-Out}$	Total output power of the link
$\mathfrak{R}$	Photodiode responsivity

$R(\tau)$	Autocorrelation function
$R_{\phi}(\tau)$	Autocorrelation function of the PTI noise
$R_L$	Load resistance of the receiver
RIN	Relative intensity noise
$RIN_{LO}$	LO laser RIN (units of $dB/Hz$ )
$RIN_S$	Signal laser RIN (units of $dB/Hz$ )
SNR	Signal-to-noise ratio
$v(t)$	Signal after the IF filter
$V_{\pi}$	Voltage needed at the modulator for a $\pi$ phase shift
$V_B$	Modulator bias voltage
$w(t)$	Signal after the SLD
$x(t)$	Normalized modulation signal
$z(t)$	Link output signal

## 1. - Introduction

Much recent work has concentrated on the development of optically coherent high frequency analog fiber optic links for use in sub-carrier multiplexed communications [1], optically controlled phased array antennas [2, 3], and the interconnection of microwave systems [4]. Conventionally, these systems have employed direct detection schemes, however recent links utilizing coherent detection have demonstrated large dynamic range and low noise figures [5, 6]. In addition, coherent detection facilitates high channel packing densities for wavelength division multiplexed (WDM) systems, has increased sensitivity over direct detection schemes, and allows for angle modulation formats.

One of the challenges facing coherent links is the degradation of performance in the presence of laser phase noise, and hence recent efforts have focused on amplitude modulation (AM) due to its relative immunity from such noise [7,8]. In particular WIRNA (WIDeband filter - Rectifier - NARrowband filter) processing has been predicted to achieve virtually linewidth-insensitive performance with the proper design of the IF filter [8,9]. However, the IF filter bandwidths needed for minimum performance degradation are often unobtainable in practice due to the high cost of wide bandwidth components. This problem is exacerbated for large optical signal powers and for high SNR links (such as are required in optically controlled phased array antenna systems).

In this paper, we present an analysis of the performance of AM-WIRNA links in the presence of phase noise using numerical methods to estimate the power spectral density (PSD) of the phase-to-intensity (PTI) noise. An approximate analysis of the effects of phase noise on AM-WIRNA system performance was done previously in Ref. [8]. However, this early approximation differs significantly from experimental results in the several cases and does not calculate the PSD of the PTI noise, which is required to address the effects of PTI noise in narrow-band links. In contrast, comparison of the results of our analysis with the experimental data presented here is shown to accurately model the effects of PTI noise on link performance. We find that phase noise sets a fundamental limit to the SNR in AM-WIRNA receivers that is independent of signal

power. For high power, high SNR systems such as antenna remoting and AM-CATV, this limit will dominate for laser linewidths greater than a few MHz. We present optimum system design parameters to maximize the SNR for a given laser linewidth. To the best of our knowledge this is the first detailed numerical analysis of phase noise effects in AM-WIRNA links. Experimental results from an externally modulated AM-WIRNA system are also presented.

This paper is organized as follows: Sections II and III describes the AM-WIRNA link, and the statistics of the relevant random variables. In Sec. IV, we derive an expression for link SNR in the presence of PTI noise, and in Sec. V the expression for PTI noise is derived. Section VI presents results from the numerical evaluation of our theory using conditions maintained during laboratory measurements of PTI noise. In Sec. VII we discuss the experimental AM-WIRNA link, and present data on the system performance which is compared with the analytical results of Sec VI. Section VIII provides conclusions.

## 2. - System Description

The system considered is an analog, externally modulated AM coherent link with a WIRNA receiver shown in Fig. 1. The signal laser is modulated by a Mach-Zender (M-Z) modulator, and the optical carrier is heterodyned down to baseband with a local oscillator (LO) laser at the receiver photodetector. The signal demodulation is accomplished by the electrical portion of the WIRNA receiver, which consists of an IF filter followed by a square law device (SLD) and a narrow band filter (NBF). The WIRNA receiver can employ either a single photodetector or a pair of photodetectors in a balanced receiver configuration. The balanced receiver has been shown to significantly reduce the effects of relative intensity noise (RIN) [10] at the cost of some minor added complexity. The experimental links presented in Sec. 7 use a single detector, although our calculations will consider both configurations.

The amplitude modulation of the signal laser is done in the small signal linear region of the Mach-Zender. At a bias voltage of  $V_B = \frac{V_\pi}{2}$  (where  $V_\pi$  is the voltage required for a  $\pi$  phase shift), the optical power transfer function of the modulator is [11]:

$$P_o = \frac{\alpha_{excess} P_{in}}{2} (1 + \sin(mx(t))) \quad (1)$$

Here,  $P_o$  is the modulated optical output power,  $P_{in}$  is the input power,  $\alpha_{excess}$  is the excess loss beyond the 3dB loss incurred by DC biasing the modulator at  $V_B$ ,  $m$  is the optical modulation index and  $x(t)$  is the normalized RF modulation signal. When the modulation index is small ( $m \ll 1$ ), the AC optical power transfer function is given by

$$p_o = \frac{\alpha_{excess} P_{in}}{2} (mx(t)) \quad (2)$$

At the small signal bias point, the amplitude of the modulated signal laser at the receiver is:

$$\hat{e}_S = \sqrt{\alpha_{fiber} \alpha_{excess} P_S (1 + \xi_S(t))} \left\{ \cos(\omega_S t + \Phi_S(t) + mx(t)) + \cos\left(\omega_S t + \Phi_S(t) + \frac{\pi}{2}\right) \right\} \hat{s} \quad (3)$$

where  $P_S$  is the power of the transmitter laser,  $\omega_S$  is the signal laser center frequency,  $\Phi_S(t)$  is its instantaneous phase,  $m$  is the modulation index,  $\alpha_{fiber}$  is the sum of all losses associated with the fiber,  $\xi_S(t)$  is the RIN noise, and  $\hat{s}$  is the polarization unit vector. Similarly, the amplitude of the local oscillator laser is

$$\hat{e}_{LO}(t) = \sqrt{2P_{LO} (1 + \xi_{LO}(t))} \cos(\omega_{LO} t + \Phi_{LO}(t)) \hat{l} \quad (4)$$

where  $P_{LO}$  is the optical power of the LO laser at the receiver,  $\omega_{LO}$  is the center frequency of the local oscillator,  $\xi_{LO}(t)$  is the LO RIN noise,  $\Phi_{LO}(t)$  is the instantaneous phase and  $\hat{l}$  is the polarization unit vector.

For maximum detection efficiency, the polarization of the signal and the LO laser fields should be parallel (corresponding to  $\hat{l} \cdot \hat{s} = 1$ ). Assuming this is the case and neglecting DC terms, the photocurrent can be expressed in complex form as:

$$i_{photo}(t) = A \left\{ \cos(\omega_{IF}t + \Phi(t) + mx(t)) + \cos\left(\omega_{IF}t + \Phi(t) + \frac{\pi}{2}\right) \right\} + n(t) \quad (5)$$

where  $\omega_{IF} = \omega_S - \omega_{LO}$  is the IF frequency,  $\Phi(t) = \Phi_S(t) - \Phi_{LO}(t)$ , and the values of the amplitude,  $A$ , and the additive noise current,  $n(t)$ , depend on whether a single or balanced detector configuration is used. We define the amplitude for a balanced receiver as:

$$A_{balanced} = \Re \sqrt{2\alpha_{fiber} \alpha_{excess} P_{LO} P_S (1 + \xi_S(t))(1 + \xi_{LO}(t))} \quad (6)$$

where  $\Re$  is the detector responsivity. The single detector amplitude,  $A_{single}$ , is half  $A_{balanced}$  since the single photodetector allows only half of the optical power to be used. The additive noise current,  $n(t)$ , consists of all the noise currents generated at the receiver. The expressions for the additive noise for both a balanced receiver and single detector configuration are given in Sec. 3. Now, assuming  $m \ll 1$ , Eq. (5) can be written as:

$$i_{photo}(t) \approx A \left\{ \cos(\omega_{IF}t + \Phi(t)) - (1 + mx(t)) \sin(\omega_{IF}t + \Phi(t)) \right\} + n(t) \quad (7)$$

Demodulation of the signal can be accomplished using the SLD which squares the current in Eq. (7). Disregarding the additive noise for the moment, the envelope of the squared photocurrent is then given as:

$$i_{SLD-envelope} = \eta_{SLD} A^2 \left( 1 + mx(t) + \frac{m^2 x^2(t)}{2} \right) \quad (8)$$

where  $mx(t)$  is the recovered signal, and  $\eta_{SLD}$  is the SLD conversion amplitude.

As can be seen from Eq. (5), the photocurrent has two random process contributions: the phase noise,  $\Phi(t)$ , and the additive noise current,  $n(t)$ . The phase noise does not affect the recovered signal in Eq. (8) because the squaring process discards the phase information of the carrier. This results in relative phase noise immunity for AM systems in comparison to angle modulated systems. However, in a real system with finite bandwidth, the spectral broadening of the photocurrent spectrum by the phase noise leads to signal distortion at the receiver. This distortion can significantly affect the demodulated signal even in AM-WIRNA links. In the next section, we consider the statistics of the phase and additive noise sources.

### 3. - Statistics of Random Processes

The random variable  $\Phi(t)$  is the difference between the instantaneous phases of the signal and LO lasers. The accumulated phase over a time period,  $\tau$ , is given by

$$\Phi_\tau(t) = \Phi(t + \tau) - \Phi(t) \quad (9)$$

It can be shown that  $\Phi_\tau(t)$  can be accurately modeled as a Gaussian, zero mean, process whose variance is given as [12]

$$\langle \Phi^2(\tau) \rangle = 2\pi \Delta\nu\tau \quad (10)$$

where  $\Delta\nu = \Delta\nu_{LO} + \Delta\nu_S$  is the combined LO and signal laser linewidths. These statistics for  $\Phi_\tau(t)$  are valid assuming a Lorentzian line shape, where the power spectral density of the instantaneous laser frequencies,  $\dot{\Phi}_{LO}(t)$  and  $\dot{\Phi}_S(t)$ , are white. This

assumption has been experimentally verified for the frequency range of 1 MHz up to the relaxation resonance of the laser, which is typically a few gigahertz [13]. Strictly speaking, the effects of the relaxation resonance on the phase-to-intensity noise should be considered. We will simplify the analysis, however, by considering the laser line shape to be a perfect Lorentzian.

The additive noise,  $n(t)$ , consists of shot noise, thermal noise, and RIN noise in the single photodetector receiver. If a balanced receiver is used, the RIN noise term in the additive noise is significantly reduced such that it can usually be neglected. The additive noise is assumed to be a white, Gaussian, zero mean process with a one sided PSD of:

$$S_n(f) = \eta_{add} \quad \text{for } 0 < f < \infty \quad (11)$$

where the expressions for  $\eta_{add}$  for the single and balanced detector configurations are [14]:

$$\eta_{\text{add-single}} = 2e\mathfrak{R}(P_S + P_{LO}) + \frac{4k_B T}{R_L} + \mathfrak{R}^2 \left( P_{LO}^2 10^{\frac{RIN_{LO}}{10}} + \alpha_{\text{fiber}}^2 \alpha_{\text{excess}}^2 P_S^2 10^{\frac{RIN_S}{10}} \right) \quad (12a)$$

$$\eta_{\text{add-balanced}} = 2e\mathfrak{R}(P_S + P_{LO}) + \frac{4k_B T}{R_L} \quad (12b)$$

where  $k_B$  is Boltzmann's constant,  $T$  is the absolute temperature,  $R_L$  is the load resistance of the receiver, and RIN is in units of  $\text{dB}/\text{Hz}$ . For signal bandwidths less than the laser resonance frequency, Eq. (12) is accurate, however for higher signal bandwidths, the RIN noise spectrum assumes a more complicated form. Here, we will assume the signal spectrum is contained below the laser resonance frequency.

#### 4. - Signal to Noise Ratio

The current  $i_{\text{photo}}(t)$  of Eq. (7), can be written as the sum of a signal,  $s(t)$ , and a noise term, viz:  $i_{\text{photo}}(t) = s(t) + n(t)$ . A typical  $i_{\text{photo}}(t)$  spectrum for a coherent system

with a distributed feedback (DFB) laser as the signal source and a 1 GHz sinusoidal modulation is shown in Fig. 2a. An external cavity (EC) laser was used as the LO. Note that the spectral width of both the modulation sidebands as well as the carrier signal is approximately 40 MHz, corresponding to the combined linewidth of the DFB laser and the EC laser (i.e.  $\Delta\nu=40$  MHz for this link). In comparison, Fig. 2b is the spectrum of the photocurrent for a coherent system with external cavity (EC) lasers for both the LO and signal sources. The combined linewidth for the external cavity lasers is very narrow ( $\Delta\nu < 100$  kHz) resulting in a very narrow photocurrent spectrum. The difference between the two spectra illustrates the spectral broadening effects of phase noise.

The signal after the IF filter,  $v(t)$ , is given by the convolution of  $i_{photo}(t)$  and the impulse response of the IF filter,  $h_{B-IF}(t)$ , thus:

$$v(t) = s(t) * h_{B-IF}(t) + n(t) * h_{B-IF}(t) = s_B(t) + n_B(t) \quad (13)$$

For phase-noise broadened signals,  $s_B(t)$  is a distorted version of  $s(t)$  as seen in Fig. 3a, which shows the IF filtered spectrum of the  $\Delta\nu = 40$  MHz link photocurrent spectrum in Fig. 2a. The spectral broadening of the phase-noise causes the “tails” of the photocurrent spectrum to be cut off by the IF filter. In contrast, the distortion by the IF filter of the  $\Delta\nu < 100$  kHz photocurrent spectrum in Fig. 2b is negligible, as shown in Fig. 3b. As will be seen, the distortion of phase broadened signals by the IF filter is the source of the phase-to-intensity noise.

The signal after the SLD is given by:

$$w(t) = |v(t)|^2 \quad (14)$$

The autocorrelation function of  $w(t)$  for stationary, zero-mean, and independent signal and noise is [15]:

$$R_w(\tau) = E[w(t)w(t+\tau)] = R_{S_b^2}(\tau) + \left(4R_{S_b}(\tau)R_{N_b}(\tau) + 2\sigma_{S_b}^2\sigma_{N_b}^2\right) + R_{N_b^2}(\tau) \quad (15)$$

where  $E[ ]$  denotes the expectation value,  $R_{S_b}(\tau)$  and  $R_{N_b}(\tau)$  are the filtered signal and noise autocorrelations,  $\sigma_{S_b}^2$  and  $\sigma_{N_b}^2$  are the filtered signal and noise variances, and

$$R_{S_b^2}(\tau) \equiv E[s_b^2(t)s_b^2(t+\tau)] \quad (16a)$$

$$R_{N_b^2}(\tau) \equiv E[n_b^2(t)n_b^2(t+\tau)] \quad (16b)$$

The first term on the right in Eq. (15) contains the useful signal, while the next two terms are, respectively, the beat between the signal and noise, and the beat of the noise with itself.

The term  $R_{S_b^2}(\tau)$  contains both the signal and the phase-to-intensity distortion. This term can be rewritten as the sum of the autocorrelation function of the squared signal *undistorted* by the IF filter,  $R_{S^2}$ , and another term due to the phase-to-intensity noise (denoted as  $R_\phi(\tau)$ ). Now,

$$R_{S_b^2}(\tau) = E[s^2(t)s^2(t+\tau)] + R_\phi(\tau) = R_{S^2}(\tau) + R_\phi(\tau) \quad (17)$$

The output of the SLD is filtered by the NBF to improve the signal quality. The filtered signal is given as the convolution of  $w(t)$  with the NBF impulse response,  $h_{B-NBF}(t)$ , such that:

$$z(t) = w(t) * h_{B-NBF}(t) \quad (18)$$

A typical spectrum of the demodulated signal after the NBF is shown in Fig. 4 for  $\Delta\nu = 40$  MHz. Note that the spectral broadening seen in the sidebands of the IF signal is

eliminated in the demodulated signal after the SLD. Despite the suppression of the spectral broadening, the noise floor of the output signal still contains a contribution from the PTI noise due to the IF filter distortion.

The autocorrelation function of  $z(t)$  is:

$$R_Z(\tau) = \left( R_{S^2}(\tau) + R_\phi(\tau) + \left( 4R_{S_B}(\tau)R_{N_B}(\tau) + 2\sigma_{S_B}^2\sigma_{N_B}^2 \right) + R_{N_B^2}(\tau) \right) * h_{B-NBF}(\tau) \quad (19)$$

The output power can be obtained by evaluating  $R_Z(\tau)$  at  $\tau = 0$ . The resulting expression has four contributions to the total output power:

$$P_{Z-out} = P_{sig} + P_{Phase} + P_{S-N Beat} + P_{N^2}, \quad (20)$$

where the first term ( $P_{sig}$ ) is due to the demodulated signal, while the next three terms are the phase-to-intensity noise ( $P_{Phase}$ ), the signal-noise beat ( $P_{S-N Beat}$ ), and the noise-squared power ( $P_{N^2}$ ).

In the absence of phase noise,  $R_\phi(\tau) = 0$ . In this case, the SNR is the ratio of the signal power to the signal-noise beat and noise-squared powers. For the typical case of  $m \ll 1$  the SNR (after the NBF) is given by:

$$SNR_{ideal} \approx \frac{A^4 m^2 \bar{x}^2(t)}{4A^2 \eta_{add} B_{NBF} + 2\eta_{add}^2 B_{NBF} (B_{IF} - f_0)} \quad (21)$$

where  $f_0$  is the center frequency of the NBF,  $B_{NBF}$  is the bandwidth of the narrow band filter,  $B_{IF}$  is the bandwidth of the IF filter, and  $\bar{x}^2(t)$  is the time average of the normalized RF signal power. The first term in the denominator of Eq. (21) is the signal-noise beat power, and the second is the noise-squared power.

In the presence of phase noise, the distortion of the signal at the IF filter introduces a new noise term (phase-to-intensity noise) to the denominator of Eq. (21) which is proportional to  $A^4$ , viz.:

$$SNR \approx \frac{A^4 m^2 \tilde{x}^2(t)}{A^4 \int_{NBF} K_{Phase}(\omega) d\omega + 4A^2 \eta_{add} B_{NBF} + 2\eta_{add}^2 B_{NBF} (B_{IF} - f_0)} \quad (22)$$

where the phase-to-intensity noise power has been expressed in terms of a normalized one-sided PSD ( $K_{Phase}(\omega)$ ) such that  $P_{Phase} \propto \langle i_{PTI}^2 \rangle = A^4 \int_0^\infty K_{Phase}(\omega) d\omega$ , where  $\langle i_{PTI}^2 \rangle$  is the mean squared PTI noise current.  $K_{Phase}(\omega)$  will be useful in Sec. 6 to generalize the numerical results. Since both the signal and the PTI noise are proportional to  $A^4$ , the phase-to-intensity noise sets a fundamental limit to the SNR which is independent of the received optical signal power. As will be shown in Sec. 6, high SNR systems that uses lasers with linewidths in the MHz range are performance-limited by the PTI noise.

### 5. - Phase-to-Intensity Noise Spectrum

To predict the performance of links with arbitrary modulation signals, it is necessary to obtain the PSD of the PTI noise. The contribution of the PTI noise,  $R_\phi(\tau)$ , is the difference between the autocorrelation function of the ideal signal and that of the filtered signal. That is:

$$R_\phi(\tau) = R_{S^2}(\tau) - R_{S_b^2}(\tau) \quad (23)$$

The spectrum of the PTI noise is the Fourier transform of  $R_\phi(\tau)$ .

It is not possible to find a closed form expression for  $R_{S_b^2}(\tau)$  (and thus  $R_\phi(\tau)$ ) because of the presence of a random variable in the phase of the signal,  $s(t)$ . Convolution with the IF filter results in integrals of the type  $\int e^{j(\Phi(\alpha))} d\alpha$  which are difficult to

evaluate. Hence, it is necessary to directly evaluate the autocorrelation function  $R_{S_b^2}(\tau)$  as the expectation value of a quadruple integral. Using the relation [16]:

$$\langle e^{j(\Phi(t))} \rangle = e^{-\frac{\sigma^2}{2}} \quad (24)$$

for a Gaussian random variable  $\Phi(t)$  and its variance  $\sigma^2$ , the integral can be cast in a tractable form. The resulting expression for  $R_{S_b^2}(\tau)$  is given in Appendix A, Eq. (A4). Reference [8] approximates the phase-to-intensity noise power as the power of the modulated portion of the IF signal which is cut off by the IF filter. In this work, we estimate the phase-to-intensity noise power by numerical evaluation of Eq. (A4). We will show in Sec. 7 that this method reveals different dependencies for the PTI noise than those found in Ref. [8].

## 6 - Numerical Evaluation

The most critical parameter in the evaluation of  $R_{S_b^2}(\tau)$  is the choice of the IF filter function. For comparison with experimental results, the IF filter model must accurately approximate the experiment while maintaining a reasonably short computation time. Hamming filters were found to have the best balance of these qualities [17]. Figure 5 is a comparison between the Hamming filter function and the effective IF filter used in the experimental link. The effective IF filter passband is the combination of the IF amplifier and the SLD passbands. As can be seen, the Hamming filter is slightly more rounded than the experimental IF filter, and has sidebands 35 dB below the main lobe. Despite these differences, the estimates of the PTI noise using the Hamming filter are in good agreement with the experimental results given in Sec. 7.1.

The numerical results can be generalized to any LO and signal laser optical powers by expressing the results in terms of a normalized power spectral density,

$K_{Phase}(\omega) \left( K_{Phase}(\omega) \equiv \frac{PSD_{PTI}(\omega)}{A^4} \right)$ , where  $PSD_{PTI}(\omega)$  is the power spectral density of the PTI noise. A plot of  $K_{Phase}(\omega)$  versus frequency for two different IF filter bandwidths with  $\Delta\nu = 50$  MHz and the typical case of  $m \ll 1$  and  $\omega_m < \frac{B_{IF}}{2}$  is shown in Fig. 6. The spectra in Fig. 6 have their maxima at  $\omega = 0$ , and decay monotonically with increasing frequency. Most of the noise power is in a bandwidth approximately equal to the IF filter bandwidth centered around  $\omega = 0$ . The frequencies of interest are  $\omega < \frac{B_{IF}}{2}$ , since the bandwidth of the RF signal is limited to this region. Here the noise spectrum is nearly constant, decaying by less than 3 dB from its maximum at  $\omega = 0$ .

Doubling the IF filter bandwidth decreases the maximum PTI noise power by 9 dB, and the total PTI noise power by 6 dB. This is apparent in Fig. 7, which is a plot of both  $K_{Phase}$  at 1GHz for two linewidths, and the total normalized phase noise,  $C \equiv \int_0^{\infty} K_{Phase}(\omega) d\omega$ , for  $\Delta\nu = 50$  MHz versus the IF filter bandwidth. For large bandwidths ( $B_{IF} \gg \Delta\nu$ ) the phase-to-intensity noise power at 1GHz is inversely proportional to  $(B_{IF})^3$  while the total phase-to-intensity noise power is inversely proportional to  $(B_{IF})^2$ . The difference between the slopes of the two lines is the result of the broadening of the phase-to-intensity noise spectrum as the IF filter bandwidth is increased (see Fig. 6). The broadening of the spectrum partially offsets the decrease in the maximum noise so that the total phase-to-intensity noise power decreases at a slower rate than the maximum phase-to-intensity noise as the IF filter bandwidth is increased. However, one of the advantages of WIRNA processing is the rejection of all out-of-band noise by the NBF. Thus, the link SNR scales proportionally with  $(B_{IF})^3$  in the phase-noise-limited regime.

The effect of the combined laser linewidth on the phase-to-intensity noise spectrum for a fixed IF filter bandwidth is illustrated in Fig. 8, where  $K_{Phase}$  at 1 GHz is plotted versus  $\Delta\nu$  for three different IF filter bandwidths. For laser linewidths much

smaller than the IF filter bandwidth ( $\Delta\nu \ll B_{IF}$ ), the signal distortion is confined to the tail of the Lorentzian lineshape and the phase-to-intensity noise power increases quadratically with the linewidth ( $\propto \Delta\nu^2$ ). As the linewidth approaches the IF bandwidth, the noise power saturates. However, links operated in this regime, ( $\Delta\nu \approx B_{IF}$ ), are not useful since the majority of the signal is lost at the IF filter.

Comparison of Figs. 7 and 8 reveals that the effect of halving the combined linewidth is *not* the same as doubling the IF filter bandwidth in a WIRNA system. Halving  $\Delta\nu$  reduces the PTI noise by 6 dB, but does not change the width of the PTI noise spectrum. Doubling  $B_{IF}$  also reduces the total noise power by 6 dB, however as seen in Fig. 6, the PTI noise spectrum is widened so that an additional 3 dB PTI noise reduction can be achieved with the use of a NBF.

The power spectrum of the phase-to-intensity noise was found to be independent of the modulation index and modulation frequency for the typical case of small  $m$  and  $\omega_m \ll \frac{\omega_{IF}}{2}$ . The PTI noise generated from the modulated sidebands is negligible compared to the PTI noise of the carrier signal due to the power difference between the two.

### 6.1 Optimum IF Filter Bandwidth

Although the phase-to-intensity noise is reduced by increasing the IF filter bandwidth, it is well known that the noise-squared term in Eq. (22) increases with increasing IF filter width [16]. In fact each of the three noise terms in the denominator of Eq. (22) dominates for different IF filter bandwidth ranges. The optimum IF filter bandwidth maximizes the SNR for a given set of link parameters. For links with high carrier-to-noise ratios (CNR), such as phased array antenna or CATV links, the noise-squared term is usually negligible for practical IF filter bandwidths. Figure 9 is a plot of the noise power at 1GHz versus the IF bandwidth for several different combined laser linewidths of a high CNR link. Here,  $A_{balanced} = 3.182 \times 10^{-3}$  [Amp],

$\eta_{add-balanced} = 6.34 \times 10^{-22} \left[ \frac{\text{Amp}^2}{\text{Hz}} \right]$ , the receiver electronic power gain is 80 dB, and the

link is modulated at 1 GHz. Note that the minimum IF filter bandwidth is 2 GHz since the modulation frequency is 1 GHz. With these conditions, the lowest noise power for all laser linewidths is  $-38.9 \text{ dB}/_{1 \text{ GHz}}$  corresponding to an optimum SNR of  $70 \text{ dB}/_{2 \text{ MHz}}$  at a modulation index of  $m = 0.1$ . The high carrier power in this example causes the PTI noise to dominate for IF bandwidths less than 10 GHz when  $\Delta\nu > 10 \text{ MHz}$ . When  $\Delta\nu = 100 \text{ MHz}$ , the minimum IF filter bandwidth needed for the SNR to be within 1 dB of its optimum value is 115 GHz. The IF filter bandwidths for smaller  $\Delta\nu$ , in this example, are more practical with  $B_{\text{IF}} = 25 \text{ GHz}$  being the minimum bandwidth needed to keep the SNR within 1 dB of its optimum value for  $\Delta\nu = 10 \text{ MHz}$ . The small additive noise power under these conditions prevents the noise-squared term from dominating for all practical IF bandwidths ( $B_{\text{IF}} < 1 \text{ THz}$ ). Thus for high CNR links, there is a broad range for the IF filter bandwidth which will maintain the SNR within 1 dB of its optimum value. However, the large IF bandwidth required to do so may force the use of a smaller than optimal filter bandwidth due to the high cost of broad-band components.

For the case of low CNR links, the noise-squared term dominates at moderate IF bandwidths. This is shown in Fig. 10 which is a plot of the noise power versus the IF filter bandwidth for several low CNR links with different  $A_{\text{balanced}}$ . All of the links have

$\eta_{\text{balanced}} = 2.512 \times 10^{-19} \left[ \frac{\text{Amp}^2}{\text{Hz}} \right]$ ,  $\Delta\nu = 100 \text{ MHz}$ , a receiver electronic power gain of 80 dB, and a 1 GHz sinusoidal modulation. The lowest noise for  $A_{\text{balanced}} = 0.3 \text{ mA}$  is  $-18.65 \text{ dB}/_{1 \text{ GHz}}$  corresponding to an optimum SNR of  $10 \text{ dB}/_{2 \text{ MHz}}$ . At very small IF bandwidths, the link is influenced by the PTI noise, while at large IF bandwidths the noise-squared term completely dominates. For this link,  $B_{\text{IF}} < 11.8 \text{ GHz}$  is needed to keep the SNR within 1 dB of the optimum. The low carrier power in this example diminishes the PTI noise relative to the signal-beat noise term and the noise-squared term such that  $B_{\text{IF}}$  can be very close to the minimum value of 2 GHz without significantly affecting the SNR. It should be noted that the SNR penalty for larger-than-optimum IF bandwidths in low CNR links is much less severe than the SNR penalty for smaller-than-optimum IF bandwidths in high CNR links.

## 7. - Experimental AM-WIRNA Link Performance

A block diagram of the experimental link is shown in Fig. 11. Two different configurations were investigated; the first used a narrow linewidth EC laser for the LO and the signal laser, while the second used an EC laser for the LO and a DFB laser for the signal source. Both the EC and DFB lasers operated at a wavelength of  $\lambda = 1.54 \mu\text{m}$ .

The EC lasers have an integrated optical isolator to minimize reflections. An external grating provides wavelength tuning, and an internal TE cooler provides temperature stability of the cavity. The EC signal laser launches  $550 \mu\text{W}$  into the fiber with a RIN of  $-161.5 \text{ dB/Hz}$  at  $55 \text{ }^\circ\text{C}$ , and the EC LO laser launches  $2.1 \text{ mW}$  into the fiber with a RIN of  $-161.0 \text{ dB/Hz}$  at  $55 \text{ }^\circ\text{C}$ . The combined linewidth of the EC LO laser and the EC signal laser is  $< 100 \text{ kHz}$ .

The DFB laser also has an integrated optical isolator to reduce reflections, and a thermoelectric (TE) cooler which allows for wavelength tuning and stabilization. The DFB signal laser launches  $5 \text{ mW}$  into the fiber with a corresponding RIN of  $-148 \text{ dB/Hz}$  at  $25.0 \text{ }^\circ\text{C}$ . The combined linewidth of the EC LO and DFB signal lasers is  $40 \text{ MHz}$ .

The AM is introduced via a Mach-Zender (M-Z) modulator which is biased at its small signal linear point. The bias introduces a  $3 \text{ dB}$  loss, and an additional  $7 \text{ dB}$  coupling loss was also measured for the modulator. The modulator  $V_\pi = 2.9 \text{ V}$  at  $1 \text{ GHz}$ . An optical attenuator is used to control the signal power arriving at the receiver. The polarization of each of the lasers is manually controlled to maximize the power at the detector.

The optical signal is incident on a single photodetector connected to a GaAs pre-amplifier with a bandwidth of  $15 \text{ GHz}$ , a gain of  $24 \text{ dB}$  and a noise figure (NF) of  $2 \text{ dB}$ . The maximum optical input power before the pre-amplifier saturates is  $1.5 \text{ mW}$ . The EC LO laser has  $770 \mu\text{W}$  power at the photodetector.

The WIRNA receiver is implemented with two amplifiers and a field effect transistor configured as a SLD. The IF amplifier has a  $3 \text{ dB}$  passband from  $1.7$  to  $7.5 \text{ GHz}$ , a gain of  $52 \text{ dB}$ , and a  $\text{NF} = 3 \text{ dB}$ . The combined  $3 \text{ dB}$  bandwidth of the IF amplifier

followed by the SLD is 5 GHz centered at 4.8 GHz. To avoid amplifier saturation, a 10 dB wideband attenuator is placed in front of the IF amplifier. Wideband attenuators are also used to limit the RF power into the SLD. The NBF consists of an amplifier with a 3 dB passband from 0.8 GHz to 1.5 GHz. The NBF amplifier gain is 42 dB with a NF of 2.5 dB.

The IF frequency is 4.9 GHz, and was found to be stable to within 75 MHz with the DFB signal laser and to within 25 MHz with the EC signal laser. No closed-loop frequency stabilization was used, although the lasers were stabilized through thermal regulation using the built in TE coolers. The DFB laser temperature was held to within  $\pm 0.01$  °C.

### 7.1 - Experimental Results

The effect of phase noise on an AM-WIRNA link is seen most clearly in a comparison of the SNR for a link with  $\Delta\nu < 100$  kHz and for a link with  $\Delta\nu \approx 40$  MHz as shown in Fig. 12. In both links, an EC laser was used as the LO with 770  $\mu$ W power at the detector. A 1 GHz RF input signal with a modulation index of  $m=0.091$  was used in both links and the maximum signal laser power at the detector was 11.5  $\mu$ W. The SLD performance was found to vary with the RF input power. In order to avoid this effect, the input power to the SLD was kept constant at -10 dBm by varying the attenuators after the IF amplifier.

The  $\Delta\nu < 100$  kHz link SNR has a linear dependence on received signal power at all signal powers tested. The linear signal power dependence indicates that the signal-beat noise term in the denominator of Eq. (22) dominates at all received signal powers. In this link, the additive noise power was dominated by both the LO RIN noise and thermal noise, so that when the output noise is dominated by the signal-beat noise the  $SNR \propto A^2 \approx \Re^2 2\alpha_{fiber}\alpha_{excess} P_{LO} P_S$ . In contrast, the  $\Delta\nu \approx 40$  MHz link has a linear signal power dependence only at low ( $< -30$  dBm) received signal powers, while at higher received signal powers, the SNR rolls off to a constant value ( $-39.4$  dB/1MHz). In this

regime, the PTI noise term in the denominator of Eq. (22) dominates, and the link performance is severely degraded compared to the  $\Delta\nu < 100$  kHz link. It is important to note that the SNR roll-off at high signal powers is not caused by the DFB signal laser RIN, since the signal power levels are not high enough to dominate over the LO laser RIN.

The theoretical predictions from the analysis above are shown as the solid lines in Fig. 12 for both the  $\Delta\nu < 100$  kHz and  $\Delta\nu \approx 40$  MHz links. For both links, the power of the IF signal was 3.3 dB below the expected value. Most of this difference can be attributed to polarization fluctuations by the LO laser as well as fiber coupling loss at the detector. The theoretical predictions shown in Fig. 12 have been adjusted down by 3.3 dB to account for the non-ideal IF signal power in order to better illustrate the accuracy of the shape of the numerical analysis. The resulting prediction for the  $\Delta\nu \approx 40$  MHz link is accurate to within 1.4 dB of the experimental results in the PTI noise limited regime.

The noise spectrum of the link operating in the phase-to-intensity noise dominated region is shown in Fig. 13 along with the numerical prediction (dotted line). The oscillations in the noise spectrum are from resonances between components in the WIRNA receiver. In the modulation range of  $\omega < 2$  GHz, the numerical prediction has a root-mean-square deviation from the averaged experimental data (averaged to smooth out the component resonances) of 1.2 dB with a maximum deviation of 3.8 dB. The non-idealities of the SLD are estimated to contribute to approximately 2 dB of the maximum difference.

In contrast to the approximation in Ref. [8] which predicts that  $K_{phase} \propto m^2$ , the noise spectrum in the phase-noise dominated regime is in fact found to be independent of the modulation index and modulation frequency for small  $m$ . In this case, the more powerful carrier signal dominates the PTI noise. It should be noted that the  $\Delta\nu$  and  $B_{IF}$  dependencies predicted in the numerical analysis above also differ from the approximation in Ref. [8].

## 8. - Summary

Although amplitude modulation is less phase-noise sensitive than angle modulation in high frequency analog optical links, it can still be performance limited by phase-to-intensity noise conversion. In this paper we have numerically evaluated the effect of phase-to-intensity noise conversion, and find that its PSD is nearly flat in the frequency range of the RF signal modulation, varying by less than 3 dB. For typical links where  $B_{IF} \gg \Delta\nu$ ,  $m \ll 1$ , and  $\omega_m < \frac{\omega_{ff}}{2}$ , the phase-to-intensity noise power in the modulation band is proportional to  $(\Delta\nu)^2$ . The total PTI noise power (before NBF filtering) is inversely proportional to  $(B_{IF})^2$ , however, in a WIRNA system the NBF rejects out-of-band noise in such a way that the PTI noise power after NBF filtering is inversely proportional to  $(B_{IF})^3$ .

Widening the IF filter bandwidth tends to decrease the phase-to-intensity noise, although the noise-squared power will increase. An optimum IF bandwidth for a given link can be found by calculating the PTI noise and minimizing the total noise power in the denominator of Eq. 22. Links with high SNR such as phased array antennas or CATV links, generally require very large IF bandwidths to attain optimized link performance when  $\Delta\nu$  is greater than a few MHz. Such links are phase-to-intensity noise limited at small IF bandwidths. Low SNR links generally require smaller IF filter bandwidths to avoid degradation from the noise-squared term. High dynamic range links, with their wide range of SNR conditions, must consider both the PTI noise domination under high SNR conditions, as well as the noise-squared domination at low SNR. In general, the IF bandwidth for such links should be designed to accommodate the PTI noise under the highest SNR conditions, since the sensitivity penalty for larger than optimal bandwidths is much less than for smaller than optimal bandwidths. It should be

noted that better IF filters could be designed using non-linear filter optimization [20], however practical considerations prevent their implementation at this time.

For  $m \ll 1$ , the PTI noise is independent of the modulation frequency and the modulation index. The PTI noise generated by the carrier signal dominates in the phase-noise limited regime.

The calculated phase-to-intensity noise PSD was within 1.2 dB of the averaged experimental data with a maximum deviation of 3.8 dB. Approximately 2 dB of the difference can be accounted for by deviations of the SLD from ideal square law behavior. The experimental link exhibited a phase-to-intensity noise limited SNR at high optical powers. The predicted SNR was within 1.4 dB of experiment in the phase-noise limited regime.

The foregoing results indicate that applications having a high CNR will be most severely affected by phase-to-intensity noise. Large IF filter bandwidths can reduce the phase-to-intensity noise, and in some cases eliminate it as the dominant noise source. However, care must be taken to optimize the IF filter bandwidth so that the noise-squared term does not degrade the link performance.

#### Acknowledgments

The authors thank Rome Laboratories and DARPA (NCIPT) for supporting this work. They are also grateful to Brian Hendrickson, Rajesh Sundaresan, and Michael Kozuch for their many helpful suggestions.

## Appendix A

The PSD of the phase-to-intensity noise spectrum is obtained from the autocorrelation function of the distorted signal given by Eq. (14). The ideal signal autocorrelation,  $R_{S^2}(\tau)$ , is straightforward to evaluate, however the filtered signal autocorrelation,  $R_{S_B^2}(\tau)$  must be evaluated numerically. We will assume that the modulation signal is sinusoidal with a modulation frequency,  $\omega_m$ .

The square of the filtered signal,  $s_B^2(t) = |s(t) * h_B(t)|^2$ , is given by the double convolution integral

$$s_B^2(t) = A^2 \iint h_B(\alpha) h_B(\beta) \left[ (1 + m \cos(\omega_m(t - \alpha))) \cos(\omega_{IF}(t - \alpha) + \Phi(t - \alpha)) \right. \\ \left. \cdot (1 + m \cos(\omega_m(t - \beta))) \cos(\omega_{IF}(t - \beta) + \Phi(t - \beta)) \right] d\alpha d\beta \quad (\text{A1})$$

Here,  $h_B(t)$  is the impulse response function of the IF filter, and  $\alpha$  and  $\beta$  are the integration variables. Substituting (A1) into equation (16a) yields:

$$R_{S_B^2}(\tau) = \frac{A^4}{4} \iiint \left[ h_B(\alpha) h_B(\beta) h_B(\eta) h_B(\varepsilon) f(\alpha, \beta, \eta, \varepsilon) \right. \\ \left. \cdot \left\langle \cos(\omega_{IF}(-\alpha + \beta + \eta - \varepsilon) + \Phi(t - \alpha) - \Phi(t - \beta) - \Phi(t + \tau - \eta) + \Phi(t + \tau - \varepsilon)) \right. \right. \\ \left. \left. + \cos(\omega_{IF}(-\alpha + \beta + \varepsilon - \eta) + \Phi(t - \alpha) - \Phi(t - \beta) + \Phi(t + \tau - \eta) - \Phi(t + \tau - \varepsilon)) \right. \right. \\ \left. \left. + \cos(\omega_{IF}(2\tau + \alpha + \beta - \eta - \varepsilon) - \Phi(t - \alpha) - \Phi(t - \beta) + \Phi(t + \tau - \eta) + \Phi(t + \tau - \varepsilon)) \right\rangle d\alpha d\beta d\varepsilon d\eta \right] \quad (\text{A2})$$

where  $\langle \rangle$  is the expectation value and  $f(\alpha, \beta, \eta, \varepsilon)$  is given as

$$\begin{aligned}
f(\alpha, \beta, \eta, \varepsilon) = & 1 + \frac{m^2}{2} \left( \cos(\omega_m(\beta - \alpha)) + \cos(\omega_m(\tau - \eta + \alpha)) + \cos(\omega_m(\tau - \varepsilon + \alpha)) \right. \\
& + \cos(\omega_m(\tau - \eta + \beta)) + \cos(\omega_m(\tau - \varepsilon + \beta)) + \cos(\omega_m(\varepsilon - \eta)) + \frac{m^2}{2} \left( \cos(\omega_m(\varepsilon - \eta - \beta + \alpha)) \right. \\
& \left. \left. + \cos(\omega_m(\varepsilon - \eta + \beta - \alpha)) + \cos(\omega_m(2\tau - \varepsilon - \eta + \beta + \alpha)) \right) \right) \quad (A3)
\end{aligned}$$

Terms centered at  $2\omega_{IF}$  (last term on the right hand side of Eq. A2) are far above the signal bandwidth and hence can be neglected in calculating the SNR.

The expectation value in (A2) can be found using Eq's. (24) and (10). The low frequency portion of  $R_{S_B^2}(\tau)$  (neglecting the term at  $2\omega_{IF}$ ) is given as

$$\begin{aligned}
R_{S_B^2-Baseband} = & \iiint \iiint h_B(\alpha) h_B(\beta) h_B(\eta) h_B(\varepsilon) f(\alpha, \beta, \eta, \varepsilon) \left[ e^{-j[\omega_{IF}(\beta - \alpha - \eta + \varepsilon)]} e^{-\pi \Delta \nu [\tau_{NOL}]} \right. \\
& \left. \bullet e^{-j[\omega_{IF}(\beta - \alpha + \eta - \varepsilon)]} e^{-\pi \Delta \nu [\tau_{NOL} + 4\tau_{OL}]} \right] d\alpha d\beta d\eta d\varepsilon \quad (A4)
\end{aligned}$$

Here,  $\tau_{NOL}$  and  $\tau_{OL}$  are taken from Appendix D of Ref. [19], where  $\tau_{NOL}$  is the overlap between the time periods  $|\beta - \alpha|$  and  $|\eta - \varepsilon|$ , and  $\tau_{OL}$  is the time when the periods  $|\beta - \alpha|$  and  $|\eta - \varepsilon|$  do not overlap.

## References

- 1) R. Olshansky, R. Gross and M. Schmidt, "Subcarrier-Multiplexed coherent lightwave system for video distribution", IEEE J. Select. Areas Commun., vol.8, no. 7, pp. 1268-1275, 1990.
- 2) P. M. Freitag and S.R. Forrest, "A coherent optically controlled phased array antenna system", IEEE Microwave Guided Wave Lett., vol. 3, no. 9, pp. 293-295, 1993.
- 3) M. R. Surette, D. R. Hjelme, and A. R. Mickelson, "An optically driven phased array antenna utilized heterodyne techniques", J. Lightwave Technol., vol. 11, no. 9, pp. 1500-1509, 1995.
- 4) P. Johnson, B. Debney, and A. Carter, "Components and applications for high-speed optical analog links," High Frequency Analog Fiber Optic Systems, SPIE, vol. 1371, pp. 87-97, 1990.
- 5) Ligeng Xu, Robert Taylor and Stephen Forrest, "True Time-Delay Phased-Array Antenna Feed System Based on Optical Heterodyne Techniques", IEEE Photon. Technol. Lett., vol. 8, no. 1, pp 160-162, 1996.
- 6) Delfin Jay M. Sabido IX, Masafumi Tabara, Thomas K. Fong, Robert F. Kalman, and Leonid G. Kazovsky, "Experimental Linewidth-Insensitive Coherent Analog Optical Link", J. Lightwave Technol., vol. 12, no. 11, Nov. 1994.
- 7) Ligeng Xu, Robert Taylor and Stephen Forrest, "The Use of Optically Coherent Detection Techniques for True-Time Delay Phased Array Antenna Systems" J. Lightwave Technol., vol. 9, no. 1, pp. 1663-1678, 1995.
- 8) Thomas K. Fong, Delfin Jay M. Sabido IX, Robert F. Kalman, Masafumi Tabara, and Leonid G. Kazovsky, "Linewidth-Insensitive Coherent AM Optical Links: Design, Performance, and Potential Applications", J. Lightwave Technol., vol. 12, no. 3, pp. 526-534, Mar. 1994.
- 9) Thomas K. Fong, Delfin Jay M. Sabido IX, Leonid G. Kazovsky, "Linewidth-Insensitive Coherent AM Analog Optical Links Using Semiconductor Lasers", IEEE Photon. Technol. Lett., vol. 5, no. 5, pp. 469-471, Apr. 1993.
- 10) G.L. Abbas, V. W. S. Chan, and T. K. Yee, "Local-oscillator excess-noise suppression for homodyne and heterodyne detection", vol. 8, no. 8, Optics Lett., pp. 419-421, Aug. 1983.
- 11) R.A. Becker "Broad-band guided wave electro-optic modulators" IEEE Quantum Electron. vol. QE-20, no. 7, pp. 723 - 727, July 1984.

- 12) K. Kikuchi, T. Okoshi, M. Nagamatsu, and N. Henmi, "Degradation of bit-error rate in coherent optical communications due to spectral spread of the transmitter and the local oscillator", *J. Lightwave Technol.*, vol. LT-2, no. 6, pp. 1024-1033, Dec. 1984.
- 13) B. Daino, P. Spano, M. Tamburrini, and S. Piazzolla, "Phase Noise and Spectral Line Shape of Semiconductor Lasers", *IEEE J. Quantum Electron.*, vol. QE-19, no. 3, pp. 266-270, 1983.
- 14) Govind P. Agrawal, *Fiber-Optic Communication Systems*. New York: Wiley, 1992, pp. 156-158 and 253-255.
- 15) Wilbur B. Davenport, Jr., and William L. Root, *An Introduction to the Theory of Random Signals and Noise*. New York: IEEE Press, 1987, pp. 257-258.
- 16) Athanasios Papoulis, *Probability, Random Variables, and Stochastic Processes*, New York: McGraw-Hill, 1991.
- 17) Clare D. McGillem, and George R. Cooper, *Continuous and Discrete Signal and System Analysis*, New York: CBS College Publishing, 1984.
- 19) L.G. Kazovsky, P. Meissnew, and E. Patzak, "ASK multipoint optical homodyne receivers", *J. Lightwave Technol.*, vol. LT-5, no. 3, pp. 770-791, June 1987.
- 20) H. Vincent Poor, *An Introduction to Signal Detection and Estimation*, New York: Springer-Verlag, 1994, chap. 7.

## Figure Captions

Fig. 1 Block diagram of an analog coherent AM-WIRNA link. The WIRNA receiver consists of a photodetector, intermediate frequency (IF) filter, square law device (SLD), and narrow band filter (NBF).

Fig. 2a Typical phase-broadened power spectrum of the photocurrent from the  $\Delta\nu = 40$  MHz AM-WIRNA experimental link. The LO laser is an external cavity (EC) laser with  $770 \mu\text{W}$  power at the receiver, and the signal laser is a distributed feedback (DFB) laser with  $11.5 \mu\text{W}$  power at the receiver.

Fig. 2b Typical power spectrum of the photocurrent from the  $\Delta\nu = 100$  kHz AM-WIRNA experimental link. Both the LO laser and the signal laser are external cavity (EC) lasers with a LO power of  $770 \mu\text{W}$  and a signal power of  $11.5 \mu\text{W}$  at the receiver.

Fig. 3a Typical power spectrum of the IF filtered photocurrent of the  $\Delta\nu = 40$  MHz AM-WIRNA experimental link illustrating the IF filter distortion on the phase-broadened photocurrent. The link conditions are the same as those in Fig. 2a, and the IF filter has a 5 GHz, 3 dB bandwidth centered at 4.8 GHz.

Fig. 3b Typical power spectrum of the IF filtered photocurrent of the  $\Delta\nu = 100$  kHz AM-WIRNA experimental link illustrating the minimal IF filter distortion for small  $\Delta\nu$  links. The link conditions are the same as those in Fig. 2b using the IF filter in Fig. 3a.

Fig. 4 Typical power spectrum of the demodulated output signal obtained from the  $\Delta\nu = 40$  MHz AM-WIRNA experimental link illustrating the suppression of the spectral broadening of the IF signal. The link conditions are the same as those in Fig. 2a. The NBF has a 3 dB bandwidth of 700 MHz centered at 1.15 GHz.

Fig. 5 A comparison of the Hamming filter response used in the numerical analysis to approximate the experimental IF filter and the actual experimental effective IF filter response. The experimental effective IF filter passband is the combined passbands of the IF amplifier and SLD which together have a 5 GHz, 3 dB bandwidth centered at 4.8 GHz.

Fig. 6 Normalized one-sided spectral density ( $K_{Phase} = \frac{PSD_{PTI}}{A^4}$ ) versus frequency from the numerical analysis with  $\Delta\nu = 50$  MHz and the typical case of  $m \ll 1$  and  $\omega_m < \frac{B_{IF}}{2}$ .

Fig. 7 Total PTI noise power versus IF bandwidth compared to the PTI noise power at 1 GHz as predicted by the numerical analysis.

Fig. 8  $K_{Phase}$  at 1 GHz versus combined laser linewidth for several IF filter bandwidths as predicted by the numerical results.

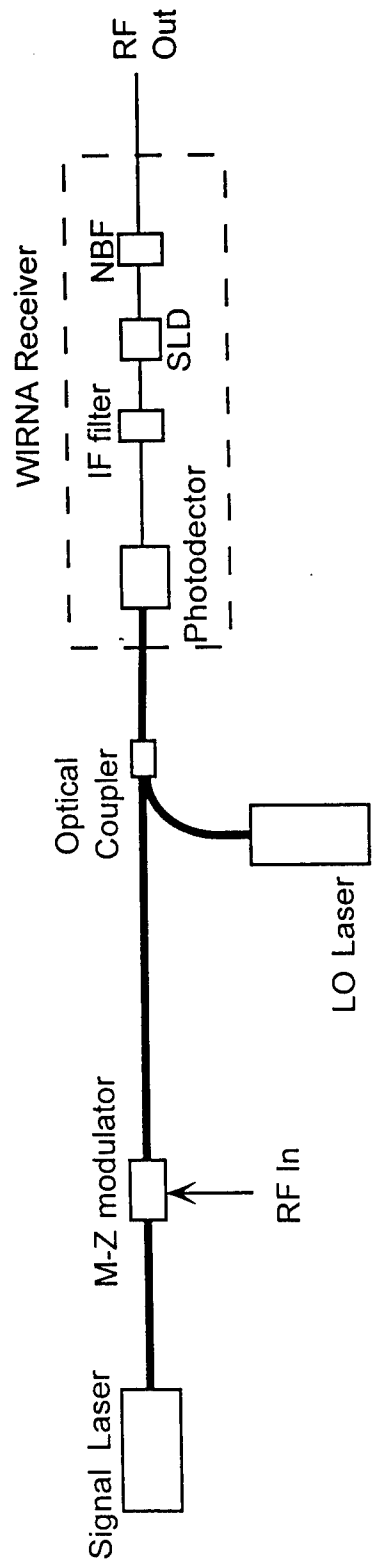
Fig. 9 Noise power versus bandwidth for a high CNR link (PTI noise dominated at moderate  $B_{IF}$ ) with  $A_{balanced} = 3.182 \times 10^{-3}$  [Amp],  $\eta_{add-balanced} = 6.34 \times 10^{-22}$  [ $\frac{\text{Amp}^2}{\text{Hz}}$ ], a receiver electronic power gain of 80 dB, and a modulation frequency of 1 GHz. The optimum IF filter bandwidth is achieved when the noise power is within < 1dB of its minimum value.

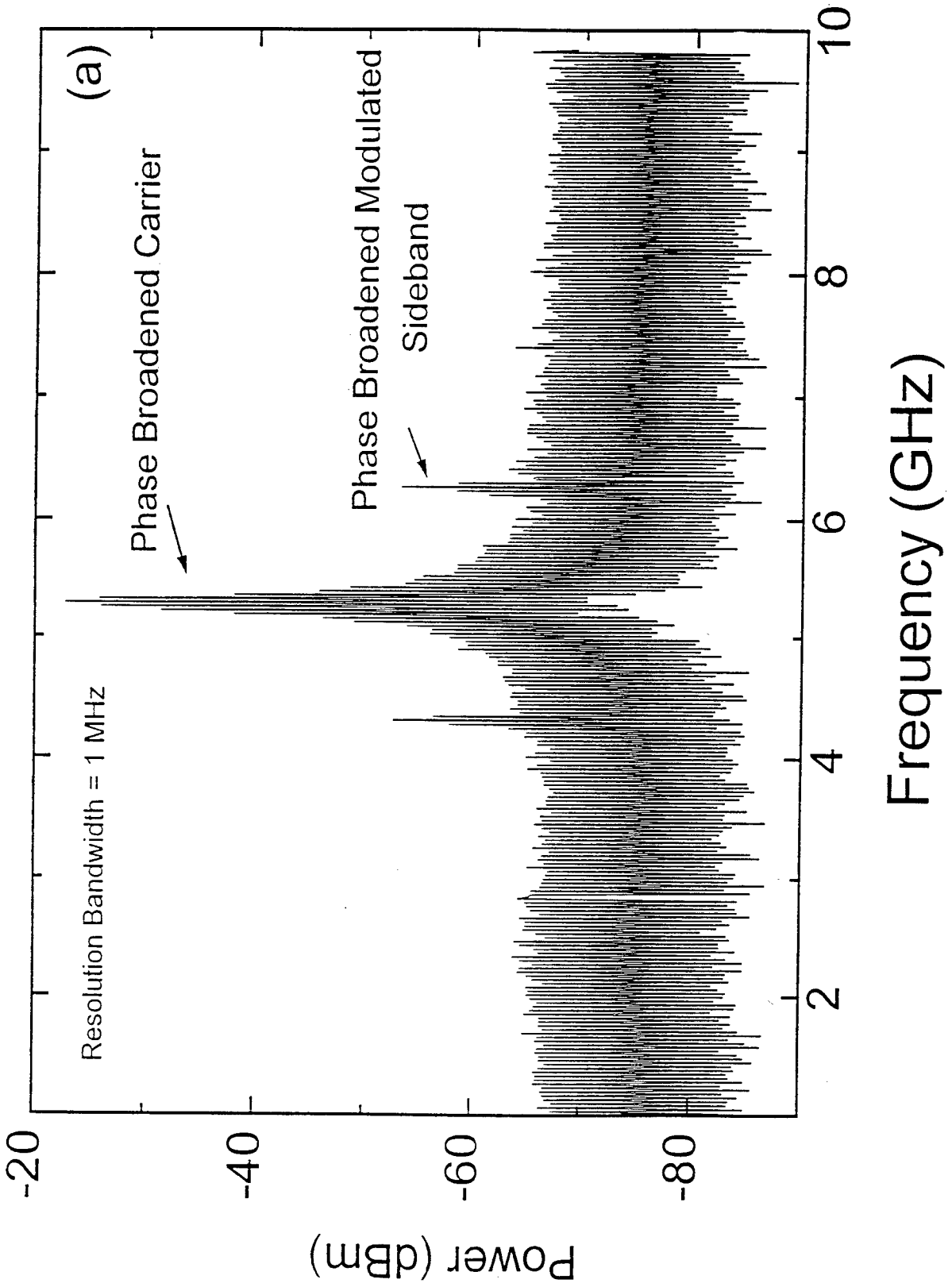
Fig. 10 Noise power versus IF filter bandwidth for a low CNR link (noise-squared term dominated at moderate  $B_{IF}$ ) with  $\eta_{balanced} = 2.512 \times 10^{-19}$  [ $\frac{\text{Amp}^2}{\text{Hz}}$ ],  $\Delta\nu = 100$  MHz, a receiver electronic power gain of 80 dB, and a 1 GHz sinusoidal modulation for several  $A_{Balanced}$  values.

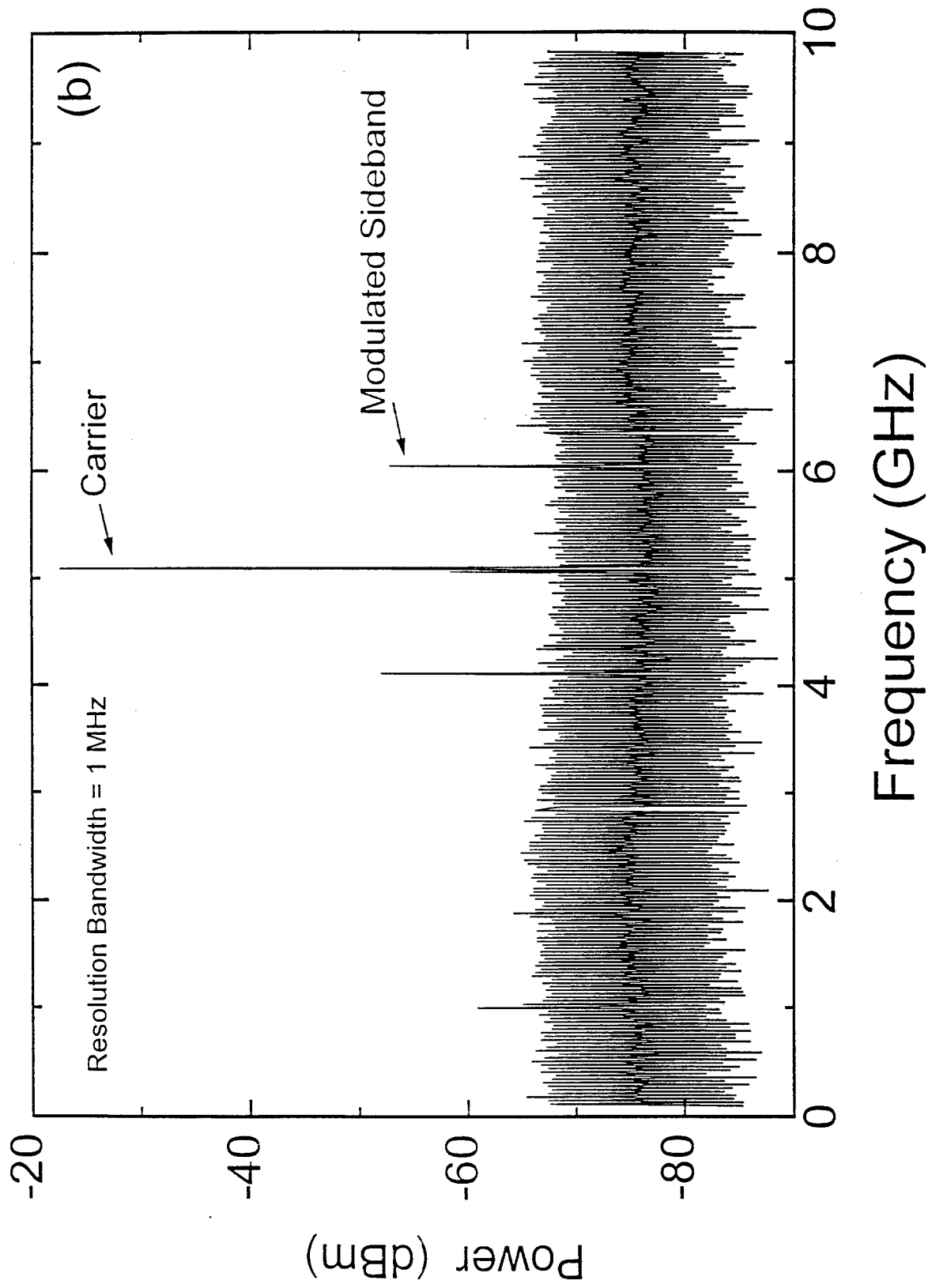
Fig. 11 Block diagram of the experimental coherent AM-WIRNA link. The LO laser is an external cavity laser, and both an external cavity laser and DFB laser are used for the signal laser in different experiments.

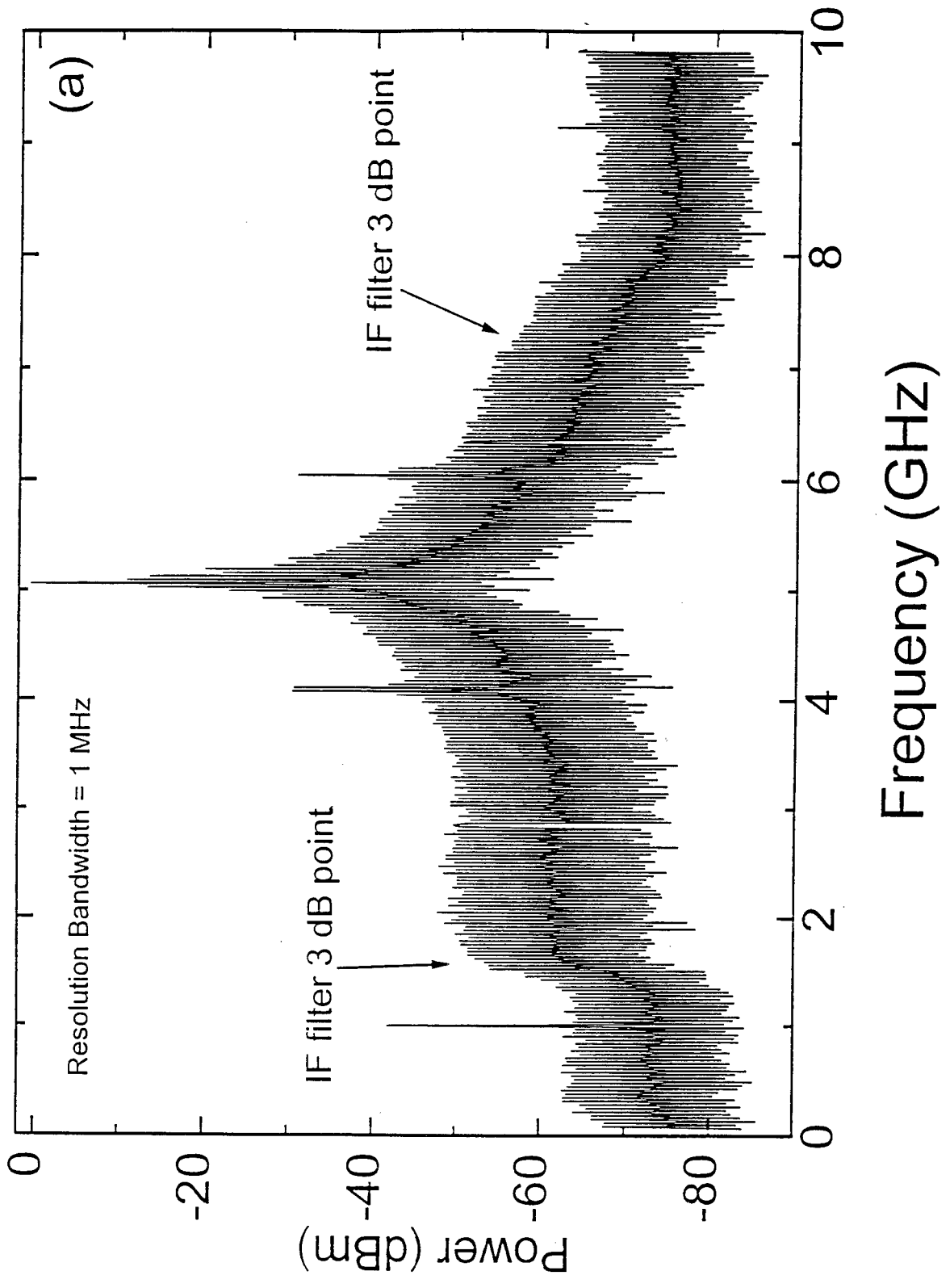
Fig. 12 Comparison of the experimental SNR versus signal power for a  $\Delta\nu = 40$  MHz link and a  $\Delta\nu = 100$  kHz link illustrating the PTI noise induced degradation of SNR. The SNR results for the numerical analysis are shown as a solid line, which is shifted by -3.3 dB from the calculation.

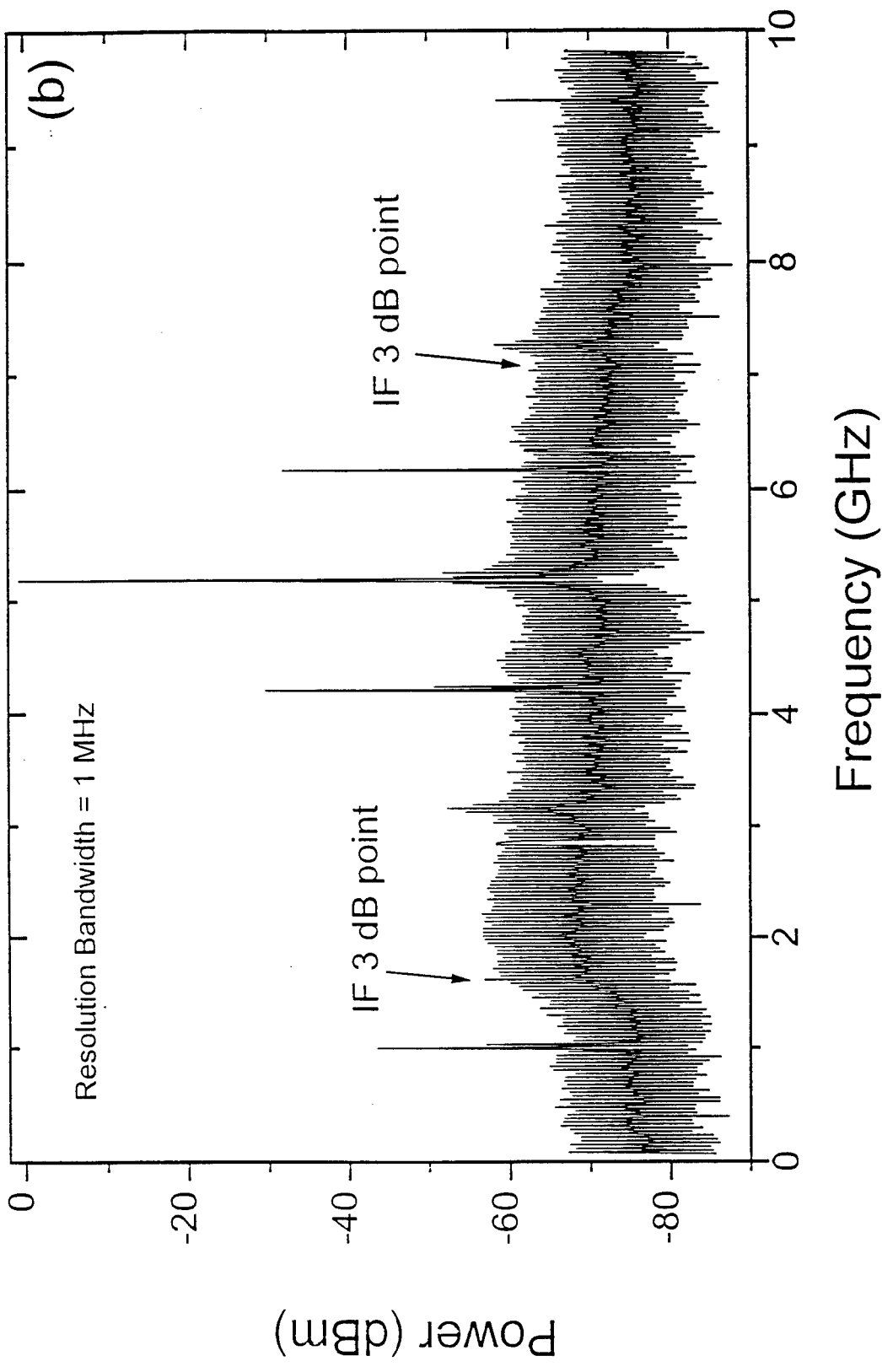
Fig. 13 Comparison of the noise spectrum for a  $\Delta\nu = 40$  MHz link in the phase-noise limited regime to the numerical results.

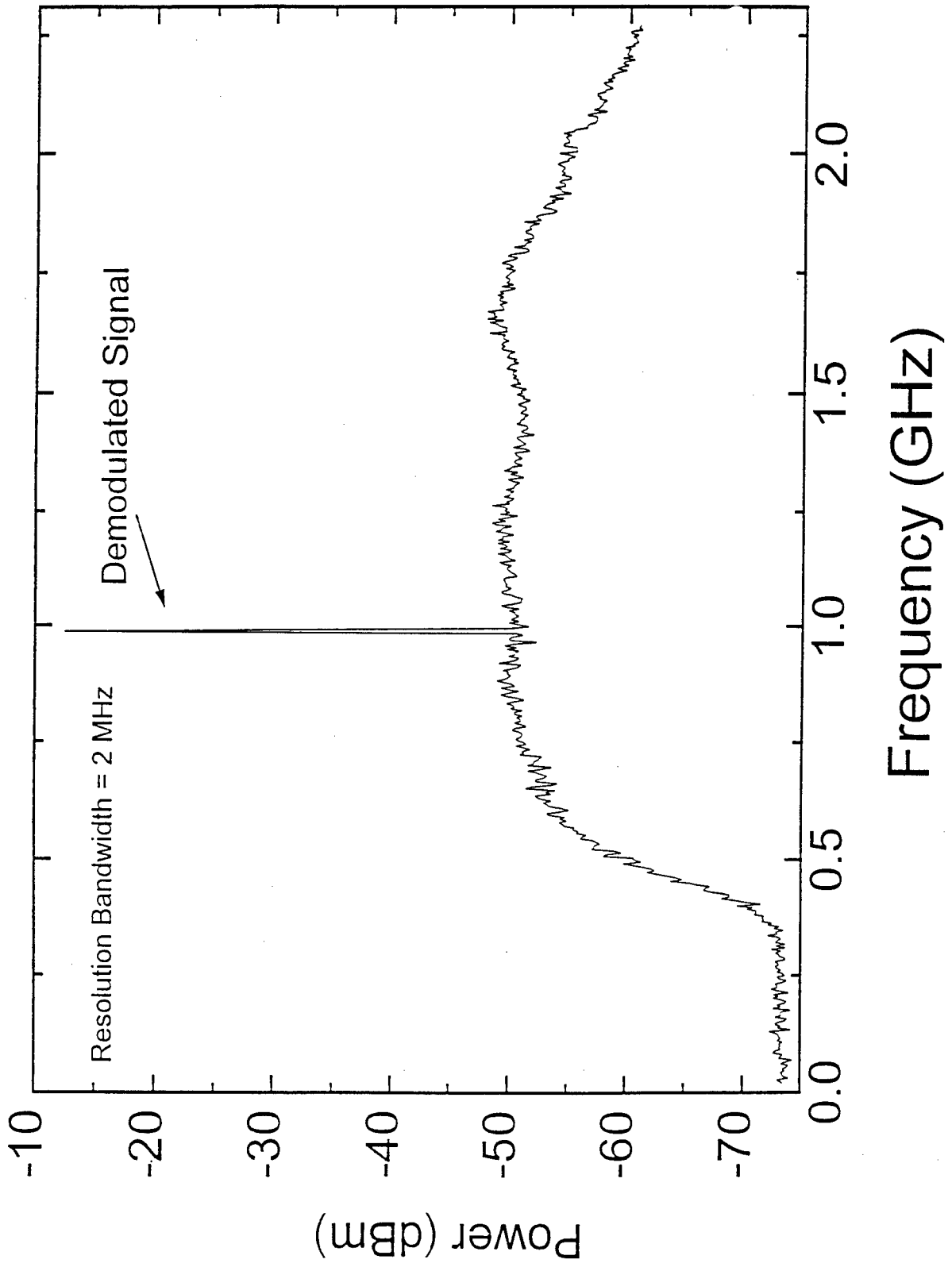


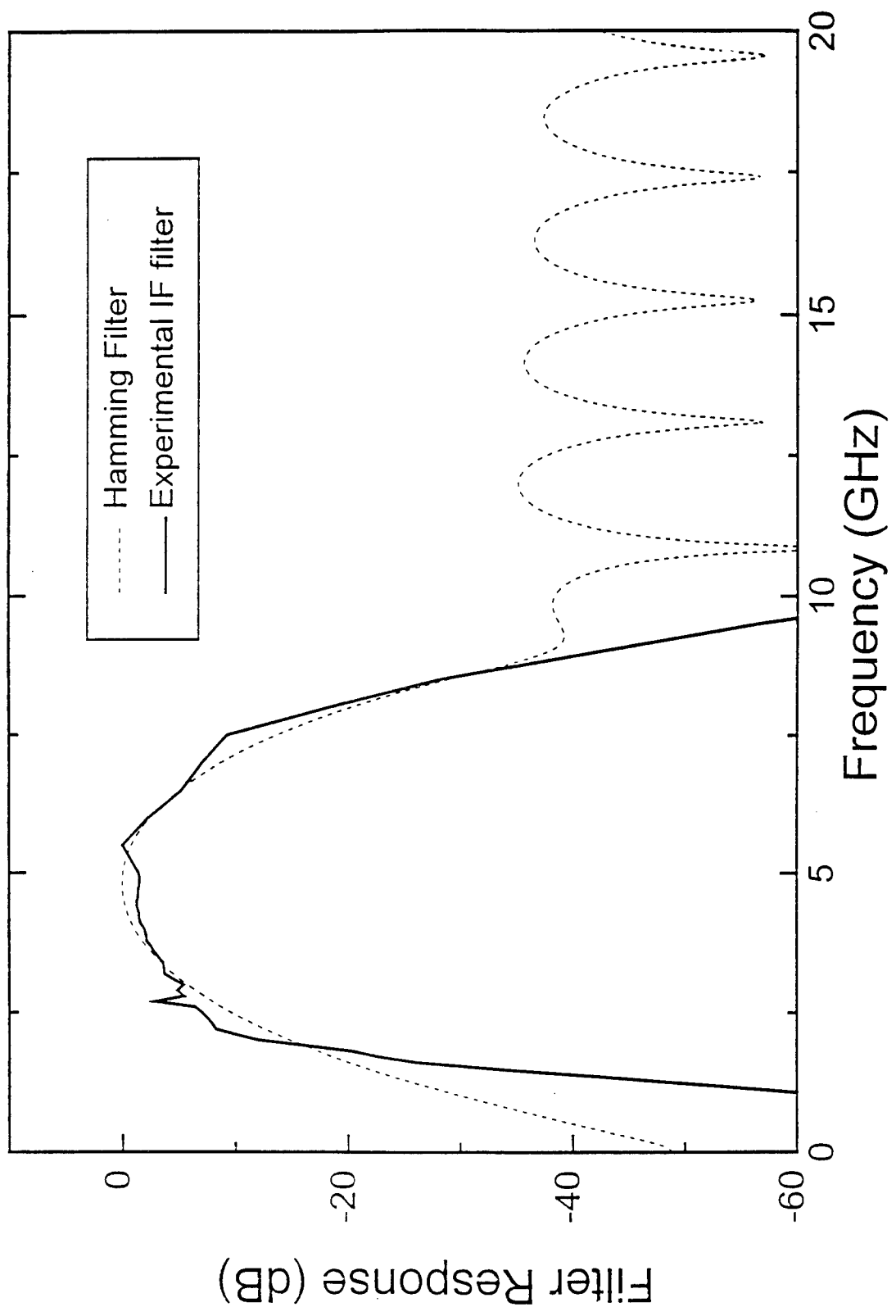


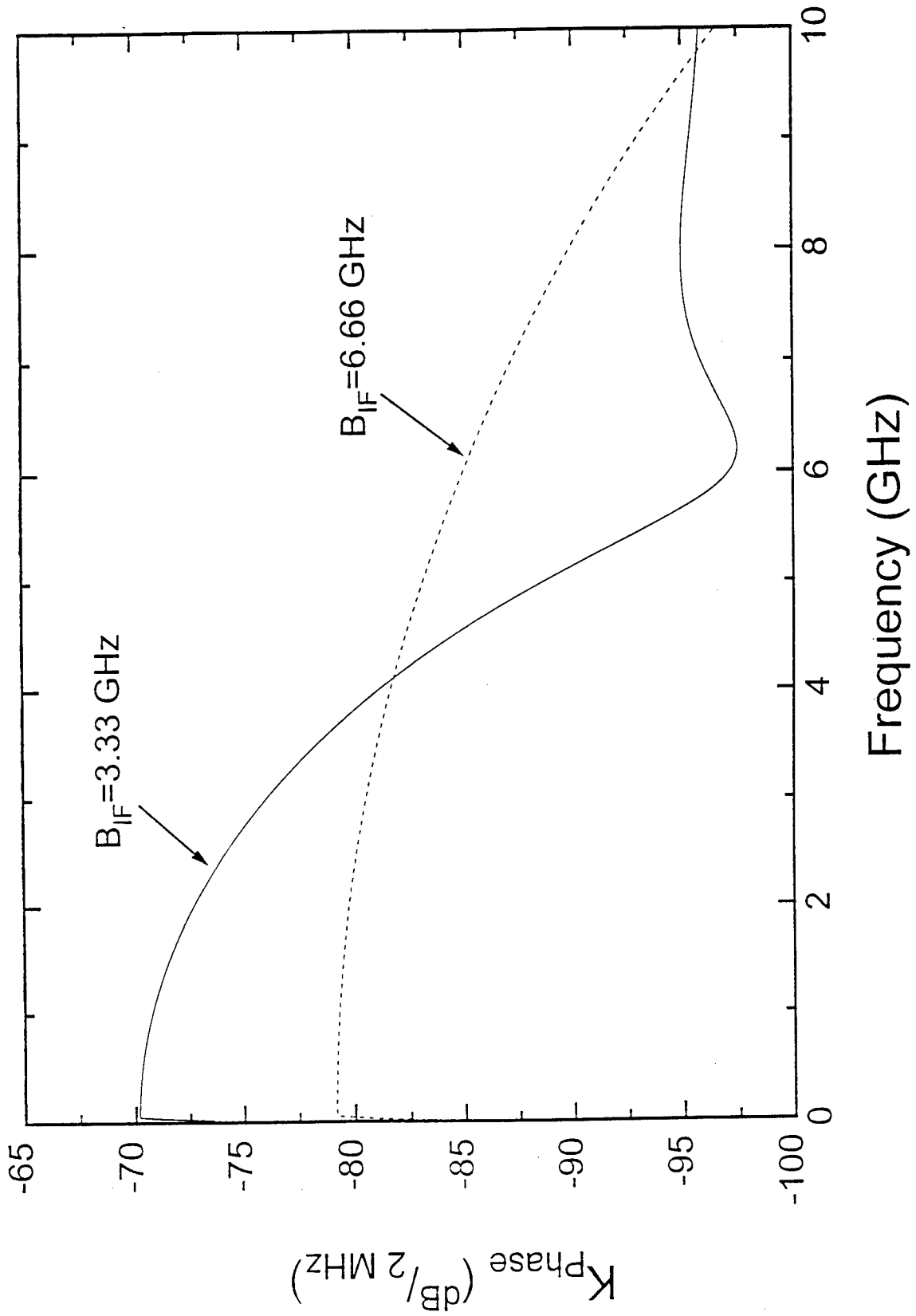


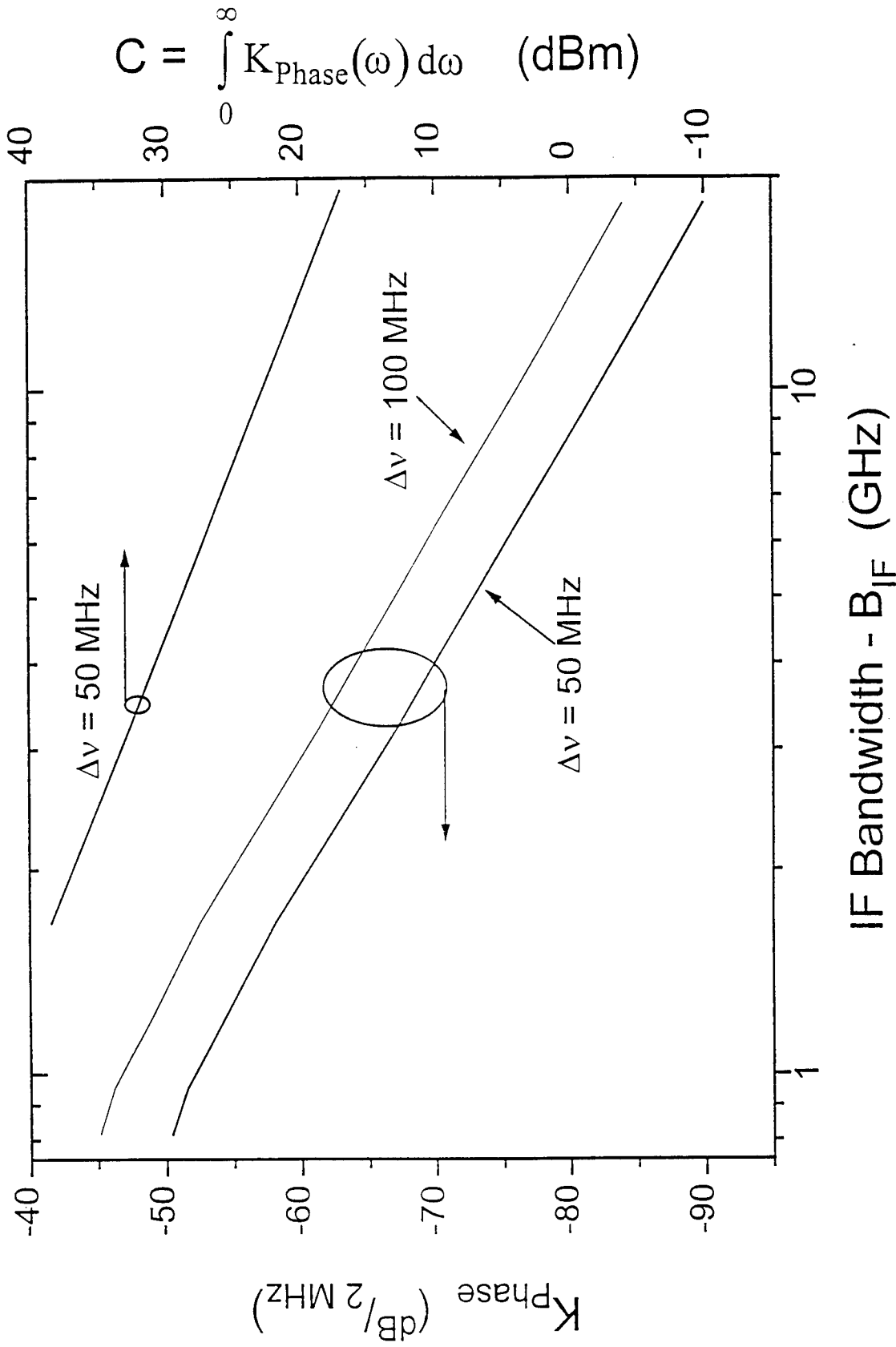


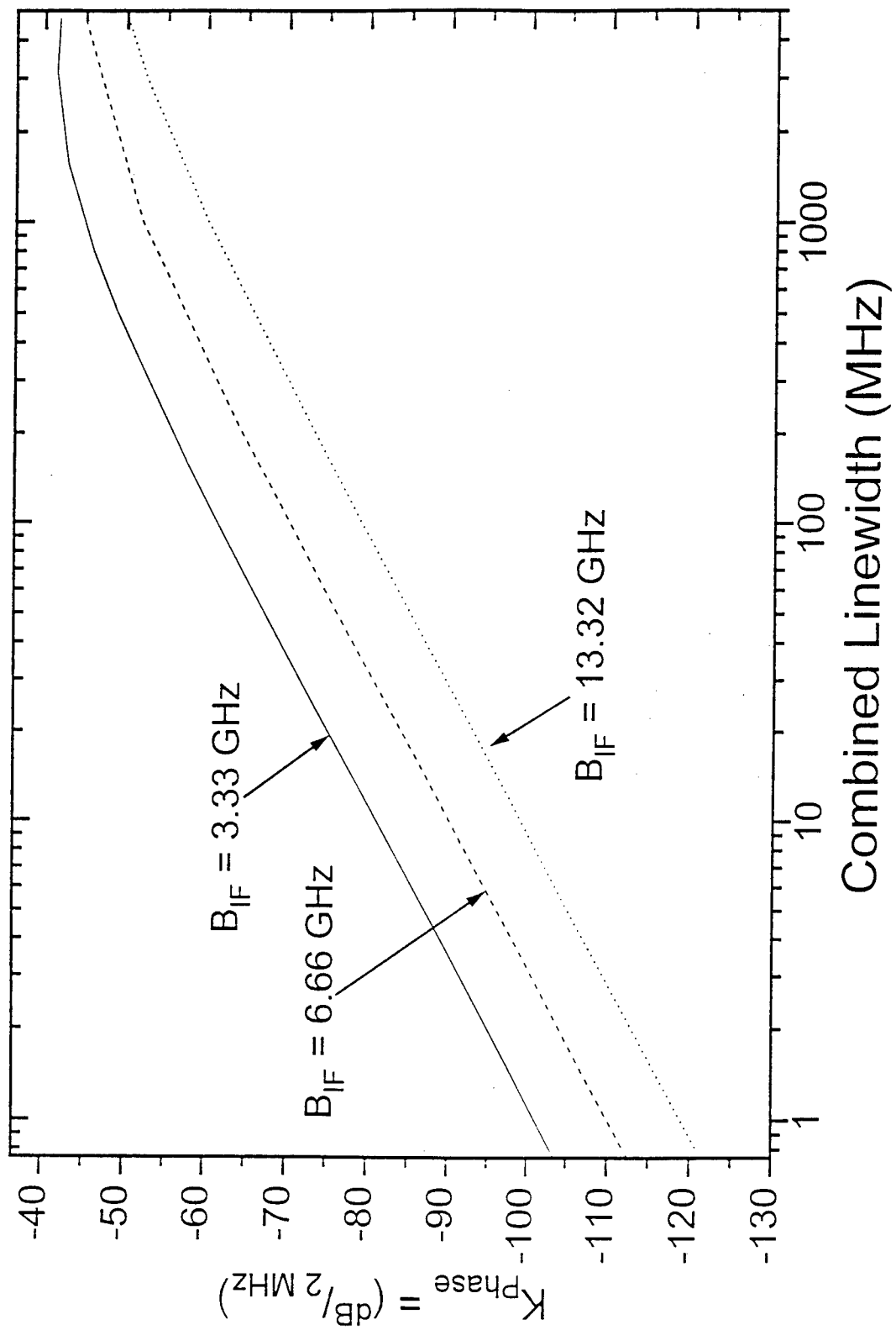


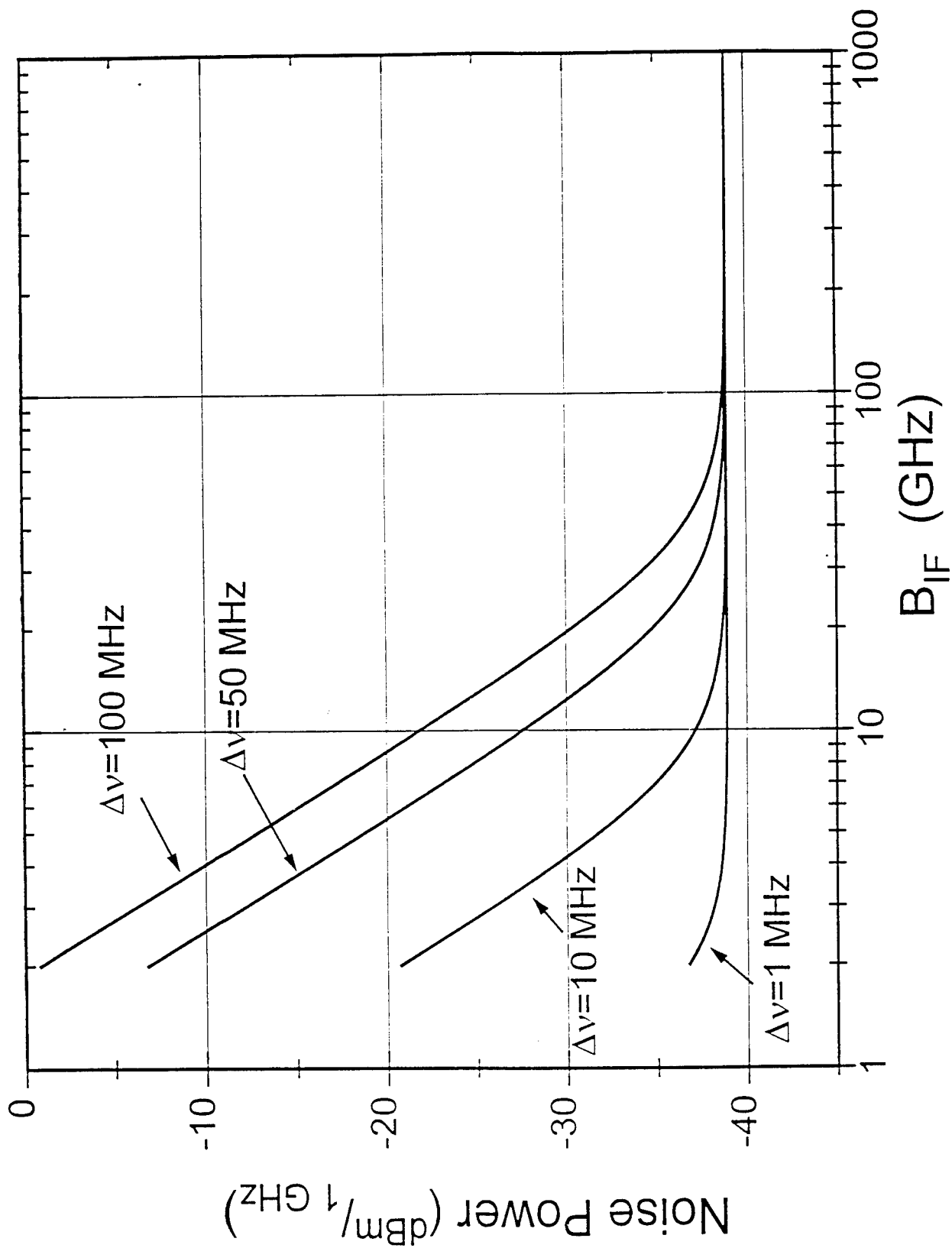


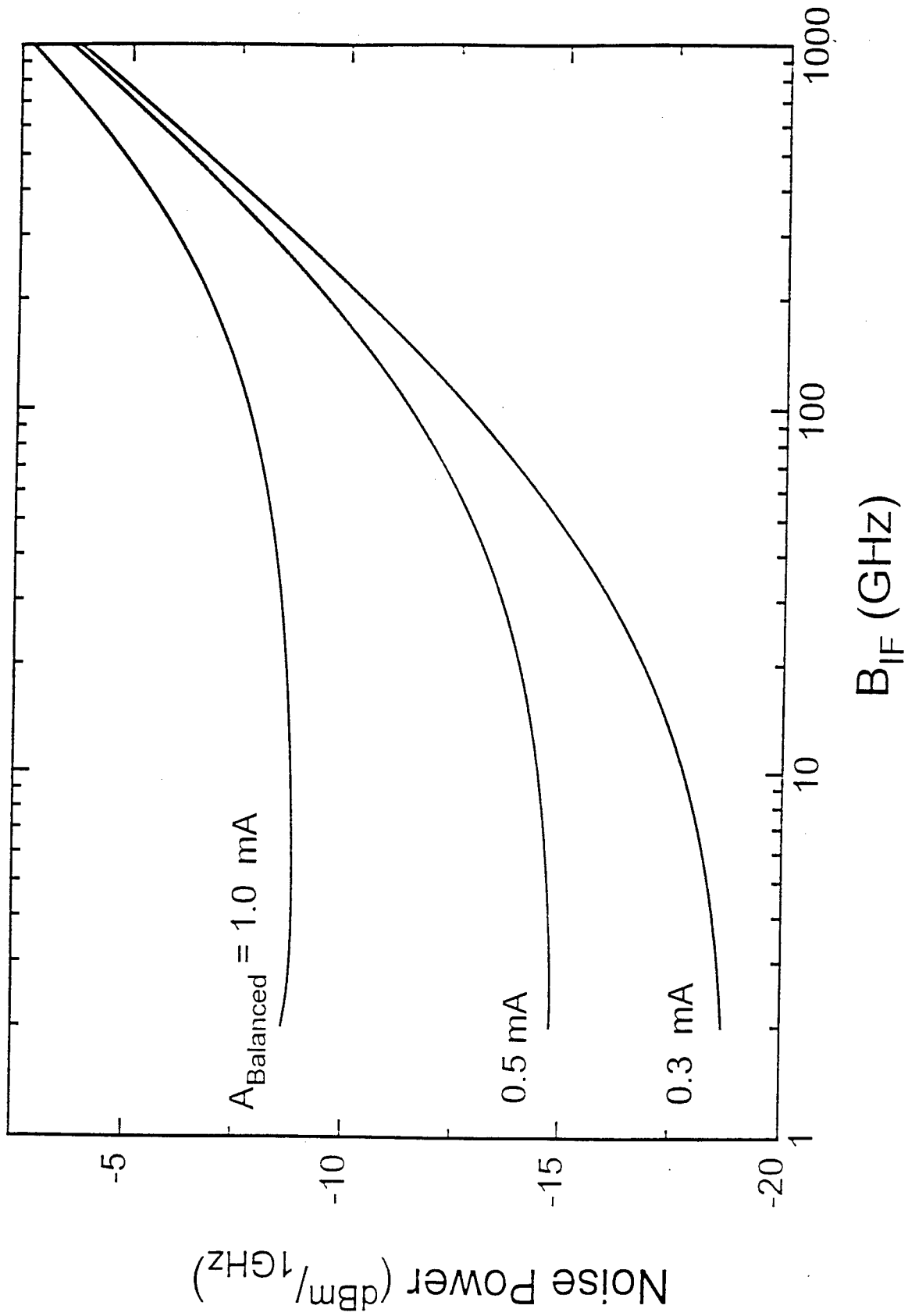


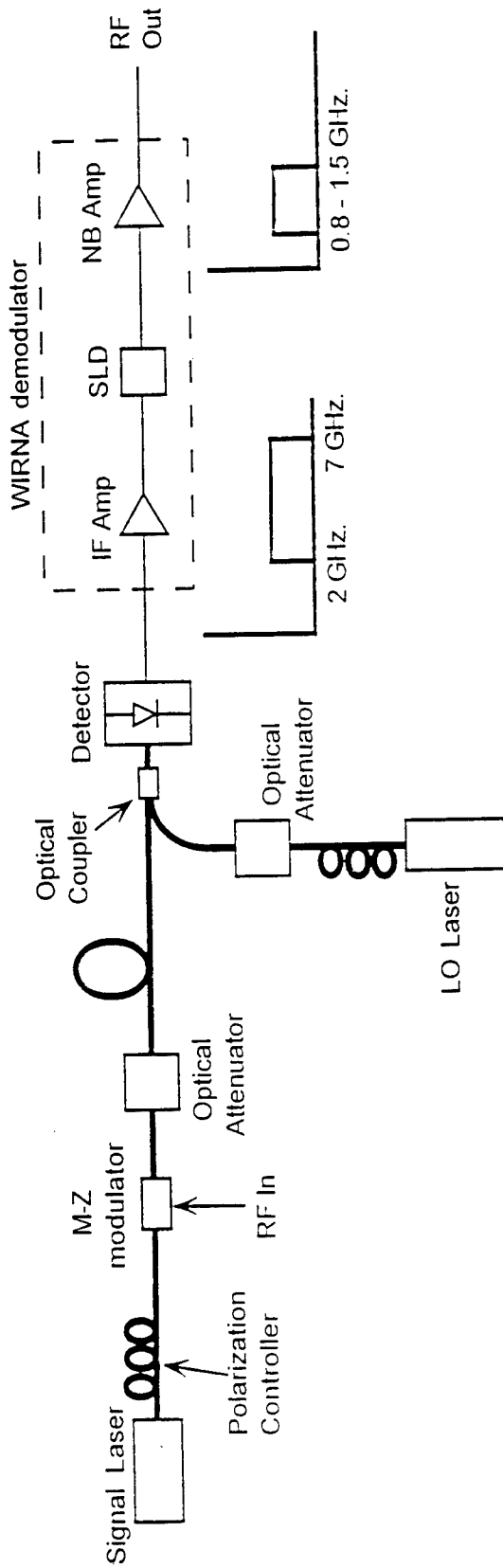


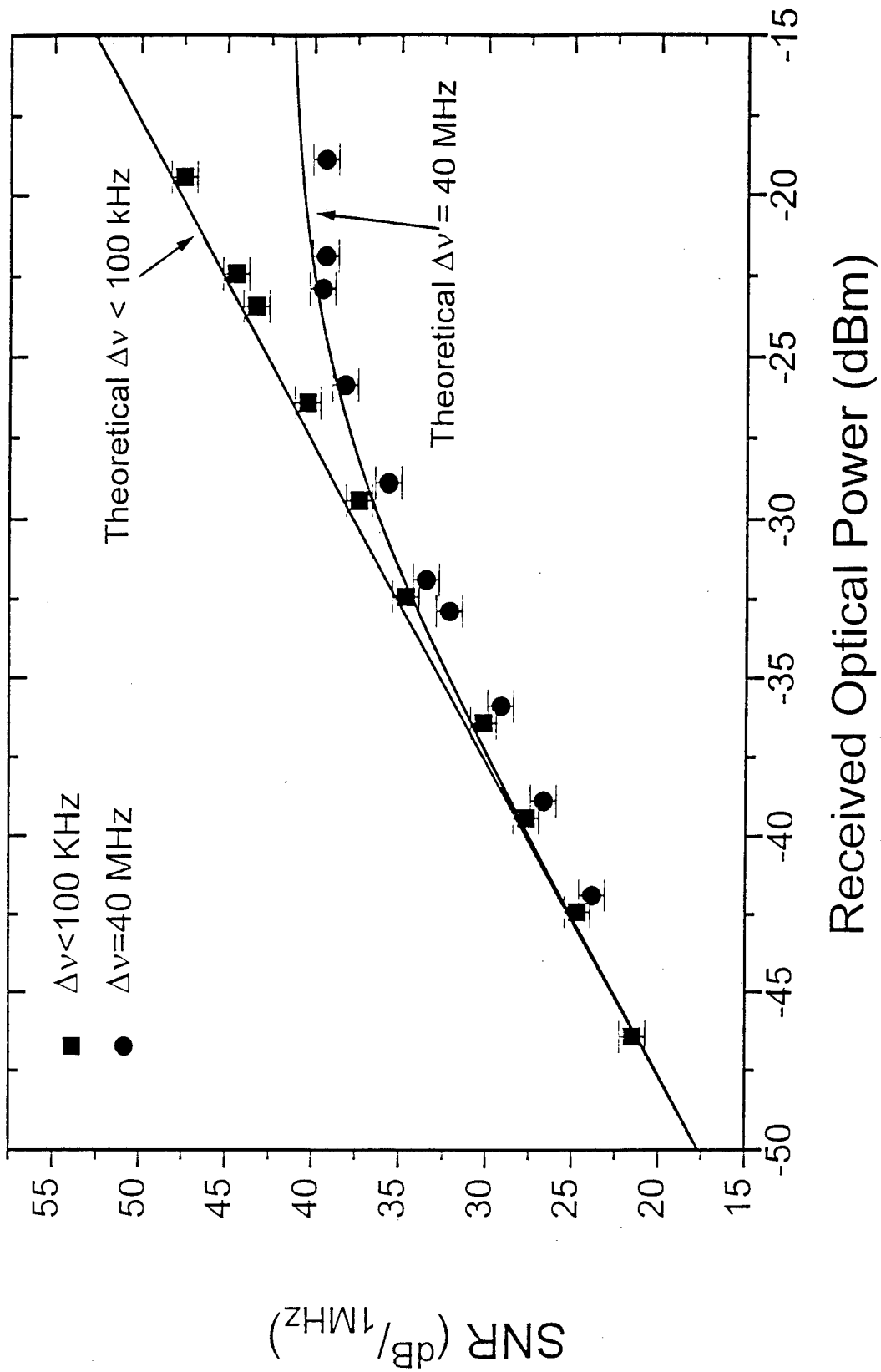


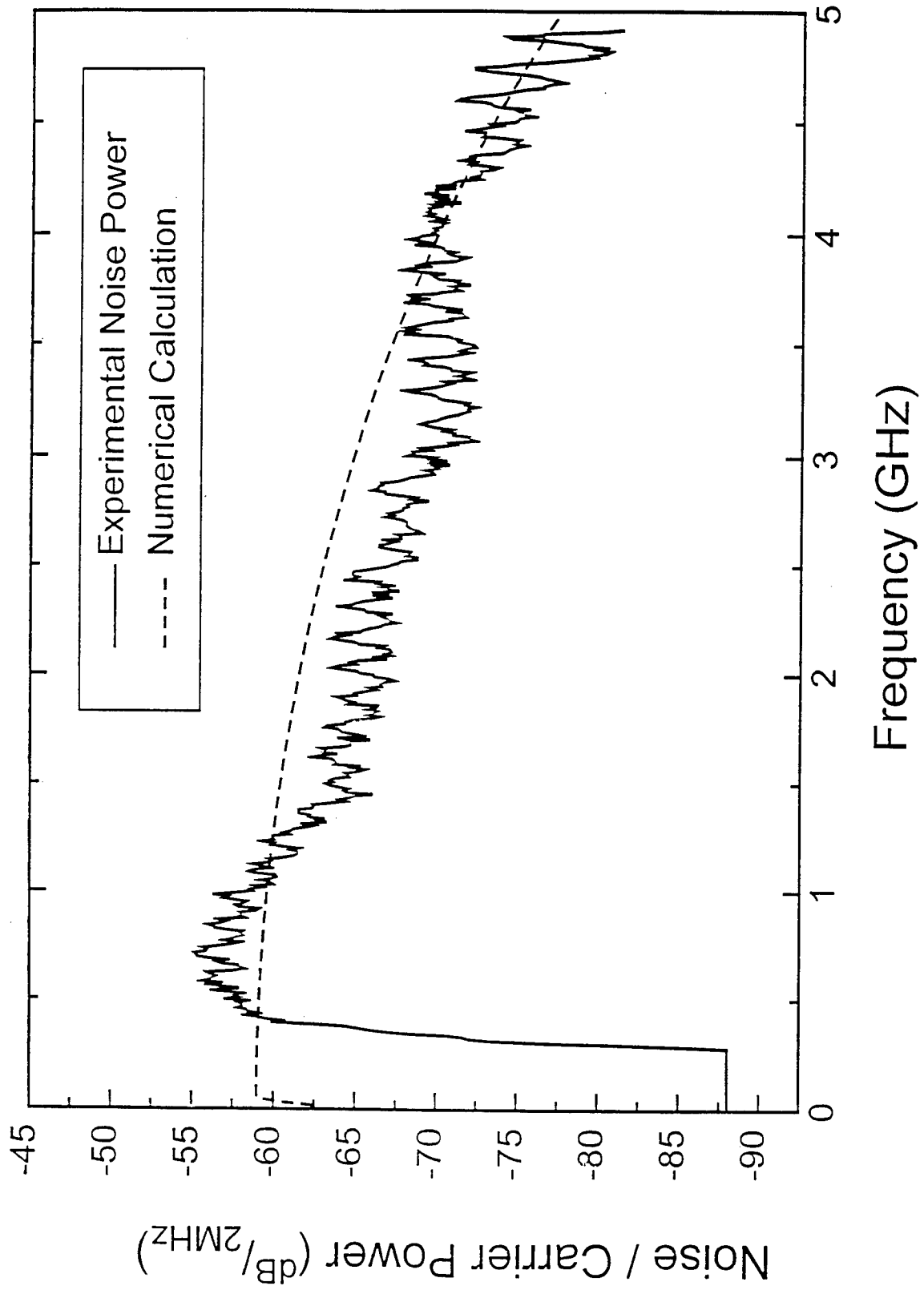












***MISSION  
OF  
ROME LABORATORY***

Mission. The mission of Rome Laboratory is to advance the science and technologies of command, control, communications and intelligence and to transition them into systems to meet customer needs. To achieve this, Rome Lab:

- a. Conducts vigorous research, development and test programs in all applicable technologies;
- b. Transitions technology to current and future systems to improve operational capability, readiness, and supportability;
- c. Provides a full range of technical support to Air Force Material Command product centers and other Air Force organizations;
- d. Promotes transfer of technology to the private sector;
- e. Maintains leading edge technological expertise in the areas of surveillance, communications, command and control, intelligence, reliability science, electro-magnetic technology, photonics, signal processing, and computational science.

The thrust areas of technical competence include: Surveillance, Communications, Command and Control, Intelligence, Signal Processing, Computer Science and Technology, Electromagnetic Technology, Photonics and Reliability Sciences.